



The University of
Nottingham

UNITED KINGDOM • CHINA • MALAYSIA

Characterisation of Hydroxyapatite- Coated Titanium for Biomedical Applications

By

Lee Jiin Woei, MRes

A thesis submitted to the University of Nottingham for the degree of

Doctor of Philosophy

AUGUST 2014

Abstract

Orthopaedic implants function to replace or support damaged or diseased bone. Due to a global rise in demand, there is a need to prolong the service life of these implants. The current work focuses on crystallised hydroxyapatite (HA)-coated titanium (Ti) implants. One specific problem during the annealing of as-deposited amorphous HA, to induce crystallisation, is the formation of unwanted titanium oxide (Ti-O) species at the HA/Ti interface that leads to HA layer disruption. This necessitates the introduction of a diffusion barrier layer at the HA/Ti interface. Another reason for implant failure is bone disintegration around the implant; therefore enhancing early bone cell growth on the implant may be beneficial.

The current work investigates the radio-frequency magnetron co-sputtering (RF-McoS) method to coat silicon-substituted hydroxyapatite (Si:HA) on commercially pure Ti (CpTi) substrates, with and without a titanium nitride (TiN) barrier coating. Processed coatings were designated according to the sputtering targets used, namely HA/TiN, Si:HA, Si:HA/TiN and Si+O₂:HA/TiN (*i.e.* reactively sputtered Si:HA/TiN in a mixed Argon, Ar, and oxygen, O₂, atmosphere). The as-deposited amorphous HA layers were crystallised by annealing at 700°C for 2 hours and 4 hours in Ar/trace O₂ (sample set 1) or for 2 hours in pure Ar (sample set 2). Coatings were assessed using a combination of complementary analytical bulk and near-surface techniques, combined with *in vitro* biological tests using an MG63 cell line to appraise the early stages of osseointegration.

In both sample sets, coatings containing TiN were generally more effective at retarding the development of rutile (TiO₂). Coatings annealed in trace levels of O₂ (set 1) were more prone to delamination due to the development of Ti₂N. Better process control was achieved following annealing in pure argon (sample set 2), with Si:HA/TiN showing significantly improved cell proliferation, whilst most closely resembling stoichiometric HA. Cell trials demonstrated both sample sets to be biocompatible, despite variations in coating morphologies, crystallinities and stoichiometries reflecting the issues of process control. Suggestions on improving the process control of these orthopaedic implant coatings are discussed.

Achievements

Conferences

- May 2014 - Poster presentation for the 9th International Materials and Technology Conference and Exhibition (IMTCE 2014). Poster title: Increasing the lifetime of orthopaedic implants.
- Jul 2012 - Oral presentation for the 8th International Materials and Technology Conference and Exhibition (IMTCE 2012).
- Apr 2012 - Poster presentation for the Global Research Workshop. Won best poster award. Poster title: Increasing the lifespan of human joint implants.

Publications

- Spowage A.C., Brewitt N.P., Lee J.W. (July 2010), The Scanning Electron Microscope – A Tool for the Failure Investigator 20: 11-13, IMM Newsletter, Institute of Materials Malaysia.

Competitions

- Jun 2011 - 3rd place winner of the Research Showcase 2011 poster and presentation competition (UK campus). Represented the University in the regional final, the Vitae Midlands Hub Regional Poster Competition. Poster title: Increasing the Lifespan of Human Joint Implants. April 2010 - Research Showcase Poster competition finalist and winner of the students' choice award (Malaysia Campus). Poster title: Surface Matters – Orthopedic Implant Failure.

Acknowledgements

I would especially like to thank Prof. Paul Brown for his patience, help and belief in me. I would also like to thank Dr. Andrew Spowage, Prof. David Grant, Dr. Colin Scotchford and Dr. Md. Enamul Hoque for their expertise and encouragement during the project. I am grateful to the Malaysia Campus (UNMC) for granting the MIDAS scholarship, which enabled me to do a bi-campus PhD at both the UK and Malaysia campuses. I thank Mr. Graham Malkinson for making a large amount of Ti substrates and Dr. Nick Botterill of Eminence for coating the samples. I thank all the staff at Wolfson namely, Mr. Keith Dinsdale, Mr. Tom Buss, Mr. George Anderson (now retired), Mrs. Julie Thornhill, Mrs. Nikki Weston, Mr. Martin Roe and Dr. Nigel Neate and Dr. Trevor Almeida for the training, their humour, expertise and willingness to brainstorm.

I cannot thank enough the friends and colleagues at both campuses who have imparted skills and supported me with their understanding, suggestions, encouragement and support. So I would like to mention Miss Treshi Perera, Dr. Anwesha Fernandes, Mr. Hyung Jin Lim, Mrs. Marwa Abbas, Miss Mariem Meggouh, Dr. Xuanli Moles, Dr. Deen Zhang, Mr. Matthew Moles, Mrs. Chunling Li, Miss Ruth Smith, Dr. Shanti Ayob, Dr. Christina Chin, Dr. Britto Satheesh, Dr. Tee Choun Zhi, Miss Yvonne Teoh, Miss Azlina Kassim, Miss Cheng Lim, Mr. Jen Haw Chong, Dr. Samuel Coe, Dr. Andy Patman, Mr. Nigel Mayglothling and many many others. I would especially like to thank Dr. Sami Hasan Quzalbash because he is awesome. Last but not least I thank my parents for the sacrifice they endured.

My bi-campus project along with the high percentage of international students at Nottingham University has been a beautiful experience that I will never forget.

Table of Contents

Abstract.....	i
Achievements.....	ii
Acknowledgements	iii
List of abbreviations	viii
List of tables.....	xi
List of figures.....	xiv
Chapter 1 Introduction.....	1
1.1 Research significance	3
1.2 Aim and objectives	7
1.3 Hypotheses.....	8
1.4 Thesis outline	9
Chapter 2 Literature Review	12
2.1 The structure and growth of bone	13
2.1.1 Basic structure of bone.....	13
2.1.2 Composition of bone.....	14
2.1.3 Bone cell growth on implant surfaces.....	15
2.1.4 Host response to biomaterial implants	16
2.2 Historical development of biomaterials.....	18
2.3 Current materials used in implants	20
2.4 Apatite and hydroxyapatite	23
2.4.1 Hydroxyapatite (HA) coatings.....	25
2.5 The role of silicon (Si) in the body	28
2.5.1 Silicon (Si) and silica (SiO ₂) substituted hydroxyapatite	29
2.6 Dissolution of Si-substituted HA	31
2.7 Titanium Nitride (TiN) as a barrier layer	32
2.8 Deposition techniques.....	33
2.8.1 Magnetron sputtering (MS).....	35
2.8.2 Radiofrequency magnetron sputtering (RF-MS)	37
2.9 Summary	38
Chapter 3 Experimental Methodology.....	40
3.1 Titanium (Ti) substrate preparation	40

3.1.1	Profilometry	42
3.2	Thin film deposition using magnetron sputtering (MS)	43
3.2.2	Sample sets and MS deposition conditions.....	44
3.2.3	Post deposition heat treatment (annealing)	48
3.3	Sample characterisation.....	50
3.3.1	X-ray diffraction (XRD)	50
3.3.2	Scanning electron microscopy / Energy dispersive X-ray spectroscopy (SEM/EDX)	54
3.3.3	X-ray photoelectron spectroscopy (XPS)	65
3.3.4	Reflection high energy electron diffractometry (RHEED)	69
3.4	<i>In vitro</i> cytocompatibility	73
3.4.1	Cell seeding and growth initiation	74
3.4.2	Metabolic Activity Assay (AlamarBlue™)	74
3.4.3	Alkaline Phosphatase Assay	75
3.4.4	DNA Hoechst Assay	77
3.4.5	Statistical Analysis.....	78
3.4.6	Cell imaging using SEM	79
3.5	Coating dissolution experiments	81
3.6	Summary	81
	Chapter 4 Results and Discussion – Set 1 Samples	83
4.1	Overview of results	86
4.2	GA-XRD investigations.....	88
4.2.1	HA/TiN coatings	88
4.2.2	Si:HA coatings	89
4.2.3	Si:HA/TiN and Si+O ₂ :HA/TiN coatings	91
4.3	SEM/EDX investigations	92
4.3.1	As-deposited coatings	93
4.3.2	HA/TiN coatings	94
4.3.3	Si:HA coatings	97
4.3.4	Si:HA/TiN coatings	100
4.3.5	Si+O ₂ :HA/TiN coatings	102
4.3.6	Summary of SEM/EDX investigations	104
4.4	RHEED investigations.....	106
4.5	XPS investigations	108

4.5.1	As-deposited coatings	110
4.5.2	Annealed coatings	111
4.6	Biological cell study	113
4.6.1	AlamarBlue (cell toxicity) tests	114
4.6.2	SEM observations of the cells.....	115
4.7	Coating dissolution studies	123
4.8	Summary of results.....	130
Chapter 5 Results and Discussion – Set 2 Samples.....		132
5.1	GA-XRD investigations.....	133
5.1.1	HA/TiN coatings	133
5.1.2	Si:HA coatings	134
5.1.3	Si:HA/TiN and Si+O ₂ :HA/TiN coatings	135
5.2	SEM/EDX investigations	138
5.2.1	Annealed coatings	138
5.3	Biological cell study	141
5.3.1	SEM observations of the cells.....	142
5.3.2	ALB.....	148
5.3.3	DNA Hoechst assay	149
5.3.4	ALP	150
5.4	Coating dissolution studies	151
5.5	Summary	153
Chapter 6 Overall Discussion		156
6.1	GA-XRD	158
6.1.1	As-deposited coatings	159
6.1.2	Annealed coatings	160
6.2	SEM/EDX.....	165
6.2.1	As-deposited coatings	166
6.2.2	Coatings annealed for 2 h (sample sets 1 and 2).....	167
6.2.3	Coatings annealed for 4 h (sample set 1)	168
6.2.4	Delamination.....	170
6.3	RHEED and XRD comparison.....	171
6.3.1	As-deposited coatings	172
6.3.2	Annealed coatings	172

6.4	XPS investigations	172
6.5	Biological cell study – set 1	176
6.5.1	ALB tests	176
6.5.2	SEM imaging of cells.....	177
6.6	Biological cell study –set 2	177
6.7	Dissolution study.....	180
6.7.1	Set 1	181
6.7.2	Set 2	181
Chapter 7 Conclusions.....		184
Chapter 8 Further Work.....		190
Chapter 9 References.....		192
Chapter 10 Appendix.....		208

List of abbreviations

Abbreviation	Full name
A	Adenine
ACP	Amorphous calcium phosphate
Adv C	Adventitious carbon
AFM	Atomic force microscopy
ALB	Alamar Blue
ALP	Alkaline phosphatase
ANOVA	Two-way analysis of variance
Ar	Argon
at%	Atomic percentage
Au	Gold
BA	Biological apatite
BE	Binding energy
BSE	Backscattered electrons
C	Carbon
Ca/P	Calcium phosphate ratio
Ca ²⁺	Calcium ions
CaCO ₂	Calcium carbonate
CaP	Calcium phosphate
CaTiO ₃	Perovskite
CDMEM	Dulbecco's Modified Eagle Medium
CFUB-MS	Closed field unbalanced magnetron sputtering
CHDA	Calcium-deficient hydroxyapatite
Co-Cr	Cobalt-chromium
Co-Cr-Mo	Cobalt-chromium-molybdenum
CpTi	Commercially pure titanium
Cu	Copper
DC	Direct current
DCPA	Dicalcium phosphate anhydrate
DCPD	Dicalcium phosphate dihydrate
ddH ₂ O	Double distilled water
ECACC	European Collection of Cell Cultures
ECM	Extracellular matrix
EDTA	Ethylenediaminetetraacetic acid
EHP	Electron-hole pair
ELI	Extra-low interstitial
EPD	Electrophoretic deposition
FDA	USA Food and Drug Administration
Fe	Iron
Fe ₂ O ₃	Hematite
FEG-ESEM	Field electron gun – environmental scanning electron microscopy
FET	Field effect transistor
GA-XRD	Glancing angle X-ray diffractometry
h	Hours
HA	Hydroxyapatite

HAS	Hemispherical analyser
HBSS	Hank's balanced salt solution
HEPES	4-(2-hydroxyethyl)-1-piperazineethanesulfonic acid
HMDS	Hexamethyldisilazane
HOB	Human osteoblast
ICDD	International Crystal Diffraction Data
ICSD	Inorganic Crystal Structure Database
IMS	Industrial Methylated Spirit
ISO	International Organisation for Standardisation
ISO	Isopropanol
LaB ₆	Lanthanum hexaboride
MCMPM	Monocalcium phosphate monohydrate
MS	Magnetron sputtering
MTT	3-(4, 5-dimethylthiazolyl-2)-2, 5-diphenyltetrazolium bromide
n	Sample number
Nb	Niobium
Ni	Nickel
O ₂	Oxygen
OCP	Octacalcium phosphate
OsO ₄	Osmium tetroxide
PE	Photoelectron
PLD	Pulsed laser deposition
PMMA	Poly(methyl) methacrylate
PO ₄ ³⁻	Phosphate groups
R _a	Surface roughness
RF	radiofrequency
RF-MS	Radio-frequency magnetron sputtering
RF-McoS	Radio-frequency magnetron co-sputtering
RHEED	Reflection high energy electron diffractometry
RPM	Revolutions per minute
RSF	Relative sensitivity factors
S.D.	Standard deviation
SAED	Selected area electron diffraction
SBF	Simulated body fluid
sccm	Standard cubic centimetres per minute
SE	Secondary electrons
SEM	Standard error mean
SEM/EDX	Scanning electron microscope / energy dispersive X-ray spectroscopy
Si	Silicon
Si:HA	Silicon-substituted hydroxyapatite
Si:HA/TiN	Silicon-substituted hydroxyapatite on titanium nitride
Si+O ₂ :HA	Silicon-substituted hydroxyapatite fabricated in Ar/O ₂ environment
Si ⁴⁺	Silicon ion
SiC	Silicon carbide
SiO ₂	Silica
SiO _x	Silicon oxide

SS	Stainless steel
T	Thymine
TCE	Thermal coefficient of expansion
TCP	Tricalcium phosphate / tissue culture plate
TEM	Transmission electron microscope
Ti	Titanium
Ti ₂ O ₃	titanium (III) oxide
Ti ³⁺	Titanium ion
Ti6Al4V	Ti with 6 wt% Aluminium and 4 wt% Vanadium
TiN or Ti ₂ N	Titanium nitride
Ti-O	Titanium oxide
TiO ₂	Rutile
TJR	Total joint replacement
W	Tungsten
W	Watt
wt%	Weight percent
XPS	X-ray photoelectron spectroscopy
XRD	X-ray diffractometry
θ	Angle theta
λ	Wavelength
$\Phi(\rho z)$	Phi-Rho-Z

List of tables

Table 2-1 The hierarchical structure, length scale and constituents of bone ^{1; 48}	15
Table 2-2 Overview of biomaterials and biomedical implants ^{1; 55}	22
Table 2-3 The biological importance of main calcium phosphate (CaP) compounds. Adapted from Bohner and Koch ^{40; 84}	27
Table 2-4 Selected coating techniques normally used for HA and TiN deposition. Adapted from ³³	34
Table 3-1 Summary table of the steps used during grinding and polishing of the commercially pure Ti discs for coating.	42
Table 3-2 Rig parameters used for sample set 1. Pre-sputter etching was first performed for all substrates, followed by TiN interlayer deposition, and lastly the simultaneous deposition of substituted and HA layer. Information that is not available is marked with N/A ¹ and information that is not applicable is marked with N/A ² . Abbreviation used is standard cubic centimetre per minute (sccm).	46
Table 3-3 Rig parameters used for sample set 2. Pre-sputter etching was first performed for all substrates, followed by TiN interlayer deposition, and lastly the simultaneous deposition of substituted and HA layer. Unavailable information is marked with N/A ¹ and information that is not applicable is marked with N/A ² . Abbreviations used are standard cubic centimetre per minute (sccm), watt (W), radiofrequency (RF), direct current (DC), revolutions per minute (RPM).	47
Table 3-4 Similar average Ca/P ratios were obtained using different magnifications.	61
Table 3-5 Representative results of the evolution of the coatings as a function of annealing time. Here, a SE images of a HA/TiN sample were depicted with a description of morphology, and complementary BSE image with Ca/P ratio. BSE images were used for EDX analysis as Si clumps were recognisable only using BSE (in silicate-substituted coatings).	64
Table 3-6 Representative table of the chemical species present in as-deposited samples.	68
Table 3-7 Representative SE images of MG63 cells grown on the samples. The following is day 1 at low (x1000) and high magnification (x4000) of the cell grown on a 2 h annealed sample.	81
Table 4-1 Summary of the characterisation data for the HA/TiN and Si:HA coatings. Key: Unavailable results (N/A); ^D indicates delaminated coating; Adventitious C (Adv. C,) perovskite (CaTiO ₃) and calcium carbonate (CaCO ₃).	86
Table 4-2 Summary of the characterisation data for the Si:HA/TiN and Si+O ₂ :HA/TiN coatings. Key: Unavailable results (N/A); ^D indicates delaminated coating; Adventitious C (Adv. C,) perovskite (CaTiO ₃) and calcium carbonate (CaCO ₃).	87
Table 4-3 Summary of crystalline phases in the annealed HA/TiN coatings.	89

Table 4-4 Summary of crystalline phases in the Si:HA/TiN and Si+O ₂ :HA/TiN samples	92
Table 4-5 Summary of surface Ca/P ratios obtained using XPS	109
Table 4-6 Day 1: Low (x1000) and high magnification (x4000) SE images of MG63 cells cultured on the 2 h annealed coatings.	117
Table 4-7 Day 1: Low (x1000) and high magnification (x4000) SE images of MG63 cells cultured on 4 h annealed coatings.	118
Table 4-8 Day 7: Low (x1000) and high magnification (x4000) SE images of MG63 cells cultured on 2 h annealed coatings.	120
Table 4-9 Day 7: Low (x1000) and high magnification (x4000) SE images of MG63 cells cultured on 4 h annealed coatings (full data set can be found in Table 10-3 in Appendix).	121
Table 4-10 Day 14: Low (x1000) and high magnification (x4000) SE images of MG63 cells cultured on 2 h ad 4 h annealed coatings.	122
Table 4-11 Low (x1000) and high magnification (x4000) SE images of MG63 cells cultured on 4 h annealed coatings on Ti control for 1, 7 and 14 days. ...	123
Table 4-12 EDX investigations of 2 h and 4 h annealed HA/TiN coatings following immersion in ddH ₂ O for 24 h	128
Table 5-1 Summary of 2nd set of samples. Key: Unavailable results are marked with N/A; D in superscript indicates delaminated coating; Adventitious C is abbreviated to Adv. C.	132
Table 5-2 Day 1: Low (x1000) and high magnification (x4000) SE images of MG63 cells cultured on the 2 h annealed coatings.	143
Table 5-3 Day 1: Low (x1000) and high magnification (x4000) SE images of MG63 cells cultured on the 2 h annealed coatings.	144
Table 5-4 Day 7: Low (1000X) and high magnification (4000X) of MG63 cells grown on 2 h annealed samples.	145
Table 5-5 Day 14: Representative image low (1000X) and high magnification (4000X) of MG63 cells grown on 2 h and 4 h annealed samples.	146
Table 5-6 The growth of MG63 cells on Ti for 1, 3, 7, and 14 days.	147
Table 10-1 The modified protocol combined the in-house method and that of Struers in order to successfully remove colloidal silica polishing liquid from the Ti substrates.	208
Table 10-2 XPS - raw data of all samples.	212
Table 10-3 Set 1, Day 7: Low (x1000) and high magnification (x4000) SE images of MG63 cells cultured on 4 h annealed coatings. All images have the same scale bar as the top two images.	213
Table 10-4 Set 1, Day 14: Low (x1000) and high magnification (x4000) SE images of MG63 cells cultured on 2 h annealed coatings. All images have the same scale bar as the top two images.	214
Table 10-5 Set 1, Day 14: Low (x1000) and high magnification (x4000) SE images of MG63 cells cultured on 4 h annealed coatings. All images have the same scale bar as the top two images.	215

Table 10-6 Set 2 Day 1: Low (x1000) and high magnification (x4000) SE images of MG63 cells cultured on 2 h annealed coatings. All images have the same scale bar as the top two images.....	216
Table 10-7 Set 2, Day 7: Low (x1000) and high magnification (x4000) SE images of MG63 cells cultured on 2 h annealed coatings. All images have the same scale bar as the top two images.....	217
Table 10-8 Set 2, Day 14: Low (x1000) and high magnification (x4000) SE images of MG63 cells cultured on 2 h annealed coatings. All images have the same scale bar as the top two images.....	218
Table 10-9 AlamarBlue.....	220
Table 10-10 DNA Hoechst Assay.....	224
Table 10-11 Alkaline phosphatase.....	228

List of figures

Figure 1-1 Process-structure-property interrelationship and the associated objectives.....	6
Figure 2-1 Structural organisation of bone ⁵⁴	14
Figure 2-2 The hexagonal structure of HA ⁷⁷	24
Figure 2-3 Schematic of a) phosphate tetrahedron, b) Ca(I) and c) Ca(II) polyhedral along with possible anion substitutions of Cl-, F- or OH- and their respective positions ⁷⁸	25
Figure 2-4 Schematic of Si-substituted HA ⁶⁶	30
Figure 2-5 Teer Coating Ltd closed field unbalanced magnetron arrangement ¹⁰¹	38
Figure 3-1 Schematic depicting the momentum transfer process, and the possible outcome as an atomic level. Picture on the left illustrates a pre-sputtering event and (right) shows the effects of immediately after collision, with sputtered atoms and secondary electrons.	44
Figure 3-2 Rig used for thin film deposition of Si-substituted HA films with TiN barrier layer. The substrates were arranged on the sample holder.	44
Figure 3-3 Schematic cross section of the coatings deposited on the Ti substrate. All coatings were exposed to Ar gas. Only Si+O ₂ :HA/TiN was exposed to a mixed atmosphere containing O ₂ and Ar. Samples are not drawn to scale.....	48
Figure 3-4 Schematic depicting the constructive interference of scattered waves ¹⁰⁶	51
Figure 3-5 Representative XRD diffraction patterns of a sample set and the formation of chemical species as a function of time.....	54
Figure 3-6 Schematic of the signals produced as a result of the interaction between an electron beam with a specimen ¹⁰⁹	55
Figure 3-7 An electron from the electron beam could be scattered elastically or inelastically at the nucleus. Above: Primary electron beam interaction with electrons in the specimen could lead to inelastically scattered electrons. An electron from the sample is ejected as a secondary electron. An ion is now formed. De-excitation of the ion could lead to the emergence of characteristic X-rays. Below: Elastic scattering at the nucleus leads to loss of energy in the form of an X-radiation called Bremsstrahlung ¹⁰⁹	56
Figure 3-8 a) Representative BSE image of an as-deposited HA/TiN sample; the pink box depicts the area at which EDX data was obtained; b) a table of element percentages of the target area, normalised to 100%.	62
Figure 3-9 a) BSE image of a HA/TiN sample annealed for 4h. Due to delamination, EDX was obtained from the “islands” that contain Ca and P; b) a table of element percentages of the target area, normalised to 100%..	62
Figure 3-10 Representative format of presentation that is used at the Results sections. EDX results of the Ca and P changes of a HA/TiN sample as a function of annealing time is depicted. The average Ca/P ratios are represented by the column graph and is associated with the primary y-axis	

(left y-axis). The Ca at% and P at% are represented by the scatter plot that is associated with the secondary axis (right y-axis). Error bars represent the standard error mean, SEM, (n=3).....	65
Figure 3-11 Low resolution spectrum of an as-deposited sample. RSF values allows the calculation of at% values, which in turn was used to obtain Ca/P values at the sample surface.	67
Figure 3-12 Deconvolved high energy spectra peaks with identified chemical species, all of which are present in the as-deposited samples.	68
Figure 3-13 Photograph of the RHEED stage; the three axes of movement are illustrated.	71
Figure 3-14 Schematic explaining the principle of the camera constant in TEM 118	72
Figure 3-15 Representative indexed diffraction rings of an annealed sample, indexed to HA and rutile.	73
Figure 3-16 Standard DNA curve. Using the equation of line of best fit, the slope of the curve was used to obtain DNA concentration. A best line fit with an $R^2 > 0.9$ was required in order for the value of the slope curve to be valid for use to calculate the DNA concentration of the samples.	78
Figure 3-17 Representative column graph of results for all assays. The error bars represent standard error of mean, n = 6. * represents the significance compared to the Ti control ($p < 0.05$), where a greater number represents a higher level of significance.	79
Figure 4-1 Representative GA-XRD patterns of the HA/TiN coatings; as-deposited, and annealed at 700°C for 2 h and 4 h, respectively.	89
Figure 4-2 Representative GA-XRD patterns of the Si:HA coatings; as-deposited, and annealed at 700°C for 2 h and 4 h, respectively.	90
Figure 4-3 Representative GA-XRD patterns for Si:HA/TiN and Si+O ₂ :HA/TiN samples: as-deposited, and annealed at 700°C for 2 h and 4 h, respectively.	92
Figure 4-4 Bar chart comparing average Ca/P ratios, and Ca and P at % values for the as-deposited coatings	94
Figure 4-5 HA/TiN coatings: as-deposited, and annealed at 700°C for 2 h and 4 h, respectively.	96
Figure 4-6 Bar charts comparing average Ca/P ratios, and Ca and P at % values for the HA/TiN coatings; as-deposited and annealed at 700°C for 2 h and 4 h.	97
Figure 4-7 Si:HA coatings: as-deposited, and annealed at 700°C for 2 h and 4 h, respectively	99
Figure 4-8 Bar charts comparing average Ca/P ratios, and Ca and P at % values for the Si:HA coatings; as-deposited, and annealed at 700°C for 2 h and 4 h.	100
Figure 4-9 Si:HA/TiN coatings: as-deposited, and annealed at 700°C for 2 h and 4 h , respectively	101

Figure 4-10 Bar charts comparing average Ca/P ratios, and Ca and P at% values for the Si:HA/TiN coatings; as-deposited, and annealed at 700°C for 2 h and 4 h , respectively.....	102
Figure 4-11 Si+O ₂ :HA/TiN coatings: as-deposited, and annealed at 700°C for 2 h and 4 h, respectively.....	103
Figure 4-12 Bar charts comparing average Ca/P ratios, and Ca and P at% values for the Si+O ₂ :HA/TiN coatings; as-deposited, and annealed at 700°C for 2 h and 4 h, respectively.	104
Figure 4-13 Representative RHEED patterns of a) An as-deposited sample, b-c) two different areas of a sample annealed at 700°C for 2 h (indexed for HA and rutile).	107
Figure 4-14 Bar charts comparing representative Ca/P ratios, and Ca and P at% values for as-deposited and annealed samples. The raw data for all the samples can be found in Table 10-2.....	110
Figure 4-15 Summary of high resolution XPS signatures for the as-deposited coatings (intensity x10 ¹).....	111
Figure 4-16 Summary of high resolution XPS signatures for the coatings (intensity x10 ¹) annealed at 700°C for 2 h and 4 h.	112
Figure 4-17 AlamarBlue tests performed on the coatings annealed at 700°C for 2 h and 4 h in Argon, for 1, 7 and 14 days. Ti and TCP substrates were used as control samples.	115
Figure 4-18 GA-XRD investigation of 2 h annealed HA/TiN coatings following immersion in ddH ₂ O for 24 h.	125
Figure 4-19 GA-XRD investigation of 4 h annealed HA/TiN coatings following immersion in ddH ₂ O for 24 h	126
Figure 4-20 SEM / EDX comparison of the annealed and dissolved coatings	129
Figure 5-1 Representative GA-XRD patterns of the HA/TiN coatings: as-deposited and annealed for 2 h.....	134
Figure 5-2 Representative GA-XRD pattern of Si:HA coatings annealed for 2 h.....	135
Figure 5-3 Representative GA-XRD pattern for Si:HA/TiN samples annealed for 2 h.....	136
Figure 5-4 Representative GA-XRD pattern for Si+O ₂ :HA/TiN samples annealed for 2 h.....	137
Figure 5-5 a) HA/TiN, b)Si:HA, c)Si:HA/TiN and d) Si+O ₂ :HA/TiN annealed at 700°C for 2 h.	139
Figure 5-6 Bar charts comparing average Ca/P ratios, and Ca and P at % values for the coatings that were annealed for 2 h.	140
Figure 5-7 AlamarBlue was used to measure the metabolic activity of the MG63 cells cultured on the various treated coatings. The error bars represent standard error of mean, n = 6. * represents the significance compared to the Ti control ($p < 0.05$), where a greater number of *represents a higher level of significance. All significant differences that were found in day 3 and was attributed to low Ti metabolic activity.	148

Figure 5-8 DNA Hoechst 33258 assay was used to measure the cell proliferation activity of MG63 osteosarcoma cultured on the various treated coatings. The error bars represent standard error of mean, $n = 6$. * represents the significance compared to the Ti control ($p < 0.05$).	150
Figure 5-9 Alkaline phosphatase (ALP) activity of MG63 osteosarcoma cells cultured on the various treated coatings. Data was normalised with corresponding DNA concentrations for each sample. The error bars represent standard error of mean, $n = 6$. No significant differences were found among the coatings ($p < 0.05$).	151
Figure 5-10 HA/TiN annealed for 2 h was dissolved for 24 h in ddH ₂ O (normalised at 36.8°; the TiN (111) peak)	152
Figure 5-11 Si:HA annealed for 2 h was dissolved for 24 h in ddH ₂ O	153
Figure 5-12 Si:HA/TiN annealed for 2 h was dissolved for 24 h in ddH ₂ O. The pattern is similar for similarly processed Si+O ₂ :HA/TiN (Figure 10-5), albeit with less intense TiO ₂ peaks and more intense Ti ₂ O ₃ peaks.	153
Figure 6-1 Representative SEM image showing HA on top of a growing MG63 cell, implicating that cell growth further delaminated the HA islands.....	177
Figure 10-1 EDX of polished Ti substrate showing no evidence of the polishing agent, colloidal silica a) SE image; b) Wt% and At% readings and c) EDX spectrum	209
Figure 10-2 XPS of polished Ti. Presence of trace levels of C and Zn.	210
Figure 10-3 XRD of Si:HA/TiN annealed for 2 h and 4 h.....	210
Figure 10-4 Representative EDX analysis of the non-island of delaminated annealed samples. (a) black box on the SEM image depicts the area at which EDX data was obtained and b) the resulting spectrum that presence of HA, Ti and N but no Si. c) White box on the SEM imaged depicts the area at which EDX data was obtained and d) the resulting spectrum that confirms Ti and O. Note the absence of Si.	211
Figure 10-5 Si+O ₂ :HA/TiN from set 2, annealed for 2 h was dissolved for 24 h in ddH ₂ O.....	219

Chapter 1 Introduction

Orthopaedic implants are biomedical devices implanted into the body to replace or augment the structural functionality of bone. Hence, the main role of all orthopaedic implants is to replace or provide structural support for damaged or diseased joints. Such implantable devices may be classified as being reconstructive implants, spinal implants, trauma / fixation devices or total joint replacements (TJR) ^{1; 2}. The development of these devices and associated surgical techniques have significantly enhanced the mobility, longevity and quality of life for millions of people around the world ^{1; 3}.

Estimation on the market value for the orthopaedic implant industry is varied but all sources have listed it to be in the billions of U.S. dollars ^{4; 5; 6; 7}. Demand for implants is increasing at approximately 10% per year ¹. TJR recipients are typically older patients (> 65 years) with degenerative diseases such as osteoarthritis, *i.e.* bone joint inflammation ^{1; 2}. The trend is changing due to factors which will be listed here. Examples include the lengthening of the average global life span ⁸, growing global population, increase in sporting injuries due to a rise in active lifestyles, an increase in sedentary working conditions / lifestyles which increases the risk of bone disease, and the push for faster healing times by clinicians ^{3; 5; 9; 10}. Also, emerging economies in the Asia Pacific, although currently occupying 10% of the world orthopaedic market, is increasingly gaining access to medical care ⁵.

The current generation of orthopaedic devices is more sophisticated than earlier versions, with fewer associated complications. However, 10-20% of implants fail within 10-15 years of service ^{1; 3}. Implant wear particles are the most common cause of failure ^{3; 6; 11}, producing symptoms such as allergic reactions, accumulation of particles in tissues, lesions and inflammation; all of which may lead to diseases such as Alzheimer's ⁸, wear-mediated osteolysis, *i.e.* the disintegration of bone cells following exposure to wear particles ¹⁰, and aseptic loosening of the implant ^{3; 12; 13; 14}. Implant replacement surgery or revision surgery is required to replace failed implants ¹. Compared to the initial procedure, a revision is more expensive ¹⁵, has a lower success rate, requires a higher level of surgical expertise and may incur additional damage to the tissue surrounding the implant ⁸. Due to the rise in demand, considerable research has been targeted at increasing biocompatibility and the effective lifetime of implants ^{6; 8; 16}.

Ti-alloys have been the most successful of materials used for load-bearing orthopaedic implant devices over the past 50 years ^{1; 3}. Hydroxyapatite (HA), with chemical formula $\text{Ca}_{10}(\text{PO}_4)_6(\text{OH})_2$, is chemically very similar to mineral bone, and hence is of interest as an implant coating, with a view to increase bone cell growth ^{1; 3; 17}. In recent work ^{18; 19}, silicon (Si) substitution of HA has been used in the attempt to further enhance HA efficacy, the rationale being that Si is important for bone mineralisation. The addition, a bioinert, thermodynamically stable and hard-wearing titanium nitride (TiN) interlayer ²⁰ may increase resistance to the generation of wear particles ²¹.

The most common commercial method used to deposit HA coatings on Ti is plasma spraying^{22; 23}. However, concerns regarding structural integrity and coating adherence may compromise long-term viability^{24; 25}. RF-MS has been shown to overcome the problems associated with plasma spraying^{24; 25}.

The model system adopted for this work is silicon (Si)-substituted HA-coated Ti, with titanium nitride (TiN) as an interlayer diffusion barrier. The role of a TiN barrier layer is appraised to assess its ability to retard the formation of unwanted chemical species during post-deposition processing that may disrupt the HA layer^{26; 27}. The structural integrity of Si-substituted HA/TiN coatings produced by RF-MS, as-deposited and annealed post-deposition, will be appraised in this work, combined with appropriate cell trials to appraise the initial stages of cell growth and apposition.

1.1 Research significance

Orthopaedic implants are used by millions around the world. Due to global changes the demand for these implants is rising^{1; 6} and research is currently being done to mitigate the issues such as implant rejection symptoms and revision surgery^{3; 6}. HA coatings on titanium (Ti)-alloy may develop unwanted titanium oxide species following post-deposition heat treatment. For example, rutile (TiO₂) scale formation acts to disrupt the HA and leads to coating delamination^{27; 28}. TiN may act as an effective diffusion barrier²⁹ between the HA and Ti due to its properties such as bioinertness^{20; 27}.

Bioactive coating properties, including that of HA and Si-substituted HA, that provide optimum cellular response and best clinical performance are not yet determined ¹⁷. The mechanism of osteoinduction by calcium phosphate compounds are yet to be known. The fabrication (coating) and post-deposition processes affect the properties of a biomaterial, such as surface roughness, chemical composition, crystallinity, topography, Ca/P ratio ^{30; 31}, and dissolution ³². High dissolution may lead to coating degradation ³³. All these properties affect the essential initial interaction and growth of bone cells on an implant ^{13; 30; 34; 35}. Having further understanding of the process-structure-property relationship would provide guidelines for implant design and control ¹⁷, such as controlling its bioinertness or bioactivity depending on the intended application ³⁶. The process-structure-property interrelationship is summarised in

The HA coating for implants must meet the requirements outlined by the International Organisation for Standardisation (ISO) and the USA Food and Drug Administration (FDA) ¹⁷. The specifications include calcium-phosphate ratio (Ca/P) ratio, crystallinity, phase composition, and surface texture ¹⁷. The surface and bulk of a sample have different properties therefore complementary surface-sensitive and bulk analytical techniques must be utilised ³⁷. The knowledge gained will have a wide variety of applications such as in the dental field. Although commercially pure titanium (CpTi) is not ideal for load-bearing implants, purity of the substrate will limit the amount of

variables in the annealed prototype biomaterial; the knowledge gained will serve as fundamental knowledge prior to moving up to more complex alloys such as Ti6Al4V.

In this context, the appraisal of Si-substituted HA coatings on Ti substrates, combined with the use of titanium nitride (TiN) diffusion barrier layers³⁸, is a novel area of research. Accordingly, this project aims to characterise the development of such Si-substituted HA/TiN/Ti, as a function of processing, and to obtain information on the early stages of biological reaction. The aim is to gain understanding of the processes that affect the structure and properties of the Si-substituted HA/TiN/Ti system, in order to gain improved control of such biomaterial design, to enhance integration into the body and extend its functional lifetime.

Knowledge gained from this research programme will cover diverse areas such as the crystallography and physical chemistry of biomaterial coatings, the principles of materials characterisation techniques including X-ray diffractometry (XRD) and electron microscopy, along with aspects of biological cell culturing. It is suggested that the findings from this work programme may assist in the development of effective strategies for the treatment of wear-mediated osteolysis.

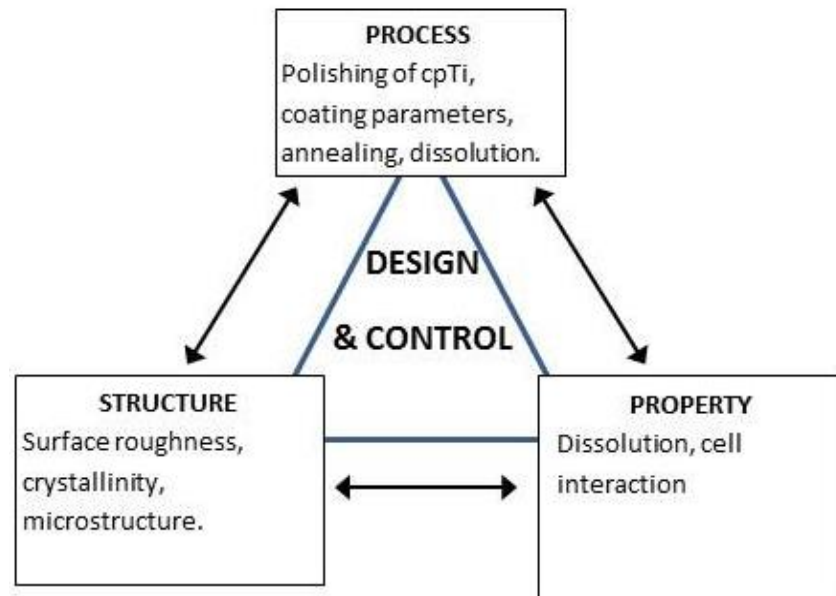


Figure 1-1 Process-structure-property interrelationship and the associated objectives

1.2 Aim and objectives

The limited lifespan of orthopaedic implants coupled with increasing global demand have caused the occurrence of implant failure to rise^{3; 8}. Modification of current existing implant coatings such as HA may prolong the service life of Ti-based orthopaedic implants. RF-MS has the ability to produce thin and well-adhered coatings which may alleviate the problem of HA delamination and particle release¹⁸. Enhancement of bone growth in the early stages of implantation may lead to prolonged lifespan^{34; 39}. Stoichiometric HA is ideal for bone growth^{40; 41}. Si is an essential mineral⁴² and its substitution trace concentrations in stoichiometric HA has been known to enhance cell growth⁴³. Diffusion between HA coating and Ti substrate could cause TiO₂ formation that disrupts the HA and inhibits bone maturation⁴⁴; a TiN interlayer may prevent the diffusion from occurring⁴⁵. The fabrication (coating) and post-deposition processes, such as annealing, affect properties such as chemical composition, topography^{30; 31}, and dissolution³². Dissolution includes the ability of the HA coating to release its Ca²⁺ and P⁴⁺ components that are essential for bone proliferation and mineralisation³². All these properties affect the essential initial interaction and growth of bone cells on an implant^{13; 30; 34; 35}.

The aim of this proof-of-concept work was to appraise the process-structure-property interrelationship of HA and novel Si-substituted HA coatings on Ti, with and without a TiN barrier layer, with regard to its biocompatibility and potential as an orthopaedic implant material. The objectives were as follow:

1. To prepare HA and 2 weight percent (wt%) Si-substituted HA coatings on Ti substrates, with and without a TiN barrier layer, using the technique of radio frequency magnetron co-sputtering (RF-McoS). As the project was preliminary, in order to limit variables, cpTi substrates were used instead of Ti alloys.
2. To appraise the morphology, structure and chemistry of the as-deposited coatings and the effects of post-deposition heat treatments.
3. To assess the dissolution processes of the annealed coatings.
4. Due to differences in surface and bulk properties, the project aimed to use a range of complementary near-surface (RHEED and XPS) and near-bulk characterisation (GA-XRD and SEM/EDX) techniques.
5. To assess the *in vitro* biological response of bone-like MG63 cells to these coatings.

1.3 Hypotheses

A range of hypotheses underpin this experimental programme. Accordingly, it is proposed that:

1. Si substitution of nanocrystalline stoichiometric HA is beneficial to bone-like cell growth and apposition, compared to unsubstituted HA.
2. TiN acts as an effective barrier layer to prevent unwanted oxidation of Ti substrates and Ti-O scale formation upon high temperature annealing.

1.4 Thesis outline

The Literature review (Chapter 2) outlines the macrostructure and microstructure of bone, with focus on initial cellular activity of the biological environment in response to an orthopaedic implant, such as osteoblast proliferation and differentiation. A brief timeline of the evolution of metallic orthopaedic implants is then given, leading to a description of current materials used for implants. Attention is given to hydroxyapatite-coated titanium (HA/Ti) implants, strategies for silicon (Si) substitution, and the role of titanium nitride (TiN) diffusion barriers. An overview of apatite minerals is also presented, covering the forms of apatite within natural bone and how stoichiometric HA has been developed as a commercial coating for implants. The role of silicon as an essential trace mineral for healthy bone growth is also reviewed, along with a review of studies that attempted to substituted HA with Si using silica (SiO_2). The processing technique of radio frequency magnetron co-sputtering (RF-McoS) is then outlined in terms of its underpinning principles of operation and advantages as a coating method. Finally, the chapter emphasises the importance of the process-structure-property relationship and the need for systematic appraisal of such biomedical coatings, with regard to morphology, structure, chemistry and cellular response, as a function of their processing histories.

The Experimental Methodology section (Chapter 3) initially outlines the protocol for polishing commercially pure titanium (CpTi) substrates. The target materials of TiN, HA and SiO_2 , and their associated RF-MS coating

parameters, are then described. The as-deposited coatings were then annealed at elevated temperature of 700°C, for 2 and 4 hours (h), in flowing argon (Ar); and hence the furnace arrangements used are described. The underpinning principles of operation of each characterisation technique utilised, *i.e.* X-ray diffractometry (XRD), scanning electron microscopy (SEM) with energy dispersive X-ray (EDX) analysis, X-ray photoelectron spectroscopy (XPS) and reflection high energy electron diffraction (RHEED) are then described, and examples of processed data are presented. The osteoblast-like MG63 cells was used as a model system to assess for improved biocompatibility. The appraisal of cell morphology and growth, for the same number of incubation days, as assessed using Scanning electron microscopy (SEM), is also described. Coating dissolution experiments, performed by incubating annealed coatings for 24 h in double distilled water (ddH₂O), are also described.

Two Results and Discussion chapters (Chapters 4 and 5) are then presented, describing the characterisation of the MS target materials, the determination of the Ca/P ratio for the appraisal of HA stoichiometry, the chemical and structural characterisation of the as-deposited and annealed coatings, the outcomes of the dissolution experiments, and the *in vitro* biocompatibility assessments, along with relevant statistical analysis, as compared with the SEM observations of bone-like cell growth and mineralisation on these coatings.

The overall results are then discussed (Chapter 6) in the context of the process-structure-property interrelationship, and compared with existing literature. In particular, the results of the complementary analytical techniques of glancing angle XRD (GA-XRD) and RHEED, and SEM/EDX and XPS are compared. The biocompatibility data is then reviewed. Finally, the conclusions (Chapter 7) drawn from this study are then presented, along with a Future Work section (Chapter 8) suggesting strategies for the continued improvement of orthopaedic coatings.

Chapter 2 Literature Review

This review is concerned primarily with titanium (Ti) alloy based biomaterials and hydroxyapatite (HA) coatings. The clinical performance of orthopaedic biomaterials and their use for a range of new applications had increased significantly over the past 50 years ³. Stringent requirements are placed on a material for its use in the biological environment ^{1; 46}. Materials for orthopaedic applications ideally need a similar elastic modulus to that of bone, high resistance to mechanical damage, high corrosion resistance, low toxicity, good overall biocompatibility, appropriate wear resistance and thermodynamic stability within the body ^{1; 3; 47}. Titanium and its alloys have demonstrated the closest fit to the above criteria, being especially true for long-term orthopaedic implantable devices ^{1; 3}. In particular, the exceptional biocompatibility of titanium alloys has been attributed to their very low solubility in body fluids and their ability to form a chemically stable surface passivating oxide film which provides corrosion resistance and reduces the risk of metal ion release ^{1; 3; 39}.

The bone-surface interaction is of particular importance to the successful implementation of a biomedical device ^{8; 39; 41}, hence it has become common place to coat Ti implants with a bioactive coating to enhance the bone-surface interaction ^{6; 16; 32; 33; 40}. Of primary importance to the performance of these coatings is the composition, surface roughness and surface energy which influence the initial interactions between the depositing bone cells and the implant surface; growth and maturation of immature bone cells on an implant

occurs shortly after implantation and the growth activity may determine the long-term service life of the implant ^{34; 39}. Although it has been mentioned that current implants have long lifespan, the lifespan still needs increasing as a result of global changes. As an example, by the end of 2030 the number of total knee replacements will grow by 673% and total hip replacements may increase by 174%, which means that the amount of painful and expensive revision surgeries will grow too ³.

2.1 The structure and growth of bone

In this section, the structure and growth of bone is described, with focus on the proliferation and mineralisation of bone cells during the early stages of growth. The skeletal system consists of ligaments, cartilage, tendons and bone, accounting for ~ 20% of the body's weight ⁴⁸. It functions to protect and support the soft organs of the body, support the body against the pull of gravity, and works with muscles to facilitate body movement.

2.1.1 Basic structure of bone

The macro and microstructure of bone has been thoroughly described in literature ^{1; 31; 49; 50; 51}. Bone is made mainly of apatite, collagen and water, comprising both compact (cortical) and spongy (trabecular) tissue. Compact (cortical) bone refers to the solid mass of bone, *e.g.* the shaft of long, weight-bearing bones like the femur which functions to carry a significant share of the skeletal load ⁴⁹. Spongy (cancellous) bone is less dense and hence lighter than

compact bone. Cancellous bone is usually found at the end of weight-bearing bones, like the femur, and functions to give supporting strength and flexibility, whilst providing the ability to generate bone marrow^{52; 53}.

2.1.2 Composition of bone

The hierarchical levels of bone are illustrated pictorially in Figure 2-1 and tabulated along with length scales in Table 2-1. Bone is a form of calcified tissue, comprising of cells and an extracellular matrix (ECM) which contains collagen as the main protein component, a small amount of organic phases, and hydroxyapatite (HA) crystals which fill the interstices between collagen fibrils⁵³.

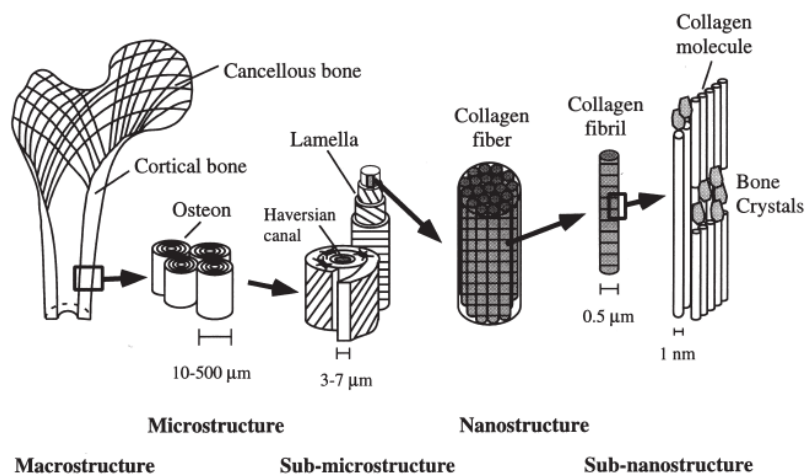


Figure 2-1 Structural organisation of bone⁵⁴

Table 2-1 The hierarchical structure, length scale and constituents of bone^{1; 48}

Hierarchical Structure	Length Scale	Constituents
Whole bone	cm – m	Cortical (compact) and cancellous (spongy) bone
Microstructure	10 - 500 μm	Single trabeculae, osteons, Haversian systems
Sub-microstructure	1-10 μm	Lamellae
Nanostructure	few hundred nanometers - 1 μm	Embedded apatite mineral and fibrillar collagen
Sub-nanostructure	< few hundred nanometers	Molecular structures of constituent elements such as collagen, non-collagenous organic proteins and mineral

2.1.3 Bone cell growth on implant surfaces

Osseointegration refers to the attachment and growth of bone cells and surrounding tissues into the implant. The surface properties of the implant, such as surface roughness, play a major role in determining the extent of osseointegration³⁰ along with chemistry and topography³. Among the building blocks of bone are osteoblasts (bone-forming cells), osteoclasts (which break down or resorb bone) and osteocytes (mature bone cells). They regulate the process of homeostasis, *i.e.* the growth, development, repair and remodelling of bone^{48; 54}. Particular attention is now given to the role of osteoblasts, located within the matrix which function to manufacture the organic components of the extracellular matrix, as well as compact bone and spongy bone⁴¹. The process of bone formation is alternatively termed

osteogenesis or ossification. Osteoblasts synthesize the organic components of bone, *i.e.* collagen, glycoproteins and proteoglycan ⁵⁵. Also, osteoblasts migrate from connective tissue to the membranes and deposit bony matrices around themselves to form mature osteocytes ³².

The post-implantation bone healing process, at the cellular level, involves various cells, a signal transduction pathway, hormones and growth factors; all of which have been described in detail in literature ^{8; 30; 35; 45; 55; 56}. The attachment, proliferation, differentiation and ultimately the long-term viability of these cells is mediated by ECM molecules such as fibronectin and associated integrins. The ECM molecules are available from the cell or from the cell culture media. Alkaline phosphatase (ALP) is expressed after differentiation and used as a marker ⁵⁵.

2.1.4 Host response to biomaterial implants

Biocompatibility is a property of the implant does not cause any toxic, allergic or inflammatory reactions within the body ^{1; 3}. Much has been written about the tissue-biomaterial response at the macro-level, primarily in connection with implants that are not biocompatible ^{3; 55}. If the implant material is toxic, the periprosthetic tissue dies ^{3; 55}. If the material is inert or biotolerant, *i.e.* biologically inactive and non-toxic, a fibrous tissue can form. Without true integration into the implant, the ultimate result is rejection. Examples of bioinert implants include Ti-alloys and cobalt-chromium (Co-Cr) alloys.

However, if the material is biologically active and non-toxic (bioactive), interfacial bone formation occurs, leading to osseointegration and implantation. Examples include implant materials coated with HA³.

The mechanism of early bone apposition on an HA-coated Ti implant has been described; early growth and maturation of immature cells on an implant may determine the long term service life of the implant³⁵. HA in body fluid releases calcium ions (Ca^{2+}) which re-deposit on to the HA surface, providing a positive electric charge. This positive charge prevents positively-charged white blood cells (macrophages) of the immune system from performing phagocytosis, despite HA being recognisable as a foreign body. Interstitial proteins with negative electric charge, such as vitronectin and fibronectin, then initiate bone cell adhesion and osseointegration⁵⁶. Negatively charged host bone marrow derived mesenchymal stem cells are repelled from the surface. Mesenchymal stem cells mature into osteoblasts and attach onto the HA surface through interactions with interstitial proteins and Ca^{2+} ions. The cells then secrete collageneous and non-collageneous matrices⁵⁷.

MG63 cells is a human-derived osteosarcoma cell line that has been used often to evaluate the biocompatibility of implant biomaterial surfaces^{8; 30; 31; 32; 58; 59; 60}. Its advantages are that it proliferates more rapidly than non-cancerous human derived bone cells, exhibits many osteoblastic traits during the early stages of apposition^{30; 31}, is well-characterised, and economical to purchase and culture. Hence, it is regarded as an osteoblast-like cell line. These cells

are resemble immature osteoblasts which exhibit phenotypic markers similar to that of mature osteoblasts^{30; 34}.

2.2 Historical development of biomaterials

The use of materials to help repair and augment the body have been documented for thousands of years^{1; 7; 61}. Before the 20th century, naturally-derived materials were used. For example, shaped wood was used as structural replacements for tissues lost during trauma or disease, whilst in ancient Egypt, seashells were used as teeth replacements⁶¹. In the early 20th century, synthetic polymers, metallic alloys and ceramics started to be used. Rapid advancements in technology and increased efficacy led to a range of applications such as dental restoratives, artificial hip joints and contact lenses. Advancements in molecular biology in the 1970s, genomics in the 1990s and proteomics in the 2000s contributed significantly to the design and development of the current range of biomaterials. Biomolecular enhancement of biomaterials refers to their bioactive components which utilise well-established molecular pathways to elicit a biological response. A commercially available example is the INFUSE Bone Graft device marketed by Medtronic, which combines bone morphogenetic protein along with synthetic components⁷.

The historical development of bone-related biomaterials, with focus on weight-bearing, total joint replacement implants, is now briefly described.

Arthroplasty, the surgical replacement of joints ⁸, initially made use of stainless steel for load-bearing, total joint replacement (TJR) implants. 316L stainless steel (also known as ASTM F138) comprising a ferrous matrix alloyed with carbon, molybdenum, nickel and chromium, was used primarily for temporary devices such as hip nails, fracture screws and plates. However, with the rise in total TJR surgery, it became evident that the very high modulus of stainless steel was unsuitable due to problems with stress-shielding and corrosion. Cobalt-chromium-molybdenum (Co-Cr-Mo) alloys (ASTM F75 and F799) were then developed, but high modulus and biocompatibility issues rendered this material unsuitable for load-bearing applications. Bone cements were used to fix the implant into bone. In order to resolve issues regarding the adverse effects of bone cement wear particles that may ultimately require revision surgery ¹⁵, the concept of uncemented implants was birthed in the 1960s ^{22; 33}. Uncemented implants rely on biological fixation using the natural bone cells of the body. Bioactive compounds, such as calcium phosphate coatings and HA, when coated on implants were found to increase bone cell attachment and proliferation ²². Research on the positive effects of silicon (Si) on bone metabolism resulted in the development of Si-substituted calcium phosphates in the 1990s ⁶². Backtrack to the mid-1970s, Ti-alloys started to gain popularity due to their lower modulus, being closer to that of bone, combined with good levels of specific strength, biocompatibility, superior osseointegrative ability and higher corrosion resistance. Commercially pure titanium (CpTi; ASTM F67) was the first Ti product to be used due to its naturally-occurring surface passivating oxide film which provides corrosion resistance and reduces the risk of metal ion release ^{1; 3; 39}.

CpTi, however, exhibits limited specific strength and hence limited its use to *e.g.* dental implants, pacemaker cases and hip cup shells. The need to improve on strength for load-bearing applications for TJR led to the development of an alloy originally developed for aerospace applications, *i.e.* Ti-6Al-4V extra-low interstitial (ELI) alloy (ASTM F136) made from Ti with 6 wt% Al and 4 wt% V. It exhibits an elastic modulus of ~ 110 GPa which is half that of 316L stainless steel. Whilst it has been used successfully for TJR, it was found that V is cytotoxic and causes adverse tissue reaction. Therefore, iron (Fe) and niobium (Nb) were introduced as a replacement for V, with the development of Ti-6Al-7Nb and Ti-5Al-2.5Fe alloys. Other alloys were also developed incorporating Al additions, such as Ti-15Mo-2.8Nb-3Al and Ti-15Mo-5Zr-3Al. However, further studies found that both V and Al ions released from the alloys into the body could cause long-term health problems, such as osteomalacia (softening of the bones) ⁶³, Alzheimer's disease (a type of dementia ⁶⁴) and peripheral neuropathy (peripheral nerve damage). These circumstances led to developments of new and improved orthopaedic implant materials ⁸.

2.3 Current materials used in implants

Four major classes of materials, *i.e.* polymeric, metallic, ceramic and composite, have been used as biomaterials ^{1; 65}. Current advancements in nanotechnology ^{45; 66; 67}, tissue engineering ³² and biology allow for more flexibility and creativity in biomaterial design and the generation of new composites. For example, materials can now be enhanced biologically in order

to exploit particular, well-established, molecular pathways. For example, biomolecule-based surface modifications may be performed on nitinol, a nickel titanium metallic alloy that exhibits shape memory effect, with the aim of increasing its efficacy for osseointegration ⁶⁸. In the field of tissue engineering, three-dimensional scaffolds with tailored architecture may be made using artificial (bioactive glass) or natural materials (biodegradable polymers) to control the proliferation and differentiation of premature osteoblasts ^{7; 8; 32; 51}. Further, polymers are used commonly as inter-positional cementing materials between bone tissue and implant surfaces and can act as articulation bearing surfaces because they exhibit appropriate creep resistance, wear rates and yield stress. In these applications, certain high density polymers exhibit low wear rates and low coefficients of friction, making them particularly suitable as bearing surfaces. As a fixative for a structural interface, they can be cured *in vivo* and moulded into shape ⁶.

Even though there are hundreds of orthopaedic applications and numerous specialties, only a few types of materials dominate the market ¹. Metal alloys were developed initially to replace long bones as load bearing members and as fracture fixation devices due to their excellent combined properties of biocompatibility and ductility ⁶⁵. Indeed, the metals and alloys cited in “Historical development of biomaterials” are still in use today, *e.g.* Ti6Al4V, Co-Ni-Cr-Mo (ASTM F562) and Co-Cr-Mo (ASTM F75 and F 76). Table 2-2 provides a brief overview of the main biomaterials used and their functions.

Table 2-2 Overview of biomaterials and biomedical implants^{1; 55}

Implant	Material
Skeletal system	
Joint replacements e.g. hip, knee	Polyethylene, 316LV (stainless steel; SS), Titanium (Ti), Ti-6%Al-4%V (Ti64 or Ti6Al4V) alloy
Bone cement	Poly(methyl) methacrylate (PMMA)
Bony defect repair	Hydroxyapatite (HA)
Bone plate for fracture fixation	Cobalt-chromium (Co-Cr) alloy, 316LV (stainless steel; SS)
Dental implant	Calcium phosphate, polyethylene, Ti, Ti-Al-V alloy, SS
Cardiovascular system	
Catheter	Silicone rubber, Teflon, polyurethane
Blood vessel prosthesis	Polyurethane, Dacron, Teflon
Heart valve	Carbon, reprocessed tissue, SS
Organs	
Heart-Lung machine	Silicone rubber
Artificial kidney (hemodialyser)	Hydrogel e.g. Cellulose, polyacrylonitrile
Artificial Heart	Polyurethane
Skin repair template	Silicone-collagen composite
Senses	
Corneal bandage	Hydrogel, Collagen
Cochlear replacement	Platinum electrodes
Contact lens	Hydrogel, Silicone-acrylate

2.4 Apatite and hydroxyapatite

Apatite refers to a group of calcium phosphate minerals with variable amounts of Ca and P, which have varied structural and physical characteristics, as well as biocompatibility^{55; 66; 69}. Deviations in the Ca/P ratio are extensively studied to understand diseases such as dental caries and osteoporosis³⁴. Ca/P deviations can arise with subtle modifications to the method of preparation from their preparation chemistry^{55; 69}, to coating parameter⁷⁰, with annealing procedures acting to modify its crystallinity^{55; 71}. Calcium phosphates can exist in either an amorphous or crystalline state²³. Amorphous calcium phosphate has been reviewed extensively by Combes and Rey²³. Here, crystalline calcium phosphate is now discussed.

Much biomedical research has been performed on calcium phosphates that are unsubstituted, substituted with various ions, or combined with other phases, for a wide variety of applications^{8; 66; 67; 72}. For example, dicalciumphosphate is used in resorbable applications^{8; 55; 73}. The chemical formula for synthetic stoichiometric HA is $\text{Ca}_{10}(\text{PO}_4)_6(\text{OH})_2$ ^{32; 74}. The structure of crystalline stoichiometric HA⁷⁵ is now described. HA has a Ca/P molar ratio of 10:6 (1.67) and a hexagonal lattice with space group $\text{P6}_3/\text{m}$ ^{66; 76}. Its lattice parameters are $a = b = 9.4225 \text{ \AA}$ and $c = 6.8850 \text{ \AA}$ and it has two formula units per unit cell. Figure 2-2 illustrates the HA lattice structure.

Figure 2-3 describes the phosphate tetrahedron, Ca(I) and Ca(II) polyhedral. Ca(I), the calcium ions at site 1, are coordinated by nine oxygen (O) atoms which form a polyhedron. Ca(II) ions at site 2 are coordinated by five O atoms and one hydroxyl (OH) group, forming an octahedron. The Ca(II) ions have a coordination number of seven, one of which is weakly bonded to another O. Therefore substitutions could occur at the Ca(II) site. Centred hydroxyl ions (OH⁻) are positioned in columns parallel to the c axis. In the unit cell of HA, OH⁻ ions lie on the plane corners at equal intervals along perpendicular columns and are surrounded by six Ca²⁺ ions out of 10 in an hexagonal arrangement. The O²⁻ ions are located on the outer parts of the hexagonal structure. More details such as number of atoms per unit cell and atomic positions of the HA structure can be found in a review paper written by Evis and Webster⁶⁶.

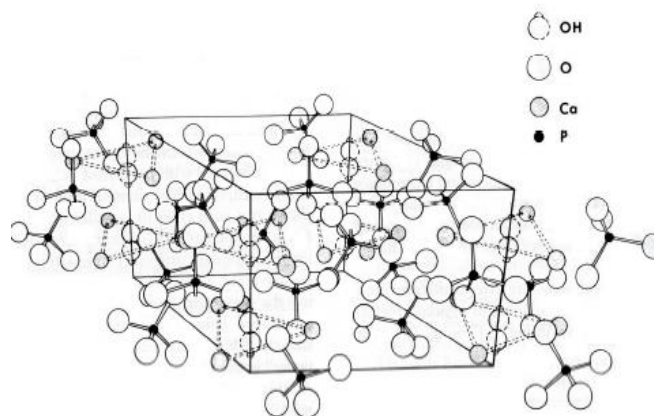


Figure 2-2 The hexagonal structure of HA⁷⁷

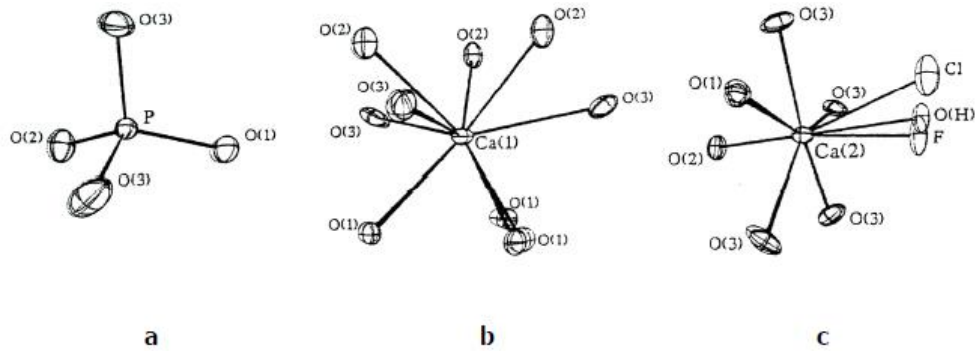


Figure 2-3 Schematic of a) phosphate tetrahedron, b) Ca(I) and c) Ca(II) polyhedral along with possible anion substitutions of Cl-, F- or OH- and their respective positions ⁷⁸

2.4.1 Hydroxyapatite (HA) coatings

Native, uncoated Ti alloy is usually insufficient for adequate bone cell attachment. Hence, implant surfaces are normally surface modified; an example being synthetic HA ^{1; 3; 36}. In order to influence healthy bone cell growth on the implant, a synthetic HA coating should resemble the properties of biological HA and not that of diseased *e.g.* osteoporotic bone ^{79; 80}. Experiments involving HA require an appraisal of the Ca/P ratio because Ca and P atoms are the most stable atoms present in calcium apatite and, most importantly, Ca/P ratio of a calcium phosphate compound is linked to its properties ^{34; 44; 47; 66; 81; 82; 83}. Different Ca/P ratios effectively determine the phase which affects the biomedical performance. In order to illustrate the importance of analysing for Ca/P ratio, below is a table of the ratios of different calcium phosphate compounds and their biocompatibility (Table 2-3)

Synthetic stoichiometric HA has a Ca/P ratio of 1.67 is biocompatible, osteoconductive, thermodynamically stable at physiological pH (7.4) and promotes healthy bone healing^{1; 3; 8; 32}, even in diseased bone⁵⁵. As can be seen (Table 2-3), naturally-occurring HA is poorly crystalline with an absence or near-absence of the hydroxyl group with various substitutions and vacancies^{23; 27; 48; 54}. Mimicking the exact structure and chemistry of biological HA would be ideal, but technology has yet to advance enough for researchers to be able to do so, but work is being done to move towards that goal and the work is based on the calcium phosphate compound, stoichiometric HA, that yields the significant and consistent biological results. Post-deposition treatment of a calcium phosphate coating may cause deviations in the Ca/P ratio which may lead to the formation of tricalcium phosphate (TCP) or other compounds⁸⁴. Therefore physical, structural and biocompatibility characteristics of HA in its bulk and nano-sized forms need to be researched^{55; 66; 69; 73}. Techniques used have been XPS or EDX^{73; 80}.

Table 2-3 The biological importance of main calcium phosphate (CaP) compounds. Adapted from Bohner and Koch ^{40; 84}.

Name	Formula	Ca/P	Biological relevance
Monocalcium phosphate monohydrate (MCPM)	$\text{Ca}(\text{H}_2\text{PO}_4)_2 \cdot \text{H}_2\text{O}$	0.50	It is very soluble and acidic. Therefore it is not biocompatible on its own. Used in combination with other CaP in commercial products.
Dicalcium phosphate anhydrate (DCPA) or Monetite	CaHPO_4	1.00	Biodegradable, osteoconductive, and biocompatible. May play a role in bone fracture healing.
Dicalcium phosphate dihydrate (DCPD) or Brushite	$\text{CaHPO}_4 \cdot 2 \text{H}_2\text{O}$	1.00	Osteoconductive, biocompatible and biodegradable. May be precursor of HA in bone. Large amounts cause inflammation.
Octacalcium phosphate (OCP)	$\text{Ca}_8\text{H}_2(\text{PO}_4)_6 \cdot 5\text{H}_2\text{O}$	1.33	Precursor of calcium phosphates in bones and teeth. Attempts to obtain OCP have been unsuccessful, slow crystallisation.
Calcium-deficient hydroxyapatite (CHDA)	$\text{Ca}_{10-x}(\text{HPO}_4)_x(\text{PO}_4)_{6-x}(\text{OH})_{2-x}$ ($0 < x < 2$)	1.33-1.67	Complex chemistry. Poorly crystalline, of submicron dimensions. Unlike natural HA, impurities are absent. Used in bone cements
Biological apatite (BA)	$\text{Ca}_{8.3}(\text{PO}_4)_4.3(\text{CO}_3-\text{HPO}_4)_{1.7}(\text{OH})_{0.3}$ BA=carbonated CDHA ($x=1.7$)	1.38-1.93	Hydroxyapatite of natural bone. Complex chemistry. Poorly crystalline with submicron dimensions,

			difficult to reproduce.
Tricalcium phosphate (phase β , whitlockite) (β -TCP)	$\text{Ca}_3(\text{PO}_4)_2$ (rhombohedral)	1.5	Obtained synthetically. Degradable in the body. Used as bone substitute / coating.
Tricalcium phosphate (phase α) (α -TCP)	$\text{Ca}_3(\text{PO}_4)_2$ (monoclinic)	1.5	Obtained by heating β -TCP above 1125°C . It is different to β -TCP in terms of crystallography, and more soluble. Used in bone cements.
Hydroxyapatite (HA)	$\text{Ca}_{10}(\text{PO}_4)_6(\text{OH})_2$	1.67	Formed using high temperature. Highly crystalline, most stable in aqueous solution, most biocompatible CaP compound. Most popularly used CaP for commercial products such as Endobon (Merck, Germany).
Amorphous calcium phosphate (ACP)	$\text{Ca}_x(\text{PO}_4)_y \cdot n\text{H}_2\text{O}$	1.2–2.2	Very soluble in liquid. May be used as main component in bone cements.

2.5 The role of silicon (Si) in the body

Si is a well characterised trace essential mineral ^{32; 42; 85}. Various *in vivo* and *in vitro* studies performed on Si ^{32; 70} have proven that it is an essential mineral for bone tissue formation ⁸⁶ and early calcification of bone cells ⁴², whilst stimulating collagen I formation ⁸⁵. Collagen I constitutes 90% of the extracellular matrix (ECM) in mature bone and mainly contributes to the

mechanical properties of bone⁸⁵. Si in high concentrations, *e.g.* 230 µg/ml in the *in vitro* study performed by Gough and colleagues, can lead to apoptosis, *i.e.* programmed cell death⁸⁷. Hence, it is important to regulate the amount of Si in the body by fabricating Si-containing biomaterials that mimic the naturally low concentration of this trace essential mineral.

2.5.1 Silicon (Si) and silica (SiO₂) substituted hydroxyapatite

Pure and ionised Si have both been tested as substitution candidates for enhancing the bioactivity of HA. Ever since Carlisle found that silicon (Si) is essential for bone cell mineralisation⁶², pure Si has been researched as substituents into bone graft materials such as calcium phosphates. Reviews of the work are listed^{17; 62}. Studies have found that Si substitution changes the structure of crystalline HA *in vitro* and *in vivo*^{18; 62; 88; 89}, which as a consequence may enhance the proliferation and mineralisation of human bone cells, or osteoblasts^{32; 70; 89}. Si substitution has been added to bioglasses³². However, questions have been raised about the true efficacy of Si-substituted calcium phosphates⁶².

Silicates, the anionic form of Si may be an alternative. Orthosilicic acid [Si(OH)₄], containing soluble silicon ion (Si⁴⁺) that is naturally present in water, as found to enhance the alkaline phosphatase and osteocalcin levels of on osteoblast-like MG63 cells⁸⁵. Alkaline phosphatase and osteocalcin are enzymes involved in osteoblast differentiation, and their concentrations are

measured to determine the extent of cell differentiation in *in vitro* tests^{32; 39; 58}. Silicon ion (Si^{4+}) substitution was found to enhance the formation of a crystalline surface apatite layer of HA after immersion in simulated body fluids (SBF)⁹⁰. Silicate groups ions (SiO_4^{4-}) is known to competitively replace the phosphate groups (PO_4^{3-}) of HA^{18; 91}. Therefore silica (SiO_2) was used in the present work as it may react with HA to form SiO_4^{4-} ⁹⁰. Substituting the Si at 2 wt% was chosen because substitution at higher wt% may increase the probability of crack propagation, unwanted TiO_2 formation, and decomposition following heat treatment^{18; 32; 66}. Too low wt% results in less substitutions; any change in structure may be too small to be quantified¹⁸. Microstructural changes to the HA has been linked to changes in biocompatibility^{18; 66}. Gauging the success of substitution could be done by assessing changes in, *e.g.*, lattice parameters or in diffraction peak positions via XRD^{19; 66; 92}, changes in surface topography (using SEM)^{90; 93} and Ca/P ratio (using EDX)¹⁸.

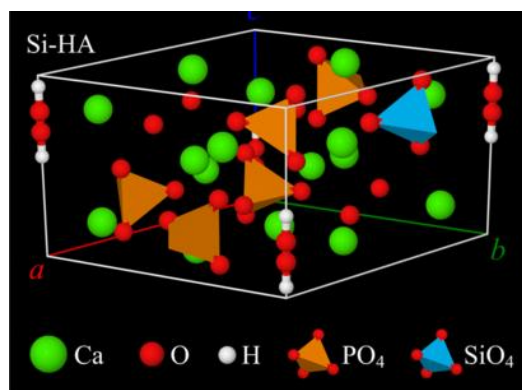


Figure 2-4 Schematic of Si-substituted HA⁶⁶

2.6 Dissolution of Si-substituted HA

The rate at which a biomaterial releases its own particles when immersed in body fluid may affect cellular growth and mineralisation^{24; 32; 62}. For example, Si^{4+} ions in solution have been found to be important for calcification and metabolism, dissolved Ca^{2+} has been associated with bone proliferation and differentiation and P^{5+} stimulates the matrix 1a protein that regulates bone formation³². Therefore dissolution behaviour of a coating may dominate the initial stages of interaction between the cell and the biomaterial, which ultimately influences long-term performance²⁴. Dissolution may be influenced by the coating properties such as surface roughness and crystallinity³², presence of amorphous phases and presence of less stable calcium phosphates prior to exposure to fluids²⁶. The dissolution mechanism is unknown. Dissolved Si from a coating may have a direct impact on growth by its uptake by cells. Alternatively, it may have an indirect mechanism whereby substitution may change the physico-chemical characteristics of the coating, such as surface topography or grain size, which in turn affects the cells⁶². Hence, for this project, attempts were made to gauge the dissolution mechanism and assess changes to its properties. *In vitro* results may not necessarily reflect *in vivo* results⁶² due to factors such as choice of simulated biological fluid⁹⁴. Therefore, careful and well-informed assessments must be made during *in vitro* testing.

2.7 Titanium Nitride (TiN) as a barrier layer

HA is brittle and has low wear resistance, and hence has limited use as a bulk implant material for load-bearing applications^{27; 51; 69}. Coating processes and subsequent annealing procedures may induce ion diffusion between the HA and Ti, in turn create unwanted chemical species such as rutile (TiO₂), resulting in compositional and structural changes on the HA layer^{26; 95}. XRD study on a TiO₂/HA layer found unidentifiable peaks⁹⁵. Such compromise of the HA structure may influence the osseointegration of an orthopedic implant⁴⁴. The addition of a bioinert, undissolvable, hard barrier layer, *e.g.* titanium nitride (TiN), between the HA and Ti could mitigate these issues and increase the suitability of HA for load-bearing implant applications.

TiN is a biocompatible and bioinert ceramic, with high hardness and good corrosion and wear resistance^{20; 27}. Due to these qualities, it has been used as a diffusion barrier on Si-based integrated circuits²⁹ and as a wear-resistant coating on hip and knee implants^{3; 27}. Further, micro-photodiode arrays have been developed as subretinal implants to replace degenerated photoreceptor cells in the retina, within which TiN was used as a component⁹⁶.

In particular, various metallic alloys, such as Ti and Co-Cr alloys, have been coated with TiN, and this has successfully increased their corrosion and wear resistance, resulting in the inhibition of allergic reactions caused by ion release from the alloy into the physiological environment²⁷.

2.8 Deposition techniques

Different surface modification methods have been investigated to improve the osseointegration of Ti implants, including mechanical methods (*e.g.* shot peening), chemical methods (*e.g.* sol-gel) and physical coating methods (*e.g.* plasma spraying), all of which have been extensively reviewed ^{8; 16; 23; 32; 56}. Methods of establishing an HA layer on a substrate are sol-gel, hot isostatic pressing, biomimetic coating, laser deposition and thermal spraying ^{27; 33}. Plasma spraying of HA is the most common method for HA deposition ^{24; 27; 56}. Recommended reviews on HA deposition are ^{33; 84}. TiN and Si have been deposited using techniques such as plasma spraying ²⁷, pulsed laser deposition and electrophoretic deposition ³³. Magnetron sputtering (MS) has been regarded as an efficient method to produce coatings that are amorphous, with controlled crystallography and other properties ^{20; 27; 97}. For example, an *in vivo* study on dogs demonstrated that MS calcium phosphate on metal implants achieved equivalent or higher bond strengths, and percentage bone contact, at the bone–implant interface, as compared with plasma-sprayed HA ⁷⁶. Sputtering amorphous TiN allows the control of its crystallographic orientation and surface topography via post-deposition processes such as heat treatment ²¹. The advantages and disadvantages of a few deposition techniques are summarised in Table 2-4 below ³³.

Table 2-4 Selected coating techniques normally used for HA and TiN deposition. Adapted from ³³

Technique	Principle	Thickness	Advantages	Disadvantages
Sputter coating	Highly energetic ions bombard targets which causes particle removal, which then condense onto a substrate as a thin film.	0.5-3.0 μm	Uniform coating thickness on flat substrates; homogeneous coating; high adhesion	Line of sight technique; alteration of HA structure; non-uniform coating density; expensive; time-consuming
Pulsed laser deposition (PLD)	A high powered laser ejects material from a target and the resulting vapour condenses on the substrate. Uses repeated laser pulses to fabricate a thin film	0.05-5 mm	Produces amorphous and crystalline coatings; able to produce a wide range of multilayer coating; porous and dense coatings; able to restore complex stoichiometry; high degree of control on parameters	Line of sight technique, need surface pretreatment; lack of uniformity; particle or splashing deposition
Plasma spraying	Metal or ceramic powder is melted an ionised inert gas (plasma) and	< 20 μm	Reduced coating degradation; low cost; rapid deposition; fast bone	Poor adhesion; non-uniformity of coating density; phase and structure transformation due to high

	impinged at high temperature and velocity towards a surface		healing	temperature up to 1200°C
Electrophoretic deposition (EPD)	Colloidal particles are held in suspension using an electric field and coats an electrode.	0.1-2.0 mm	Good for ceramic coatings; uniform thickness; rapid; ability to coat complex shapes; low cost; highly adhesive HA or TiN coatings	Cracked coatings; coating may decompose due to high sintering temperature.
Sol-gel	Involves the formation of usually inorganic non-metallic solid coating from solution.	0.1-2.0 µm	Low temperatures; ability to coat complex shapes; high purity; good adhesion; relatively cheap.	High permeability; difficult to control porosity; cracked coatings; not suitable for industrial scaling.

2.8.1 Magnetron sputtering (MS)

A comprehensive review on the basics of magnetron sputtering is included ⁹⁸.

In the basic sputtering process, a cathode target is bombarded by energetic ions. The bombardment causes the removal, *i.e.* sputtering, of target atoms which condense onto a substrate, as a thin film. Secondary electrons (SEs) are simultaneously emitted from the surface of the target and these electrons

function to maintain the plasma. Magnetrons use a magnetic field configured parallel to the surface of the target, thereby constraining the motion of SEs to the vicinity of the target. One pole of the magnet is formed by a ring of magnets situated at the outer edge of the target, whilst the other pole is positioned at the central axis of the target. The SEs are therefore trapped, which increases the probability of ionizing electron-atom collisions. This acts to increase sputtering and hence deposition rates onto the substrate ⁹⁸. Modes of magnetron sputtering are direct current (DC), radiofrequency (RF)⁸⁴. DC mode is a highly used technique that utilises a conductive target material to deposit thin films. The disadvantages include target poisoning and poor deposition rates. The RF mode increases ionisation by microwaves, RF coils or increased magnetic confinement ⁹⁹. These modes can allow non-reactive or reactive sputtering. Non-reactive sputtering is the direct deposition of a sputtered target / sputtered targets in an inert gas. RF magnetron sputtering has been used to coat HA on Ti-alloys ¹⁰⁰. Reactive sputtering uses a reactive physical vapour deposition process ²⁰. A mix of an inert and a reactive gas atmosphere is produced and the reactive gas reacts with the target to form a new material in the plasma which then condenses onto a substrate. An example is using Ar/N₂ gas with a Ti target to deposit TiN on a substrate ⁹⁷. Magnetron sputtering is known to produce TiN with a preference for the (111) direction, which is the hardest-wearing form of TiN ^{21; 38}.

2.8.2 Radiofrequency magnetron sputtering (RF-MS)

RF-MS is suitable for coating insulating materials with specific chemical and topographical properties^{24; 71}. The HA layer can be substituted via RF-McoS. The HA target is sputtered concomitantly with a 2nd target, *e.g.*, Si. The 1st target will be supplied with a higher power than the 2nd target¹⁹. As phosphate groups are easily substituted or even evaporated during the sputtering process, it may be difficult to control the resulting Ca/P ratio of the as-deposited coating, which in turn may affect the Ca/P ratio post-deposition^{18; 100}. Silicate ions (Si^{4+}) is known to competitively replace the phosphate groups (PO_4^{3-}) of HA¹⁸. Due to its biologically relevant characteristics, stoichiometric HA with a ratio of 1.67 is the gold standard for effective bone cell growth (please refer to Table 2-3)⁶⁹. Different research groups are attempting to further develop control of HA and magnetron co-sputtered substituted HA^{19; 24; 25; 71}.

A major benefit of RF-MS is the creation of amorphous HA coating. Post deposition techniques such as heat treatment (annealing) is important because amorphous HA dissolves easily in physiological fluid. Annealing could also control properties such as grain size; nano-sized HA mimics the size of natural/biological HA, which is optimal for natural bone growth⁶⁶. Careful control is required because thermal expansion mismatches of multilayered coatings could decrease bond strength, and disrupt the HA layer³³. Therefore the project aims to assess the re-crystallisation behaviour of the current coatings of interest by applying 1 heating temperature at 2 time points.

Hence, RF magnetron sputtering is the most suitable technique for controlling the composition of HA, *i.e.* the Ca/P ratio, with annealing procedures being used to define the crystallinity of HA ⁵⁶. Samples reported on in this thesis were prepared using Teer Coating's patented closed field unbalanced magnetron sputtering (CFUB-MS) system ⁹⁸, which incorporated a rotating substrate holder surrounded by vertically opposed magnetrons. Magnetrons with opposite polarities were placed adjacent to each other to close the magnetic field lines Figure 2-5 ¹⁰¹.

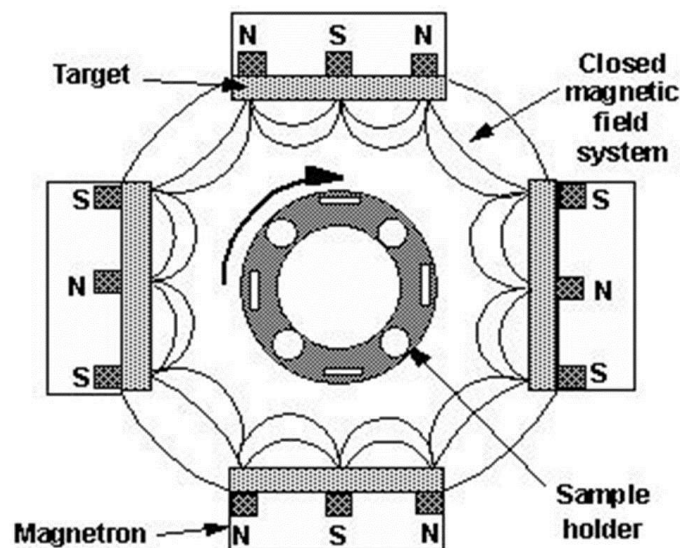


Figure 2-5 Teer Coating Ltd closed field unbalanced magnetron arrangement ¹⁰¹

2.9 Summary

Research on the controlled modification of Ti alloy surfaces has shown that surface chemistry greatly affects the response of biological cells ³⁶. Gaining improved understanding of biological cell-biomaterial surface interactions will deepen understanding of the process-structure-property interrelationship, in

order to develop implants with tailored bioinertness or bioactivity depending on the application.

The materials involved in this project are well-characterised, *i.e.* CpTi as the structural basis of orthopaedic implants; Si or SiO₂, being an essential mineral for bone growth; HA which exhibits a structure similar to bone and is commercially established as a bioactive coating for orthopaedic implants; and TiN which is a hard, bioinert material used commercially as a diffusion barrier. However, little work has been performed using them in combination as a biomedical implant. Further, the MS coating method used is novel. This literature review has outlined the reasons behind assessing the process-structure-property interrelationship of a potential biomaterial, 2 wt% Si:HA on Ti with TiN as a diffusion barrier, coated using RF-McoS.

Chapter 3 Experimental Methodology

This chapter describes the procedures used to coat and characterise the samples, along with the protocols for *in vitro* cell testing. The polishing procedures used for the preparation of the Ti substrates are described initially, followed by an outline of the RF magnetron sputtering process for the HA, 2 wt% Si-substituted HA and TiN coatings. The characterisation techniques of X-ray photoelectron spectroscopy (XPS), reflection high energy electron diffraction (RHEED), scanning electron microscopy / energy dispersive X-ray analysis (SEM/EDX), and glancing angle X-ray diffractometry (GA-XRD) are then described. Finally, details of cell growth and *in vitro* biological assays are given.

3.1 Titanium (Ti) substrate preparation

Commercially pure grade 1 titanium sheets (CpTi; Timet, UK) were wire eroded into 10 mm diameter discs of thickness 1 mm. Then the discs were mounted onto a hot-plate heated brass block using holding wax and sequentially manually polished to a mirror finish ($R_a \sim 47 \pm 10$ nm) using silicon carbide (SiC) paper of reduced grit size (10 minutes per grade), *i.e.* P240 (mean grit size 58.5 ± 2 μm), P400 (35.0 ± 1.5 μm), P600 (25.8 ± 1 μm), P800 (21.8 ± 1 μm), P1200 (15.3 ± 1 μm), P2500 (8.4 ± 0.5 μm) and P4000 (5.0 μm). The discs were then polished for 15 minutes using a mixture of colloidal silica (0.1 μm , pH 9.0; Buehler®, Germany) and 10 % hydrogen peroxide (30% w/v; Fisher Scientific, UK) and then washed with water for 10 minutes. The discs were then wiped with diluted soap solution with cotton

wool and rinsed under the cold water tap for 15 seconds. The brass block was then re-heated to re-melt the holding wax and the discs transferred using tweezers into a beaker containing acetone. The discs were then sonicated for 10 minutes in acetone, 1 minute in concentrated detergent solution, 1 minute in isopropanol, and then dried under a flow of hot air. If colloidal silica (SiO_2) was still present on the samples, they were wiped with cotton wool and acetone, flushed with isopropanol, and then re-dried under flowing hot air. The current washing protocol was an adaptation of the in-house protocol with that of Struers¹⁰², in order to effectively remove the colloidal SiO_2 . Successful removal was confirmed via XPS and SEM/EDX (appendix). A summary of the polishing protocol is given in Table 3-1.

Table 3-1 Summary table of the steps used during grinding and polishing of the commercially pure Ti discs for coating.

Step	Technique	Silica Carbide Grit/ Solvent	Mean grain size d_{50} value (μm)	Time (mins)	RPM
Grinding	Silicon carbide (SiC) paper	P240	58.5 ± 2	10	250-300
		P400	35.0 ± 1.5		
		P600	25.8 ± 1		
		P800	21.8 ± 1		
		P1200	15.3 ± 1		
		P2500	8.4 ± 0.5		
		P4000*	5.0^*		
Polishing	MD-Cloths TM with MD-Disc TM (Struers)	Colloidal silica with 10% H ₂ O ₂ (30% w/v)	0.1 μm	15	
		Water		10	
Washing	Sonicator	Acetone		10	
		dH ₂ O with concentrated detergent		1	
		Isopropanol (IPA) or Industrial Methylated Spirit (IMS)		1	

*P4000 is not an official Federation of European Producers of Abrasives (FEPA) grade.

3.1.1 Profilometry

Since surface roughness is known to affect cell growth^{32; 45; 60; 103}, sample sets with an average surface roughness (R_a) of 47 ± 10 nm ($n=20$) were identified for the coating procedure. Substrate roughnesses were appraised using a Mitutoyo Surftest SV600 with Surfpak-SV software (v.1.002). Roughness calibration was performed using a Mitutoyo Precision reference specimen (R_a

= 2.95 μm). The profilometer comprised a diamond-tipped stylus with 5 μm radius tip. An evaluation length of 5 mm was used to appraise all the samples at a scan speed of 0.2 mm/s. Samples were cleaned using cotton wool and acetone or isopropanol, prior to taking the readings.

3.2 Thin film deposition using magnetron sputtering (MS)

Basically, an ionising plasma is created and HA, TiN and SiO₂ targets are sputtered via momentum transfer (Figure 3-1) ¹⁰⁴. An oscillating magnetic field excites Argon (Ar) gas atoms and accelerates their free electrons to create a non-equilibrium, high frequency plasma. The reaction also yields H₂O, CO and CO₂ molecules that are evacuated by the vacuum system. An Edwards 750 diffusion pump, connected to the chamber base by an Edwards high-vacuum butterfly valve, provided the vacuum for this system. An Edwards E2M40 rotary pump backs the diffusion pump to achieve a vacuum of approximately 10⁻² torr. The chamber pressure was operated at <10⁻³ torr and >10⁻⁴ torr, as measured by Pirani and Penning gauges, respectively. The chamber was backfilled with either argon, or an argon/oxygen mixture, using MKS 1179A12CS1BV 100 sccm mass flow controllers. The argon flow was set at 36 sccm for all coatings equating to a pressure 2 x 10⁻³ torr. Where used, oxygen was flowed at 5 sccm creating a partial pressure of 3 x 10⁻⁴ torr. As in Figure 3-2, the substrates are placed on a circular sample holder that has the ability to rotate.

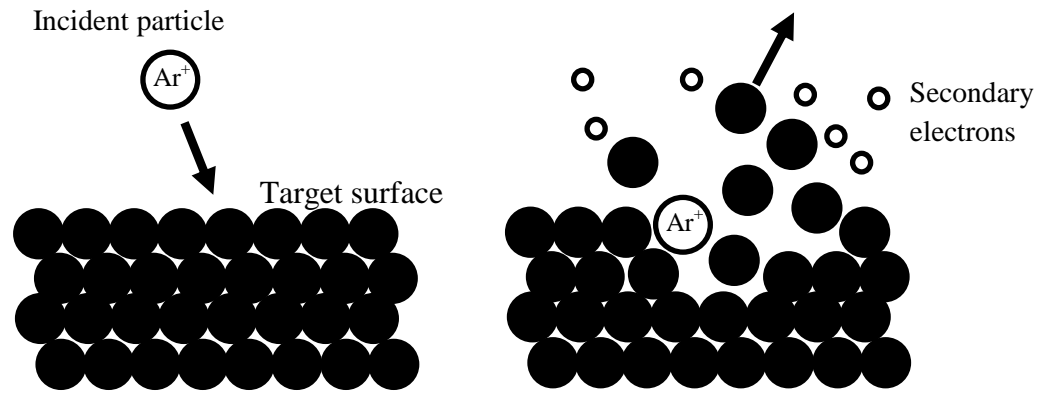


Figure 3-1 Schematic depicting the momentum transfer process, and the possible outcome as an atomic level. Picture on the left illustrates a pre-sputtering event and (right) shows the effects of immediately after collision, with sputtered atoms and secondary electrons.

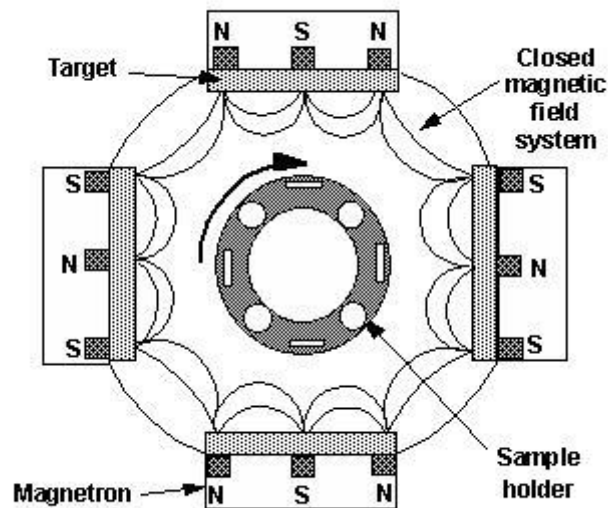


Figure 3-2 Rig used for thin film deposition of Si-substituted HA films with TiN barrier layer. The substrates were arranged on the sample holder.

3.2.2 Sample sets and MS deposition conditions

Due to intellectual property policies, the exact parameters for both sets are incomplete. However, any available information will be provided. Two sets of coatings were performed. The 1st set was used primarily for materials

characterisation with a few biological tests, whereas the 2nd set was used to perform further biological studies. The raw materials used for the coating procedure are: 10mm diameter Ti discs as substrates, TiN target, Si target and SiO₂ target. Deposition for the 1st set is summarised in Table 3-2. In set 1, prior to deposition, the MS specimen chamber was pumped down to 2×10^{-5} torr. Then, the Ti substrates were etched with Ar to remove contamination or oxidation at the top layer of the Ti substrates. In inert Ar atmosphere, the etched substrates were coated with a Ti adhesion layer followed by TiN coating. HA with and without SiO₂ / Si were then sputtered onto the TiN layer. Some samples do not have a TiN layer and therefore the HA and/or SiO₂/Si were sputtered on the Ti adhesion layer.

Due to the lack of samples in set 1, a 2nd sample set was created in order to perform a wider range of biological cell studies. The coatings were intended to be similar to that of the 1st set, although it was unclear whether the sputtering conditions used were the same. Set 2 parameters are in Table 3-3. During the pre-sputter etch of set 2, the HA and SiO₂ targets were etched using RF powers 60W and 2W, respectively, whereas no power was supplied to the Si target. Reactive sputtering was used to deposit the TiN layer where Ti targets were sputtered in a Ar/N₂ gas atmosphere. The targets were 58mm diameter discs of thermally sprayed HA, SiO₂ or Si from Plasma Biotol, Derbyshire.

Table 3-2 Rig parameters used for sample set 1. Pre-sputter etching was first performed for all substrates, followed by TiN interlayer deposition, and lastly the simultaneous deposition of substituted and HA layer. Information that is not available is marked with N/A¹ and information that is not applicable is marked with N/A². Abbreviation used is standard cubic centimetre per minute (sccm).

Description	Time (mins)	O₂ gas (sccm; partial pressure)	Ar gas (sccm; partial pressure)	Si and SiO₂ target power density	Base pressure (Torr)
Etching (all substrates)	10	N/A ²	N/A ¹	N/A ²	2x10 ⁻⁵
Deposition of Ti adhesion layer	5	N/A ²	N/A ¹	N/A ²	N/A ¹
TiN deposition	30	N/A ²	N/A ¹	N/A ²	2x10 ⁻⁵
Coating Si-substituted HA	360 (4 h)	N/A ²	36; 2x10 ⁻³ Torr	Set such that substitution occurs at 2% wt.	N/A ¹
Coating Si+O₂:HA	360 (4 h)	5; 3x10 ⁻⁴ Torr	36; 2x10 ⁻³ Torr	Set such that substitution occurs at 2% wt.	N/A ¹

Table 3-3 Rig parameters used for sample set 2. Pre-sputter etching was first performed for all substrates, followed by TiN interlayer deposition, and lastly the simultaneous deposition of substituted and HA layer. Unavailable information is marked with N/A¹ and information that is not applicable is marked with N/A². Abbreviations used are standard cubic centimetre per minute (sccm), watt (W), radiofrequency (RF), direct current (DC), revolutions per minute (RPM).

Description	Time (mins)	Bias (V in pulsed DC)	HA target (W; RF)	SiO ₂ target (W; RF)	Si target (W; RF)	Ti target (Amps; DC)	N ₂ gas (sccm)	Ar gas (sccm)	Base pressure (Torr)	Rotation (RPM)
Etching (all substrates)	10	-200	60	2	N/A ²	N/A ²	N/A ²	41	N/A	2
TiN deposition										
1.Target etching	30	-500	N/A ²	N/A ²	N/A ²	0.5	N/A ²	23	<3.0x10 ⁻⁵	2
2.Adhesion layer deposition	5	-100	N/A ²	N/A ²	N/A ²	6	N/A ²	23	<3.0x10 ⁻⁵	2
3.TiN deposition	30	-60	N/A ²	N/A ²	N/A ²	6	16	23	<3.0x10 ⁻⁵	2
Si or SiO₂ substitution and HA deposition	Time (mins)	Bias (V in pulsed DC)	HA target (W; RF)	SiO ₂ target (W; RF)	Si target (W; RF)	Ar gas (sccm)	O ₂ gas (sccm)	Deposition Pressure (Torr)	Base vacuum (Torr)	Rotation (RPM)
Si:HA	360	-25	N/A ¹	N/A ¹	N/A ²	N/A ¹	N/A ²	1.6x10 ⁻³	2.2x10 ⁻⁶	2
Si:HA/TiN	360	-25	N/A ¹	N/A ¹	N/A ²	N/A ¹	N/A ²	1.6x10 ⁻³	2.2x10 ⁻⁶	2
HA/TiN	360	-25	N/A ¹	N/A ¹	N/A ²	N/A ¹	N/A ²	1.6x10 ⁻³	1.6x10 ⁻⁵	2
Si+O ₂ :HA/TiN	360	-25	N/A ¹	N/A ¹	N/A ¹	N/A ¹	N/A ¹	1.6x10 ⁻³	1.4x10 ⁻⁵	2

Both parameters were used to make the following samples:

- 2wt% Si : HA / Ti
- 2wt% Si : HA / TiN / Ti
- 2wt% Si + O₂ : HA / TiN / Ti and
- HA / TiN / Ti

For ease of reference, these samples will be referred to as Si:HA, Si:HA/TiN, HA/TiN and Si+O₂:HA/TiN, respectively (schematically summarised in Figure 3-3). As a reminder, Si substitution was performed using either an SiO₂ target (inert Ar atmosphere), or an Si target in a Ar/O₂ atmosphere with and without a TiN interdiffusion barrier layer.

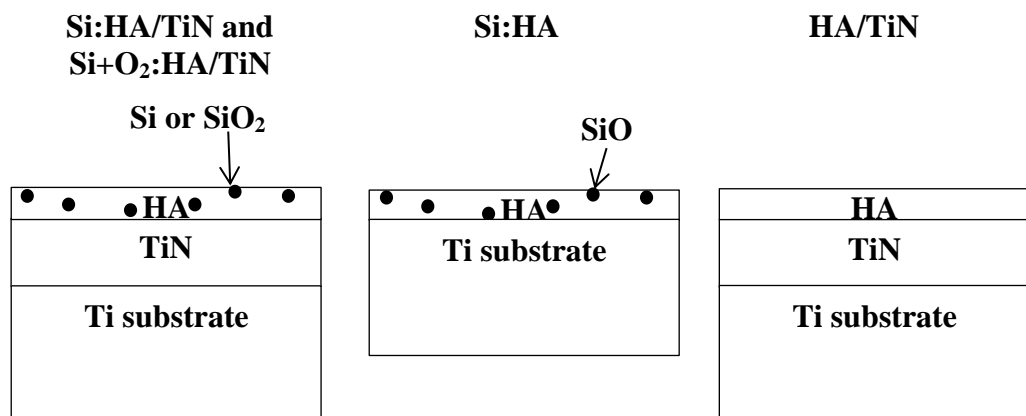


Figure 3-3 Schematic cross section of the coatings deposited on the Ti substrate. All coatings were exposed to Ar gas. Only Si+O₂:HA/TiN was exposed to a mixed atmosphere containing O₂ and Ar. Samples are not drawn to scale.

3.2.3 Post deposition heat treatment (annealing)

As-deposited HA is amorphous and would dissolve readily in biological fluid^{22; 23}. Hence, annealing is performed in order to crystallise the HA to make it

less susceptible to dissolution and hence more functional in the biological environment. A tube furnace with Ar supply was used for the annealing of the samples.

The as-deposited MS amorphous coatings were annealed at 700°C in flowing Ar in a tube furnace (Lenton Thermal Design, UK). Ar was used as it is an inert gas and would not react with the coating^{22; 105}. Set 1 was annealed for 2 hours and 4 hours. Due to time constraints and based on the results from set 1, set 2 was annealed for 2 hours. Prior to annealing, the specimen tube was purged with Ar for 3 hours until the O₂ partial pressure level was less than 2×10^{-8} Torr, as measured by mass spectrometry. The temperature was ramped at a rate of 20°C/min and then the samples were held for 2 h in flowing Ar at 100 sccm. The furnace was then left to cool naturally in the flowing Ar atmosphere. After annealing set 1, it was discovered that the rubber rings of the furnace were old and may have introduced trace levels of oxygen, which consequently influenced the annealed coatings. New rubber rings were installed into the furnace for sample set 2 which resulted in more controlled coatings. More details will be described in Results and Discussion.

3.3 Sample characterisation

3.3.1 X-ray diffraction (XRD)

An X-ray is an electromagnetic wave of wavelength $10^{-10} - 10^{-11}$ m, which is comparable to the atom plane spacing within a crystalline solid. Hence, X-ray diffractometry (XRD) may be used for the appraisal of bulk crystallography and the grain size of processed materials.

The schematic diagram at (Figure 3-4) presents an overview of the XRD apparatus used. A beam of X-rays is emitted from an X-ray tube, an evacuated vessel within which high energy electrons accelerated from a hot tungsten (W) filament are focused onto a water-cooled copper (Cu) target. The X-ray source consists of characteristic X-rays and background Bremsstrahlung radiation. The X-rays emerge from the tube via a thin Beryllium window, which has a low atomic number, and are then filtered and collimated. The emission then takes the form of monochromatic beam of specific wavelength ($\lambda_{\text{Cu K-alpha}} = 1.5406 \text{ \AA}$). The X-rays are scattered by the atoms within the samples and a set of reconstructed intensities are formed in a number of precise directions, according to the crystallographic arrangement of atomic planes within the sample. The results, in the form of a diffraction pattern, provide information on the sample crystal structure, *i.e.* the arrangements of the atoms in space.

Huygen's principle for wave propagation may be used to assist with the description of X-ray wave scattering and diffraction. As atoms in a crystalline solid are arranged in a regular array, the incident X-rays are scattered in a

hemispherical pattern by the outer shell electron clouds that exist around the atoms of the crystal lattice, through a process of absorption and re-emission, *i.e.* resonance. Depending on the Bravais lattice, the crystal plane spacings and the X-ray wavelength, constructive interference of the scattered wavelets occurs in precise directions.

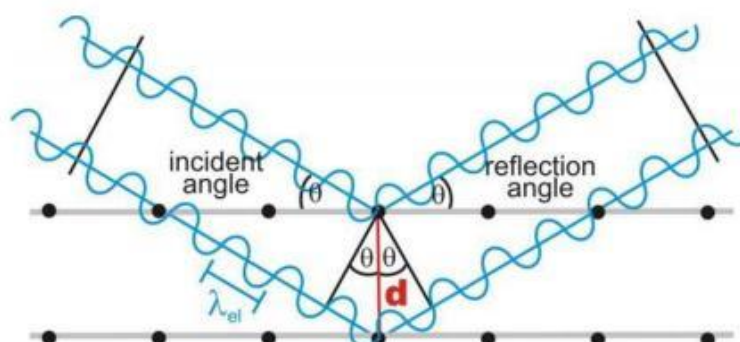


Figure 3-4 Schematic depicting the constructive interference of scattered waves¹⁰⁶

For a specific angle (θ), if the distance travelled by scattered X-rays from two crystal planes differs by an integer number (n) of wavelengths, then the scattered X-rays are in phase and constructive interference occurs¹⁰⁷ Hence, Bragg's law may be used to predict the positions of the diffracted intensity maxima. Bragg's law is given by $n\lambda = 2d\sin\theta$, where d corresponds to the lattice spacing, λ the X-ray wavelength and θ is the diffraction angle. The diffraction pattern is predicted by plotting the angular positions (2θ) of the reconstructed intensities.

XRD patterns characteristic of individual or mixed phases were obtained from the various sample sets as a function of processing. Near surface

crystallographic information could then be appraised according to the information content within the diffracted peak positions, intensities and profiles.

3.3.1.1 Glancing angle XRD (GA-XRD)

Glancing angle XRD (GA-XRD) is based on the same principles as XRD, except that the X-rays are positioned at a very shallow, glancing angles to the specimen, typically $< 1^\circ$, in order to appraise very thin layers of material comprising the near sample surfaces. For these experiments, a Bruker AXS D8 Advance X-ray diffractometer ($\text{Cu}_{K\alpha}$ radiation) in glancing angle mode was used. Samples were mounted on Perspex holders and rotated at 30 rpm. The experimental parameters were as follows: 0.7° incident beam; 0.2 mm slit size; 2θ range of $25\text{--}65^\circ$; and a dwell time of 24 s for 0.04° step sizes. Total analysis time per sample was 7.5 hours ($n=2\text{--}3$).

A Bruker glass slit (Glasspalt kpl) was used for calibration to establish the $\sim 1^\circ$ incident angle prior to each session of data acquisition. The crystallographic phases of the sample were identified using DIFFRAC^{plus} software (Bruker). Prior to sample data acquisition the targets used to coat the samples were examined in order to determine their crystallography the ability of the equipment to detect them. Due to sample size restriction of the D8 Advance (Bruker), the D8 Discover (Bruker) was used with the parameters of 2θ of $5\text{--}80^\circ$, 40kV and 30mA, dwell time of 4s, and 0.0025 step size. The peak

positions match those of stoichiometric HA International Crystal Diffraction Data (ICDD) reference number: 01-074-0565 but does not match the relative intensities. The Si target was analysed using Chi 0, 40kV and 30mA, 2θ of 20-90°, dwell time of 4s, and 0.0025 step size. The crystallographic phases of the sample were identified using X'Pert Highscore Plus (Panalytical) and conformed to inorganic crystal structure database (ICSD) reference number: 98-004-8759. The SiO₂ target was analysed using similar parameters (with the exception of 2θ of 15-55°) as the Si target and was confirmed to be quartz (ICDD ref code: 01-085-0798).

3.3.1.2 XRD data analysis

The DIFFRAC^{plus} software uses the International Centre for Diffraction Data (ICDD) database. The diffraction data was appraised and candidate phases identified and indexed using the ICDD, based on peak position, intensity and peak shape. Indexed diffraction patterns were then stacked for comparison using Excel as a function of sample processing e.g. Figure 3-5.

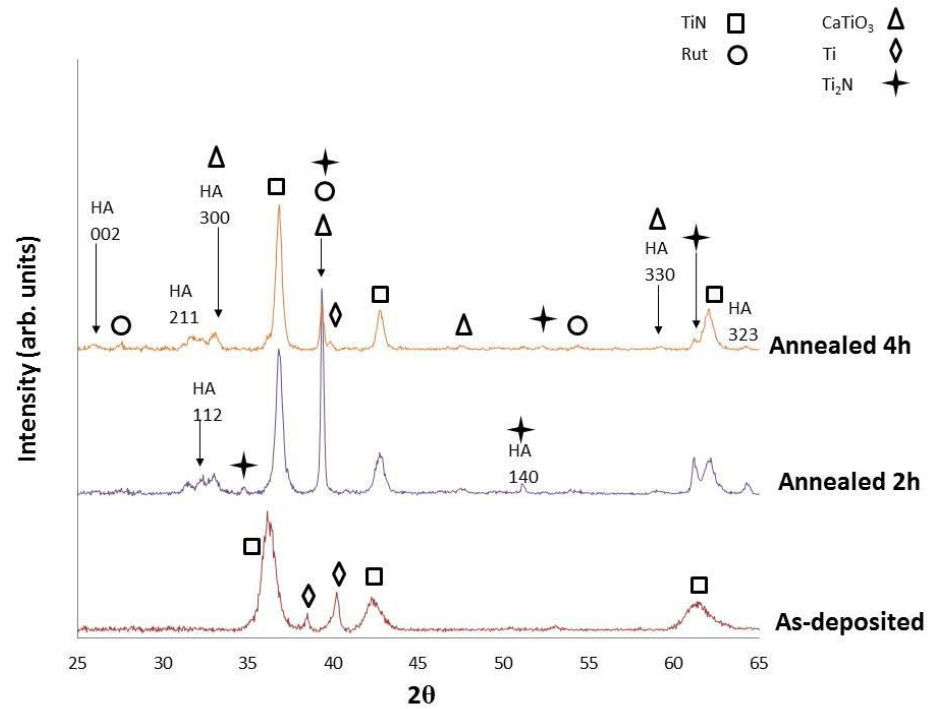


Figure 3-5 Representative XRD diffraction patterns of a sample set and the formation of chemical species as a function of time.

3.3.2 Scanning electron microscopy / Energy dispersive X-ray spectroscopy (SEM/EDX)

Scanning electron microscopy (SEM) using secondary electrons and backscattered electrons and energy dispersive X-ray (EDX) analysis were used to assess surface morphology and provide a semi-quantitative appraisal of near surface chemistry ($\sim 1 \mu\text{m}^3$ interaction volume), respectively¹⁰⁸.

Electrons exhibit a wave-like or particle-like behaviour. High energy electrons may be scattered by the atomic nuclei or by atomic electrons. During

scattering, a high energy incident electron has the ability to eject a core shell electron away from the attractive field of a nucleus, *i.e.* photoionisation. As a result, a range of secondary signals can be produced, such as secondary electrons which are used in SEM imaging, or characteristic X-rays as used for elemental analysis (EDX) ¹⁰⁸.

3.3.2.1 Electron-material interactions

In the SEM, electrons are accelerated through a high voltage and acquire kinetic energy. The electron-optic column is used to define a focused beam of electrons which is rastered over the sample. The kinetic energy is dissipated in the sample, yielding a variety of signals as summarised in Figure 3-6. The main signals used are secondary electrons (SE), backscattered electrons (BSE) and characteristic X-rays.

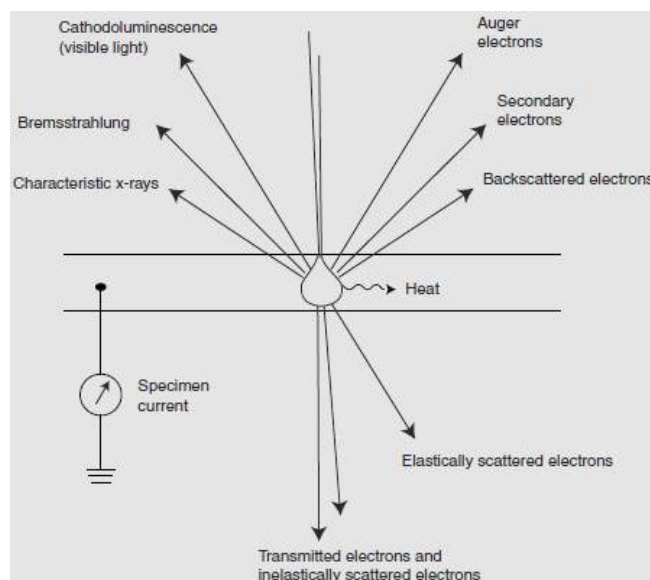


Figure 3-6 Schematic of the signals produced as a result of the interaction between an electron beam with a specimen ¹⁰⁹.

The exciting (primary) electrons may interact with atomic electrons or with atomic nuclei within the sample. The primary beam electrons may be scattered elastically (no energy loss) or inelastically (with loss of energy). The inelastic scattering of electrons gives rise to secondary electrons (< 50 eV), and characteristic X-rays, as illustrated in Figure 3-7. Secondary electrons (SE) are easily absorbed within the sample and hence only those created near the surface may be emitted and used to image sample topography.

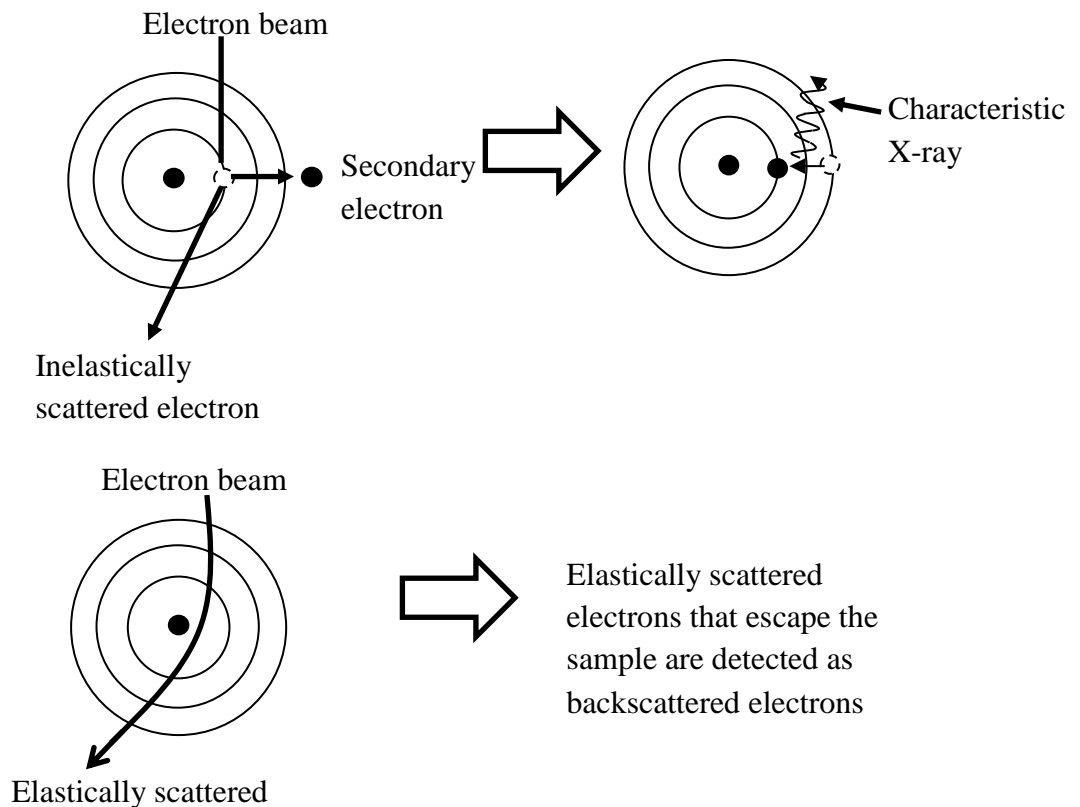


Figure 3-7 An electron from the electron beam could be scattered elastically or inelastically at the nucleus. Above: Primary electron beam interaction with electrons in the specimen could lead to inelastically scattered electrons. An electron from the sample is ejected as a secondary electron. An ion is now formed. De-excitation of the ion could lead to the emergence of characteristic X-rays. Below: Elastic scattering at the nucleus leads to loss of energy in the form of an X-radiation called Bremsstrahlung¹⁰⁹.

Backscattered electrons (BSE) result from elastic scattering at atomic nuclei, with primary beam electrons being elastically scattered back out of the sample. Hence, BSE have energies on the scale of the primary beam and hence may escape from a greater depth from the sample, with strength of scattering being dependent on atomic number. BSE is used to create images with contrast levels dependent of locally averaged atomic number, and hence may be used to appraise sample composition. The lighter the image, the heavier element it contains because more electrons are able to enter the detector ¹¹⁰.

Photoionisation, *i.e.* core level electron displacement, is followed by the relaxation of electrons from higher energy shells to the lower energy core state leading to characteristic X-ray emission (K, L, M and N series) with wavelength (energy) dependent on the element. The Oxford Instruments INCA program was used to illustrate the emitted X-rays in the form of an energy spectrum. In addition, Bremsstrahlung otherwise termed background radiation could be seen in EDX spectra; it is caused by the inelastic scattering of electrons. As the energy loss is variable, Bremsstrahlung appears as a continuum background in the EDX spectra ¹⁰⁹.

3.3.2.2 EDX basics

The core principle underpinning the applicability of energy dispersive X-ray (EDX) analysis is that characteristic X-rays emission are being used to identify the elemental constituents within a sample. An EDX system has three

key components: an X-ray detector, a pulse processor and an analyser to convert X-rays into voltage signals. A characteristic X-ray causes the generation of electron-hole pairs (EHPs - the number of which depend on the energy of the incident X-ray) within a Si-based solid state device. The EHPs are separated by a built in voltage (*e.g.* in the vicinity of the depletion region within a p-n junction) to produce a current. A field effect transistor (FET) preamplifier transforms the charge into a voltage signal whereby the energy of a particular X-ray correlates with a precise voltage step which is accurately measured by the pulse processor. The analyser assigns a digital number to the energy of the incident X-ray and adds a count to the corresponding channel in the display. The Oxford Instruments INCA Energy program was used to interpret X-ray data, on a pulse by pulse basis, as a function of energy¹¹¹. The program also minimises noise, thereby allowing the detection of low energy X-rays. The system has the ability to differentiate between events that occur close in time, in order to avoid the problem of X-ray pulse pile-up.

An X-ray spectrum consists of a varying, curved background, characteristic X-ray peaks, and statistical noise. Accordingly, overlap between the tails of neighbouring peaks or between lines corresponding to different X-ray shells may occur which complicates quantitative analysis. The INCA Energy program uses a least squares approach to deconvolute overlapping peaks within an unknown spectrum with reference to the profile of a standard spectrum. In order to suppress statistical noise and the background, the spectrum is deconvolved using a zero area 'top-hat' function. The top-hat function filters the unknown spectrum and the standard profile. The profile is

then fitted to the unknown spectrum using a least squares routine. Matrix corrections are then employed to convert the measured intensity of X-ray peaks from the sample relative to the standard profile. Absorption correction is then employed to account for the absorption of X-rays as they traverse the sample. INCA uses the XPP matrix correction scheme developed by Pouchou and Pichoir¹¹². It is based on a Phi-Rho-Z, $\Phi(\rho z)$, approach which utilises exponentials to describe the shape of the $\Phi(\rho z)$ sigmoidal curve¹¹². An iterative method is applied to calculate the area under each peak to yield the atomic and weight percentages of each element present in the unknown sample. The INCA program allows for the selection of specific elements and the subsequent calculation of atomic and weight percentages.

3.3.2.3 SEM imaging and EDX analysis – example data

The chemical composition and morphology of the as-deposited and annealed layers were assessed using an FEI XL30 field electron gun – environmental scanning electron microscope (FEG-ESEM) configured with an Oxford Instruments INCA EDX analysis system. Prior to imaging, an Edwards E306 high vacuum evaporator unit was used to coat the samples with a thin layer of graphitic carbon to assist with imaging because the HA coating is non-conductive and would suffer from the problem of surface charging during imaging. The samples were imaged using secondary electrons at 20 kV, spot size 4, working distance 10 mm. Further, all samples were appraised at x5000 magnification using BSE imaging at three areas: the disc edge, between middle and edge, and the middle of each sample. Complementary EDX

analysis was performed to appraise the chemical composition of the samples. Approximately 500,000 spectrum counts were acquired per sample area and the atomic percentages (at%) and weight percentages (wt%) percentages were normalised. The FEG-ESEM features a state-of-the-art field-emission gun (FEG) based on a Schottky emitter. It is constructed using a tungsten filament with a ~ 10 nm tungsten (W) tip coated with a thin layer of zirconium oxide to increase its electrical conductivity. The FEG-SEM provides very high beam current densities within a very small spot size, allowing for very high levels of spatial resolution and very good signal-to-noise ratios for chemical analysis ⁷⁴.

EDX acquisition was performed using the ASTM standard 1998 (2008) as a guide ¹¹³. Prior to acquisition of coatings, a stoichiometric HA standard (Ca/P ratio of 1.67) was coated with carbon and analysed using the above parameters in order to ensure that the system was able to accurately detect stoichiometric Ca/P ratio and was not affected by magnification (Table 3-4). In a sample that contains elements of multiple concentrations, the probability at which the characteristic X-rays reach the detector may be compromised if the area of analysis was changed. By analysing for any magnification effects, it allows the simultaneous acquisition of complementary EDX analysis with suitably magnified images.

Table 3-4 Similar average Ca/P ratios were obtained using different magnifications

Magnification	Average Ca/P ratio \pm S.E. (3 areas of 1 sample)
500x	1.70 \pm 0.03
100x	1.66 \pm 0.02

The acquisition method for the as-deposited and non-delaminated annealed samples will be described briefly, followed by an outline of the method used for the appraisal of annealed samples that had experienced some delamination. Figure 3-8a represents a BSE image of an as-deposited HA/TiN sample. An acquisition box drawn around the periphery of the image corresponds to the area sampled for EDX analysis. Figure 3-8b is the elements identified within the field of view are summarised with both wt % and at %. In particular, the Ca/P ratio was calculated by dividing Ca at% / P at%.

For the case of EDX analysis of delaminated samples, EDX data was acquired only from the HA “islands” (Figure 3-9). The delaminated patches only exhibited signals due to Ti and O. Three areas per sample were analysed and average compositional values calculated for each sample for the purpose of comparison of the evolution of the coatings as a function of the deposited structure and the annealing time.

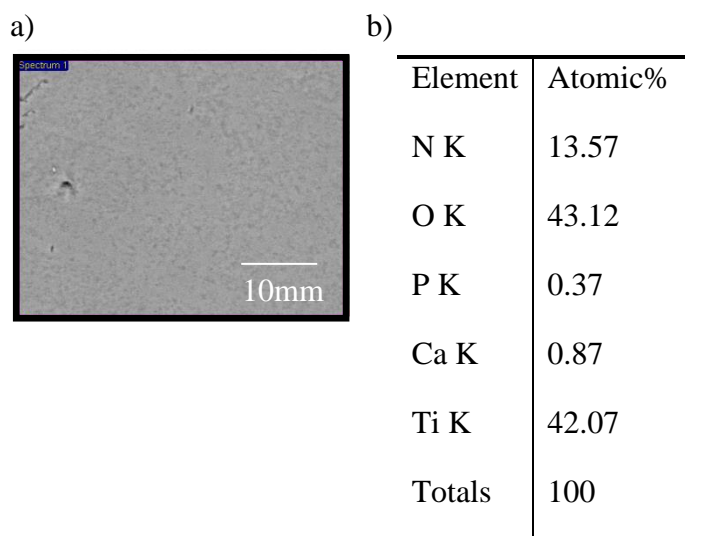


Figure 3-8 a) Representative BSE image of an as-deposited HA/TiN sample; the pink box depicts the area at which EDX data was obtained; b) a table of element percentages of the target area, normalised to 100%.

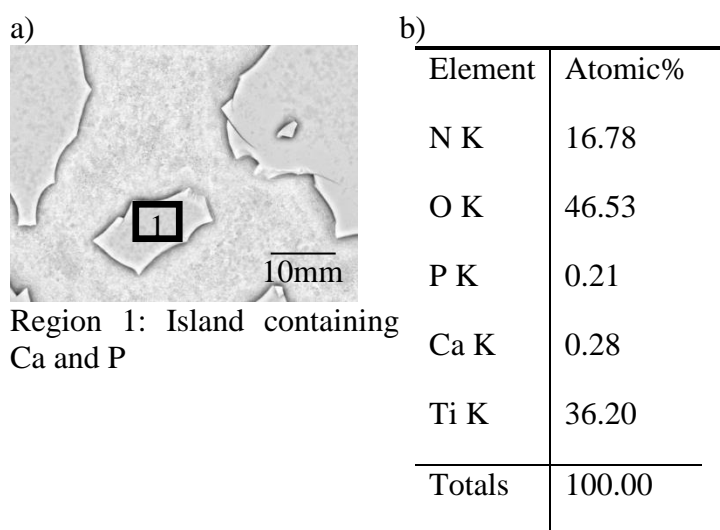
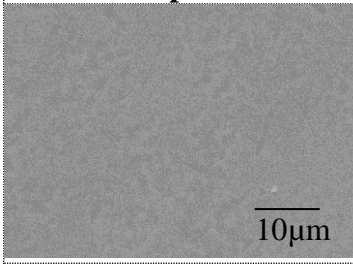
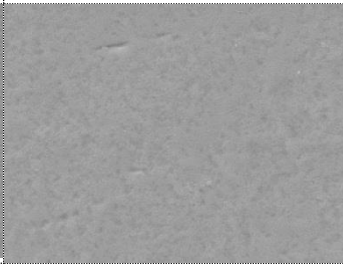
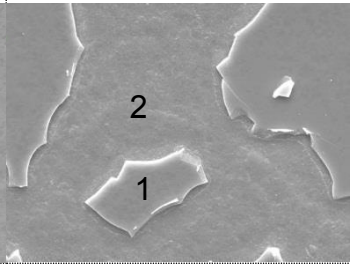
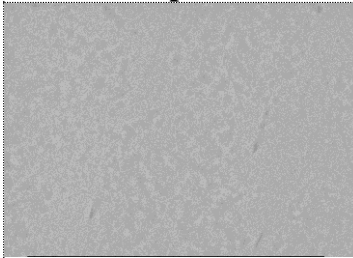
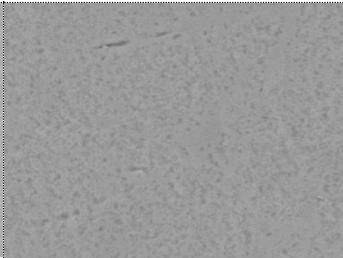
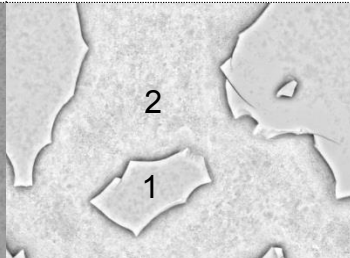


Figure 3-9 a) BSE image of a HA/TiN sample annealed for 4h. Due to delamination, EDX was obtained from the “islands” that contain Ca and P; b) a table of element percentages of the target area, normalised to 100%.

Table 3-5 shows representative results of a HA/TiN sample; with complementary SE and BSE images presented alongside the average Ca/P ratio as a function of annealing time. Figure 3-10 presents a summary (column

bar) of the average Ca/P ratio, average Ca at% and average P at% for the three areas analysed on the sample. This format of presentation will be used later in the Results Chapters. The average Ca/P ratio is presented on the primary axis, whilst the Ca at% and P at% values relate to the secondary axis.

Table 3-5 Representative results of the evolution of the coatings as a function of annealing time. Here, a SE images of a HA/TiN sample were depicted with a description of morphology, and complementary BSE image with Ca/P ratio. BSE images were used for EDX analysis as Si clumps were recognisable only using BSE (in silicate-substituted coatings).

SE images of HA/TiN coated Ti		
As-deposited	2h	4h
		
Smooth coating.	More textured coating.	Delaminated coating. Region 1: islands of remnant coating containing Ca and P. Region 2: exposed substrate. exhibiting Ti and O.
BSE images of HA/TiN coated Ti		
As-deposited	2h	4h
		
Ca/P ratio: 2.42 ± 0.08	Ca/P ratio: 2.41 ± 0.03	(1) Ca/P ratio: 2.15 ± 0.23

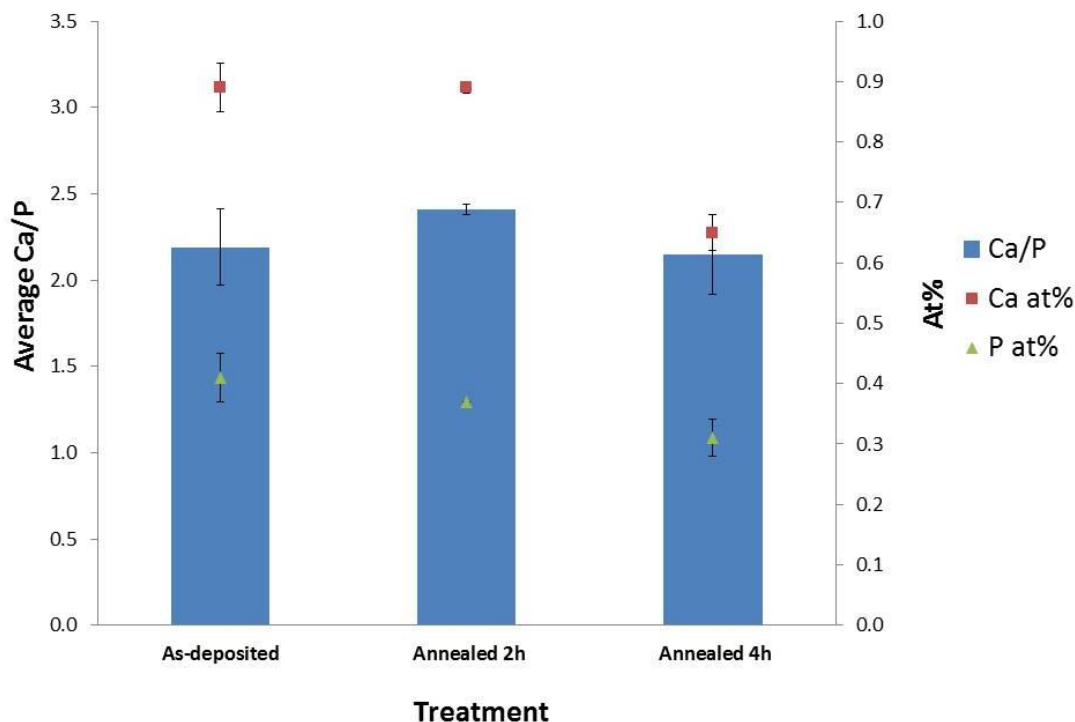


Figure 3-10 Representative format of presentation that is used at the Results sections. EDX results of the Ca and P changes of a HA/TiN sample as a function of annealing time is depicted. The average Ca/P ratios are represented by the column graph and is associated with the primary y-axis (left y-axis). The Ca at% and P at% are represented by the scatter plot that is associated with the secondary axis (right y-axis). Error bars represent the standard error mean, SEM, (n=3).

3.3.3 X-ray photoelectron spectroscopy (XPS)

X-ray photoelectron spectroscopy (XPS) is sensitive to the top few atomic layers of a material and hence may be used to obtain information about the binding energy and chemical state of the atoms at a specimen surface. X-ray scattering at near surface atoms of a material causes photoionisation, *i.e.* the ejection of a core electron or a valence electron. A hemispherical analyser (HAS) filters the ejected electrons as a function of energy before bringing the electrons to a detector. As core level electrons are quantised, the resultant energy spectra exhibit distinct peaks that are characteristic of the electronic

structure of the chemical species at the sample surface. The kinetic energy of each photoelectron (PE) is characteristic to the element that emits it; hence a spectrum is developed by recording the energy of these photoelectrons. Relative sensitivity factors (RSFs) are used to scale the intensities of the PE peaks and play a vital role in calculating surface atomic concentrations^{114; 115}.

3.3.3.1 XPS data analysis

A VG ESCALab Mk II XPS with twin unmonochromated Mg/Al anode was used to obtain information about the chemical state and surface composition of the films, across a PE energy range of 0 – 1200 eV. The XPS was operated at 12 kV and 20mA using Al anode ($h\nu = 1486.6\text{eV}$) with SPECTRA-8 acquisition software. Casa XPS software (version 2.3.15) was used to analyse and quantify the data. All samples were charge corrected with respect to the adventitious carbon peak (C 1s) with a value of 284.6 eV. Low resolution spectral survey scans and high resolution scans were obtained for Ca 2p, O 1s, Ti 2p, C 1s, P 2p and Si 2p signatures, with each being fitted with a Shirley background. RSFs were used to calculate at% values, which enabled comparison with complementary EDX Ca/P ratios (Figure 3-11). For the high resolution scans (Figure 3-12), spectral peaks were manually selected and peak deconvolution was performed using Gaussian-Lorentzian (GL30) line shapes for the case of overlapping peaks. The deconvolved peaks are then used to obtain binding energies, as compared to NIST XPS Database 20, version 3.5. Figure 3-12 for annealed sample HA/TiN is illustrative of this peak fitting process. Table 3-6 summarises the chemical species and bonding

states present in the as-deposited and processed samples. High resolution scans and chemical species and bonding states will be presented in the Results section.

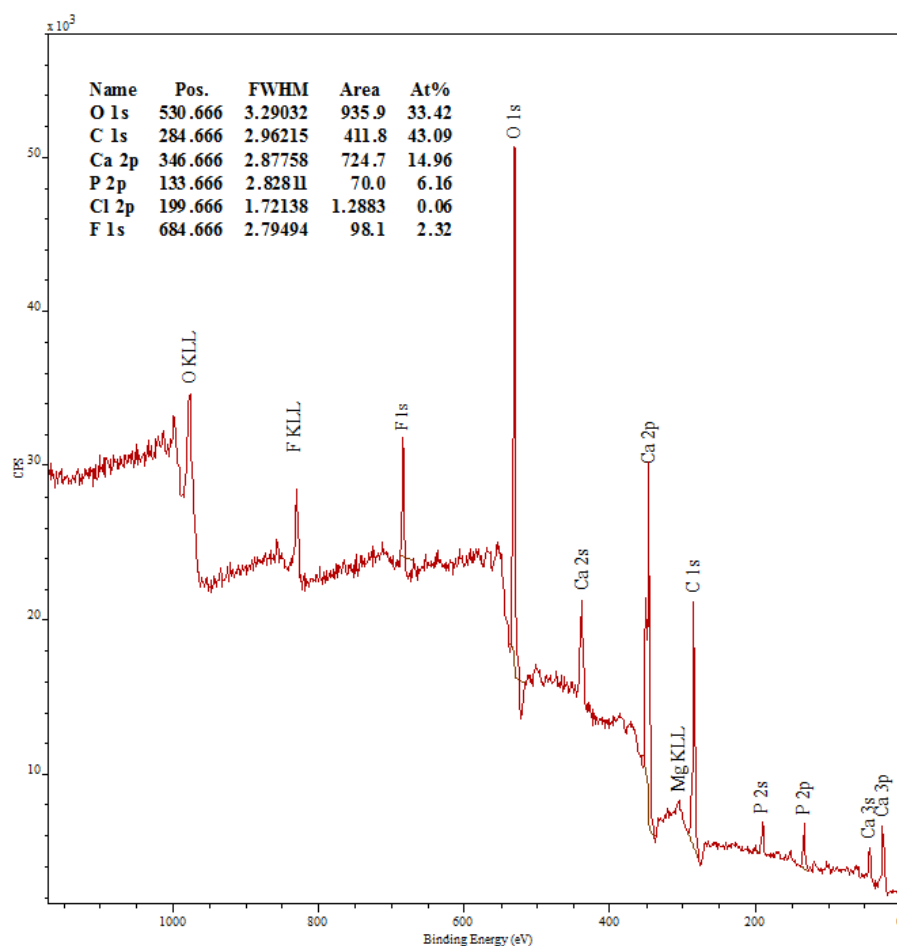


Figure 3-11 Low resolution spectrum of an as-deposited sample. RSF values allows the calculation of at% values, which in turn was used to obtain Ca/P values at the sample surface.

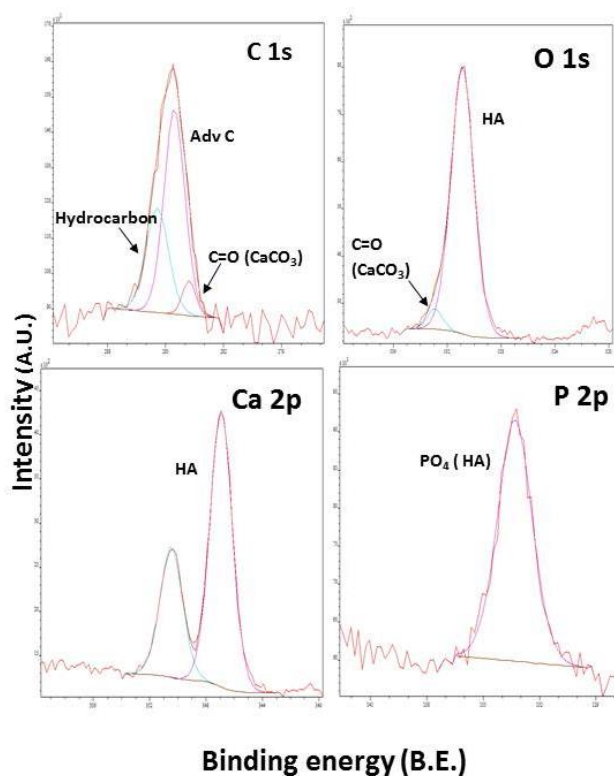


Figure 3-12 Deconvolved high energy spectra peaks with identified chemical species, all of which are present in the as-deposited samples.

Table 3-6 Representative table of the chemical species present in as-deposited samples.

As-deposited coatings (all samples)		
Peak	B.E. (eV)	Species
C 1s	284.4-284.5	adv C
	285.3-286.4	hydrocarbon
	288.2-289.06	C=O (CaCO ₃)
O 1s	530.9-531	HA
	531.7-533.1	C=O (CaCO ₃)
C 1s 2nd	284.6-284.8	adv C
	285.1-286.6	hydrocarbon
	287.9-288.1	C=O (CaCO ₃)
Ca 2p_{3/2}	346.7-347.1	Ca (HA)
P 2p_{3/2}	133.34	HA (PO ₄)

3.3.4 Reflection high energy electron diffractometry (RHEED)

Reflection high energy electron diffractometry (RHEED) is a variant technique that is performed using a transmission electron microscope (TEM) to assess the crystallography of the top few atomic layers of a sample. Firstly, the principles surrounding the operation of a TEM will be described.

TEM allows specimens of < 100 nm thickness to be examined at a resolution approaching the atomic scale. The resolution of electron transparent specimens is not defined by the wavelength of the incident high-energy electron beam, but is practically limited by aberrations associated with the electron-optical lenses. In a conventional TEM, electrons are produced by thermionic emission from a LaB_6 or W filament, or by field emission from a single crystal W filament, and accelerated to high energy, typically 100 to 400 keV. The TEM may be used to image the microstructure of a sample, or to interrogate the localised crystal structure using selected area electron diffraction (SAED), according to the set-up of the electron-optic projector lenses.

For the case of SAED pattern formation, the TEM objective aperture is removed, a selected area aperture is inserted into the intermediate image plane, and the projector optics are focused on the back focal plane of the objective lens. A small area of a specimen then contributes to the projected electron diffraction pattern for the purpose of structure characterisation.

There are three modes of image contrast formation in the TEM, depending on how scattered or transmitted electrons are utilised. Elastic electron-electron interactions cause scattering at low angle, while electron-nucleus interactions result in higher-angle scattering:

- Mass-thickness contrast is as used for the investigation of amorphous specimens, *e.g.* sample areas with a higher atomic number / thicker region will appear dark.
- Diffraction contrast is used for the investigation of crystalline specimens. Low index projections of a crystalline sample with many crystal planes close to the Bragg condition for diffraction will appear dark¹¹⁶.
- Phase contrast, as used for the imaging of samples at high resolution.

In this context, it is noted that elastically scattered electrons are used to form the diffraction patterns in RHEED through direct interaction with the sample surface in glancing angle geometry – with the immediate benefit that no sample preparation is required¹⁰⁸. The specimen coating is loaded on a RHEED stage and positioned vertically, directly beneath the projector lens of the TEM. Figure 3-13 depicts a RHEED stage which has four axes of movement for the x-y translation, rotation and tilt of the sample, in order to access a specific projection of the sample surface with the incident electron beam¹¹⁷. The electron beam interacts at a glancing angle of $\sim 1^\circ$ and samples a surface area of $\sim 1 \text{ mm}$ ¹⁰⁸.

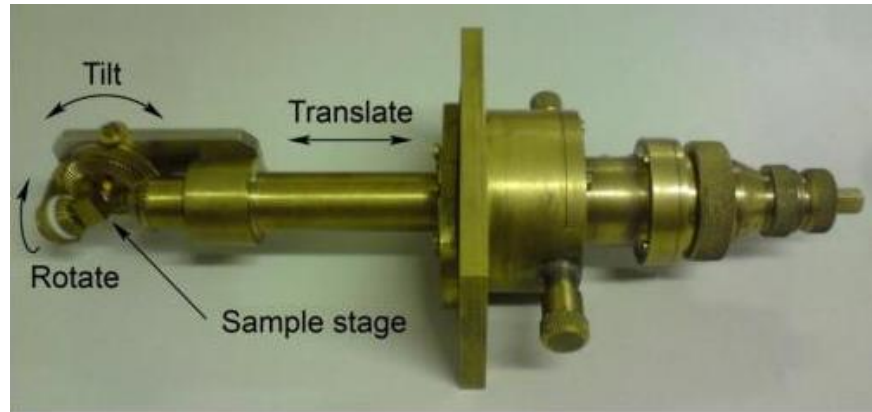


Figure 3-13 Photograph of the RHEED stage; the three axes of movement are illustrated.

3.3.4.1 RHEED data acquisition

The near surface structure of the as-deposited and annealed coatings were appraised using a RHEED stage mounted beneath the projector lens of a Jeol 2000fx TEM, containing a lanthanum hexaboride (LaB_6) filament source and operated at 200 kV. A sample of nanocrystalline hematite (Fe_2O_3) of known lattice parameter was used for calibration of the RHEED camera constant, λL , with ImageJ software being used to measure the sample diffraction spacings, d_{hkl} . By using the equation $\lambda L = R_{hkl} d_{hkl}$, the crystal plane spacings, d_{hkl} , of an unknown specimen could then be calculated (Figure 3-14) and their corresponding diffraction spots indexed with reference to International Centre for Diffraction Data (ICDD) cards, for the purpose of sample phase identification.

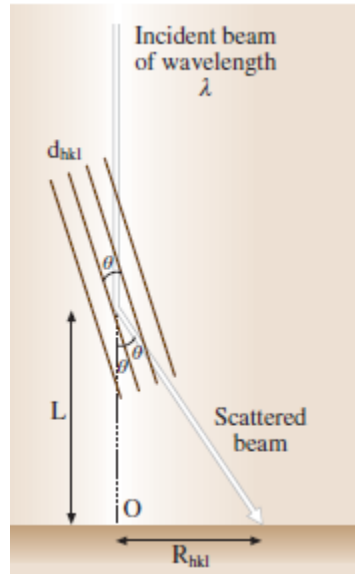


Figure 3-14 Schematic explaining the principle of the camera constant in TEM¹¹⁸

Using the diffraction pattern for the hematite standard, one ring of known d_{hkl} spacing was chosen, and an average value obtained for R_{hkl} , which allowed the camera constant $\lambda L = R_{hkl}d_{hkl}$ to be determined. In order to determine the d_{hkl} spacings for the processed crystalline coatings following annealing, at least six diffraction ring measurements were taken to gain an average value for R_{hkl} . To improve accuracy, a diffraction ring of high angle was selected. The circumference was used as a tracing guide to construct a circle which allowed the ring centre to be located. The camera constant was then divided by R_{hkl} to obtain a value for the associated d_{hkl} spacing. The sequence of d_{hkl} ring spacings was then compared with International Centre for Diffraction Data (ICDD) cards for the purpose of near surface sample phase identification (*e.g.* Figure 3-15). Images of annealed samples akin to Figure 3-15 will be presented in the Results section. In practice, the as-deposited coatings were

amorphous and hence could not be easily analysed using ImageJ due to a lack of crystalline rings.

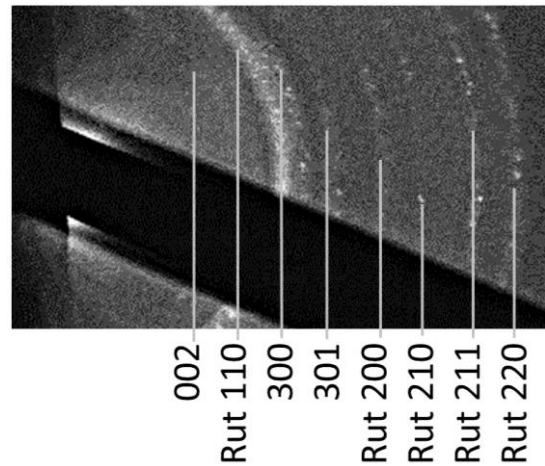


Figure 3-15 Representative indexed diffraction rings of an annealed sample, indexed to HA and rutile.

3.4 *In vitro* cytocompatibility

In vitro cell testing was performed in order to assess cytocompatibility and the ability of the modified coatings to enhance cell growth in the early stages of implantation. MG63 cells, a human-derived osteosarcoma osteoblastic cell line, were utilised. In order to avoid contamination, aseptic techniques were employed during all stages of cell culturing. All samples were sterilised using UV light irradiation ($\lambda = 280 - 320$ nm) for 90 minutes per sample side.

3.4.1 Cell seeding and growth initiation

MG63 cells (human osteosarcoma), obtained from the European Collection of Cell Cultures (ECACC), were cultured using complete Dulbecco's Modified Eagle Medium (CDMEM). CDMEM consists of DMEM media supplemented with 10% fetal bovine serum, 2% antibiotics / antimycotics, 2% HEPES (4-(2-hydroxyethyl)-1-piperazineethanesulfonic acid) Buffer, 1% L-Glutamine, 1% non-essential amino acids (Invitrogen, UK) and 75 mg ascorbic acid / 500 ml media (Sigma, UK). The cells were cultured in 75 cm³ flasks (Falcon, UK) and incubated in a 37°C, 5% CO₂ incubator. The medium was changed every two days and the cells were split at 80% confluency. During splitting, the cells were dissociated from the flasks using 0.05 mg cm⁻³ trypsin–ethylenediaminetetraacetic acid (EDTA) solution in 10 mM HEPES buffer, centrifuged at 1200 rpm for four minutes and re-suspended in fresh media. Sterilised samples were placed in 48 well plates (Nunc, UK), *i.e.* one sample per well; triplicates for each parameter were used. 500 µl of PBS was pipetted onto samples and aspirated prior to seeding in order to wet the samples. Cells were then seeded at a density of 40,000 cells cm⁻². 1 ml of media was then added to each well and incubated for 1, 7 and 14 days for sample set 1; and 1, 3, 7 and 14 days for sample set 2, respectively.

3.4.2 Metabolic Activity Assay (AlamarBlue™)

The AlamarBlue™ assay (ALB assay) is a colorimetric, cell viability indicator that tests for proliferation and cytotoxicity. ALB contains a non-fluorescent blue dye called resazurin. It relies on the metabolic activity of viable cells to

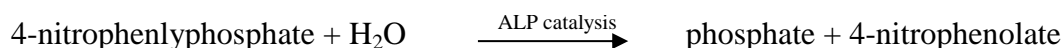
reduce it to bright-red fluorescent resorufin ¹¹⁹. This oxidation-reduction reaction occurs in the mitochondrial electron transport chain and involves reductases, *i.e.* enzymes that catalyse reduction reactions. Fluorescence is produced upon exposure to UV light and can be read using a fluorescence plate reader ¹¹⁹.

At each time point, the media was removed and the samples were washed three times with PBS solution. AlamarBlue™ (Serotec, UK) and Hank's balanced salt solution (HBSS; Gibco, UK) were mixed at a ratio of 1 in 10 in the dark, as ALB is photo-sensitive. The solution was then warmed in a water bath to 37°C, and added into each well, including the TCP wells as a control. The plates were then covered, wrapped in aluminium foil, and incubated for 80 minutes in the 37°C, 5% CO₂ incubator. The samples were then further incubated on a plate shaker for 10 minutes at 150 rpm. AlamarBlue™/HBSS solution was aliquoted in 100 µl duplicates from each well and transferred into 96 well plates. The fluorescence was acquired using a BioTek Instruments FLx800 fluorescence plate reader, connected to KCJunior software, at 560 nm excitation and 590 nm emission filters. Unreduced AlamarBlue™ from the TCP wells was subtracted from the values obtained from the samples to remove the background signal.

3.4.3 Alkaline Phosphatase Assay

The Alkaline Phosphatase (ALP) assay was used to gauge cell differentiation. At the beginning of the differentiation phase of the cell cycle, osteoblasts

produce the enzyme ALP. The ALP kit (Randox, UK) contains a substrate of 4-nitrophenylphosphate and a diethanolamine buffer solution. The substrate reacts with water and the enzyme catalyses a dephosphorylation reaction to produce a pale yellow 4-nitrophenolate:



Cellular ALP activity is directly proportional to the production rate of 4-nitrophenolate and is measured colorimetrically. After each time point, the media was removed from the well plates and washed three times with PBS solution. 1 ml aliquots of double distilled water (ddH₂O) were added to each well. A freeze / thaw method was used to rupture the cells and their organelles to release nuclear material, *i.e.* samples were frozen at -20°C and then left to defrost at room temperature. Freeze / thawing was performed for three cycles. The following was then performed in the dark. The cell lysates were aliquoted in 50 µl in duplicates into 96 well plates and mixed with 50 µl of ALP solution. The plates were then covered and shaken at 300 rpm on a plate shaker for 15 minutes. The absorbance was measured using a BioTek ELx800 plate reader, connected to KCJunior software, with a primary wavelength of 405 nm and a reference wavelength of 620 nm. The readings were then normalised using the DNA concentration from the DNA Hoechst Assay.

3.4.4 DNA Hoechst Assay

Cell proliferation of the MG63 cells was determined by quantifying the total DNA content at the same above time points. The DNA Hoechst dye binds to the adenine-thymine (A-T) base pairs that are present in double stranded DNA. As a result, fluorescence increases and shifts the emission maximum from 500 to 460 nm¹²⁰ Readings were compared against a standard curve using DNA standards.

The same cell lysates obtained from the 3-cycle freeze / thaw method were used. The following was performed in the dark. Duplicates for each sample was aliquoted in 100 µl and mixed with 100 µl of Hoechst 33258 stain (Sigma, Dorset, UK) and shaken at 300 rpm on a plate reader for 5 minutes.

Fluorescence was then read on a BioTek Instruments FLx800 fluorescence plate reader with 360 nm excitation and 460 nm emission filters, connected to KCJunior software. Readings were compared against a standard curve using DNA standards (Figure 3-16). The DNA standards were pre-mixed calf thymus DNA stock solution that was diluted using TNE buffer to yield concentrations at 10, 6, 5, 4, 3, 2, 1, 0.5, 0.25 and 0.125 µg/ml, respectively. The DNA concentrations of each sample was then plot using a column graph similar to the above.

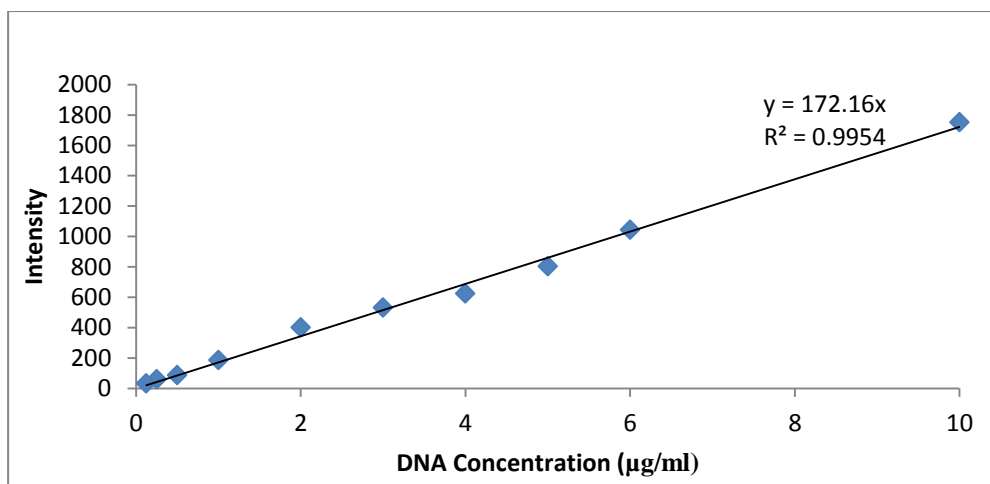


Figure 3-16 Standard DNA curve. Using the equation of line of best fit, the slope of the curve was used to obtain DNA concentration. A best line fit with an $R^2 > 0.9$ was required in order for the value of the slope curve to be valid for use to calculate the DNA concentration of the samples.

3.4.5 Statistical Analysis

The mean, standard deviation (S.D.) and standard error (S.E.) were analysed for two iterations. Statistical analysis was performed using the Prism software (version 6; GraphPad Software, California, USA). Two-way analysis of variance (ANOVA) with a confidence interval of 95% ($p=0.05$) was used with Bonferroni post-test to compare the significance of change in the coatings with time. The error bars presented represent standard error of mean with $n = 6$. Please refer to the example data on Figure 3-17.

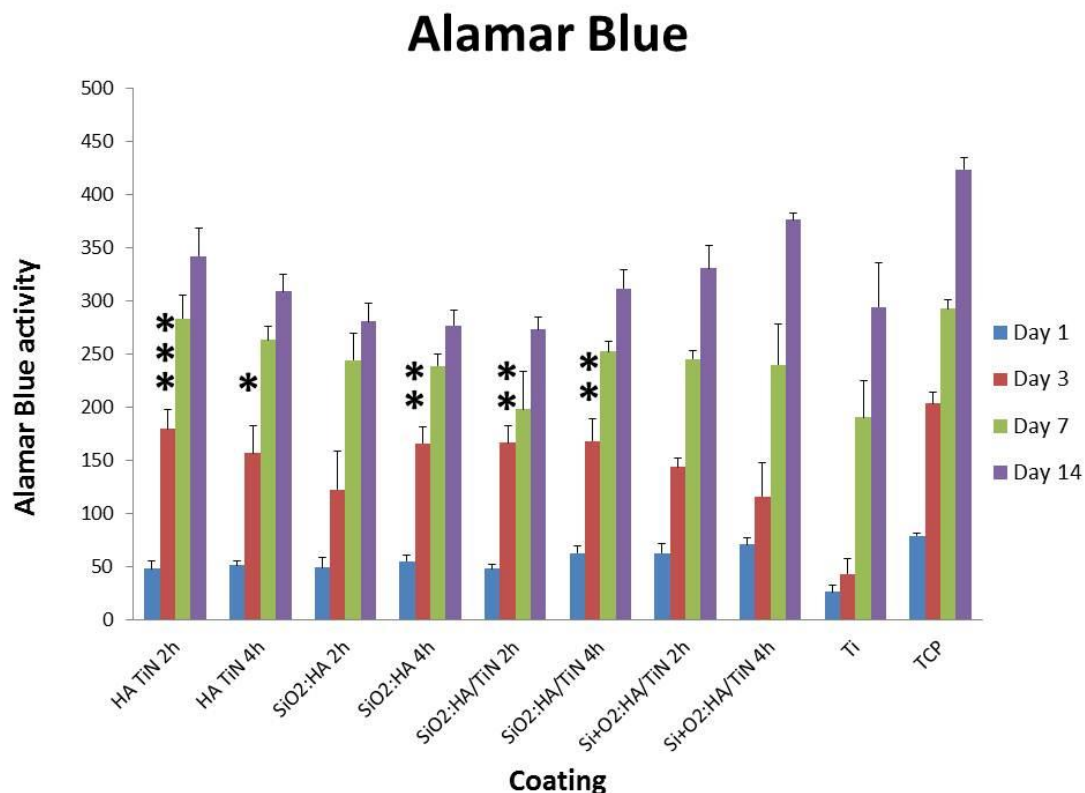


Figure 3-17 Representative column graph of results for all assays. The error bars represent standard error of mean, $n = 6$. * represents the significance compared to the Ti control ($p < 0.05$), where a greater number represents a higher level of significance.

3.4.6 Cell imaging using SEM

Alongside the samples used for the above tests, a separate batch of sterilised samples designated for SEM imaging were seeded with cells in 48 well plates and incubated for the same time points. At the stipulated time points, media was removed, the samples were then washed three times in PBS solution and replaced with fixative, *i.e.* 3% glutaraldehyde in 0.1 M sodium cacodylate buffer and left in the fume cupboard for 30 minutes. The fixative was then replaced with 7% sucrose solution in 0.1 M sodium cacodylate buffer. The cacodylate buffer solution was used to wash the samples 3 times at 5 minute intervals. The cells were then immersed in osmium tetroxide (OsO_4) for 45

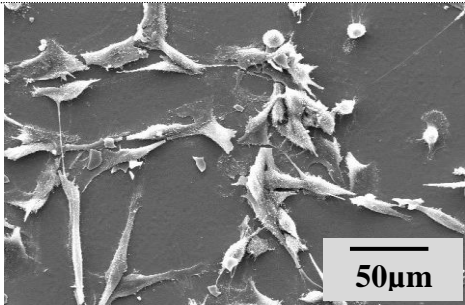
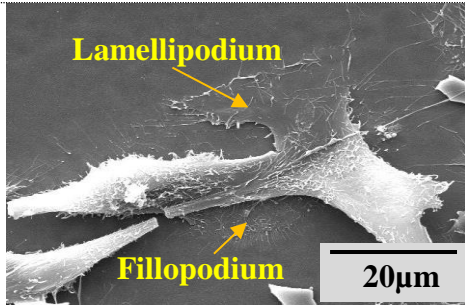
minutes. Dehydration of the cells was then performed using an ethanol / distilled water gradient: 20% for 2 minutes, 40% for 5 minutes, 60% for 5 minutes, 70% for 5 minutes, 80% for 5 minutes, 90% for 5 minutes, 100% for 5 minutes (100% ethanol dehydration was performed twice) and hexamethyldisilazane (HMDS) reagent for 5 minutes, twice. HMDS is a low-cost, time-saving method for assisting with the air-drying of cells for SEM imaging ¹²¹. HMDS cross-links proteins and has a reduced surface tension, both of which add strength to the sample during air-drying and hence it reduces fracturing and subsequent collapsing of specimens ¹²¹. The samples were then left in HMDS and loosely covered in aluminium foil to dry overnight.

The samples were mounted on Al SEM stubs using carbon adhesive tabs. Then, they were gold (Au) coated using an Emscope SC500 sputtering device for two minutes in Ar, which gave a gold thickness of ~5 nm. Samples were then viewed under the SEM at 20kV, in high vacuum mode using a Philips XL30 field emission gun (FEG) ESEM. SE images were obtained at low (x1000) and high (x4000) magnification after 1, 7 and 14 days for sample set 1 and 1, 3, 7 and 14 days for sample set 2.

3.4.6.1 Example SEM data

SE images of the cultured cells were obtained after 1, 7 and 14 days for sample set 1 and 1, 3, 7 and 14 days for sample set 2. Table 3-7 illustrates the morphology of the cells after 1 day, imaged at low (x1000) and high (x4000) magnification.

Table 3-7 Representative SE images of MG63 cells grown on the samples.
The following is day 1 at low (x1000) and high magnification (x4000) of
the cell grown on a 2 h annealed sample.

DAY 1	Annealed 700°C 2h	
	1000X	4000X
HA/TiN		

3.5 Coating dissolution experiments

Samples were incubated in 37°C and in ddH₂O for 1, 3, 7 and 14 days and subsequently analysed via SEM/EDX and XRD using the methodologies as described above. The example data were displayed similarly as described in the sections entitled “SEM imaging and EDX analysis – example data” and “XRD data analysis”.

3.6 Summary

The procedures used for the deposition and characterisation of the coatings in this work have been presented. Ti substrates were polished to a mirror finish and those with a surface roughness (R_a) range of $\sim 47 \pm 10$ nm were selected for coating. The coatings were deposited using a RF magnetron sputtering process utilising a patented closed field unbalanced magnetron sputtering

(CFUB-MS) system by Teer Coatings over a range of processing conditions. Reactive sputtering may have been used to fabricate the TiN barrier layers. Novel 2 wt% silicate substituted hydroxyapatite were developed. The 4 coatings were: HA/TiN, Si:HA, Si:HA/TiN and Si+O₂:HA/TiN. The amorphous as-deposited coatings were annealed for 700°C for 2 h and 4 h in an Ar atmosphere to re-crystallise the HA. Diffraction techniques of GA-XRD and RHEED were used to characterise the structure of the thin coatings. XPS and EDX allowed for compositional analysis of the coating layers and their surface. The biological performance of Si:HA/TiN and Si+O₂:HA/TiN were then compared with samples of relatively known performance HA/TiN and Si:HA.

Chapter 4 Results and Discussion – Set 1 Samples

The microstructures of the four coating types, namely, HA/TiN, Si:HA, Si:HA/TiN and Si+O₂:HA/TiN on commercially pure Ti substrates were investigated, after deposition using RF-McoS and following thermal annealing. The cellular response to these developed coatings was then appraised.

In the Overview of results section, two tables, Table 4-1 and Table 4-2, are presented summarising data sets from the GA-XRD diffraction patterns, SEM images, EDX Ca/P ratios, XPS Ca/P ratios and RHEED patterns for all the as-deposited and annealed coatings. Detailed explanations of the results obtained using each characterisation technique are then presented, with emphasis on the structural evolution of the coatings as a function of annealing time, gas environment, Si-substitution conditions and the addition of a TiN diffusion barrier interlayer. Each characterisation section is divided into sub-sections dedicated to each coating.

For example, in the section entitled “GA-XRD investigations”, the sub-sections describe the structural evolution of each coating on the basis of the various crystalline phases identified within the diffraction patterns. In particular, the effectiveness of the TiN interlayer to retard the development of TiO₂ is appraised, along with the efficacy of HA crystallisation as a function of annealing.

In the “SEM/EDX investigations” section, SEM/EDX characterisation is described with emphasis given to the developed morphology of the coatings as a function of annealing, and the appraisal of the average calcium phosphate (Ca/P) ratios, Ca at% and P at% values of the differentially treated samples. This section begins by comparing the Ca/P values for all the as-deposited samples in order to appraise the efficacy of the magnetron sputtering process in creating stoichiometric amorphous HA. Then the coatings are compared as a function of annealing with emphasis on the morphological changes as a result of crystallisation.

In “RHEED investigations”, surface sensitive RHEED data is presented to complement the structural data from GA-XRD. Representative RHEED ring patterns indexed with *hkl* Miller indices were presented.

In “XPS investigations” an appraisal of the surface chemistry using XPS, being a complementary technique to EDX. A summary table of the surface Ca/P ratios is presented for comparison, along with graphs depicting the average Ca/P ratios, as well as Ca at% and P at% values for each post-deposition treatment. In particular, deconvoluted high spectral resolution scans are presented, along with a description of the development of the surface chemistry of these samples as a function of deposition and annealing.

In “Biological cell study” an *in vitro* alamarBlue cell test for sample set 1 was performed to appraise the potential of the coatings to enhance early bone growth by using bone-like MG63 osteosarcoma cells, cultured for 1, 7 and 14

days. SEM imaging was performed to appraise cell growth as a function of incubation time and coating annealing time. Sample set 2 coatings were also characterised and subjected to biological cell studies using alamarBlue, alkaline phosphatase, DNA Hoescht and osteocalcin, cultured for 1, 3, 7 and 14 days respectively, again using bone-like MG63 osteosarcoma cells.

4.1 Overview of results

Table 4-1 and Table 4-2 are summaries of the GA-XRD data, followed by SEM/EDX, XPS and RHEED data.

Table 4-1 Summary of the characterisation data for the HA/TiN and Si:HA coatings. Key: Unavailable results (N/A); ^D indicates delaminated coating; Adventitious C (Adv. C), perovskite (CaTiO₃) and calcium carbonate (CaCO₃).

Method	HA/TiN As-deposited	HA/TiN Annealed at 700 °C for 2 h	HA/TiN Annealed at 700 °C for 4 h	Si:HA As-deposited	Si:HA Annealed at 700 °C for 2 h	Si:HA Annealed at 700 °C for 4 h
GA-XRD	Ti ₂ N, TiN, Ti	Ti ₂ N, TiN, Ti, TiO ₂ , & HA possibly mixed with CaTiO ₃	Ti ₂ N, TiN, Ti, TiO ₂ , & HA possibly mixed with CaTiO ₃	Ti ₂ N, TiN, Ti	Ti ₂ N, TiN, Ti, TiO ₂ , Ti ₂ O ₃ & HA possibly mixed with CaTiO ₃	Ti ₂ N, TiN, Ti, strong TiO ₂ , Ti ₂ O ₃ & HA possibly mixed with CaTiO ₃
SEM	Smooth coating	Textured coating	Delaminated coating & islands	Smooth coating	Granular	Floccular
EDX (Ca/P ratio)	2.19±0.22 (1.90, 2.05, 2.63)	2.41±0.03 (2.35, 2.43, 2.43)	2.15±0.23 ^D (1.83, 2.03, 2.59)	1.89±0.12 (1.69, 1.88, 2.10)	2.13±0.11 (2.03, 20.3, 2.34)	1.98±0.09 (1.87, 1.91, 2.16)
XPS (Ca/P ratio)	1.71, 1.68	2.43	2.26, 3.82	1.52, 1.75	2.34, 3.23	0, 4.05
XPS	Adv. C, Hydrocarbon, CaCO ₃ , HA	TiO ₂ , adv. C, Hydrocarbon, CaCO ₃ , HA, possibly mixed with CaTiO ₃	TiO ₂ , adv. C, Hydrocarbon, CaCO ₃ , HA, possibly mixed with CaTiO ₃	Adv. C, Hydrocarbon, CaCO ₃ , HA	TiO ₂ , adv. C, Hydrocarbon, CaCO ₃ , HA, possibly mixed with CaTiO ₃	TiO ₂ , adv. C, Hydrocarbon, CaCO ₃ , HA, possibly mixed with CaTiO ₃
RHEED	Amorphous	HA and TiO ₂	N/A	Amorphous	HA and TiO ₂	N/A

Table 4-2 Summary of the characterisation data for the Si:HA/TiN and Si+O₂:HA/TiN coatings. Key: Unavailable results (N/A); ^D indicates delaminated coating; Adventitious C (Adv. C,) perovskite (CaTiO₃) and calcium carbonate (CaCO₃).

Method	Si:HA/TiN As-deposited	Si:HA/TiN Annealed at 700 °C for 2 h	Si:HA/TiN Annealed at 700 °C for 4 h	Si+O ₂ :HA/TiN As-deposited	Si+O ₂ :HA/TiN Annealed at 700 °C for 2 h	Si+O ₂ :HA/TiN Annealed at 700 °C for 4 h
GA-XRD	Ti ₂ N, TiN, Ti	Ti ₂ N, TiN, Ti, TiO ₂ & HA possibly mixed with CaTiO ₃	Ti ₂ N, TiN, Ti, strong TiO ₂ & HA possibly mixed with CaTiO ₃	Ti ₂ N, TiN, Ti	Ti ₂ N, TiN, Ti, TiO ₂ & HA possibly mixed with CaTiO ₃	Ti ₂ N, TiN, Ti, strong TiO ₂ & HA possibly mixed with CaTiO ₃
SEM	Smooth coating	Delaminated coating & islands	Delaminated coating & islands	Smooth coating & slight indents	Delaminated coating & islands	Delaminated coating & islands
EDX (Ca/P ratio)	2.20±0.21 (1.95, 2.05, 2.61)	2.08±0.01 ^D (2.06, 2.07, 2.10)	1.96±0.30 ^D (1.61, 1.70, 2.56)	2.33±0.22 (2.00, 2.23, 2.75)	1.41±0.10 ^D (1.29, 1.33, 1.60)	1.93±0.15 ^D (1.65, 2.00, 2.14)
XPS (Ca/P ratio)	1.83, 1.91	0, 2.32	2.51, 3.24	1.61, 1.85	4.19	1.53, 2.66
XPS	Adv. C, Hydrocarbon, CaCO ₃ , HA	TiO ₂ , adv. C, Hydrocarbon, CaCO ₃ , HA, possibly mixed with CaTiO ₃	TiO ₂ , adv. C, Hydrocarbon, CaCO ₃ , HA, possibly mixed with CaTiO ₃	Adv. C, Hydrocarbon, CaCO ₃ , HA	TiO ₂ , adv. C, Hydrocarbon, CaCO ₃ , HA, possibly mixed with CaTiO ₃	TiO ₂ , adv. C, Hydrocarbon, CaCO ₃ , HA, possibly mixed with CaTiO ₃
RHEED	Amorphous	N/A	N/A	Amorphous	HA and TiO ₂	N/A

4.2 GA-XRD investigations

4.2.1 HA/TiN coatings

Figure 4-1 presents a representative X-ray diffraction pattern of the as-deposited HA/TiN coatings, with evidence for the presence of (poly)crystalline TiN, Ti₂N and Ti (Inorganic Crystal Structure Database (ICDD) reference codes: 00-017-0386, 00-044-1294 and 00-038-1420, respectively). However, no broad amorphous peaks indicative of the presence of HA were evident for any of the as-deposited coatings, possibly due to the thinness of the HA layers which were estimated to be < 200 nm.

Representative diffraction patterns for the HA/TiN coatings, annealed at 700°C for 2 h and 4 h, respectively, are also shown in Figure 4-1 with peak intensities normalised to TiN (111) at $\sim 38^\circ$. The annealed samples showed the development of crystalline HA peaks, as a function of annealing, with more HA (ICDD code 01-074-0565) peaks emerging, *i.e.* HA (211), (112) and (300), with increasing annealing time, in addition to tentative evidence for the presence of perovskite, CaTiO₃ (ICDD code 98-006-6605). In addition, peaks attributable to Ti₂N and TiN became sharper with increasing annealing times, indicative of the enhanced crystal growth of these phases. The Ti peak intensities were observed to decrease as the TiN, Ti₂N and HA phases crystallised, being attributable to densification of the annealed coatings. Evidence for the development of some rutile (TiO₂) was also found for the coatings annealed for 4 h. Table 4-3 is a summary of the crystalline phases present at every treatment stage.

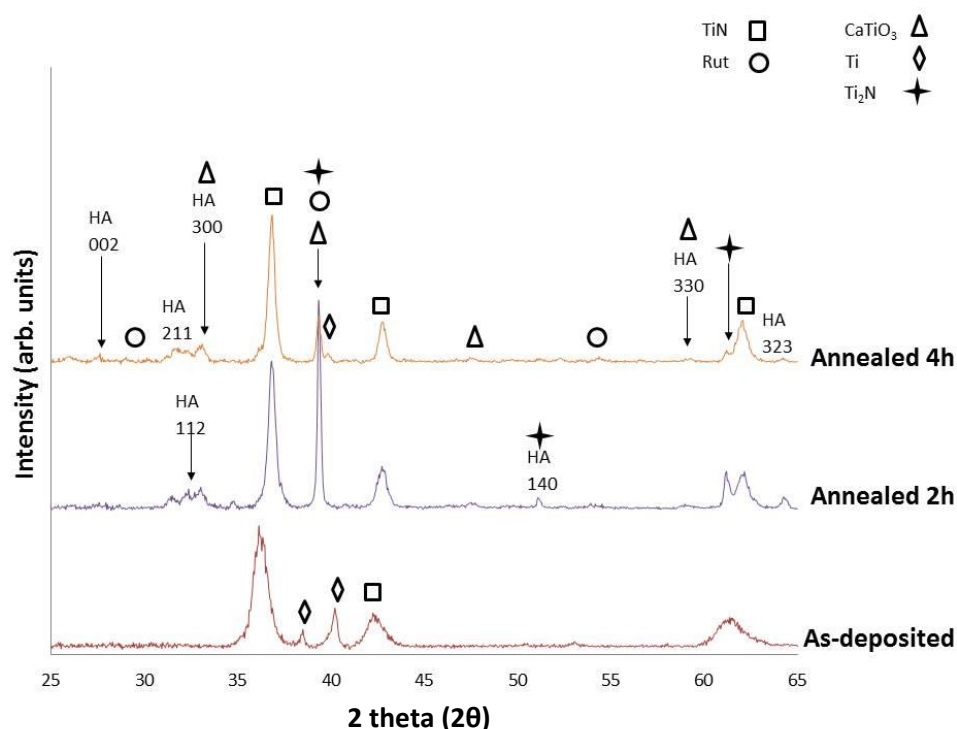


Figure 4-1 Representative GA-XRD patterns of the HA/TiN coatings; as-deposited, and annealed at 700°C for 2 h and 4 h, respectively.

Table 4-3 Summary of crystalline phases in the annealed HA/TiN coatings

Treatment	Crystalline phases					
As-deposited				TiN	Ti ₂ N	Ti
Annealed 700°C 2 h	HA	CaTiO ₃		TiN	Ti ₂ N	
Annealed 700°C 4 h	HA	CaTiO ₃	TiO ₂	TiN	Ti ₂ N	Ti

4.2.2 Si:HA coatings

Figure 4-2 presents representative GA-XRD patterns for the Si:HA coatings, as-deposited and annealed at 700°C for 2 h and 4 h, respectively, without normalisation in this case. Only peaks from the Ti substrate are present for the as-deposited samples, again consistent with the thin HA layer being amorphous. After annealing for 2 h, peaks attributable to titanium (III) oxide (Ti₂O₃; ICDD: 00-010-0063) were identified, along with rutile (TiO₂; ICDD:

00-021-1272). Peaks attributable to the development of crystalline HA, similar to those identified for the annealed HA/TiN coatings, were also observed, along with the possibility of some peaks indicative of perovskite (CaTiO_3 ; ICDD: 98-006-6605). Again, more peaks attributable to HA developed with increasing annealing time was consistent with increased crystallisation and densification of the HA. However, more intense rutile (TiO_2) peaks also appeared after 4 h of annealing, indicative of rapid oxidation of the Ti substrate. Table 4-4 is a summary of the crystalline phases present at every treatment stage.

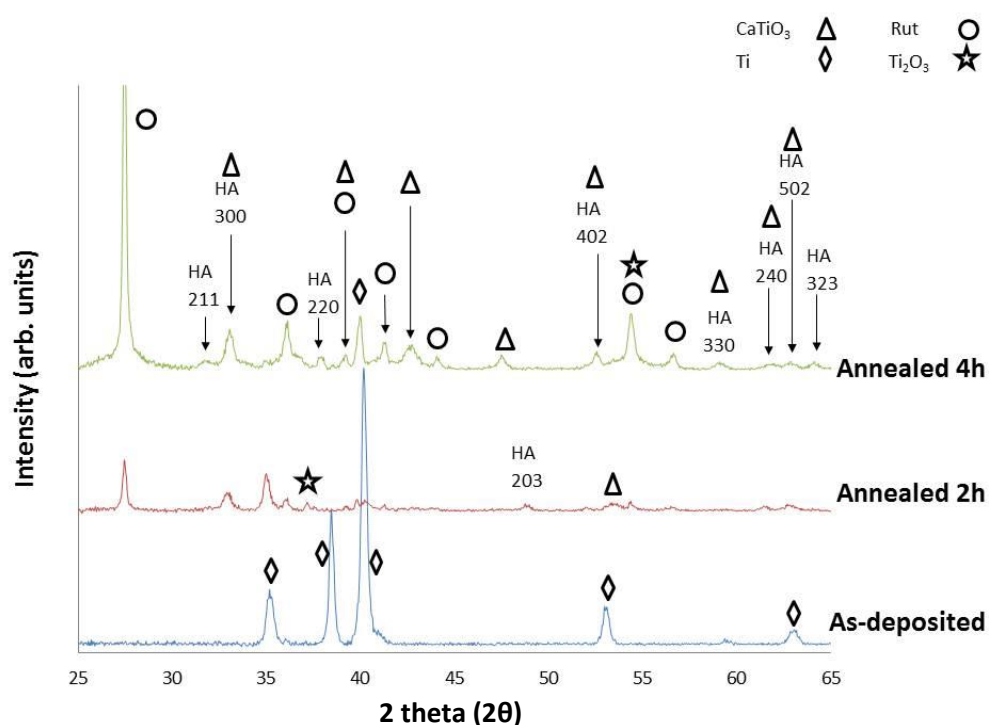


Figure 4-2 Representative GA-XRD patterns of the Si:HA coatings; as-deposited, and annealed at 700°C for 2 h and 4 h, respectively.

Table 4 Summary of crystalline phases within the Si:HA coatings

Treatment	Crystalline phases				
As-deposited					Ti
Annealed 700°C 2 h	HA	CaTiO ₃	TiO ₂ (rut)	Ti ₂ O ₃	Ti
Annealed 700°C 4 h	HA	CaTiO ₃	TiO ₂ (rut)	Ti ₂ O ₃	Ti

4.2.3 Si:HA/TiN and Si+O₂:HA/TiN coatings

Figure 4-3 similarly presents representative GA-XRD patterns for the Si:HA/TiN and Si+O₂:HA/TiN coatings, and will be discussed similarly. As additional detail, Figure 4-3 is specific to Si+O₂:HA/TiN and for Si:HA/TiN, please go to Figure 10-3. The as-deposited samples had the same TiN, Ti₂N and Ti peaks as in the HA/TiN coatings. The annealed samples (annealed at 700°C for 2 h and 4 h) also showed the development of crystalline HA, along with the presence of some rutile after 2 h which intensified after 4 h of annealing. The rutile intensity, however, was not as high as that shown by the Si:HA coatings, indicating that the TiN barrier layer had had some success in retarding the growth of titanium oxide at the coating/substrate interface. Table 4-4 is a summary of the crystalline phases present at every treatment stage.

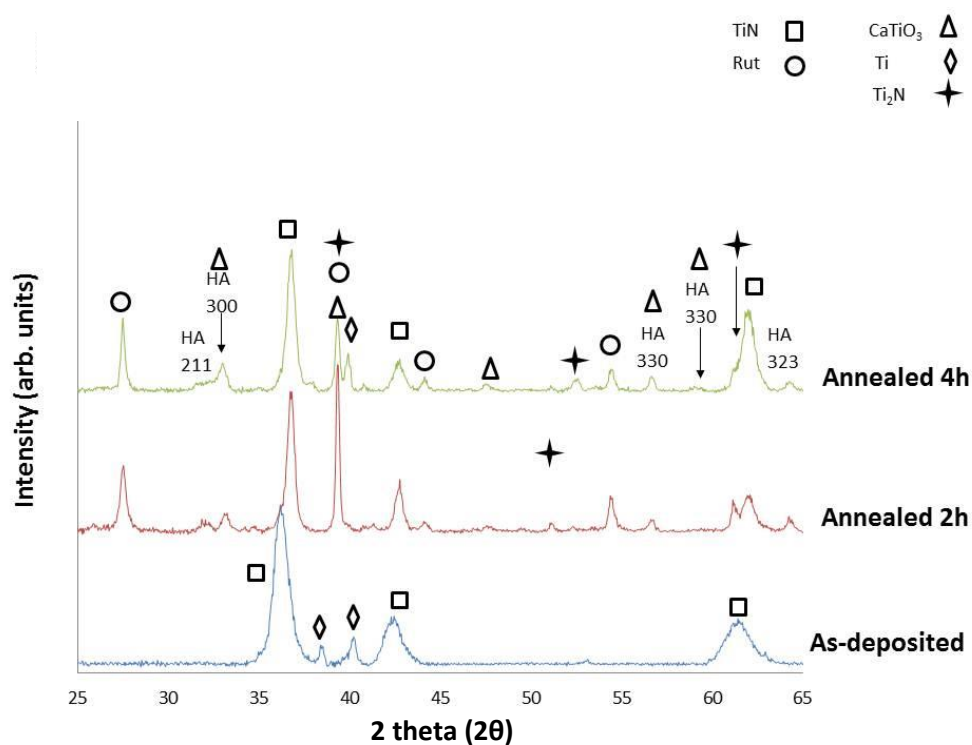


Figure 4-3 Representative GA-XRD patterns for Si:HA/TiN and Si+O₂:HA/TiN samples: as-deposited, and annealed at 700°C for 2 h and 4 h, respectively.

Table 4-4 Summary of crystalline phases in the Si:HA/TiN and Si+O₂:HA/TiN samples

Treatment	Crystalline phases					
As-deposited				TiN	Ti ₂ N	Ti
Annealed 700°C 2 h	HA	CaTiO ₃	TiO ₂	TiN	Ti ₂ N	Ti
Annealed 700°C 4 h	HA	CaTiO ₃	TiO ₂	TiN	Ti ₂ N	Ti

4.3 SEM/EDX investigations

SEM imaging and EDX data acquisition were performed at 20kV, spot size 4 and a working distance of 10 mm. Imaging was performed using both secondary electron (SE) and backscattered electron (BSE) modes, whilst EDX was performed in the BSE mode. EDX spectra were obtained at x5, 000

magnification with an acquisition time of 50 s, in order to acquire ~ 500,000 spectrum counts. Three areas per sample were appraised and, using the all elements mode, calcium-phosphate (Ca/P) ratios were determined and averaged for each coating for comparison.

The Ca/P ratio is commonly appraised during bone biomaterial research^{8; 12; 34; 47; 51; 76; 90; 122} since variations in the Ca/P ratio for amorphous and crystalline HA affects its properties and ultimately its biocompatibility^{34; 51}. Hence, Ca/P ratio assessments are used as an indicator for the suitability of coatings to attract and grow healthy bone cells. It has been suggested that the Ca/P ratio for annealed HA must be at 1.67 for optimum bioactivity due to its similarity with natural bone and relatively low solubility in physiological fluid⁸.

4.3.1 As-deposited coatings

SE imaging of the as-deposited coatings appeared specular, with little contrast variation, indicative of uniform coverage, and hence are not shown here. Figure 4-4 presents bar charts summarising the Ca/P ratios and Ca at% and P at% values for the as-deposited coatings. The Ca/P ratios are 2.19 ± 0.22 , 1.89 ± 0.12 , 2.20 ± 0.21 , and 2.33 ± 0.22 for HA/TiN, Si:HA, Si:HA/TiN, and Si+O₂:HA/TiN, respectively. The ratios were found to be similar across the sample set, although the absolute Ca and P at% values were found to be lower in the Si+O₂:HA/TiN coatings. Using a partial pressure of O₂ was found to inhibit Ca and P deposition¹²³. The as-deposited Si:HA coating had the lowest average Ca/P ratio as compared with the other as-deposited coatings because it has the highest P at% compared to the TiN-containing samples. It is

most likely that the titanium ions (Ti^{3+}) and N^{3-} ions resulted from reactive sputtering of the Ti target in Ar/N_2 atmosphere during TiN deposition¹²⁵. Perhaps the P in the HA lattice was substituted by Ti^+ and/or N^+ , which may explain the lesser P at% in the TiN samples.

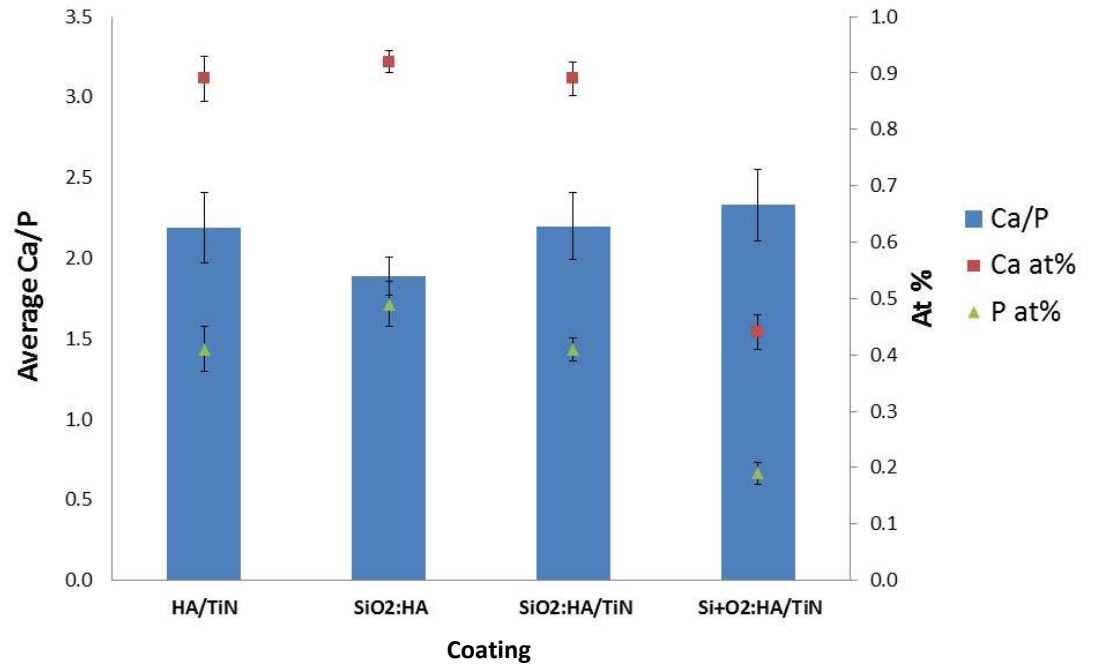


Figure 4-4 Bar chart comparing average Ca/P ratios, and Ca and P at % values for the as-deposited coatings

4.3.2 HA/TiN coatings

Figure 4-5 presents representative SEM and EDX data for the as-deposited and annealed HA/TiN coatings. The as-deposited HA/TiN coatings exhibited smooth morphologies. After 2 h of annealing, the coating had a slightly more textured appearance. After 4 h of annealing, patches of the coatings delaminated, giving rise to two regions; *i.e.* islands of remnant HA and regions of exposed substrate which exhibited just Ti and O signals in EDX (see Appendix, Figure 10-4). The average Ca/P ratios for the as-deposited, 2 h annealed and 4 h annealed samples were 2.19 ± 0.22 , 2.41 ± 0.03 and $2.15 \pm$

0.23, respectively. The average Ca/P ratios for the as-deposited and 2 h annealed HA/TiN coatings were not significantly different, although there was a significant decrease in the Ca/P ratio for the HA/TiN coating annealing for 4 h. Similarly, the absolute Ca and P at% values for the as-deposited and 2 h annealed coatings did not change significantly (Figure 4-6). However, after 4 h of annealing, the Ca and P at% values were significantly reduced, with a corresponding reduction in the Ca/P ratio. Ca and P evaporation may have occurred, facilitated by the Ar gas flow ¹²⁴. An oxygen atom of Ca (II) of the HA lattice is weakly bound to the HA lattice therefore facilitating evaporation

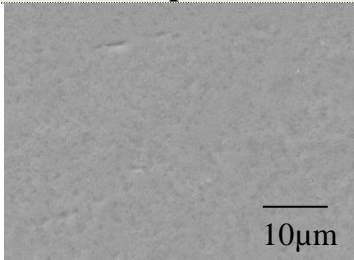
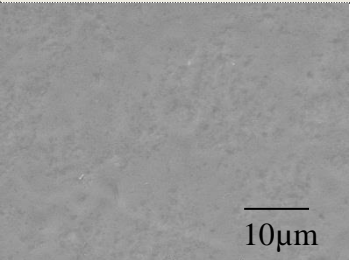
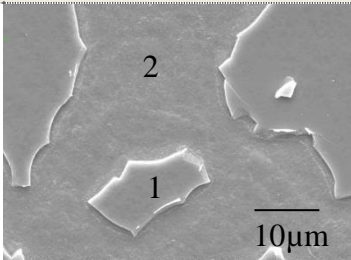
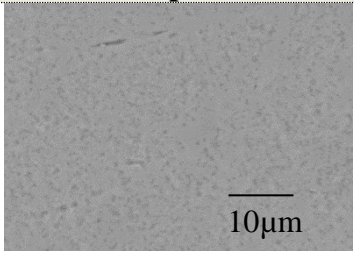
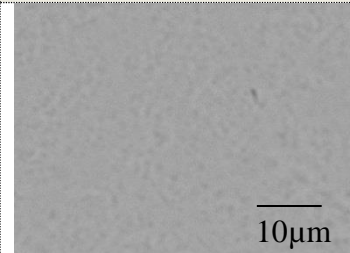
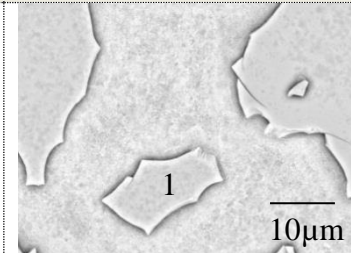
SE images of HA/TiN		
As-deposited	2 h	4 h
		
Smooth coating.	More textured coating.	Delaminated coating. (1): islands of remnant coating containing Ca and P. (2): exposed substrate, exhibiting Ti and O.
BSE images of HA/TiN		
As-deposited	2 h	4 h
		
Ca/P ratio: 2.19 ± 0.22	Ca/P ratio: 2.41 ± 0.03	(1) Ca/P ratio: 2.15 ± 0.23

Figure 4-5 HA/TiN coatings: as-deposited, and annealed at 700°C for 2 h and 4 h, respectively.

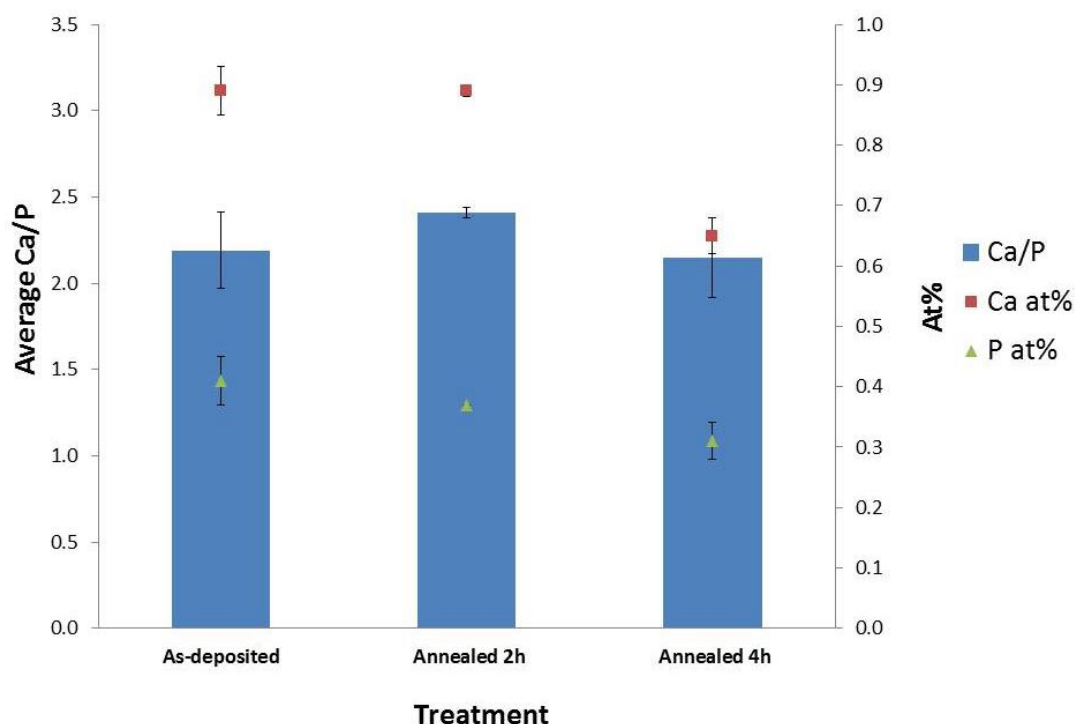


Figure 4-6 Bar charts comparing average Ca/P ratios, and Ca and P at % values for the HA/TiN coatings; as-deposited and annealed at 700°C for 2 h and 4 h.

4.3.3 Si:HA coatings

Figure 4-7 presents representative SEM images and EDX data for the as-deposited and annealed Si:HA coatings. The as-deposited Si:HA coatings again exhibited smooth morphologies. Some Si clumps $\sim 2 \mu\text{m}$ in size were also identified. After 2 h of annealing, the Si:HA coatings developed a slight granular appearance. However, after 4 h of annealing the coatings became floccular with clusters of calcium phosphate. The average Ca/P ratios of the as-deposited, and 2 h and 4 h annealed samples are 1.89 ± 0.12 , 2.13 ± 0.11 and 1.98 ± 0.09 , respectively. The ratios had much more variation in the HA composition, as a function of annealing, as compared with the unsubstituted HA/TiN coatings. EDX investigation of the 4 h annealed sample (Figure 4-7,

regions 1 and 2) had similar Ca/P ratios across the sample indicating that a uniform HA coating had been retained. EDX analysis also confirmed the presence of Ti and O, again indicative of the oxidation of the substrate with prolonged annealing time, consistent with the GA-XRD data.

Figure 4-8 presents a comparison of average Ca/P ratios, and average Ca and P at% values for the Si:HA coatings. Upon annealing the average Ca/P ratio increased, and remained similar for both annealing times. However, there was a significant decrease for both Ca at% and P at% values for the annealed coatings, as compared to the as-deposited coatings.

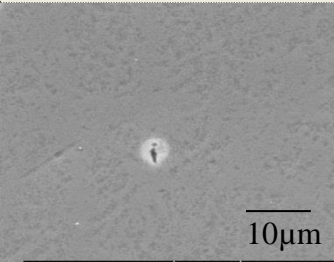
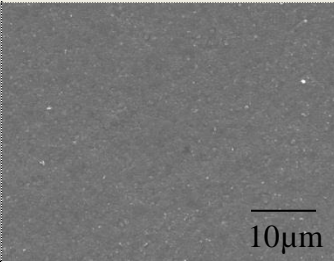
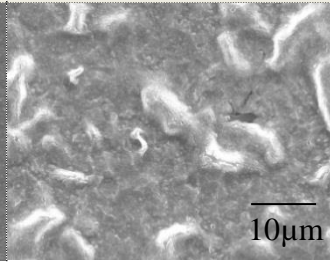
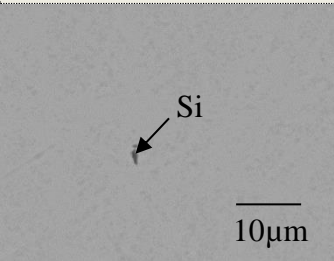
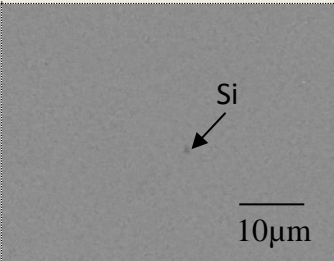
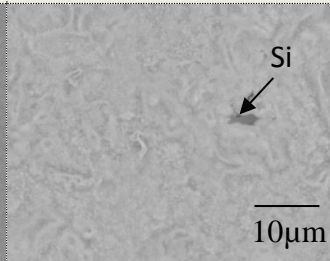
SE images of Si:HA		
As-deposited	2 h	4 h
		
Smooth with Si clumps	Granular	Floccular with some larger grains
BSE images of Si:HA		
As-deposited	2 h	4 h
		
Ca/P ratio: 1.89 ± 0.12 Si clumps 2µm in length.	Ca/P ratio: 2.13 ± 0.11 Si clumps 2µm in length.	Ca/P ratio: 1.98 ± 0.09 Si clumps 2µm in length.

Figure 4-7 Si:HA coatings: as-deposited, and annealed at 700°C for 2 h and 4 h, respectively

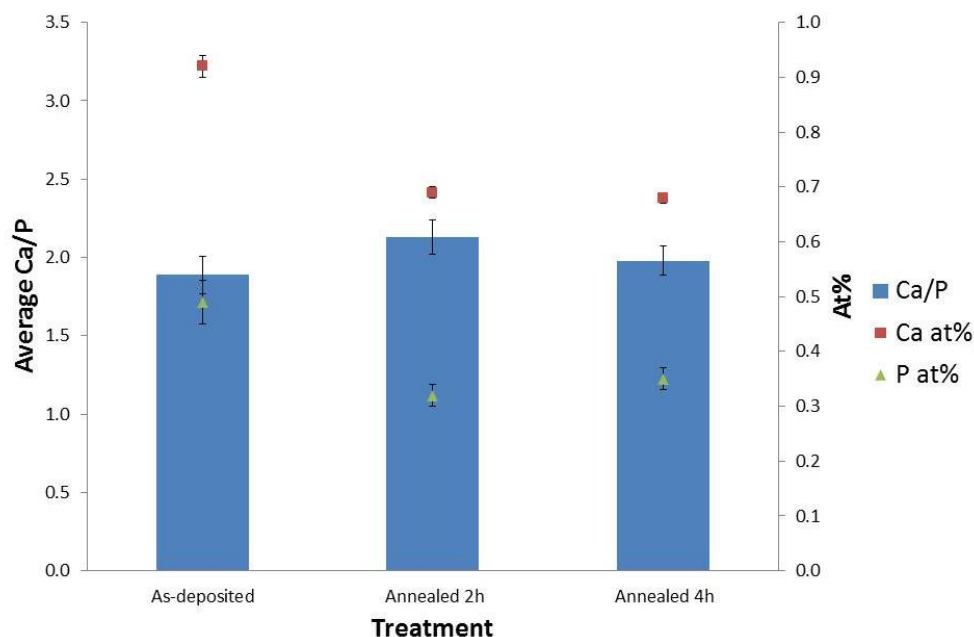


Figure 4-8 Bar charts comparing average Ca/P ratios, and Ca and P at % values for the Si:HA coatings; as-deposited, and annealed at 700°C for 2 h and 4 h.

4.3.4 Si:HA/TiN coatings

Figure 4-9 presents SEM and EDX data for the Si:HA/TiN coatings. The as-deposited Si:HA/TiN coatings again exhibited relatively smooth morphologies. After 2 h of annealing, the Si:HA/TiN coatings delaminated, leaving a mixture of HA islands and exposed oxidised regions of the Ti substrate (see Appendix Figure 10-4). More extensive delamination occurred after 4 h of annealing. The ratios for the as-deposited, 2 h annealed and 4 h annealed samples were 2.20 ± 0.21 , 2.08 ± 0.01 , 1.96 ± 0.30 , respectively. Figure 4-10 compares average Ca/P ratios, and average Ca and P at% values of the Si:HA/TiN coatings. As for the previous coatings, the Ca and P at% values decreased within the annealed samples.

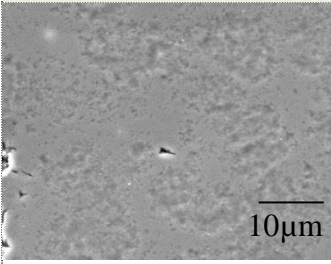
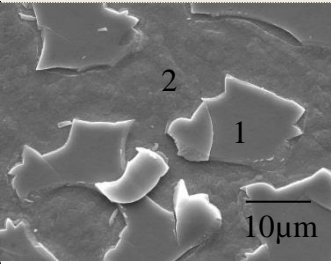
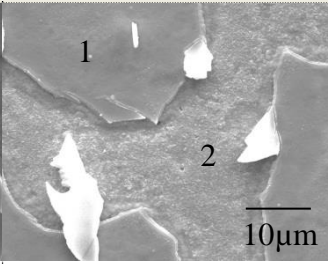
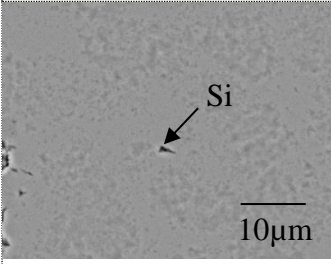
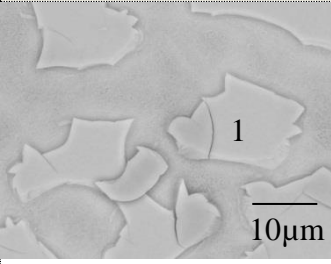
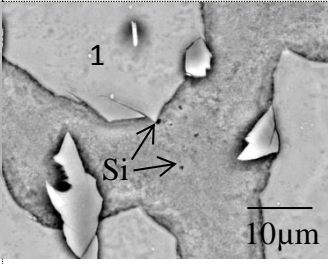
SE images of Si:HA/TiN		
As-deposited	2 h	4 h
		
Smooth coating & Si clumps	Delaminated coating (1): islands of remnant coating containing Ca and P. (2): exposed substrate. exhibiting Ti and O.	Delaminated coating (1): islands of remnant coating containing Ca and P. (2): exposed substrate. exhibiting Ti and O.
BSE images of Si:HA/TiN		
As-deposited	2 h	4 h
		
Ca/P ratio: 2.20 ± 0.21	(1) Ca/P ratio: 2.08 ± 0.01	(1) Ca/P ratio: 1.96 ± 0.30

Figure 4-9 Si:HA/TiN coatings: as-deposited, and annealed at 700°C for 2 h and 4 h , respectively

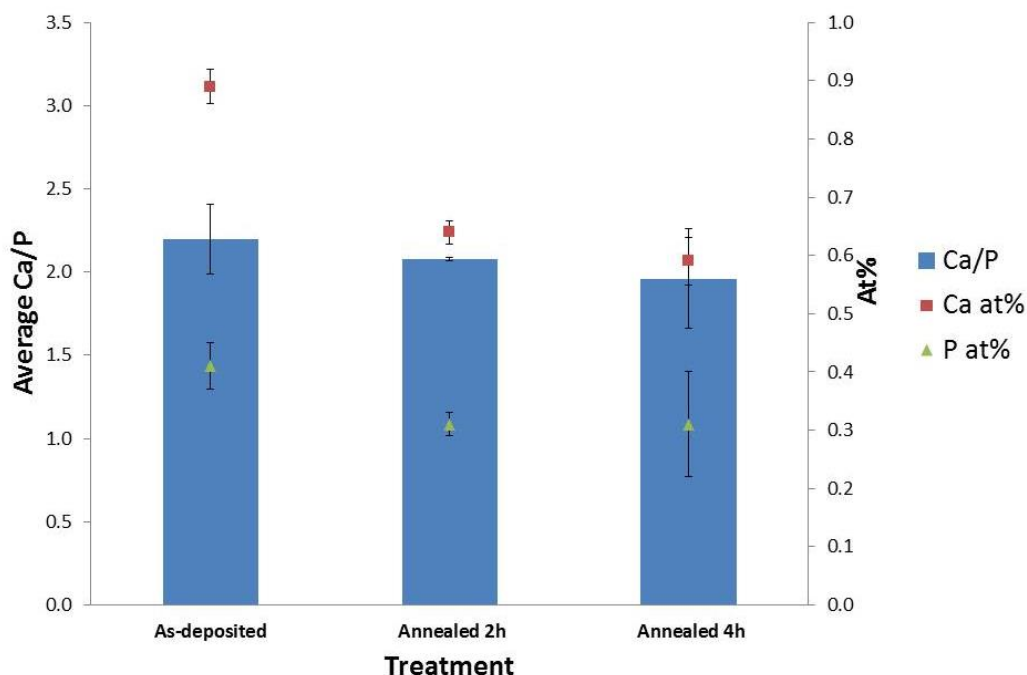


Figure 4-10 Bar charts comparing average Ca/P ratios, and Ca and P at% values for the Si:HA/TiN coatings; as-deposited, and annealed at 700°C for 2 h and 4 h, respectively.

4.3.5 Si+O₂:HA/TiN coatings

Figure 4-11 presents representative SEM and EDX data for the Si+O₂:HA/TiN coatings. The as-deposited coatings again exhibited relatively smooth morphologies, following that of the Ti substrate (along with some artefact Si-containing clumps from the polishing process). After 2 h of annealing, the HA/TiN coating delaminated, leaving HA/TiN islands and exposed regions of the oxidised Ti substrate (see Appendix Figure 10-4). There was more extensive delamination after 4 h of annealing. The as-deposited, 2 h annealed sample and 4 h annealed samples have the ratios of 2.33 ± 0.22 , 1.41 ± 0.10 , and 1.93 ± 0.15 , respectively.

Figure 4-12 compares average Ca/P ratios, and average Ca and P at% values of the Si+O₂:HA/TiN coatings. Again, the Ca and P at% values decreased as a consequence of annealing, showing the largest decrease for the entire sample set.

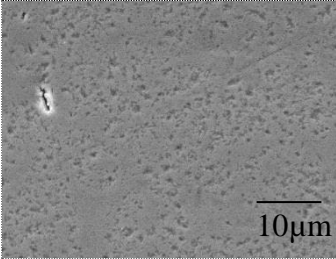
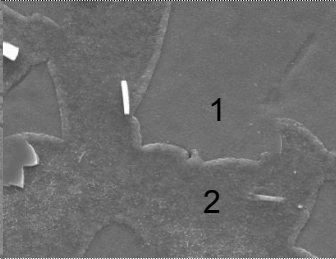
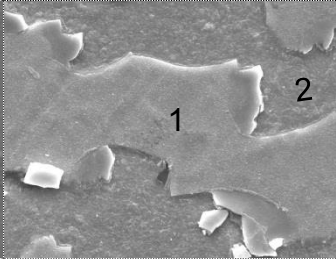
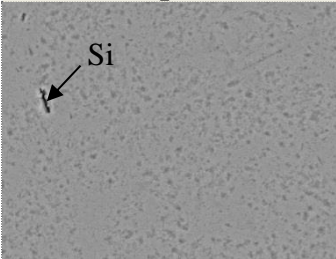
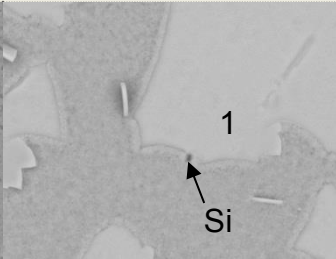
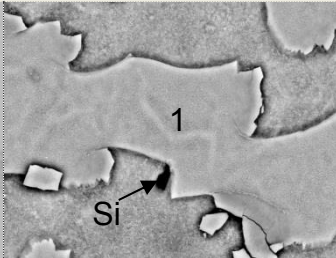
SE images of Si + O ₂ :HA/TiN		
As-deposited	2 h	4 h
		
Smooth coating & Si clumps	Delaminated coating. (1): islands of remnant coating containing Ca and P. (2): exposed substrate. exhibiting Ti and O.	Delaminated coating. (1): islands of remnant coating containing Ca and P. (2): exposed substrate. exhibiting Ti and O.
BSE images of Si + O ₂ :HA/TiN		
As-deposited	2 h	4 h
		
Ca/P ratio: 2.33 ± 0.22	(1) Ca/P ratio: 1.41 ± 0.10	(1) Ca/P ratio: 1.93 ± 0.15

Figure 4-11 Si+O₂:HA/TiN coatings: as-deposited, and annealed at 700°C for 2 h and 4 h, respectively.

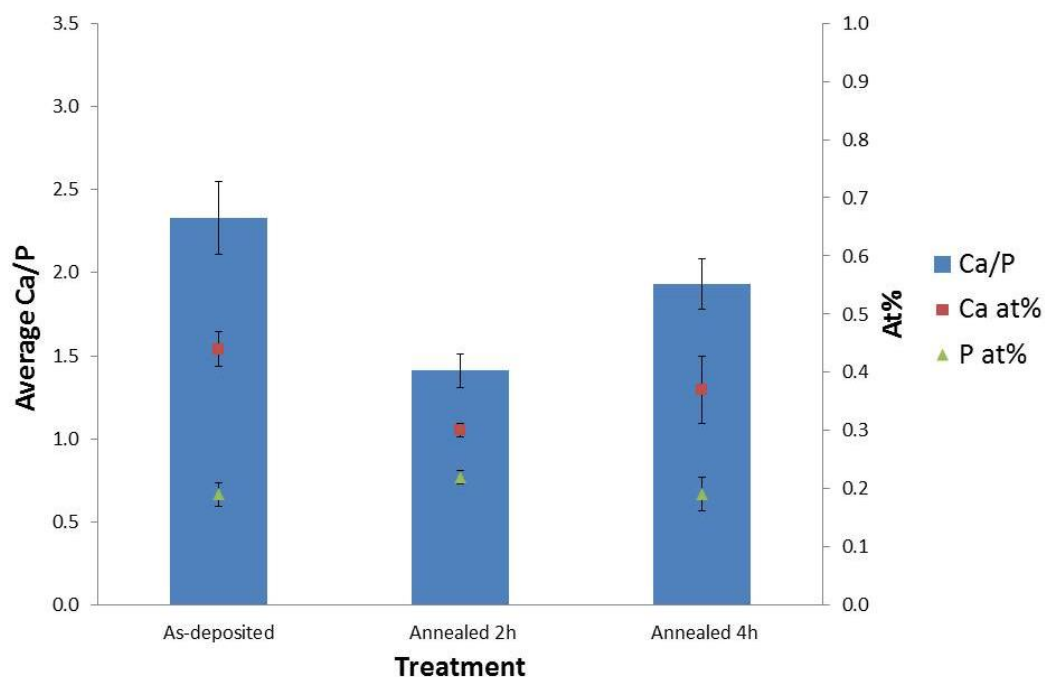


Figure 4-12 Bar charts comparing average Ca/P ratios, and Ca and P at% values for the Si+O₂:HA/TiN coatings; as-deposited, and annealed at 700°C for 2 h and 4 h, respectively.

4.3.6 Summary of SEM/EDX investigations

In summary, as-deposited coatings and coatings annealed at 700°C for 2 h and 4 h, respectively, were investigated systematically using SEM and EDX. In general, the as-deposited coatings followed the morphology of the polished Ti substrates, whilst changes in coating texture were observed as a consequence of annealing. Samples with a TiN interlayer were much more likely to delaminate with annealing, leaving residual HA/TiN islands and exposed regions of oxidised Ti substrate. In terms of the rate of delamination, Si-substituted samples with a TiN interlayer tended to delaminate more quickly than unsubstituted samples with a TiN interlayer upon annealing. Si-substituted HA coatings without TiN interlayers were less susceptible to delamination. Hence, residual strain associated with the TiN barrier layer is

implicated in the delamination process, possibly accentuated by the Si substitution of the HA. The $\sim 2\ \mu\text{m}$ Si-containing clumps, considered artefacts from the substrate polishing process, could also act as strain centres, contributing to the process of localised delamination.

The average Ca/P ratios had a trend away from the composition of the amorphous, as-deposited HA layers, with a corresponding reduction of the Ca and P at% values as a consequence of annealing. It is noted that the as-deposited Si:HA coatings without a TiN interlayer had the lowest Ca/P ratios and most closely resembled the composition of stoichiometric HA, compared to the other coatings. It is likely that the presence of TiN caused the lowering of P. Among the as-deposited coatings, the as-deposited Si+O₂:HA/TiN coatings had the lowest Ca at% and P at% values, which is consistent with a previous finding¹²³. Question of process control of the reactive magnetron sputtering technique when depositing HA in the presence of other elemental species on to a TiN diffusion barrier layer are raised.

Further, the Ca/P ratios for all the annealed HA samples on TiN barrier layers were lower than that for the as-deposited HA. Phosphate and Ca(II) groups are weakly bound to HA lattice⁶⁶ and are easily substituted or evaporated during the sputtering process^{18; 100}. Perhaps the Ti ions produced during TiN deposition¹²⁵ competitively substituted P and Ca. During annealing, Ca and P evaporation could be caused by Ar flow¹⁸.

When combined with the trend for delamination of coatings with a TiN barrier interlayer during the process of annealing (designed to induce crystallisation of the HA), it is clear that a delicate balance is needed when processing the as-deposited coatings. It is recognised that the TiN barrier layer is needed to inhibit oxidation of the Ti substrate which would otherwise lead to unwanted scale formation. However, care is needed to establish the most appropriate temperatures, times and ambient conditions for annealing in order to induce HA crystallisation whilst avoid the onset of coating delamination.

No evidence for the presence of Si within the deposited and annealed HA coatings was obtained from EDX analysis (please refer to Figure 3-8 in Appendix) reflecting the limited sensitivity of this technique for substitution level concentrations. Hence, complementary XPS was used to appraise the surface chemistry of these coatings.

4.4 RHEED investigations

Figure 4-13 presents representative RHEED patterns for the various coatings, both as-deposited (Figure 4-13a) and after 2 h of annealing at 700°C (Figure 4-13b, c). The RHEED pattern representative of an as-deposited sample (Figure 4-13a), taken from a HA/TiN sample, shows a hazy glow and no ring formations, consistent with an amorphous deposit. The RHEED patterns representative of the annealed coatings (Figure 4-13b, c) tended to show diffraction spots / rings with *hkl* Miller indices consistent with the development of crystalline HA and TiO₂. The continuous ring pattern of Figure 4-13b taken from a HA/TiN sample is consistent with the development

of a large number of small grains of HA and rutile. Similarly, the ring pattern of Figure 4-13c, taken from a different part of the surface of the same sample, exhibits a ring pattern of more discrete diffraction spots, indicative of the development of a number of larger, more well-defined HA and rutile grains in this region. All the diffraction spots sit on the same rings, confirming that the small and large grains are the same phases.

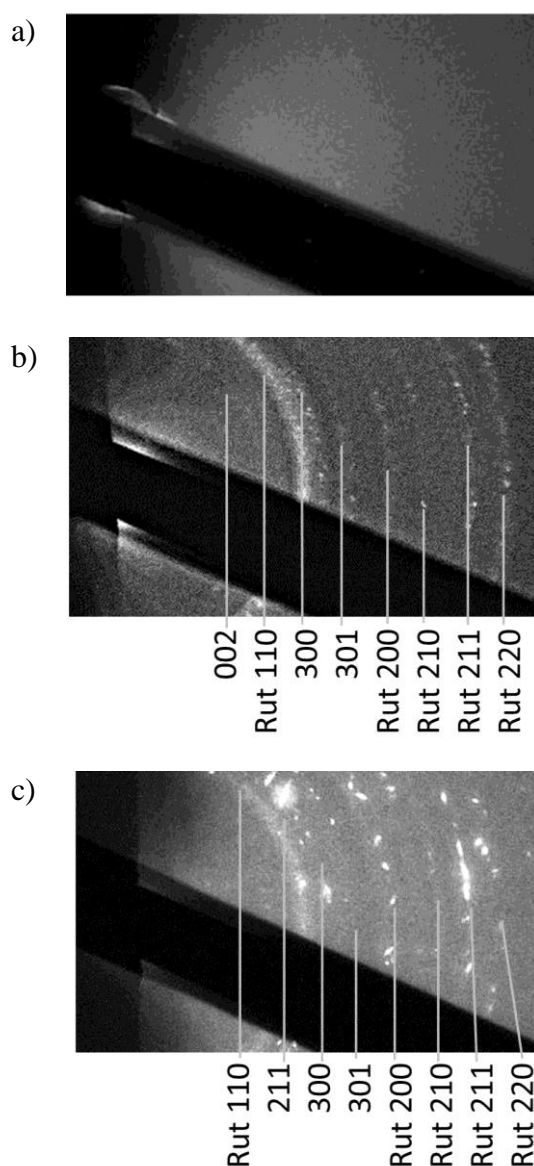


Figure 4-13 Representative RHEED patterns of a) An as-deposited sample, b-c) two different areas of a sample annealed at 700°C for 2 h (indexed for HA and rutile).

4.5 XPS investigations

A VG ESCALab Mk II XPS was used to obtain information about the surface chemistry of the coatings. Casa XPS software (version 2) was used to analyse and quantify the spectroscopic data, between 0-1200 eV. All spectra binding energies were charge corrected to the adventitious carbon peak (C 1s) at 284.6 eV and correlated with the NIST XPS Database and Ohtsu *et al*¹²⁶. Low resolution survey scans and high resolution scans were obtained for Ca 2p, O 1s, Ti 2p, C 1s, P 2p and Si 2p signatures, and fitted with Shirley backgrounds.

Table 4-5 is a summary of the coatings for comparison. It was found that the Ca/P ratios for the as-deposited coatings were close to generally that of stoichiometric HA. After annealing, the Ca/P ratios varied greatly, indicating significant losses of P. presents a bar graph of the XPS determined Ca/P ratios, and the Ca and P at% values for the as-deposited and annealed HA/TiN, Si:HA, Si:HA/TiN and Si+O₂:HA/TiN coatings. Again, the main theme to emerge is that the Ca and P at% values decreased upon annealing, with a corresponding increase in Ca/P ratios, consistent with a loss of P during HA grain growth (Figure 4-14). Interestingly, the trend in development of the near surface chemistry of these samples was not consistent with the trend indicated by EDX analysis which samples the bulk of the coatings.

Table 4-5 Summary of surface Ca/P ratios obtained using XPS

	Sample					
	HA/TiN as-deposited	HA/TiN 700°C for 2 h	HA/TiN 700°C for 4 h	Si:HA as-deposited	Si:HA 700°C for 2 h	Si:HA 700°C for 4 h
Ca/P	1.71, 1.68	2.43	2.26, 3.82	1.52, 1.75	2.34, 3.23	0, 4.05
	Si:HA/ TiN as- deposited	Si:HA/TiN 700°C for 2 h	Si:HA/TiN 700°C for 4 h	Si+O ₂ :HA/TiN as-deposited	Si+O ₂ :HA/TiN 700°C for 2 h	Si+O ₂ :HA/TiN 700°C for 4 h
Ca/P	1.83, 1.91	0, 2.32	2.51, 3.24	1.61, 1.85	4.19	1.53, 2.66

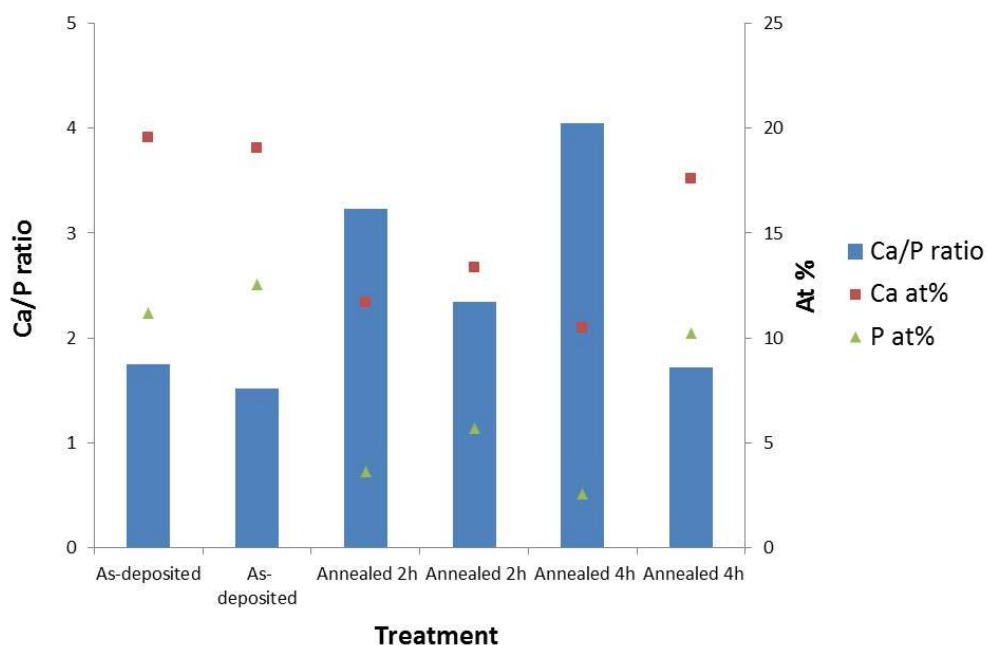


Figure 4-14 Bar charts comparing representative Ca/P ratios, and Ca and P at% values for as-deposited and annealed samples. The raw data for all the samples can be found in Table 10-2.

4.5.1 As-deposited coatings

The high spectral resolution scans will now be described in detail. Figure 4-15 presents and summarises the spectral data acquired from the surfaces of all the as-deposited samples, being consistent with the ranges of binding energies reported in literature ¹²⁷, and confirming the presence of adventitious C, hydrocarbon, CaCO_3 and HA. Not surprisingly, a Ti 2p signature from the substrate was not detected for these ~ 200 nm thick coatings, given that XPS has a limited sensitivity to the top few nanometres.

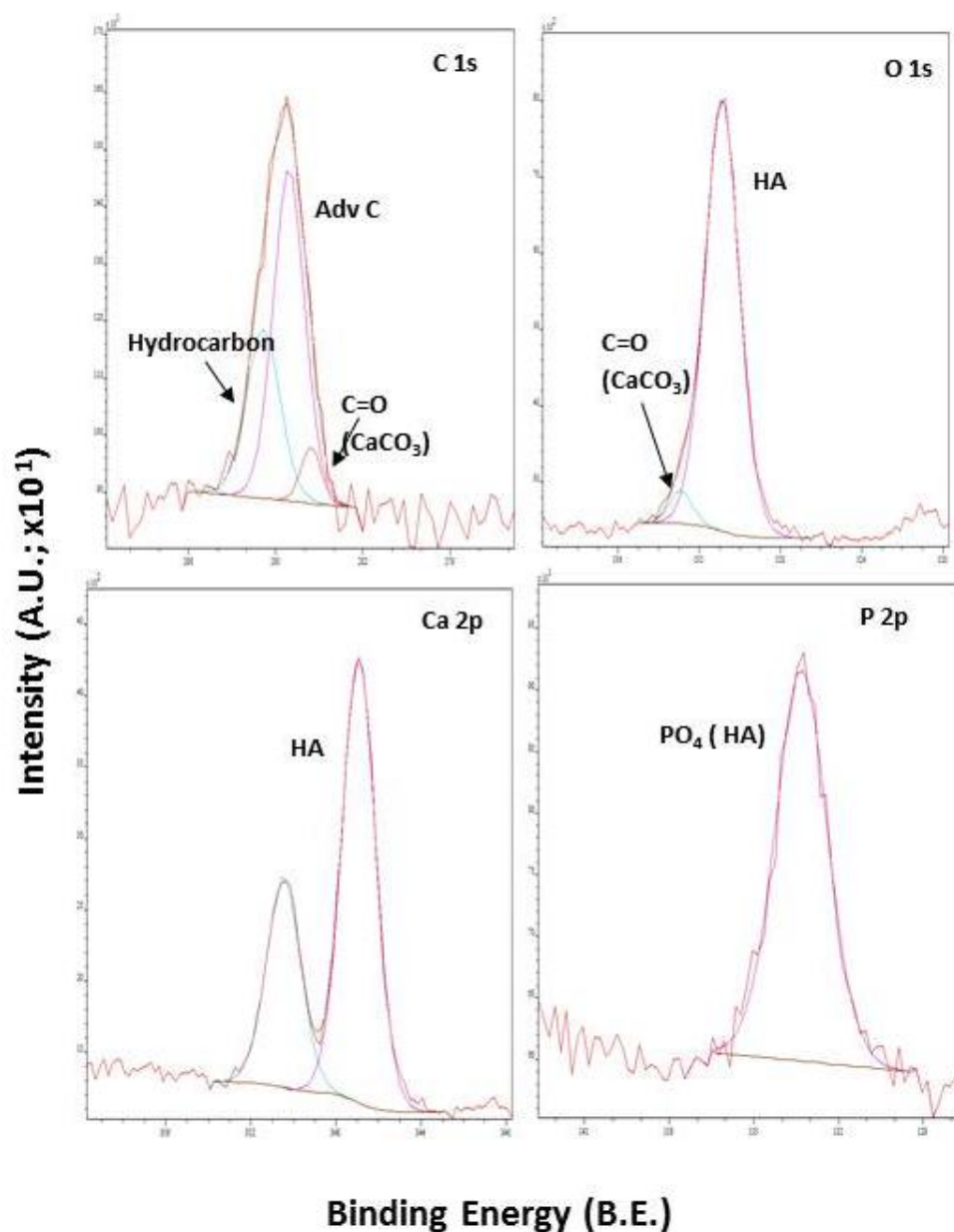


Figure 4-15 Summary of high resolution XPS signatures for the as-deposited coatings (intensity $\times 10^1$)

4.5.2 Annealed coatings

Figure 4-16 presents a summary of the possible phases at the surfaces of the coatings annealed at 700°C for 2 h and 4 h, respectively. It is recognised that the binding energy ranges for CaTiO_3 , HA, CaCO_3 and TiO_2 overlap, with

some tentative evidence of tricalcium phosphate ⁹⁰. However, the data is consistent generally with the GA-XRD results.

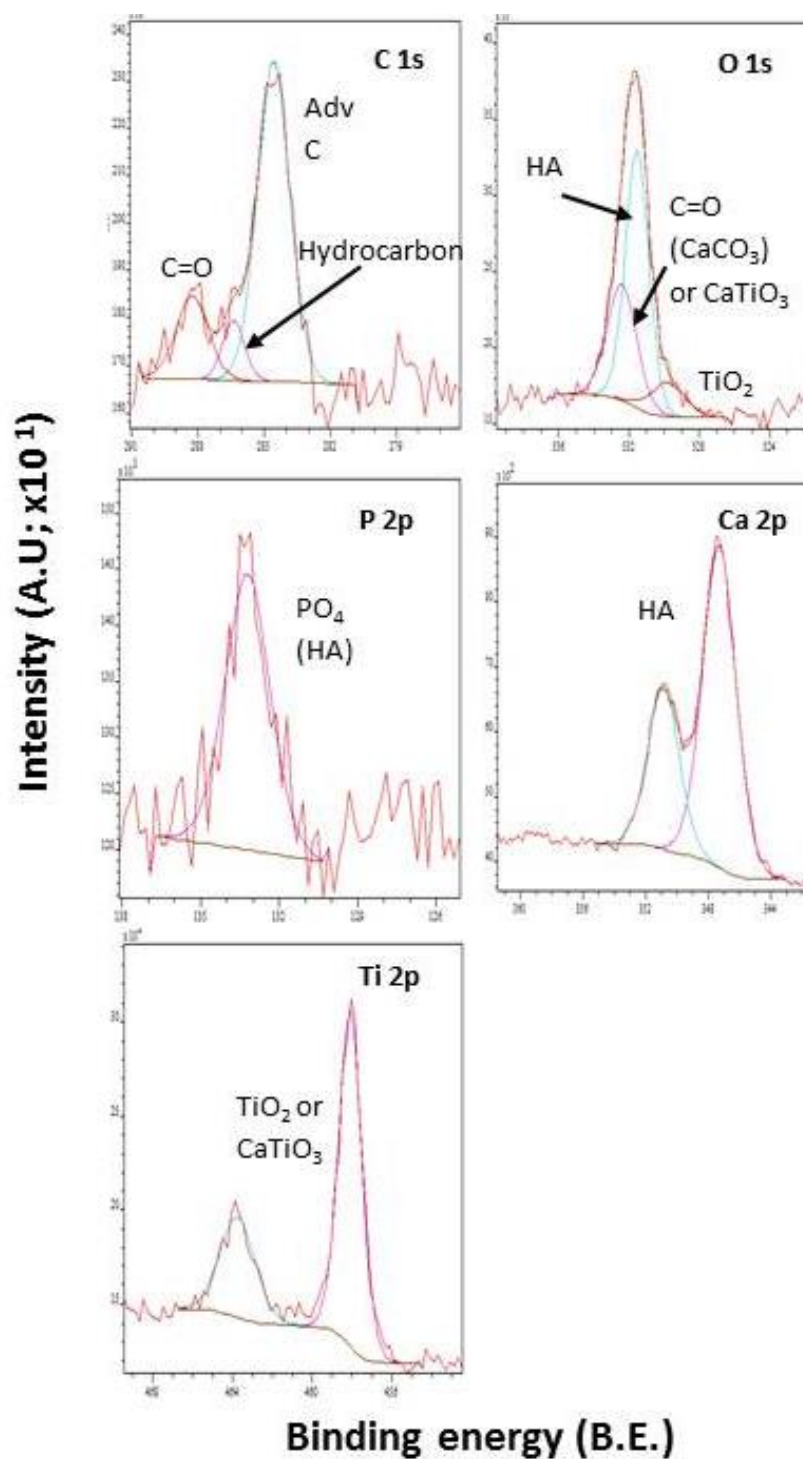


Figure 4-16 Summary of high resolution XPS signatures for the coatings (intensity $\times 10^1$) annealed at 700°C for 2 h and 4 h.

In particular, the Ti 2p_{3/2} and Ti 2p_{1/2} peaks had a separation of 5.7 eV¹²⁷. In the annealed samples the Ca 2p peak also exhibited a doublet, whilst the Ca 2p_{3/2} peak also showed a shoulder at about 1 eV from the main peak and hence was assigned to either CaCO₃ or CaTiO₃; it was difficult to differentiate between these surface species due to their very similar binding energies. The at% value for Ca ranged from 7.5% - 15% for the annealed samples as compared with 17.8% -19.9% for the as-deposited samples. The increased fluctuation of the Ca at% was again attributable to the loss of P. The at% value for P ranged from 9.6-12.4% for the as-deposited coatings compared to 2.1-10.4% for the annealed coatings.

Signatures attributable to Si or silicate were not detected in either the as-deposited or the annealed samples. The binding energy for N is at 397 eV, which is lower than the Ti binding energy of 457-458.1 eV. N was not detected in either the as-deposited or the annealed samples suggesting that the TiN diffusion barrier layer was not exposed at the surface. Hence, it is inferred that the presence of TiO₂ detected in the annealed samples arises from oxidised regions of the Ti substrate breaking through the HA/TiN coating and becoming exposed at the surface.

4.6 Biological cell study

In vitro cell testing was performed to appraise the potential of these implant coatings to prolong implant lifespan. MG63 cells, a human-derived osteosarcoma osteoblastic cell line, were utilised on the set 1 samples. The ability of these developed coatings to enhance the early stages of cell growth

was assessed initially, whilst the cytocompatibility of the coatings was also assessed. In order to avoid contamination, aseptic techniques were employed during all stages of cell culturing.

4.6.1 AlamarBlue (cell toxicity) tests

AlamarBlue (cell toxicity) tests were performed using MG63 osteosarcoma cells on the annealed coatings, and compared with reference Ti, for cultivation times of 1, 7 and 14 days, respectively. TCP was an internal control used to verify the experimental quality. Figure 4-17 summarises the results. Samples were analysed for 1 run for the 2 h annealed coatings ($n = 3$) and 2 runs for the 4 h annealed coatings ($n = 6$). For all the coatings, only the Si+O₂:HA/TiN coating had a slight increase in activity on day 14. Otherwise, there was no significant difference in performance of these surface modified coatings, as compared to the Ti control sample. However, it is noted that the TCP control sample had an increase in activity up to day 14.

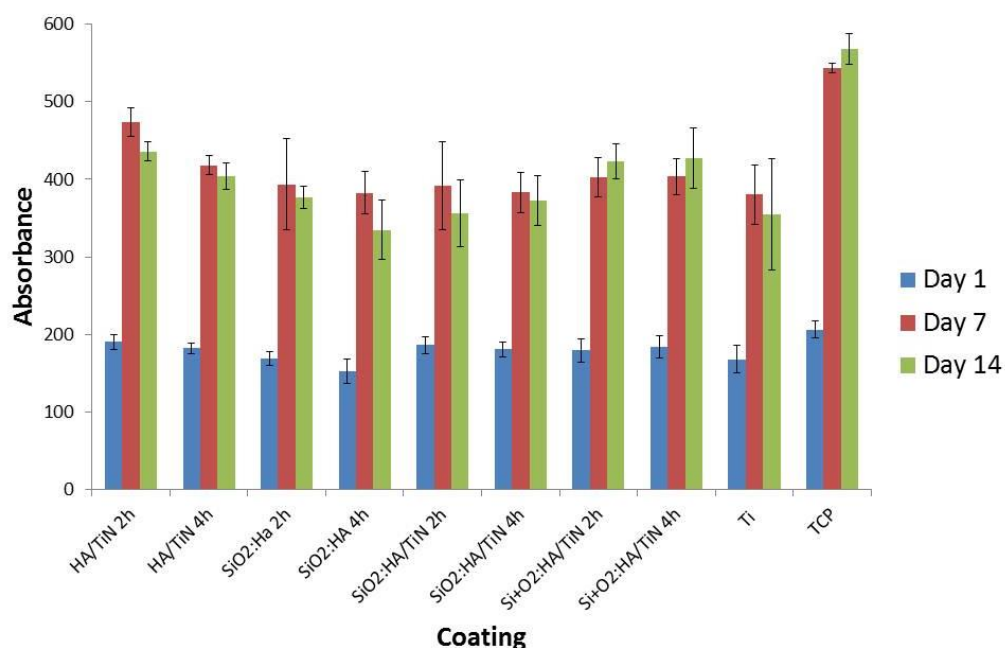


Figure 4-17 AlamarBlue tests performed on the coatings annealed at 700°C for 2 h and 4 h in Argon, for 1, 7 and 14 days. Ti and TCP substrates were used as control samples.

4.6.2 SEM observations of the cells

MG63 cells were grown on a separate set of the annealed set 1 coatings and harvested at the different time points. They were then coated with gold and imaged using an XL30 FEG-SEM in high vacuum mode (acceleration voltage of 20kV, WD of 10.7mm, at x1000 and x4000 magnification).

4.6.2.1 Day 1

On day 1, it was observed that the MG63 cells were similar in morphology and uniformly spread across all of the 2 h and 4 h annealed coatings, as

illustrated by Table 4-6 and Table 4-7. Variations in the surface morphologies of the coatings could also be discerned, according to the coating schemes used.

For the 2 h annealed samples (Table 4-6), the HA/TiN the Si:HA/TiN coatings appeared similar to the coatings prior to dissolution / exposure to the cells. Interestingly, the Si:HA coatings exhibited a more of a mixture of floccular and smooth regions, whilst the Si+O₂:HA/TiN coatings no longer exhibited HA islands, but developed into a more uniform, textured surface. For the case of the 4 h annealed samples (Table 4-7), the HA/TiN, Si:HA/TiN and Si+O₂:HA/TiN coatings all appeared similar to the coatings prior to dissolution / exposure to the cells, whilst the Si:HA coating exhibited a mixture of floccular and smooth regions. From these observations, it is apparent that the cell lamellipodia and filopodia are content to attach to any of these surfaces, regardless of the variations in texture or surface chemistry, consistent with all the coatings being biocompatible.

Table 4-6 Day 1: Low (x1000) and high magnification (x4000) SE images of MG63 cells cultured on the 2 h annealed coatings.

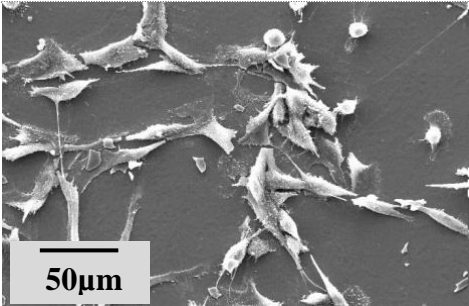
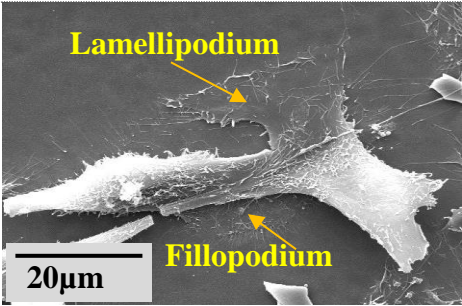
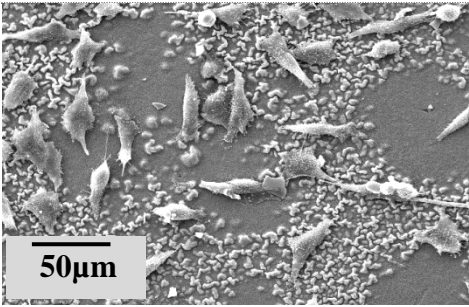
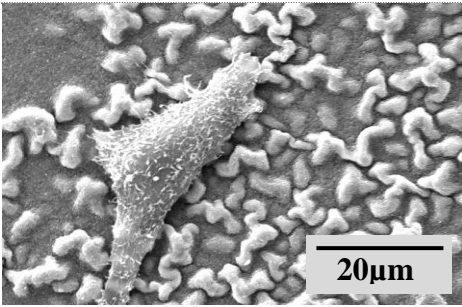
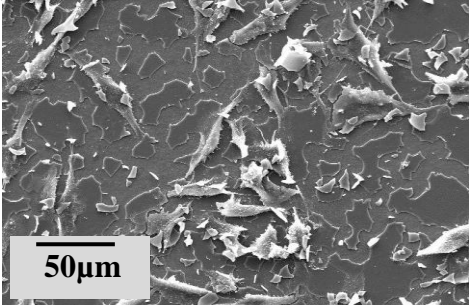
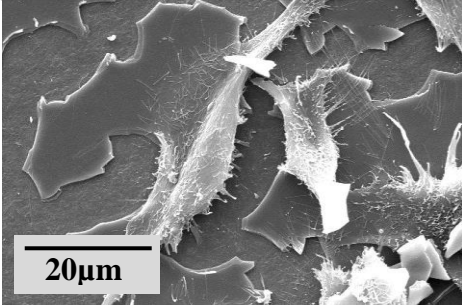
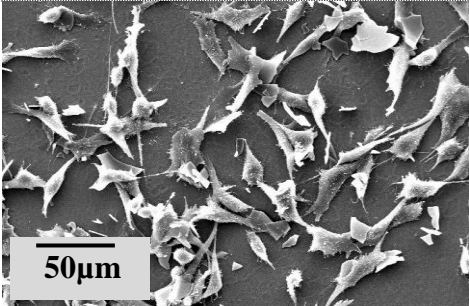
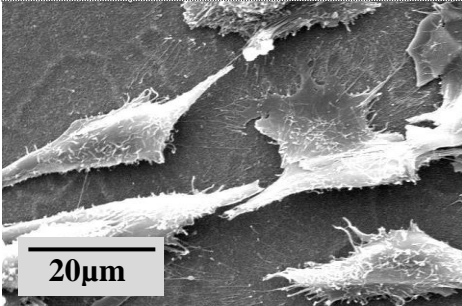
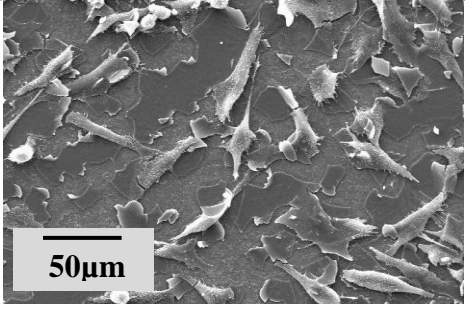
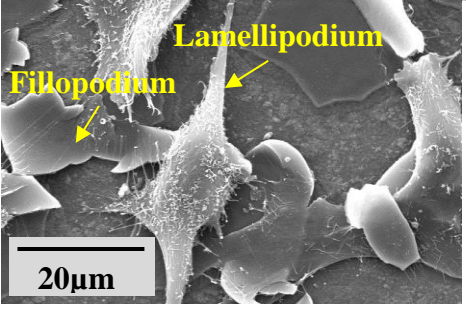
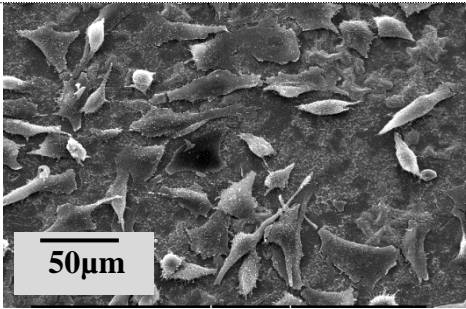
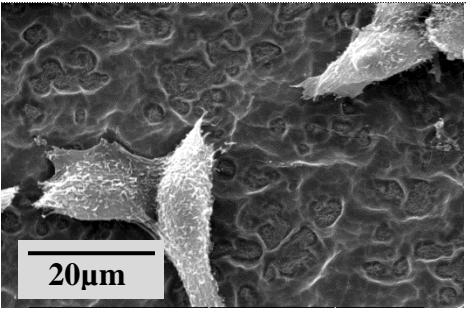
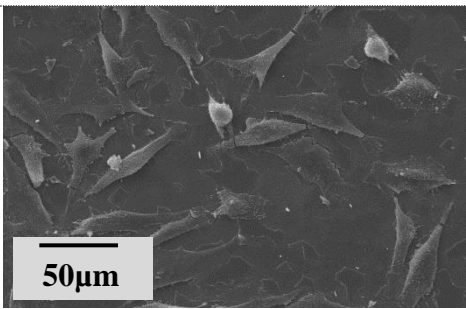
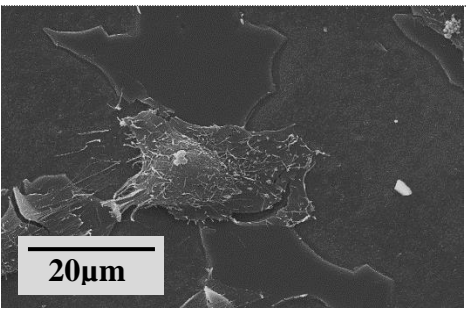
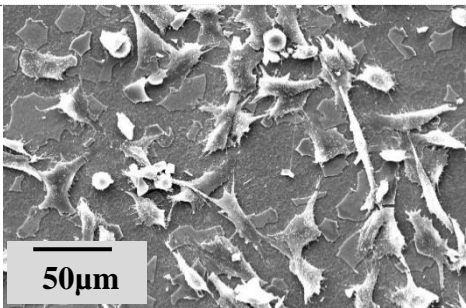
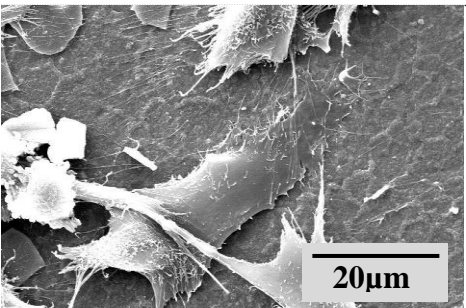
DAY 1	Annealed 700°C 2 h	
	x1000	x4000
HA/TiN		
Si:HA		
Si:HA/TiN		
Si+O ₂ :HA/TiN		

Table 4-7 Day 1: Low (x1000) and high magnification (x4000) SE images of MG63 cells cultured on 4 h annealed coatings.

Day 1	Annealed 700°C 4 h	
	x1000	x4000
HA/TiN		
Si:HA		
Si:HA/TiN		
Si+O ₂ :HA/TiN		

4.6.2.2 Day 7

By day 7, cells cultured on all the coating surfaces exhibited normal osteosarcoma morphologies and adopted confluent layers (Table 4-8). The cell morphologies on day 7 were generally more elongated and there were no evident differences in cell morphology between the samples.

Table 4-9 shows a representative sample that was annealed for 4 h, the low magnification SE images of the sample appear to show cells packed together more densely than for the other samples. Full set of data for the 4 h samples can be found in Table 10-3 in Appendix.

Table 4-8 Day 7: Low (x1000) and high magnification (x4000) SE images of MG63 cells cultured on 2 h annealed coatings.

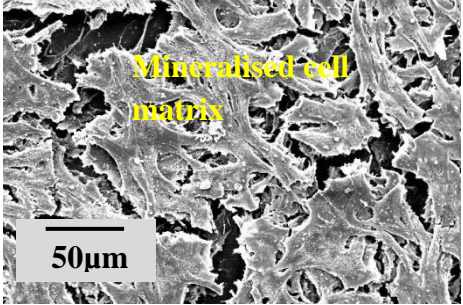
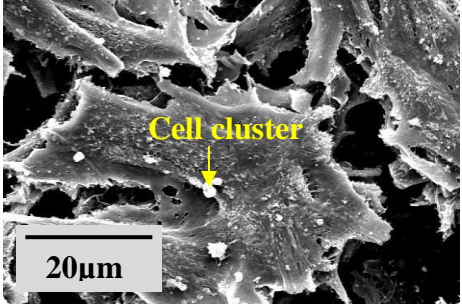
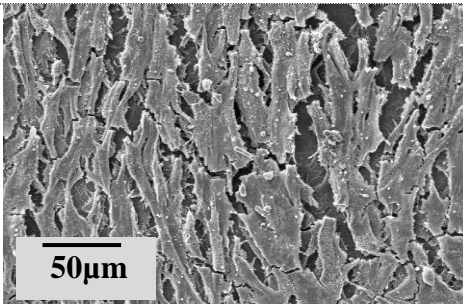
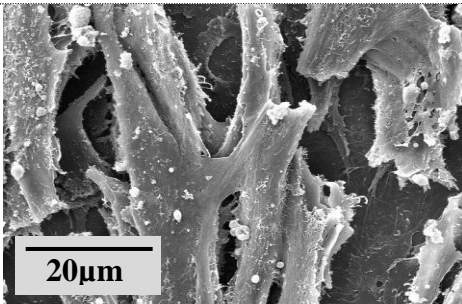
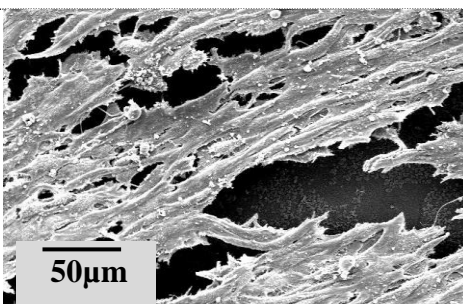
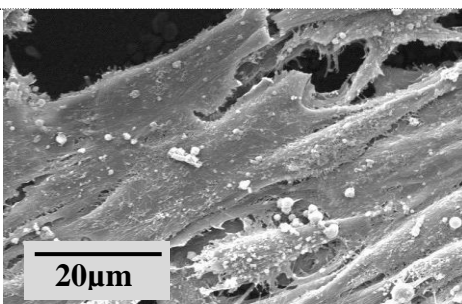
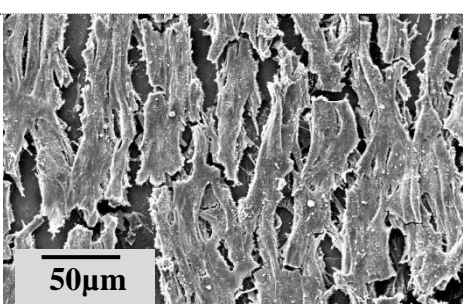
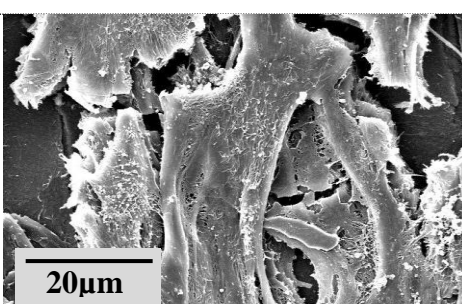
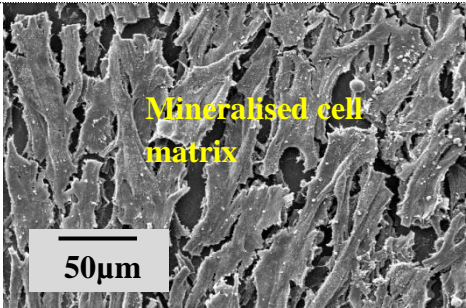
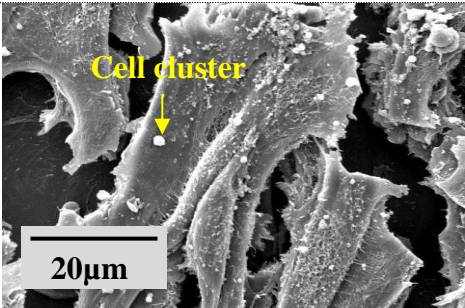
DAY 7	Annealed 700°C 2 h	
	x1000	x4000
HA/TiN		
Si:HA		
Si:HA/TiN		
Si+O ₂ :HA/TiN		

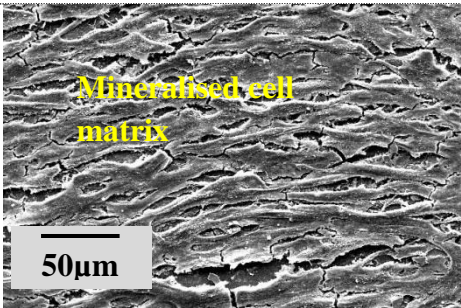
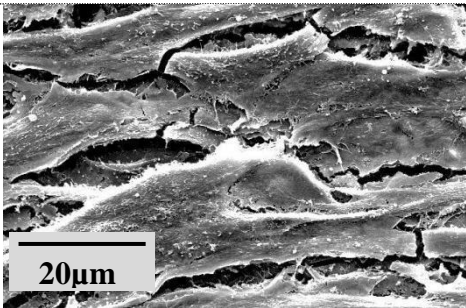
Table 4-9 Day 7: Low (x1000) and high magnification (x4000) SE images of MG63 cells cultured on 4 h annealed coatings (full data set can be found in Table 10-3 in Appendix).

DAY 7	Annealed 700 ⁰ C 4 h	
	x1000	x4000
Representative		

4.6.2.3 Day 14

Cell clustering was observed along with lamellipodia extended to neighbouring cells, and formation of denser layers at day 14. There was no discernable difference in morphology between the samples at this time point regardless of annealing time (2 h and 4 h) and therefore representative images are shown in Table 4-10; the full data set can be found in Table 10-4 and Table 10-5). The cells all had formed multi-layered and elongated mineralised cell matrices with evidence for cell clustering.

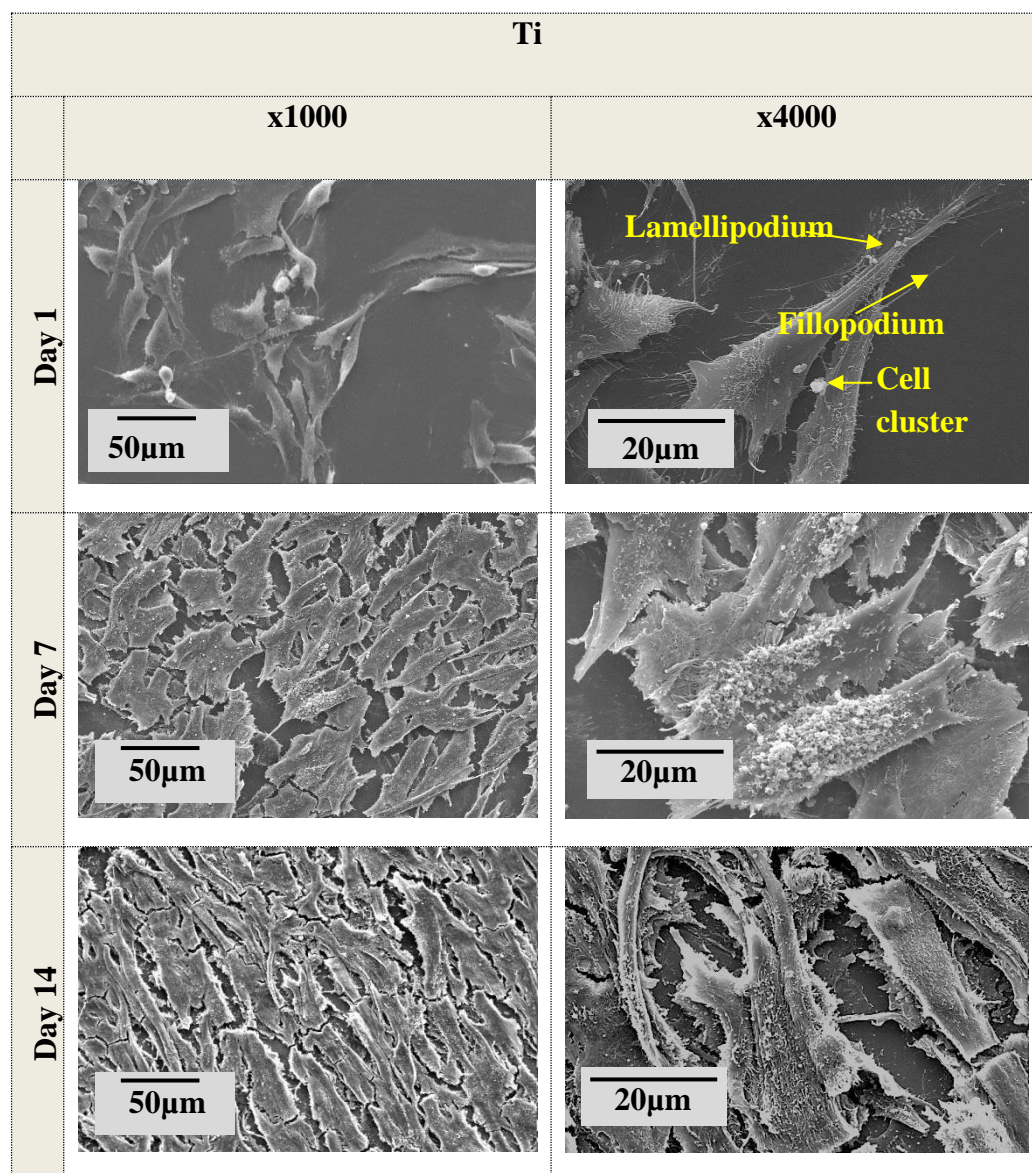
Table 4-10 Day 14: Low (x1000) and high magnification (x4000) SE images of MG63 cells cultured on 2 h and 4 h annealed coatings.

DAY 14	Annealed 700 ⁰ C 2 h and 4 h	
	x1000	x4000
Representative		

4.6.2.4 Cell growth on Ti control

Table 4-11 illustrates the morphologies of MG63 cells on the Ti control sample. The cells again became progressively packed together, forming multilayers of cells, with a lessening of boundaries and the formation of mineralised matrices with increasing time. It is evident that a process of coating dissolution occurs as a consequence of exposing the coatings to cells. Accordingly, in order to gain more insight into this aspect of the cell culturing process, a more detailed investigation of the coating dissolution process was performed, as reported on in the next section.

Table 4-11 Low (x1000) and high magnification (x4000) SE images of MG63 cells cultured on 4 h annealed coatings on Ti control for 1, 7 and 14 days.



4.7 Coating dissolution studies

It is suggested that the dissolution properties of the coatings could affect cellular response at the first stages of growth. For this reason as-deposited

amorphous HA which is rapidly dissolved needs to be crystallised by annealing in order to limit the dissolution process.

Due to time constraints, only HA/TiN coatings annealed for 2 h and 4 h was appraised for its dissolution properties. The coatings were immersed in double distilled water (ddH₂O) for 24 h at 37°C, followed by GA-XRD investigation (with peaks normalised to TiN₁₁₁). The structures of the dissolved coatings were then compared with those of the as-deposited and annealed coatings.

As shown in Figure 4-18, it is apparent that the dissolved coatings exhibited the same crystalline phase as in the undissolved coatings. However, the relative intensities of the respective diffraction peaks changed. In particular, the number of distinct HA peaks were reduced, with remaining peaks attributable of HA₃₀₀ (or (CaTiO₃)₁₂₁) and HA₃₂₃, being consistent with the progression of coating dissolution.

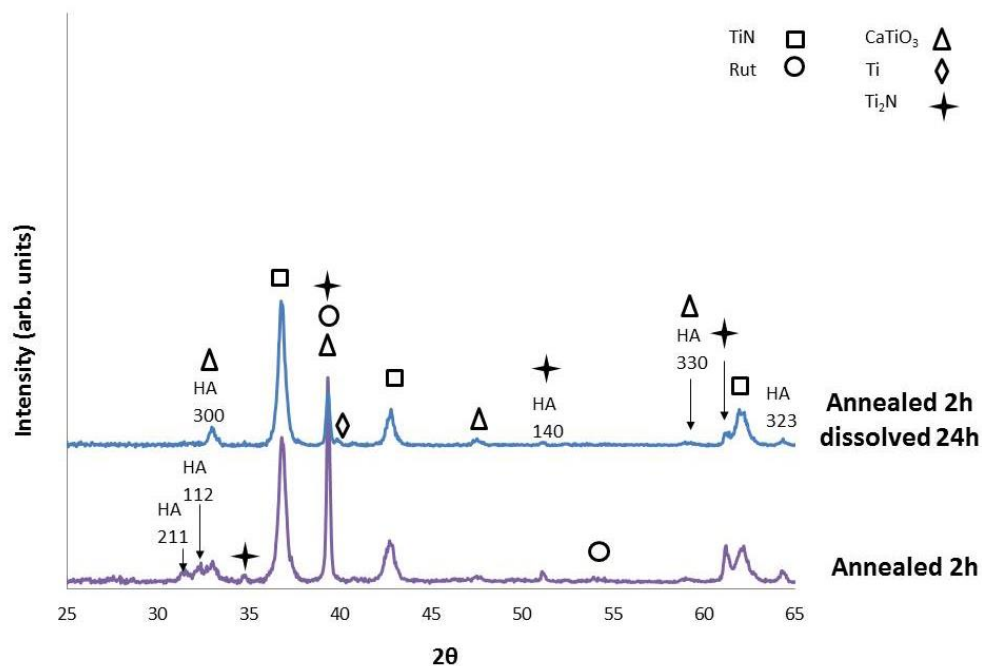


Figure 4-18 GA-XRD investigation of 2 h annealed HA/TiN coatings following immersion in ddH₂O for 24 h.

Similarly, as shown in Figure 4-19, it was observed that the crystal phases within the 4 h annealed coatings immersed in ddH₂O for 24 h were the same as those phases within the undissolved sample. Again, the relative intensities of the peaks changed, with a reduction in the number of HA peaks, *i.e.* with loss of HA₂₁₁ and HA₁₁₂ peaks and retention of HA₃₀₀ (or (CaTiO₃)₁₂₁) and HA₃₂₃ peaks. Further, the number of peaks attributable to rutile (TiO₂) increased as the HA layer was dissolved away.

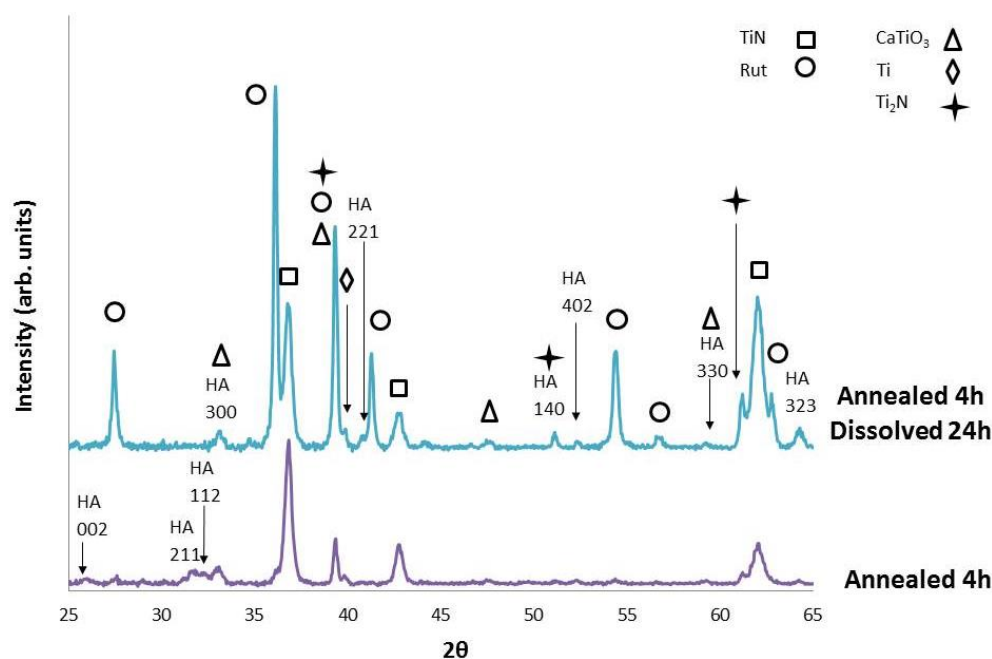


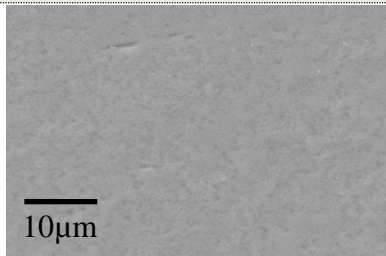
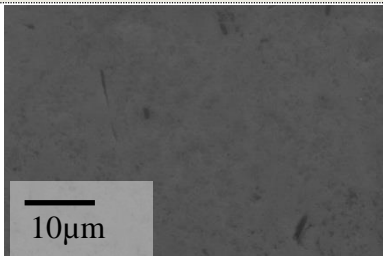
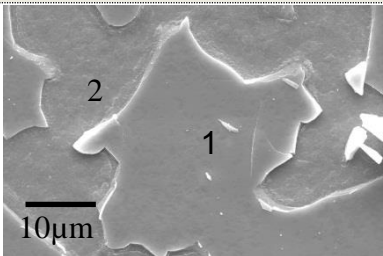
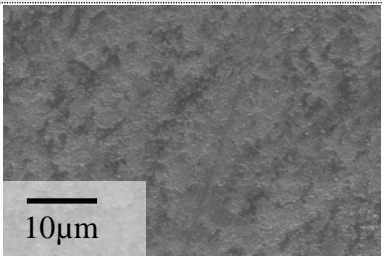
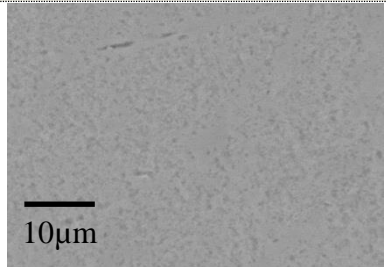
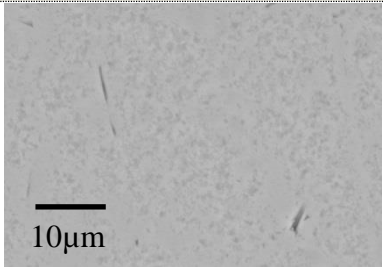
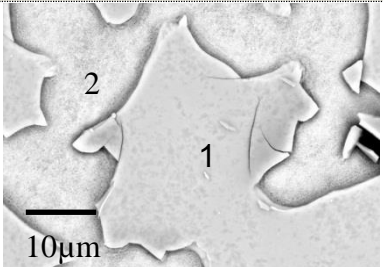
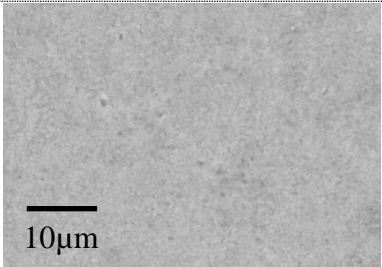
Figure 4-19 GA-XRD investigation of 4 h annealed HA/TiN coatings following immersion in ddH₂O for 24 h

Complementary SEM / EDX investigations were performed on these dissolved coatings, as summarised in Table 4-12. SE imaging demonstrated that the surfaces of the 2 h annealed coatings following 24 h of immersion in ddH₂O were more textured than the undissolved sample, whilst the HA/TiN islands defining the 4 h annealed coatings had disappeared to be replaced by a more granular topography.

BSE imaging was used to assist with the EDX analysis of one sample from each dissolved coating. The Ca/P ratios, and Ca and P at% values were then compared with the as-deposited and annealed coatings (Figure 4-20). In particular, it was found that the Ca/P ratio of the 2 h annealed coating

following dissolution increased considerably as compared with the undissolved coating. The Ca/P ratio for the 4 h annealed coating following dissolution decreased as compared with the undissolved coating. This variability in response was attributed to the effect of patchiness arising from delamination of the 4 h annealed coating. Nevertheless, the Ca and P at% values both decreased as a consequence of dissolution, as expected.

Table 4-12 EDX investigations of 2 h and 4 h annealed HA/TiN coatings following immersion in ddH₂O for 24 h

SE images of HA/TiN			
2 h	2 h dissolved	4 h	4 h dissolved
			
Slightly textured	Increased texture	Delaminated coating (1): islands containing Ca and P. (2): presence of Ti and O.	Disappearance of islands. Granular.
BSE images of HA/TiN			
2 h	2 h dissolved	4 h	4 h dissolved
			
Ca/P ratio: 2.41 ± 0.03 (2.35, 2.43, 2.43)	Ca/P ratio: 3.34 ± 0.66 (2.20, 3.33, 4.50)	(1) Ca/P ratio: 2.15 ± 0.23 (1.83, 2.03, 2.59)	Ca/P ratio: 1.19 ± 0.15 (0.93, 1.20, 1.44)

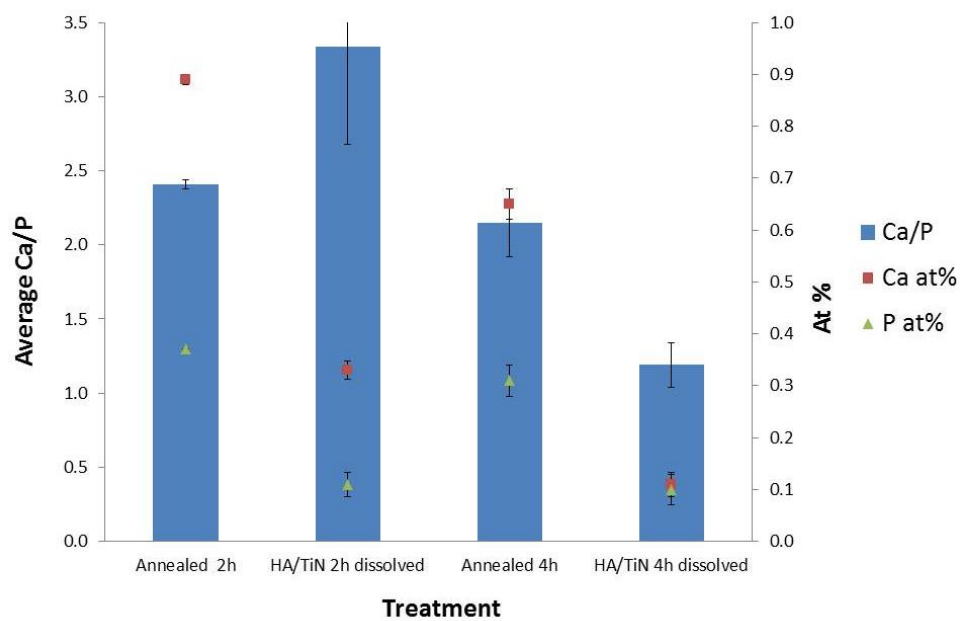


Figure 4-20 SEM / EDX comparison of the annealed and dissolved coatings

4.8 Summary of results

The as-deposited HA layer was not detected by GA-XRD due to its thinness and amorphous nature. GA-XRD only depicted evidence for Ti_2N and TiN corresponding to the diffusion barrier layer and Ti from the bulk substrate. SE imaging showed that the surface morphologies followed that of the Ti substrate (with some evidence for Si containing clumps attributed to embedded SiO_2 residual from the substrate polishing procedure). EDX investigations generally indicated that the Ca/P ratios were significantly higher than those returned by XPS. The discussion section will attempt to elucidate the discrepancies between the EDX and XPS results. The Ca/P ratio at the near-surface returned by XPS was close to that of stoichiometric HA (1.67). XPS and EDX analyses both found that the as-deposited samples have adventitious C. RHEED confirmed that the as-deposited HA coatings were amorphous.

The results for the annealed samples are summarised above. HA was crystallised by annealing, in order to limit its dissolution within biological fluid. The coatings were annealed at 700°C for 2 h and 4 h and their developed structures investigated. The HA was successfully crystallised with HA diffraction peaks being detected by both GA-XRD and RHEED. GA-XRD indicated that the HA peak intensities did not change significantly between the two time-points of 2 h and 4 h, indicating rapid onset of HA crystallisation and the stabilisation. A reduction in the intensity and number of peaks attributable to TiO_2 in samples with a TiN diffusion barrier layer is consistent with the

effectiveness of TiN at inhibiting the oxidation of the Ti substrate during annealing. However, SEM investigations demonstrated that samples containing TiN interlayers tended to delaminate upon annealing and produce “islands” of HA/TiN. In the absence of a TiN diffusion barrier, Si:HA samples tended to exhibit a floccular surface along with more developed TiO₂ at the coating/substrate interface.

With regard to the composition of the developed HA layers, differences were returned by the techniques of EDX and XPS. XPS samples the near layer surface and EDX attempts to appraise the composition of a very thin film from a larger interaction volume that extends into the bulk Ti substrate. Variations in the analysis could also reflect the patchy nature of some of the delaminated samples following annealing. However, it is noted that EDX analysis indicated that annealing was associated with a loss of P, in turn leading to a general increase in Ca/P ratios as compared with the as-deposited samples, in keeping with the XPS analysis. HA/TiN annealed for 2 h and 4 h were dissolved in ddH₂O for 24 h. SEM/EDX and GA-XRD both confirmed that the HA had dissolved.

Chapter 5 Results and Discussion – Set 2 Samples

The second set of coatings was annealed at 2 h at 700°C in Ar. XRD and SEM/EDX analyses were then performed using the same parameters (refer to Experimental Methodology).

Table 5-1 Summary of 2nd set of samples. Key: Unavailable results are marked with N/A; D in superscript indicates delaminated coating; Adventitious C is abbreviated to Adv. C.

Method	HA/TiN As-deposited	HA/TiN Annealed at 700°C for 2 h	Si:HA Annealed at 700°C for 2 h	Si:HA/TiN Annealed at 700°C for 2 h	Si+O ₂ :HA/TiN Annealed at 700°C for 2 h
XRD	TiN, Ti	TiN, Ti & HA possibly mixed with CaTiO ₃	Ti, strong TiO ₂ , Ti ₂ O ₃ & HA possibly mixed with CaTiO ₃	TiN, Ti, strong TiO ₂ , & HA possibly mixed with CaTiO ₃	TiN, Ti & HA possibly mixed with CaTiO ₃
SEM	Smooth and follows Ti substrate (not shown)	Granular with pollen- like protrusions	Granular	Delaminated coating & islands	Granular
EDX (Ca/P ratio)	N/A	2.41±0.11 (2.21, 2.43, 2.59)	2.06±0.18 (1.71, 2.16, 2.30)	1.58±0.19 ^D (1.33, 1.48, 1.94)	1.65 (only one area detected P)
XRD Dissolution	N/A	TiN, Ti & HA possibly mixed with CaTiO ₃	Ti, strong TiO ₂ , & HA possibly mixed with CaTiO ₃ , Ti ₂ O ₃	TiN, Ti, strong TiO ₂ , & HA possibly mixed with CaTiO ₃	TiN, Ti TiO ₂ & HA possibly mixed with CaTiO ₃

5.1 GA-XRD investigations

The XRD methodology and method of pattern matching employed was the same as those for set 1. The XRD patterns revealed that the same chemical species were found for the previous set, with a few differences.

5.1.1 HA/TiN coatings

Figure 5-1 presents representative X-ray diffraction patterns of the as-deposited HA/TiN coatings and coatings annealed for 2 h. The as-deposited diffraction pattern is representative of all as-deposited coatings; Si:HA does not have the TiN peak(s). Similar to set 1, there was evidence for the presence of crystalline Ti (Inorganic Crystal Structure Database (ICDD) reference codes 00-038-1420). Also similarly to set 1, no broad amorphous peaks indicative of the presence of HA were evident, again possibly due to the thinness of the HA layers which were estimated to be < 200 nm. Unlike in set 1, no broad TiN peaks signifying amorphous TiN peak was detected. The crystalline TiN peak was attributable to ICDD code 00-017-0386.

Figure 5-1 also shows representative HA/TiN coatings, annealed at 700°C for 2 h, with peak intensities normalised to TiN (111). The annealed samples showed the development of crystalline HA peaks as a result from annealing. The HA corresponds to ICDD code 01-074-0565, with peaks corresponding to *i.e.* HA (211), (112) and (300), in addition to tentative evidence for the presence of perovskite, CaTiO_3 (ICDD code 98-006-6605). The peak

attributable to TiN (at 33°) had small shoulders, which may be indicative of some Ti_2N growth (ICDD code 00-044-1294). The Ti peak intensities were observed to decrease as the TiN and HA phases crystallised, being attributable to densification of the annealed coatings. Evidence for the development of some rutile (TiO_2) was also found for the annealed coatings.

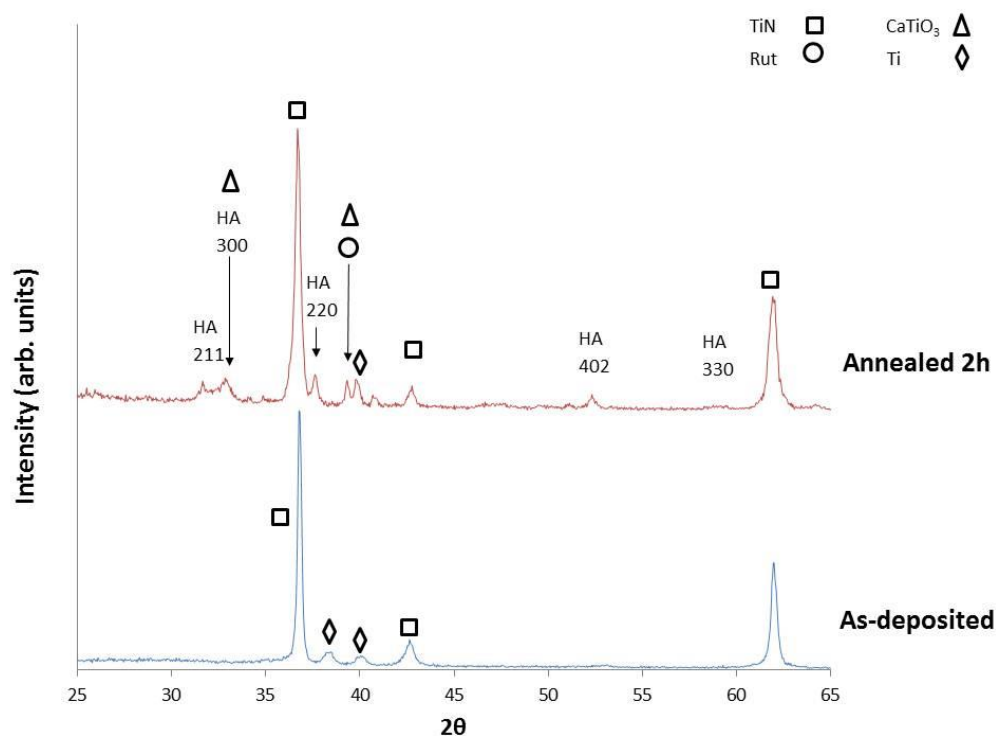


Figure 5-1 Representative GA-XRD patterns of the HA/TiN coatings: as-deposited and annealed for 2 h.

5.1.2 Si:HA coatings

Figure 5-2 presents representative GA-XRD patterns for the Si:HA coatings, annealed for 2 h without normalisation in this case. Similar to set 1, peaks attributable to titanium (III) oxide (Ti_2O_3 ; ICDD: 00-010-0063), rutile (TiO_2 ; ICDD: 00-021-1272), crystalline HA (similar to those identified for the annealed HA/TiN coatings), and some perovskite (CaTiO_3 ; ICDD: 98-006-

6605). The HA₃₀₀ peak is approximately 3 times more intense than the HA₂₁₁ peak. However, the same peaks for annealed HA/TiN had about the same relative intensity. The change in relative intensities between the samples may be a sign of Si substitution¹⁸.

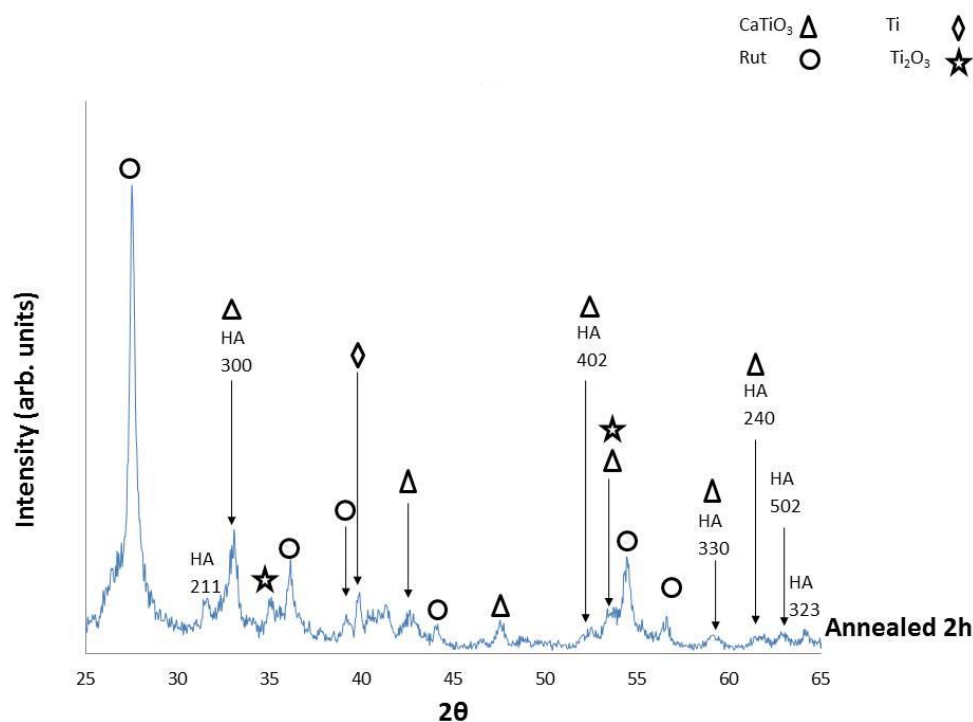


Figure 5-2 Representative GA-XRD pattern of Si:HA coatings annealed for 2 h.

5.1.3 Si:HA/TiN and Si+O₂:HA/TiN coatings

Representative GA-XRD patterns for the Si:HA/TiN (Figure 5-3) and Si+O₂:HA/TiN coatings (Figure 5-4). The results were similar to set 1. The annealed samples also showed the development of crystalline HA, along with the presence of some TiO₂ after 2 h. The TiO₂ intensity, was not as high as

that shown by the Si:HA coatings, indicating that the TiN barrier layer had had some success in retarding the growth of titanium oxide at the coating/substrate interface. Again the HA₃₀₀ peak is more intense than the HA₂₁₁ peak compared to the same peaks for the annealed HA/TiN, indicating possible Si substitution into the HA lattice.

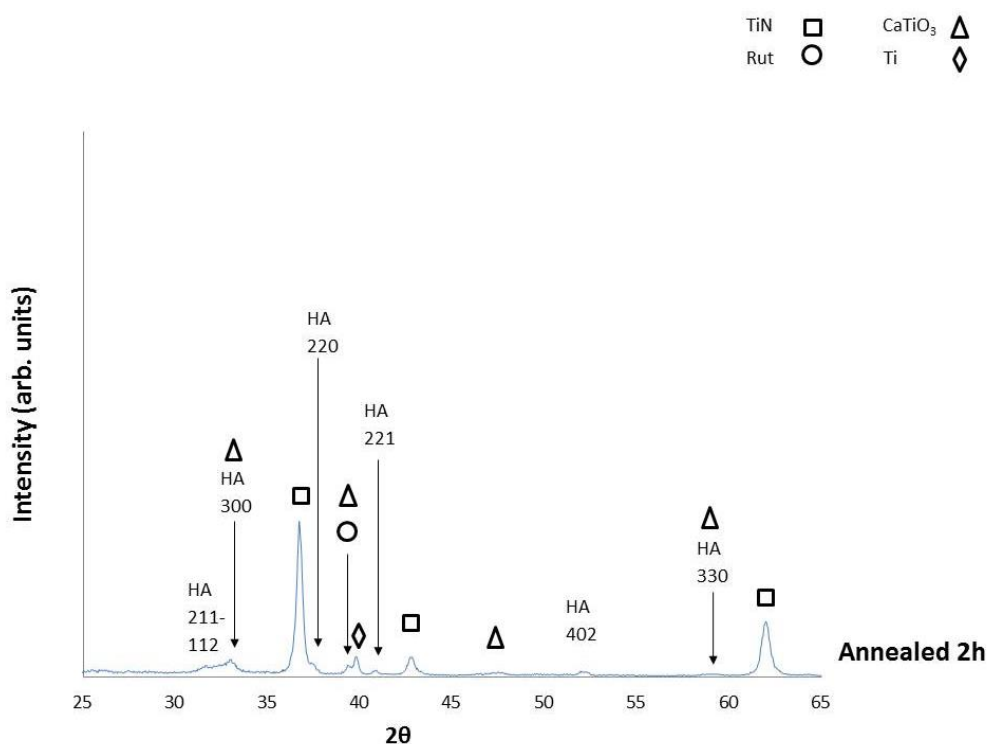


Figure 5-3 Representative GA-XRD pattern for Si:HA/TiN samples annealed for 2 h.

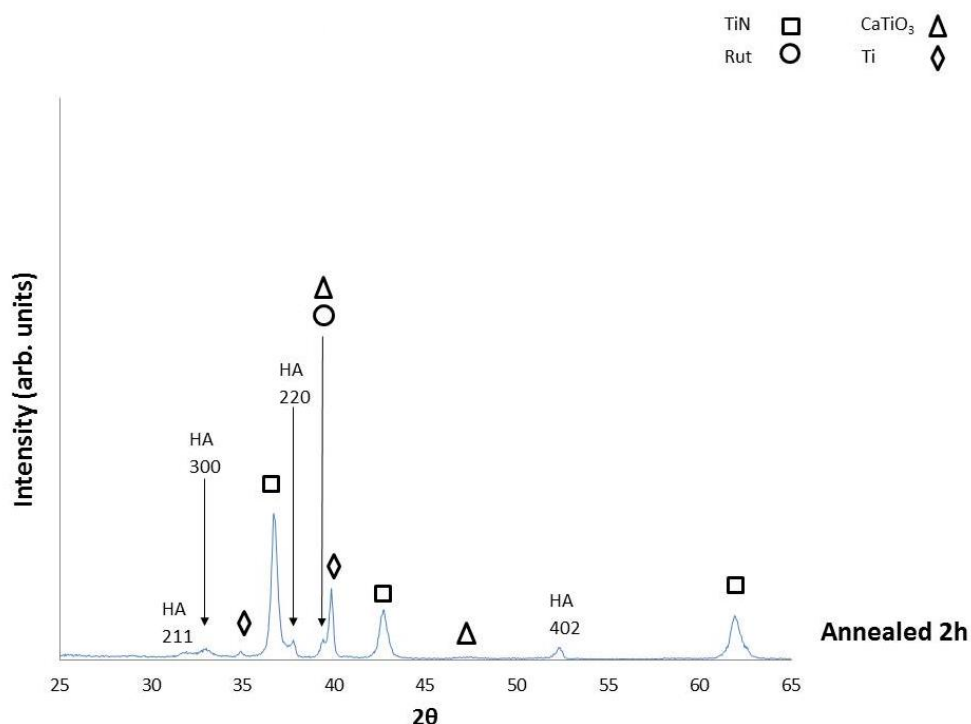


Figure 5-4 Representative GA-XRD pattern for Si+O₂:HA/TiN samples annealed for 2 h.

In summary, the GA-XRD patterns of as-deposited and annealed coatings of the set 2 samples contained similar crystallographic structures compared with the set 1 samples, with the exception of the presence of crystalline TiN peak in the set 2 sample (amorphous coatings) and absence of Ti₂N peaks in the annealed samples. The GA-XRD patterns of the annealed TiN-containing samples (set 2) showed a lack of Ti₂N and a more significant reduction of TiO₂ compared to the samples of set 1. Similarly to set 1, the ratio of intensities between the 2 main HA peaks, HA₃₀₀ and HA₂₁₁ changed due to Si-substitution. The HA₃₀₀ peak is about 3 times more intense for Si-substituted HA whereas HA/TiN had the same relative intensities. This trend was similar between sample sets.

5.2 SEM/EDX investigations

SEM and EDX acquisition was performed using the same parameters for set 1. The followed SE and BSE images along with calcium-phosphate (Ca/P) ratios are presented in the same format as for set 1.

5.2.1 Annealed coatings

Figure 5-5 presents representative SEM and EDX data for the all the coatings that were annealed for 2 h. After 2 h of annealing, the HA/TiN coating was textured with pollen-like topography. Compared to the other coatings in this section, Si:HA/TiN was the only coating that showed delamination Figure 5-5c. The pattern of delamination was similar to previously coated samples; HA islands on a Ti-O matrix. Size of Si grains was smaller than the previous sample set, perhaps indicating a smaller presence of colloidal silica residues (from polishing the Ti substrates). Unlike the Si+O₂:HA/TiN sample of set 1 that was annealed for 2 h, the same sample from set 2 did not exhibit a delaminated morphology. However, significant P loss was experienced; during EDX acquisition, the P levels were very low. The Ca/P ratios for HA/TiN, Si:HA, Si:HA/TiN and Si+O₂:HA/TiN annealed for 2 h were 2.41 ± 0.11 , 2.06 ± 0.18 , 1.58 ± 0.19 and 1.65 (only one area detected P), respectively. The average Ca/P ratios, as well as Ca and P at % values for the coatings that were annealed for 2 h can be seen in Figure 5-6.

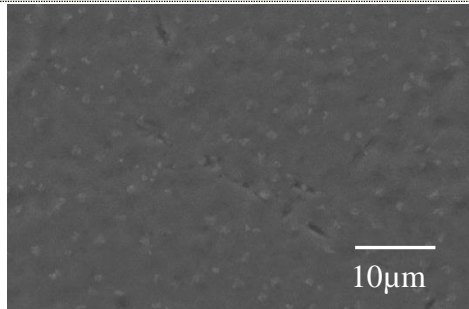
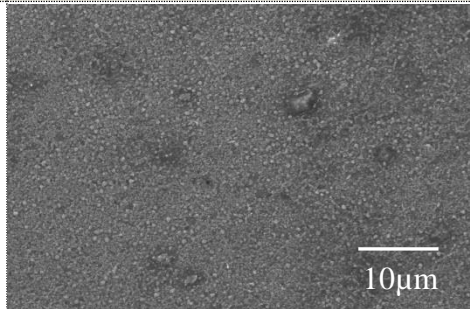
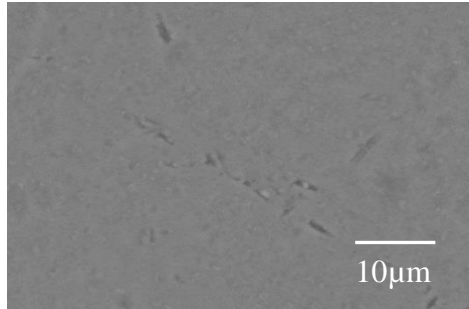
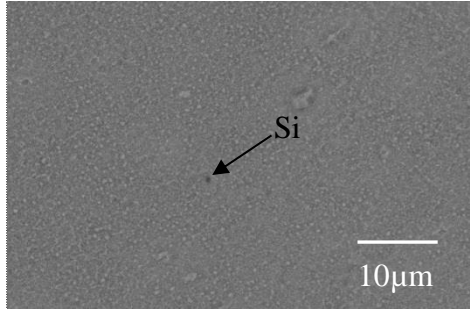
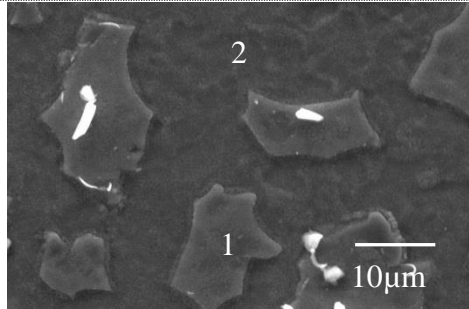
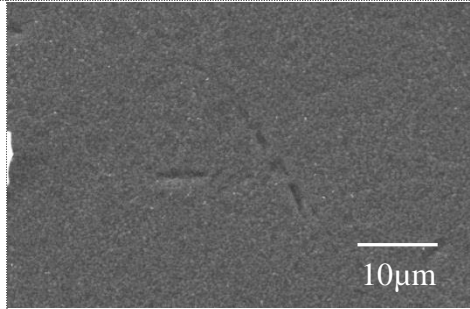
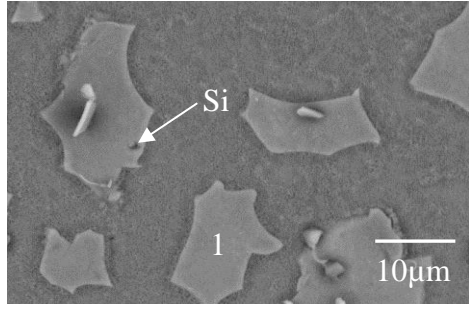
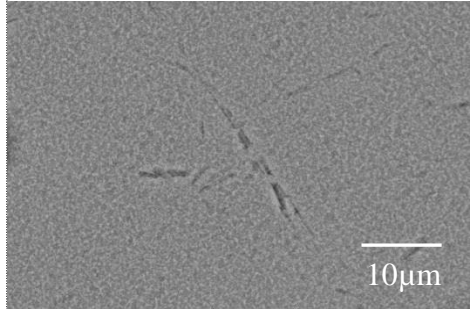
a) SE image of HA/TiN 2 h	b) SE image of Si:HA 2 h
	
Textured with pollen-like protrusions of 1 μm diameters.	Granular appearance
BSE image of HA/TiN 2 h	BSE image of Si:HA 2 h
	
Ca/P ratio: 2.41 ± 0.11	Ca/P ratio: 2.06 ± 0.18 Si of 500nm - 1μm in diameter.
c) SE image of Si:HA/TiN 2 h	d) SE image of Si+O₂:HA/TiN 2 h
	
(1): Island containing Ca and P (2): Substrate exhibiting Ti and O.	Granular appearance, smoother looking than Si:HA.
BSE image of Si:HA/TiN 2 h	BSE image of Si+O₂:HA/TiN 2 h
	
Ca/P ratio: 1.58 ± 0.19 Size of Si approximately 200nm.	Ca/P ratio: 1.65 (1 area detected P).

Figure 5-5 a) HA/TiN, b) Si:HA, c) Si:HA/TiN and d) Si+O₂:HA/TiN annealed at 700°C for 2 h.

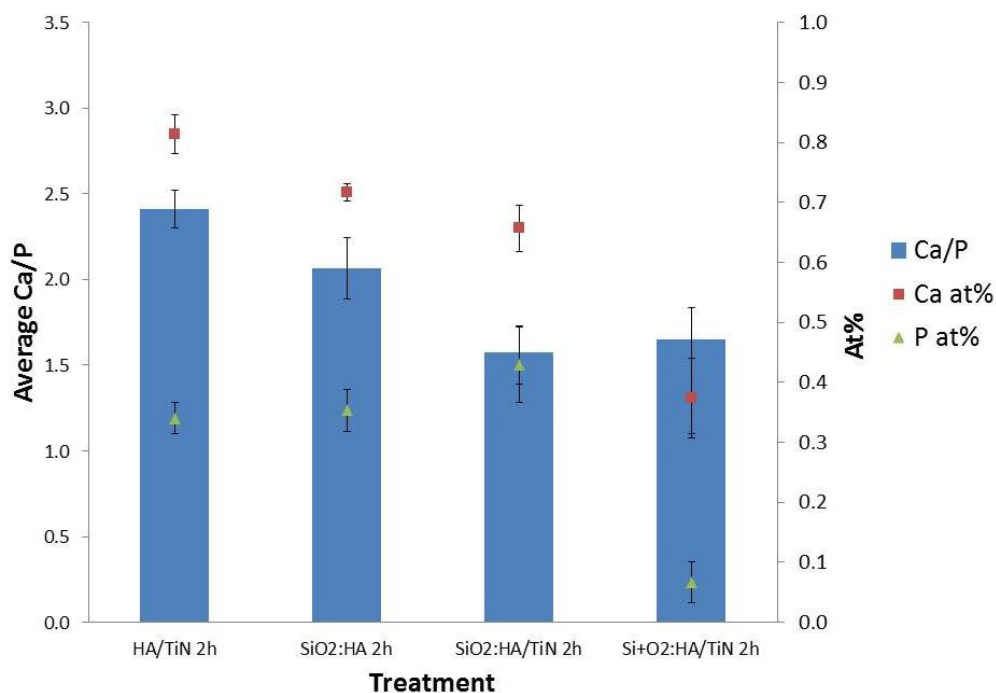


Figure 5-6 Bar charts comparing average Ca/P ratios, and Ca and P at % values for the coatings that were annealed for 2 h.

In summary, as-deposited coatings and coatings annealed at 700°C for 2 h, were investigated systematically using SEM and EDX. In general, the as-deposited coatings (not shown) followed the morphology of the polished Ti substrates. The as-deposited samples contained crystalline TiN and not amorphous TiN. Unlike TiN-containing samples of set 1, only Si-substituted HA on TiN showed residual HA/TiN islands and exposed regions of oxidised Ti substrate. Consistent with set 1, Si-substituted HA coatings without a TiN interlayer also showed. Hence, residual strain associated with the TiN barrier layer is implicated in the delamination process, possibly accentuated by the Si substitution of the HA. Si-containing clumps were also found and considered artefacts from the substrate polishing process, could also act as strain centres, contributing to the process of localised

delamination. The annealed Si+O₂:HA/TiN coatings had the lowest Ca at% and P at% values which is consistent with a previous finding¹²³ and with the same sample type in set 1. Question of process control of the reactive magnetron sputtering technique when depositing HA in the presence of other elemental species on to a TiN diffusion barrier layer are raised.

Further, the Ca/P ratios for all the annealed Si-substituted HA samples on TiN barrier layers were close to stoichiometric HA compared to HA/TiN and Si:HA. It is recognised that the TiN barrier layer is needed to inhibit oxidation of the Ti substrate which would otherwise lead to unwanted scale formation. Again, there was no evidence of Si presence within HA/TiN, however this may be reflecting the limited sensitivity of EDX for substitution level concentrations.

5.3 Biological cell study

SEM imaging, ALB, alkaline phosphatase (ALP) and DNA Hoechst were performed on the 2nd set of samples for 2 runs (n=6) using MG63 cells for 1, 3, 7 and 14 days. The method including statistical analysis was described in the Experimental Methodology section. Result of $p < 0.05$ was considered slightly significant (bars would be marked with *), results of $p < 0.01$ was considered significant (marked with **) and $p < 0.001$ (***) was regarded as very significant. CpTi was used as a control while tissue-culture plastic was used as only as internal quality control for verification of experimental quality.

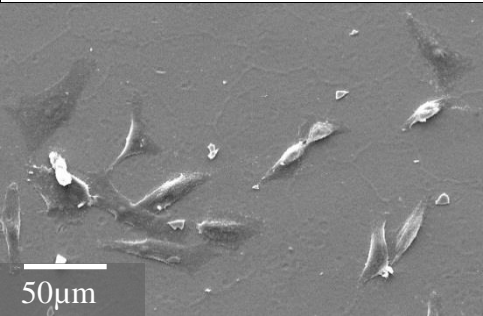
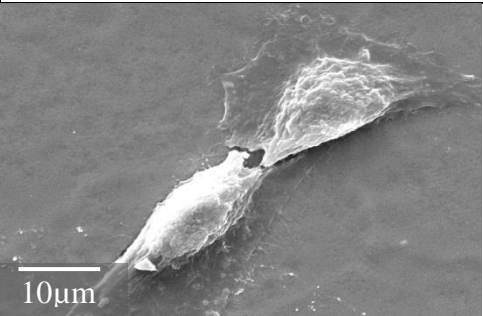
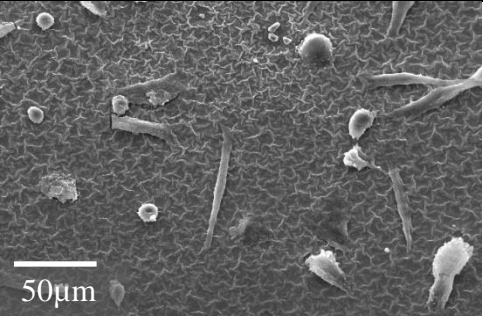
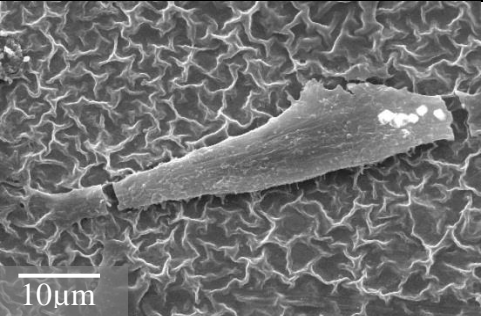
5.3.1 SEM observations of the cells

MG63 cells were seeded onto the annealed samples using a similar methodology as previously described. The below figures show representative SEM images on dehydrated and Au sputtered cells. Detailed SEM images can be found in Table 10-6, Table 10-7 and Table 10-8.

5.3.1.1 Day 1

On day 1, MG63 cells were grown on coatings that were annealed for 2 h (Table 5-2). Single MG63 cells were spread throughout the samples. They were similar in morphology. The sample surfaces differed in appearance only according to whether they contain TiN or not. TiN-containing samples have textured surfaces, with HA/TiN has visibly less textured surface morphology. The surfaces of the Si:HA samples were floccular. The high amount of cell clusters could be caused by human errors. The lamellipodia and filopodia of the cells would attach onto any surface type, whether textured, floccular or smooth.

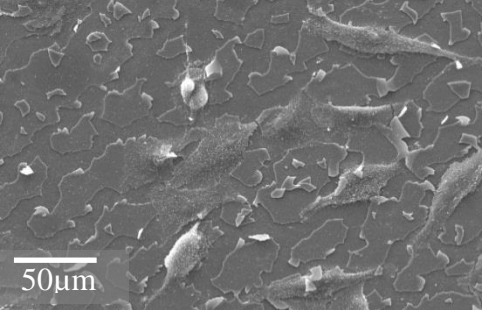
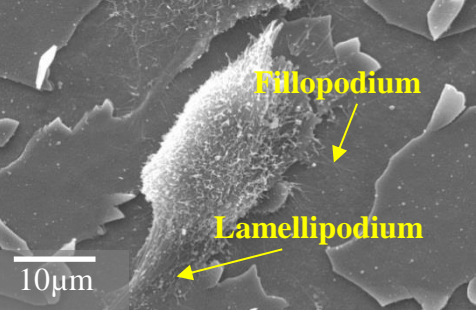
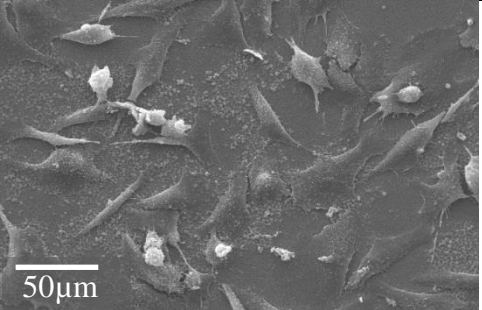
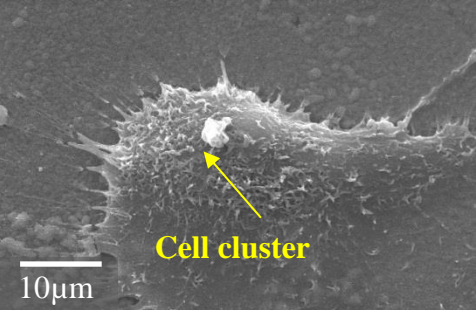
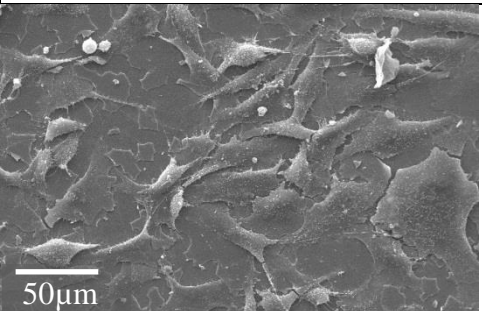
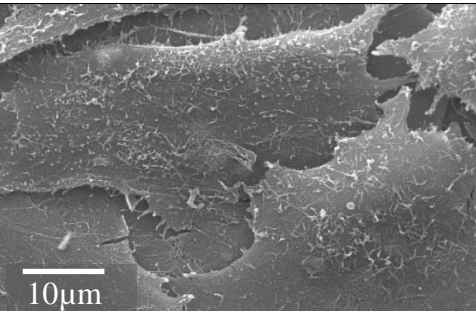
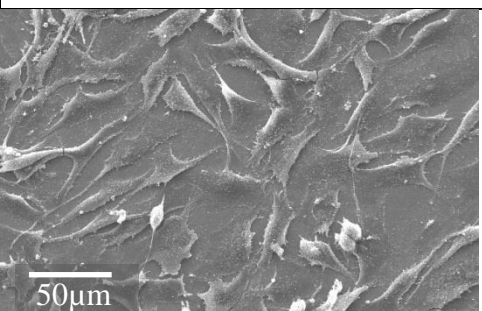
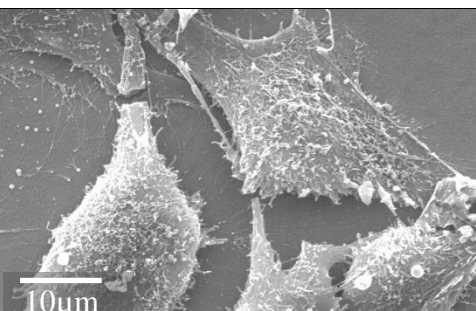
Table 5-2 Day 1: Low (x1000) and high magnification (x4000) SE images of MG63 cells cultured on the 2 h annealed coatings.

	Day 1 - 700°C 2 h	
	Low Magnification	High Magnification
TiN-containing		
Si:HA		

5.3.1.2 Day 3

On day 3 (Table 5-3), the MG63 cells on all treated coatings exhibited normal osteosarcoma cell growth with cell clusters. The morphology was also more elongated and there was no difference in morphology between the samples. HA/TiN and Si:HA/TiN show delamination. There are yet no changes in cell morphology despite HA delamination and the presence of smooth and rougher samples.

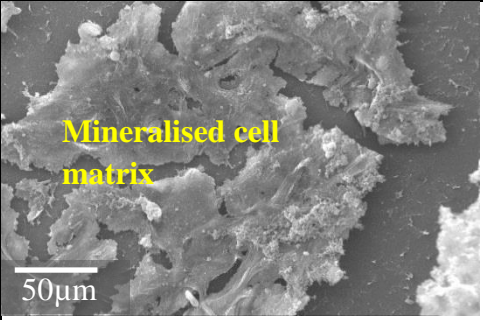
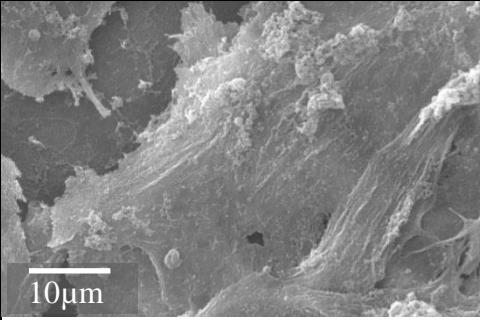
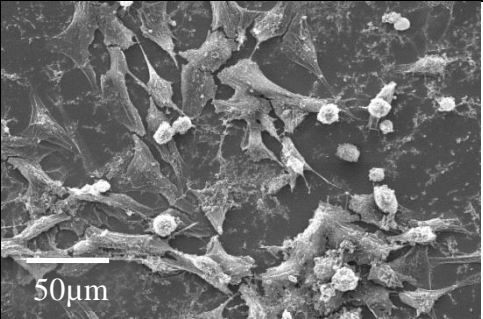
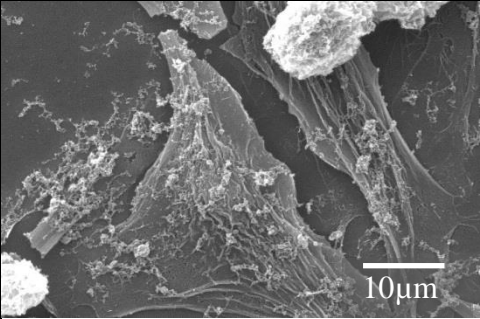
Table 5-3 Day 1: Low (x1000) and high magnification (x4000) SE images of MG63 cells cultured on the 2 h annealed coatings.

Day 3 - 700°C 2 h	
	<div>Low Magnification</div> <div>High Magnification</div>
HA/TiN	 
Si:HA	 
Si:HA/TiN	 
Si+O ₂ :HA/TiN	 

5.3.1.4 Day 7

On day 7, the MG63 cells exhibited normal osteosarcoma cell growth (representative images in Table 5-4, images on cell growth on each coating can be found in Table 10-3). Multiple overlapping layers of cells were observed, which indicate the formation of a mineralised cell matrix. There was evidence of cell clusters.

Table 5-4 Day 7: Low (1000X) and high magnification (4000X) of MG63 cells grown on 2 h annealed samples.

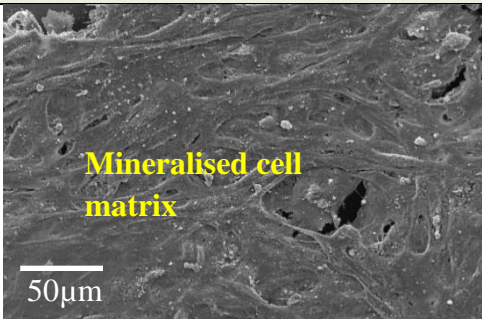
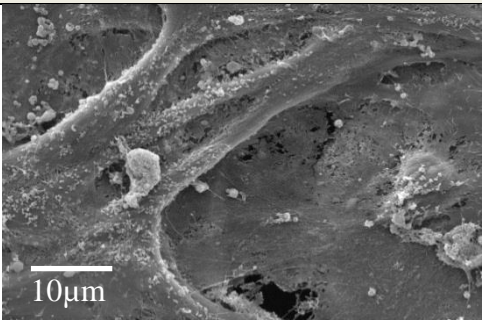
	Day 7 - 700°C 2 h	
	Low Magnification	High Magnification
TiN-containing		
Si:HA		

5.3.1.5 Day 14

There was no difference in cell morphology grown amongst samples annealed for 2 h and 4 h on day 14, and is represented in Table 5-5. Images on cell

growth on each coating can be found in Table 10-4 and Table 10-5. The cells have formed mineralised cell matrices.

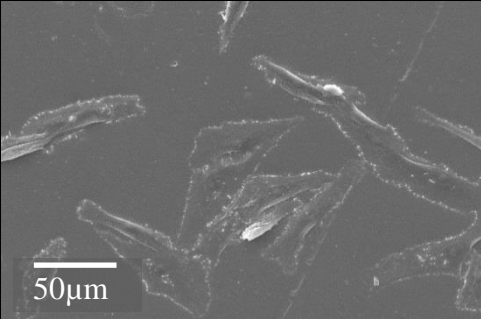
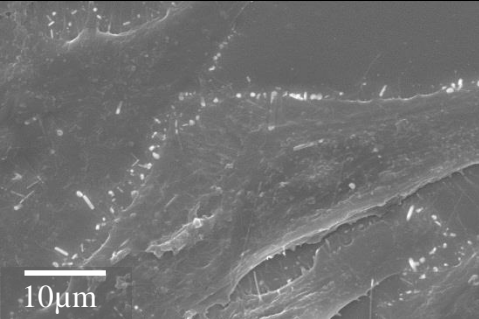
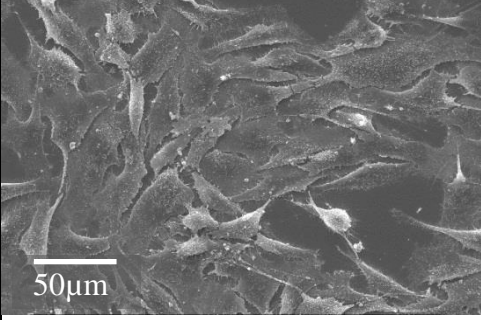
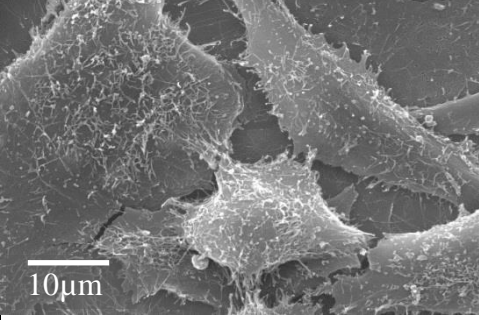
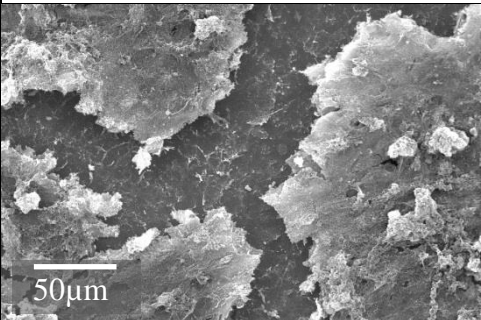
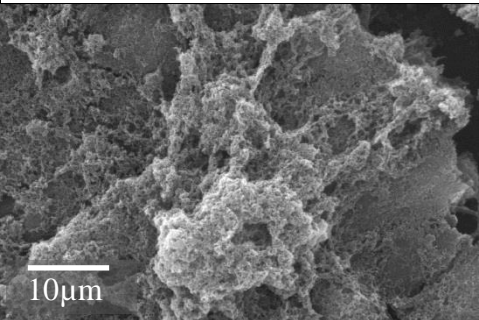
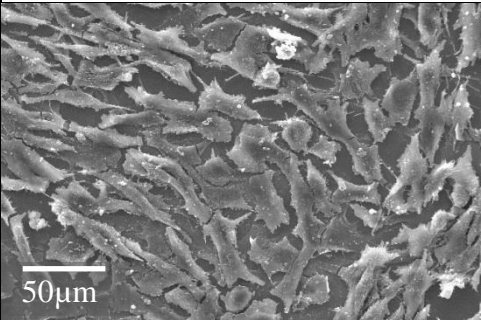
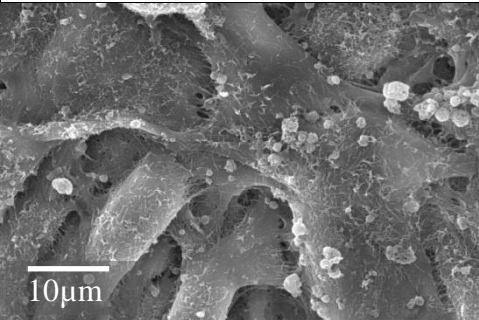
Table 5-5 Day 14: Representative image low (1000X) and high magnification (4000X) of MG63 cells grown on 2 h and 4 h annealed samples.

	Day 14 - 700°C 2 h and 4 h	
	Low Magnification	High Magnification
All samples	 <p>Mineralised cell matrix</p> <p>50µm</p>	 <p>10µm</p>

5.3.1.6 Cell growth on Ti control

Table 5-6 represents the growth of MG63 cells on Ti. The growth is similar to those as described in set 1 and exhibited normal MG63 cell growth. Growth of TCP was similar and therefore was not included in the thesis.

Table 5-6 The growth of MG63 cells on Ti for 1, 3, 7, and 14 days.

Days 1, 3, 7 and 14 - Ti		
Day	Low Magnification	High Magnification
Day 1		
Day 3		
Day 7		
Day 14		

5.3.2 ALB

All samples showed increased metabolic activity at each successive time point (Figure 5-7). The samples that showed significance had metabolic growths that were significantly higher than the Ti control and may be caused by the low reading for Ti. At 7 and 14 days, there were no significant differences between samples and the Ti control. The coatings may have dissolved causing attenuated cell growth and/or cell metabolism may ultimately be unaffected by coating type over time. The coatings were not cytotoxic (ALB can be used to test for cytotoxicity).

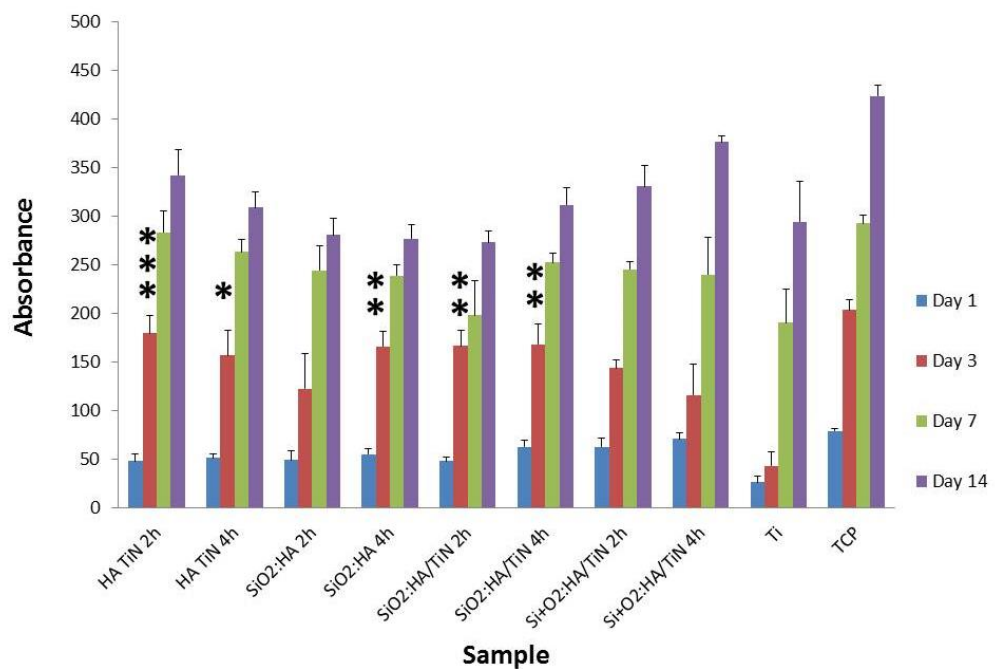


Figure 5-7 AlamarBlue was used to measure the metabolic activity of the MG63 cells cultured on the various treated coatings. The error bars represent standard error of mean, $n = 6$. * represents the significance compared to the Ti control ($p < 0.05$), where a greater number of * represents a higher level of significance. All significant differences that were found in day 3 and was attributed to low Ti metabolic activity.

5.3.3 DNA Hoechst assay

The DNA content of cells was used as an indicator of cell population. The DNA Hoechst 33258 assay was used to quantify the changing concentration of DNA as a function of time for the MG63 cells (Figure 5-8). It was hypothesised that Si:HA/TiN that lacks TiO₂ would enhance cell growth.

Ti showed the least DNA content throughout days 1-14. From days 3-14 the DNA concentration for all samples were all visibly greater than the control (cpTi), with significance at Si:HA/TiN 2 h samples compared to the Ti control. There was no significant difference between both sample sets. In general, all treated samples were rougher than the control Ti. The treated samples R_a ranged from 0.047-0.163 μ m whereas R_a for Ti was 0.027-0.068 μ m. A greater DNA quantity was expected on all treated surfaces as the roughness promotes cell adhesion and proliferation¹²⁸. HA and Si are also known to promote cell functions (adhesion/proliferation/differentiation).

There were decreases in DNA concentration on day 14 for cells grown on Si+O₂:HA/TiN 2 h samples. Perhaps a loss in cells occurred. After performing the ALB assay, the cells would be washed at least 5 times with PBS prior to commencing the DNA and ALP assays. Perhaps the delaminated samples caused weak surface-cell adhesion, resulting in them being aspirated away and resulting in cell loss. The cells were difficult to lyse as there were dense growth which was even visible to the naked eye. So perhaps clumps of

unlysed cells (increased amount of cells) were still in solution even after freeze-thaw cycles which affected some of the results.

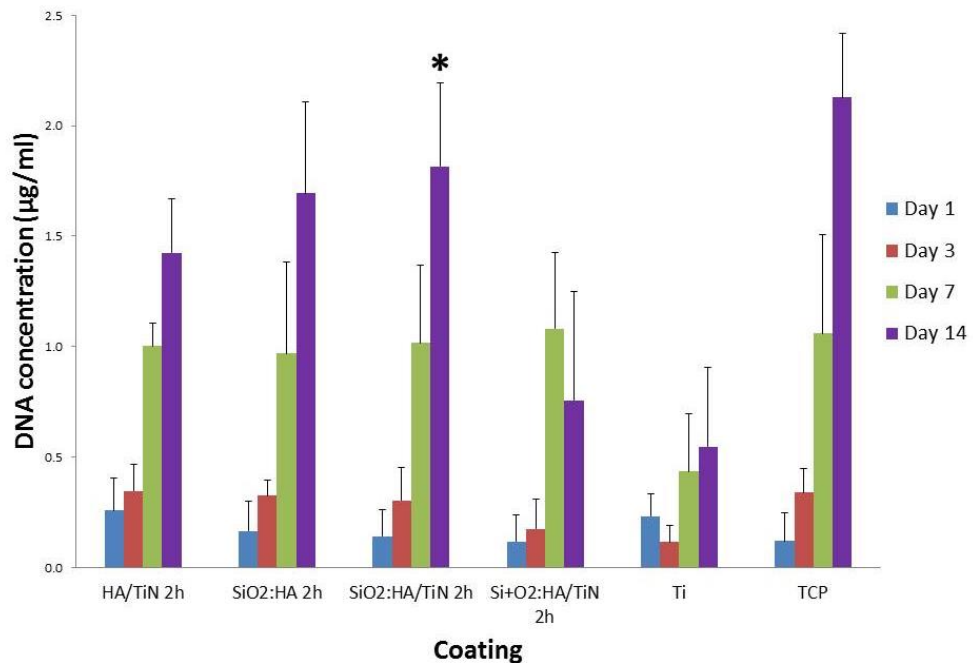


Figure 5-8 DNA Hoechst 33258 assay was used to measure the cell proliferation activity of MG63 osteosarcoma cultured on the various treated coatings. The error bars represent standard error of mean, $n = 6$. * represents the significance compared to the Ti control ($p < 0.05$).

5.3.4 ALP

ALP assay was used to gauge osteoblast differentiation. It was normalised with DNA to obtain the ALP activity per μg (Figure 5-9). The large standard error of mean could be due to technical application, which requires greater sensitivity compared to TCP (that has smaller standard error mean, SEM). By day 14 Ti has the highest ALP activity. Si:HA 2 h and 4 h as well as Si:HA/TiN 2 h showed the lowest activities overall. Si+O₂:HA/TiN was the

only sample that decreased in activity from day 7 to 14, possibly due to human error. The differences with Ti on each time point were insignificant. There appears to be an inverse correlation between the ALP activity and DNA concentration, which may coincide with literature that gene expression of proliferation decreases when gene expression for ALP increases.

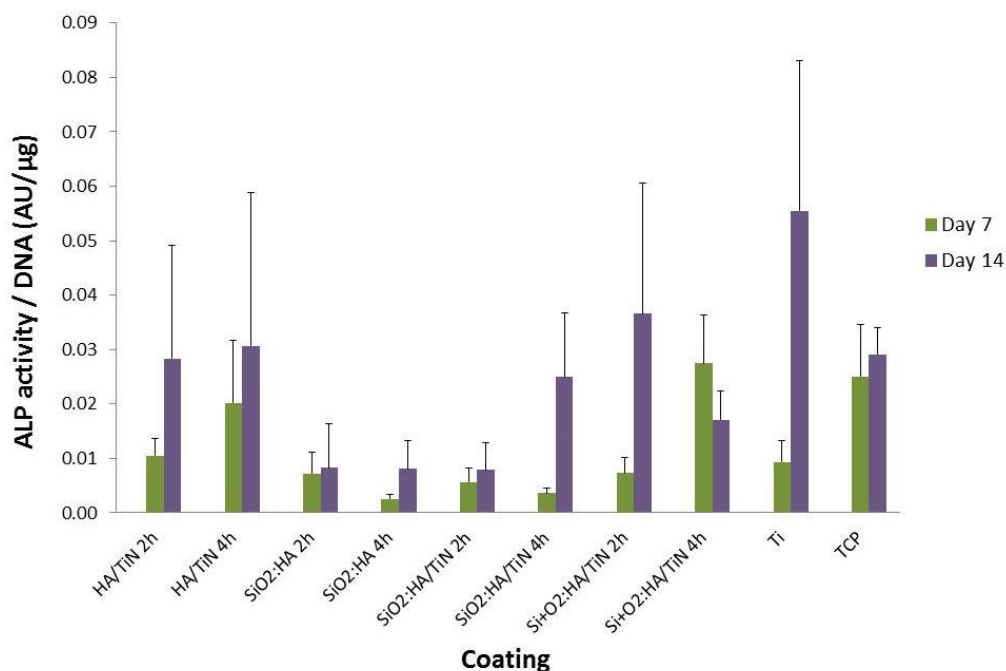


Figure 5-9 Alkaline phosphatase (ALP) activity of MG63 osteosarcoma cells cultured on the various treated coatings. Data was normalised with corresponding DNA concentrations for each sample. The error bars represent standard error of mean, $n = 6$. No significant differences were found among the coatings ($p < 0.05$).

5.4 Coating dissolution studies

All XRD patterns were normalised to TiN (111) peak at 36.8° , unless stated otherwise i.e. for samples without the TiN interlayer. HA/TiN 2 h annealed samples were dissolved in ddH₂O at 37°C for 24 h (Figure 5-10). The patterns

contain HA, CaTiO_3 , TiO_2 and TiN peaks. It can be observe that there is an increase in HA peaks after dissolution.

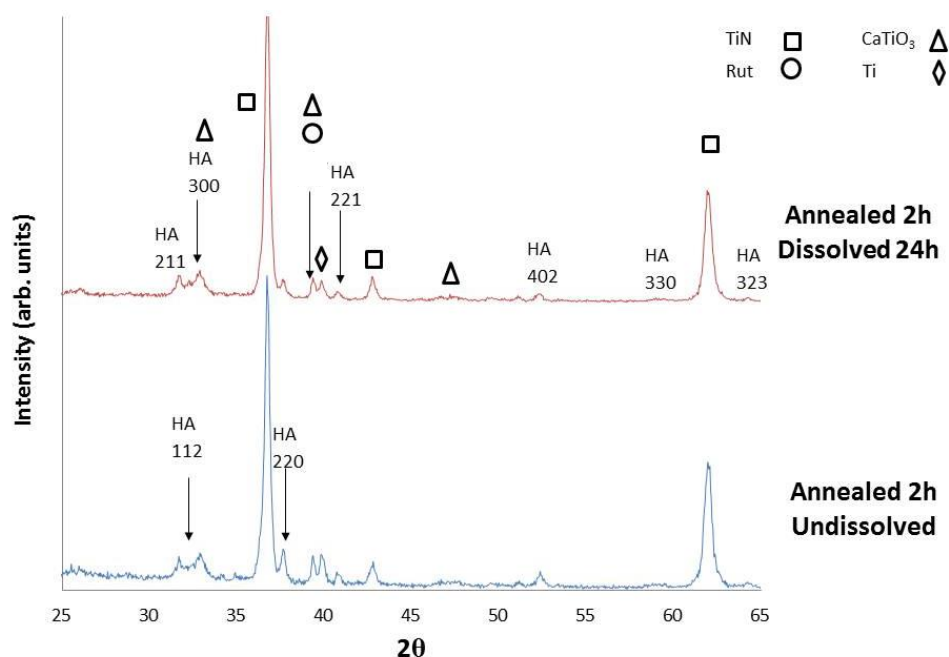


Figure 5-10 HA/TiN annealed for 2 h was dissolved for 24 h in ddH₂O (normalised at 36.8°; the TiN (111) peak)

Figure 5-11 shows Si:HA 2 h dissolved for 24 h had formed new TiO_2 peaks with increase in existing TiO_2 peaks and increase in HA peaks especially at HA (211). A similar trend is seen in Si:HA/TiN and Si + O₂:HA/TiN (representative Figure 5-12, Si+O₂:HA/TiN data in Figure 10-5); except with less intense TiO_2 , proving the efficacy of TiN as a diffusion barrier layer. In contrast with dissolved HA/TiN, the samples had increased HA₂₁₁ peaks and increase TiO_2 ; the difference in dissolution behaviour could be attributed to Si-substitution into the HA lattice, where the Si-containing coatings had an orientation preference during dissolution, and increase in TiO_2 formation.

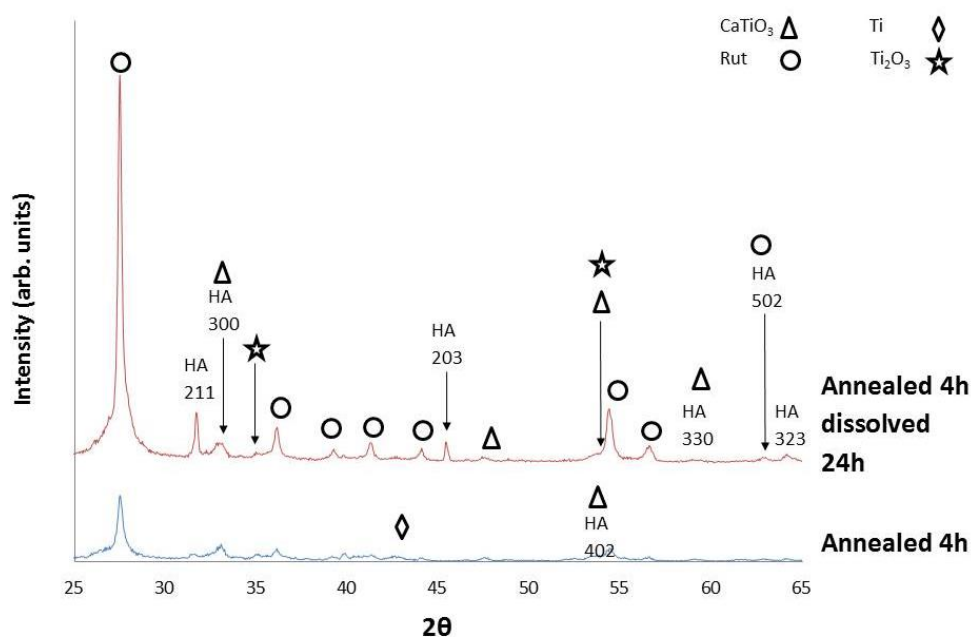


Figure 5-11 Si:HA annealed for 2 h was dissolved for 24 h in ddH₂O

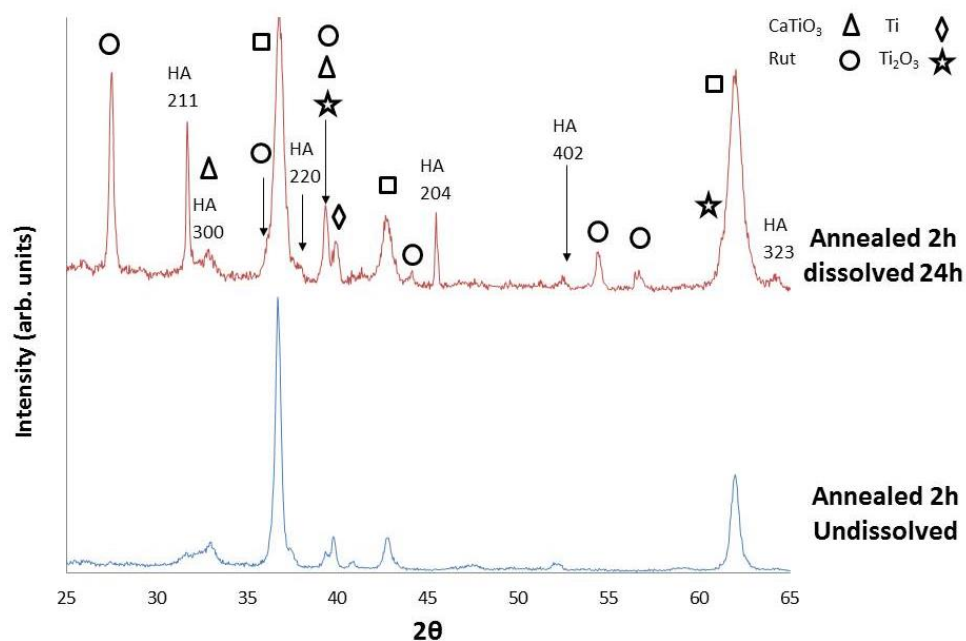


Figure 5-12 Si:HA/TiN annealed for 2 h was dissolved for 24 h in ddH₂O. The pattern is similar for similarly processed Si+O₂:HA/TiN (Figure 10-5), albeit with less intense TiO₂ peaks and more intense Ti₂O₃ peaks.

5.5 Summary

Due to the lack of samples in set 1, a 2nd sample set was created in order to perform a wider range of biological studies. The 2nd set of samples was

processed using similar coating and annealing methodologies as the previous set. The samples were analysed via SEM/EDX and XRD using the same parameters as for the previous set. However, RHEED and XPS analyses were not performed. In terms of the as-deposited samples, only as-deposited HA/TiN was analysed. Not all annealed sample coatings were analysed.

In terms of XRD analyses, all coatings that contained the TiN interlayer was normalised to the TiN (111) peak. XRD analyses showed that as-deposited HA/TiN contained crystalline TiN and Ti peaks. All annealed coatings with the TiN interlayer contain HA, CaTiO_3 , TiO_2 and TiN. Annealed Si:HA contained the same peaks as in the annealed samples with the exception of TiN and also increased levels of TiO_2 and presence of Ti_2O_3 . SEM images show that annealed HA/TiN and annealed Si+O₂:HA/TiN were granular at 2 h annealing. The topography of the Si:HA 2 h annealed sample was granular in appearance. Only Si:HA/TiN 2 h annealed sample contained delamination. Si was detected using BSE and the size ranged between 500nm to 2 μm .

MG 63 cells were seeded onto annealed samples for 1, 3, 7, and 14 days using the same protocol as the previous set. SEM imaging, ALB, ALP and DNA Hoechst were performed. In general, the SEM images show that the MG63 cells had normal growth, and there was no observational difference in the morphology and growth of the MG63 cells regardless of sample type. There were observational differences in the dissolution of the sample surfaces. The

coatings were not cytotoxic as evidenced by ALB, Si:HA/TiN annealed for 2 h encouraged cell growth but not mineralisation.

The samples were dissolved for 24 h in ddH₂O. Only HA/TiN 2 h samples were dissolved in ddH₂O for 24 h and 72 h. All XRD patterns were normalised to TiN (111) peak at 36.8°, unless stated otherwise i.e. for samples without the TiN interlayer. The HA/TiN 2 h samples appears to not be affected by dissolution. For all the other samples depicted in this section, the general trend was that there was an increase in TiO₂ peaks, increase in HA peaks, increase in HA (211) intensity and peak broadening as well as intensity in the TiN peaks at 42.64° and 61.84°.

Chapter 6 Overall Discussion

This section has a few themes:

- The microstructure of the as-deposited and annealed coatings in the presence of trace O₂ levels will be discussed.
- In terms of the development of the structure and composition of stoichiometric HA as a result of annealing, the current chapter will attempt to separate the real compositional variations from the issues of appropriateness of the EDX and XPS techniques for thin film characterisation.
- The development of unwanted Ti-O scale formation at the HA/Ti interface and hence the need for a TiN diffusion barrier.
- The composition and structure of TiN diffusion barrier and its association with coating delamination.
- Evidence of Si incorporation in to the HA lattice
- Cellular response of the coatings.

This section discusses the characterisation techniques normally used to investigate the surfaces of surface-coated titanium (Ti) used as biomedical implant materials as well as the techniques used to study the interface between the surface of coated Ti implants and the surrounding biological environment.

The biomedical implant surface should ideally be fully characterised in terms of its chemistry, crystal structure, metallurgy and morphology prior to *in vitro* cell trials ⁶⁵. Techniques normally used to characterise such properties are the scanning electron microscope (SEM), profilometry and atomic force microscopy (AFM) to test surface roughness and morphology; X-ray photoelectron spectroscopy (XPS) and reflection high energy electron diffraction (RHEED) are used to assess the surface crystal structure and chemistry, respectively, to complement energy dispersive X-ray (EDX) and X-ray diffractometry (XRD). EDX analysis in the SEM provides for more bulk information on the sample chemistry and structure ⁶⁵.

The surface properties of a thin film on a biomedical implant determines its efficacy *in vivo* such as increasing effective bone apposition ²⁴. The properties in particular crystallinity are influenced by the coating method ⁴⁴, coating parameters ^{24; 71; 100}, annealing parameters such as time and temperature ²⁵, and type of substrate ¹²⁹ as the ions in the coating and substrate may interdiffuse during annealing ^{44; 95}. In the literature found so far, there is no research that employed the exact conditions used for this project. Therefore, comparisons of the results are made using literature that matches the current results as closely as possible.

In order to better control the surface properties of HA, it first needs to be amorphous followed by after-deposition treatment. RF magnetron sputtering tends to produce HA of low crystallinity ³³. Annealing of the as-deposited

samples was necessary for grain growth and re-crystallisation to inhibit dissolution in biological fluid ^{24; 25}. As annealing is influenced by time, coatings were annealed for 2 h and 4 h to gauge on the optimum annealing time.

In order to perform additional biological experiments, a 2nd sample set was prepared using the similar coating parameters and annealed at 700°C for 2 h under Ar. The annealed samples were characterised using GA-XRD and SEM prior to the cell trials. Please refer to Table 4-1 and Table 4-2 for summaries of the set 2 results. Similarly to set 1, all XRD patterns were normalised to TiN (111) peak at 36.8°, except for Si:HA.

6.1 GA-XRD

Stoichiometric HA powder and HA sputtering target were successfully analysed using the same parameters for sample analysis (not shown). The stoichiometric crystallinities were consistent with stoichiometric HA. In this section, the two sample sets will be compared with references to the SEM/EDX results. A few peaks in the diffraction patterns were tentatively assigned to more than one chemical species because of these different possible reactions after annealing, and these possible reactions have overlapping ICDD/ICSD data.

6.1.1 As-deposited coatings

Perhaps due to the thinness of the coating, no broad peaks of amorphous HA nor those of SiO_x were found¹⁸ All samples from set 1 contained sharp Ti peaks (from the substrate) and broad TiN peaks. The Ti substrate was assigned to ICDD number 00-044-1294 and with hexagonal structure. TiN was assigned to ICDD number 00-038-1420, a preferential orientation at the (111) direction, is stoichiometric and has a face-centred cubic structure^{20; 21}.

For set 2, Figure 5-1 which contains the as-deposited coating diffraction pattern, did not register broad amorphous HA peaks but had crystalline TiN (Inorganic Crystal Structure Database (ICDD) reference codes: 00-017-0386 with a preferred orientation in the (111) direction. The formation of TiN phases depend on sputtering conditions such as temperature, ionisation efficiency and nitrogen partial pressure¹³⁰. For set 2, only HA/TiN was analysed and will be assumed as representative for all as-deposited samples.

The 2nd set of coatings has a similar pattern as the 1st set, the TiN peaks were sharp indicating crystalline TiN. The difference in TiN crystallinity in both sets is most likely caused by the difference in the sputtering conditions. However, full disclosure of the conditions was prohibited due to intellectual property policies. Both sets registered a red-shift in TiN peaks in the annealed samples compared to as-deposited samples (Figure 4-1 and Figure 5-1). The

reason for the red-shift could be attributed to the increased number of Ti vacancies during annealing ²¹.

6.1.2 Annealed coatings

The main objective for GA-XRD analysis is to assess the re-crystallisation of HA, the efficacy of TiN in preventing TiO₂ formation, and incorporation of Si into the HA lattice. HA delamination due to TiO₂ limits service life of the implant and TiO₂ inhibits bone cell maturation ⁴⁵. Therefore TiN as an interlayer attempts to retard the above process. Increase in annealing time increased the intensities and amount of peaks for the above-mentioned with the exception of Ti₂N.

Firstly, HA formation will be described. HA crystallisation was expected as previous studies have shown that HA and Si:HA on cpTi prepared using RF magnetron sputtering crystallised from 550°C ^{18; 25; 71}. The diffraction pattern positions coincide with stoichiometric HA (ICDD 01-074-0565, hexagonal lattice), the preferred orientation at the (300) direction along with absence of the characteristic (002) peak (annealed patterns at Figure 4-1, Figure 4-2, Figure 4-3, Figure 4-18, Figure 5-1, Figure 5-2, Figure 5-3, and Figure 5-5). Literature found so far on RF magnetron sputtered HA and low Si wt%-substituted HA on substrates of cpTi or Ti6Al4V would display the 4 main peaks, *i.e.* (002) peak as well as (211), (112), and (300) peaks, in similar relative intensities of the stoichiometric HA target ^{28; 71; 124; 129; 131; 132; 133}. The possible presence of perovskite (CaTiO₃; ICSD 98-006-6605 with an

orthorhombic structure) could have influenced the relative intensities of HA in the (211), (112) and (300) direction, as both overlap. CaTiO_3 could be formed from diffusion of HA components and Ti (from TiN)⁴⁴. It was suggested that a random crystallinity could be caused by rotating the samples during the RF magnetron sputtering process¹⁰⁰.

There has been previous work where the (002) peak was absent after annealing. An example is when Yonggang and colleagues used RF magnetron sputtering to fabricate a HA and calcium pyrophosphate composite coating at 200W (HA):600W(calcium pyrophosphate) followed by annealing at 550°C and 650°C⁷¹. A 2nd example is 60%wt Si-substituted HA prepared using a sol-gel method and then annealed in a furnace at 1250°C⁹³. Perhaps a high percentage of the additional material accompanying the HA influenced the crystallography of the annealed HA. Coating properties are affected by sputtering conditions such as bias voltage¹³³ and discharge power⁷¹. The mechanism as to how the sputtered layers are built up has not been completely understood¹³¹.

BSE imaging detected Si clusters but no Si peak was found via XRD and XPS. However there is evidence of Si substitution into the HA lattice. Due to the multilayered nature of the samples, there are overlapping peaks of other chemical species and therefore only the most intense HA peaks (211), (112) and (300) will be compared between samples. Substitution of an ion into a HA lattice results in a decrease in peak numbers, shifts in peaks of less intense,

and broader peaks^{18; 134}. In both sample sets (annealed patterns of Figure 4-2 and Figure 4-3), the substituted samples have reduced (211) peaks and/or little to no (112) peak unlike HA/TiN (Figure 4-1)¹⁸. The relative intensities between (300) and (211) changed from 1:1 ratio (HA/TiN) to 1:3 (substituted samples). The change in relative intensities contradicts the finding by Thian and colleagues who analysed HA substituted with Si between 0.8 – 4.9 wt%; the (211) peak is more intense than the (300) peak¹⁸. The difference in crystallinity could be due to coating^{24; 71; 100} and annealing parameters²⁵. Coating parameters may influence the crystallinity as well^{24; 71; 100}; a possible difference could be that Thian and colleagues applied a DC current during sputtering of the Si target¹⁸ whereas the current project applied RF for the Si target. In the case of the project, the coatings were annealed at 700°C for 2 h and 4 h in Ar, whereas Thian and colleagues annealed their coatings at 600°C for 3 h in a water-vapour Ar atmosphere¹⁸.

HA should ideally remain stoichiometric at post-deposition treatment and have no decomposition products for optimum biocompatibility^{8; 95}. There have been previous reports which stated that as a result of exposure to heat, HA decomposes into CaO and various calcium phosphate phases (the most common being tricalcium phosphate)^{23; 27; 40}. Having a mix of calcium phosphate phases and oxidised Ca would influence the solubility properties and hence biocompatibility⁵⁵. Also, there is varying evidence on their biocompatibility / ability to enhance cell growth⁴⁰. In sets 1 and 2 the above-mentioned phases were not present, which coincide with XRD analyses on

magnetron sputtered HA and Si:HA coatings^{18; 24; 25}, as well as XRD analysis on precipitated silicon-substituted HA heat treated at 700°C for 2 h¹³⁵.

The as-deposited coatings of set 1 contain amorphous TiN, which upon annealing produced TiN and Ti₂N. The phenomena is consistent with Tarniowy and colleagues¹³⁶. The crystalline TiN has a (111) preferred orientation and is the hardest of the TiN subspecies¹³⁷. The Ti₂N was assigned to ICDD number of 00-017-0386 with a preference at the (002) direction and has a tetragonal lattice structure.

The most similar work that coated HA/Ti composites on Ti alloy using thermal reactive plasma spraying in an Ar/N₂ atmosphere^{27; 138}. It can be generally observed that the composites with HA/Ti of <1.4 weight ratio produced crystalline Ti₂N^{27; 138} and, in the case of Roşu and colleagues, the HA layer was decomposed²⁷. The above literature may infer that Ti₂N may have encouraged HA delamination.

N₂ gas was used during sputtering of the Ti adhesion layer prior to TiN deposition. Magnetron sputtering that included N₂ gas, usually mixed with Ar gas, have resulted in the production of Ti₂N¹³⁹. Surprisingly, in set 2 reactive sputtered Ti target in an Ar/N₂ atmosphere produced crystalline TiN (more

details later). A number of factors other than Ar/N₂ could play a role in Ti₂N formation, such as power density¹³⁹.

For Si:HA annealed samples (2 h and 4 h), the chemical species formed were HA, TiO₂ (ICDD: 00-021-1272 with tetragonal lattice structure) and Ti₂O₃ (ICDD: 00-010-0063, rhombohedral structure) with possible CaTiO₃. At 4 h, the above increased in intensity and peak numbers. As expected, the absence of TiN layer allowed diffusion of Ti and O (from HA) atoms which formed various Ti-O species. Compared to other samples, this coating has the highest TiO₂ intensity at the main peak at 27.50°¹⁴⁰.

Annealed set 2 samples did not contain a mixed phase of TiN/Ti₂N unlike set 1 (Figure 5-1 and Figure 5-3). In general, all sample types regardless of set number increased in rut (TiO₂) from 2 h to 4 h. TiN-containing coatings have TiO₂ peaks that are lower in number and intensity than non-TiN containing samples (Si:HA samples), which confirms the efficacy of TiN in preventing TiO₂ formation. Set 1 annealed samples have increased TiO₂ peaks and increased susceptibility to delamination compared to set 2. Perhaps Ti₂N played a role in delaminating the HA coating upon annealing. Perhaps a single crystalline TiN phase is more successful at preventing TiO₂ formation and delamination. Susceptibility to TiO₂ formation is as follows: without TiN > TiN/Ti₂N > TiN. Balance between crystallisation and rutile formation must be maintained. Although Si clusters were identified via BSE and EDX, the XRD data did not detect any SiO_x peak. The possible reason could be due to the low weight percentage of Si. Similar to set 1, the absence of the (112) and/or (211)

HA peaks are proof that Si decreases the grain size of the coating and inhibits grain growth. It could be surmised that as-deposited crystalline TiN with a 111 preference successfully prevents Ti_2N and TiO_2 formation upon annealing. Amorphous TiN may encourage Ti_2N formation upon annealing. Due to intellectual property policies, lack of disclosure regarding the sputtering conditions has resulted in a knowledge gap regarding the process-structure-property interrelationship of Si-substituted HA with/without TiN on Ti substrate.

6.2 SEM/EDX

The morphology of the samples was assessed via SEM. Ca/P ratios of the samples were quantified using EDX because Ca and P are the most stable atoms in the apatite of bone. Different Ca/P values signify different degrees of biocompatibility. A complementary technique is XPS (below), however XPS emphasises on the surface whereas EDX has emphasis on the bulk. It was difficult for both techniques to accurately quantify Ca/P ratios due to surface roughness and sample heterogeneity^{113; 115}. However, both techniques provide insight into the dynamic change of the surface (XPS) and bulk (EDX) as a result of annealing time.

This section is divided into 3 subsections – as-deposited, annealed 2 h and annealed 4 h. Comparisons will be made between sets 1 and 2. The work may be the first of its kind. Therefore the results will be compared and inferred

from previous work that resembles an aspect of the current work. For example, Thian and colleagues used magnetron co-sputtered Si-substituted HA on cpTi and annealed it at 700°C for 3h^{18; 43}; the results are used to make comparisons with substituted samples annealed at 700°C for 2 h and 4 h .

In order to confirm the accuracy of in-house EDX, an HA standard was analysed with the same parameters used for sample analysis. The atomic percentages obtained equated to an average Ca/P ratio of 1.70 (n=3), which was similar to that of stoichiometric HA (1.67).

6.2.1 As-deposited coatings

Figure 4-5, Figure 4-7, Figure 4-9, and Figure 4-11 have SEM images of as-deposited samples that do not have cracks and conform to the striations and pits from the substrate polishing, which is consistent with previous experiments^{18; 24}. The films had Ca/P ratios that were higher than that of stoichiometric HA (1.67) and could be rounded to 2; which is consistent with previously performed work^{22; 24; 25; 71}.

Theoretically, a stoichiometric HA target would result in the sputtering of an HA layer with a Ca/P ratio of stoichiometric HA. However the increased Ca/P ratios of the deposited samples, compared to the stoichiometric HA target, could be caused by the decreased incorporation of phosphorus ions (PO_4^{3-}). Various hypotheses exist in terms of the mechanism such as the preferential

sputtering of calcium onto the film, the possible pumping away of phosphorus (PO_4^{3-}) ions before they could be deposited on the substrate, the sputtering away of the phosphorus ions due to weak binding of oxygen^{22; 25}, and the competitive replacing of the PO_4^{3-} by the silicate ion during substitution¹⁸. Substitutions may cause structural rearrangements such as lattice defects⁷¹.

6.2.2 Coatings annealed for 2 h (sample sets 1 and 2)

SEM images of set 1 samples (Figure 4-5) showed a textured surface for HA/TiN but delaminated, granular, or floccular surfaces for Si-substituted HA with and without TiN (Figure 4-7, Figure 4-9 and Figure 4-11). There is phenotypic evidence that the incorporation of Si; finer-grained material is more susceptible to thermal shock possibly leading to delamination¹⁴¹.

Similarly to the set 1 samples that were annealed for 2 h, HA/TiN of set 2 was not delaminated (Figure 5-5a). There is a difference in morphology however, pollen-like protrusions were observed for the 2nd set. Si+O₂:HA/TiN has granular morphology with pits and depressions that are attributed to the substrate unlike the delamination observed in set 1. The difference in HA/TiN and Si+O₂:HA/TiN could be due to the possible difference in post-deposition treatment and/or difference in sputtering conditions. Sets 1 and 2 for Si:HA have granular morphology after 2 h annealing. The granular morphology at 2 h is consistent with previous in-house experiments¹⁴². The difference in morphologies between sets 1 and 2 could be attributed to the sputtering conditions, presence of different Ti_xN_x phases or possible presence of trace

levels of O₂ during annealing. Delamination was observed for Si:HA/TiN (of set 2), which is consistent with set 1. Perhaps a combination of TiN and Si encourages delamination, with TiN/Ti₂N interlayer having a more potent effect on delamination.

In order to mitigate the surface roughness effects on the EDX, the Ca/P ratios of delaminated samples were obtained only from HA islands. For set 1, the Ca/P ratio for the 2 h annealed samples were lower than their as-deposited counterparts, which is consistent with previously performed work which used RF magnetron sputtering and annealed at 600°C for 2 h²⁵. Annealed samples have decreased Ca and P atomic percentages which is consistent with Thian and colleagues¹⁸. In set 2, HA/TiN and Si:HA have similar Ca/P ratio averages as in set 1. Si:HA/TiN has significantly lower Ca/P ratio compared to set 1. As for Si+O₂:HA/TiN (set 2), only 1 area out of the 3 areas detected P, meaning that the sample has lost a significant amount of PO₄²⁻. An explanation is that the Ca and P evaporated due to the constant flow of the Ar gas during annealing or that the silicate ion has also replaced PO₄³⁻¹⁸.

6.2.3 Coatings annealed for 4 h (sample set 1)

Please refer to SEM and EDX summary tables (Table 4-1 and Table 4-2). In set 1, HA/TiN, Si:HA/TiN and Si+O₂:HA/TiN were delaminated into HA and TiO₂ phases. RF magnetron sputtered HA on Ti6Al4V annealed for 4 h at 600°C²⁵ and HA+TiN composite coating produced using reactive plasma

thermal spraying²⁷ resulted in cracked and delaminated coatings, respectively. The delaminated HA/TiN (set 1) complemented the above work (Figure 4-5). Si:HA exhibited floccular morphology with Ca-P precipitates (Figure 4-7); similar to magnetron sputtered Si-substituted HA that was annealed at 700 °C for 3 h under a moist Ar atmosphere^{18; 143}. The utilisation of TiN affects the surface morphology after annealing; the absence of TiN allowed for HA and TiO₂ to form mixed phases whereas TiN allowed for separation (delamination) into HA and TiO₂ phases (Figure 4-5 and Figure 4-9).

Changes in average Ca/P ratios could be attributed to evaporation of Ca and P or PO₄³⁻ replacement by Si⁴⁺¹⁸. All Si-substituted samples have lower Ca/P ratio compared to HA/TiN (EDX rows at Table 4-1 and Table 4-2). Along with the XRD data, perhaps it can be confirmed that Si⁴⁺ substitution has occurred in the bulk. However, it is difficult to confirm the substitution at the surface because there appears to be no trend with the Ca/P ratio. A complementary technique, XPS (XPS rows at Table 4-1 and Table 4-2). Set 1 samples annealed at 4 h generally have increased fluctuation in Ca and P atomic percentages compared to those annealed at 2 h (Figure 4-6, Figure 4-8, Figure 4-10). Perhaps TiN and Ti₂N crystallises non-uniformly and the increased roughness more adversely affects quantification and increases signal-to-noise ratio. More significantly, TiN-containing samples have P dropped to 0.1 percent and at the detection limit¹⁰⁸.

6.2.4 Delamination

Several authors have analysed RF magnetron sputtered silicate-substituted and unsubstituted HA followed by annealing at various temperatures from 200°C to 750°C at various time periods from 30s to 4 h^{25; 71; 144}. The average Ca/P ratios in set 1 could also be rounded to 2 (please refer to EDX rows of annealed samples at Table 4-1 and Table 4-2). SEM images of delaminated samples can be seen at Figure 4-5 and Figure 4-9 for set 1; and Figure 5-5c (set 2).

Mismatches in thermal expansion coefficients (thermal coefficient of expansion; TCE) between the thin films during annealing will result in residual stresses which encourage delamination in both sets of samples^{132; 140; 145; 146}. Further investigation into the mechanisms behind TiN delamination will be needed. TCE values are approximations as they vary according to fabrication technique¹⁴⁷, range of temperature used to calculate TCE^{146; 147; 148}, forms of material^{147; 148}, film thickness¹⁴⁶, and crystallite size¹⁴⁰.

The hypothesis of the post-deposition results was to produce non-delaminated annealed coatings with stoichiometric Ca/P ratios, however the results have produced the opposite. The set 1 samples were more susceptible to delamination than set 2. A possible explanation is that as-deposited set 1 has smaller TiN grain and would be more susceptible to thermal shock¹⁴¹. Therefore during annealing the interlayer itself cracked, and in turn possibly

contributed to HA island formation. The presence of TiN phases may affect post-deposition surface morphology and average Ca/P ratios. SEM/EDX showed that N was detected at the HA islands but the non-islands only contained Ti and O. Therefore delamination occurred at the interlayer causing the formation of HA islands, and exposing the Ti substrate which naturally formed TiO_2 .

Si clusters have smaller fluctuations in size in set 1 ($2\mu\text{m}$) compared set 2 (500nm - $2\mu\text{m}$). Since the size effect of different substitution ions influence crystallisation¹⁴⁹, perhaps there is a size effect in determining morphology. Intellectual property policies prohibit full disclosure of the sputtering conditions and therefore an understanding of the reason behind the delamination could not be obtained. Other issues may be due to 1. furnace malfunction that introduced trace O_2 and; 2. Possible contamination of residual colloidal SiO_2 polishing suspension on the Ti substrate, which acted as strain centres and facilitated delamination.

6.3 RHEED and XRD comparison

RHEED was performed only for set 1 samples and therefore it would be compared with GA-XRD results for set 1 samples as well.

6.3.1 As-deposited coatings

The as-deposited films were amorphous due to the presence of diffuse rings and/or no rings. This is consistent with XRD, therefore the HA at the surface and bulk was amorphous.

6.3.2 Annealed coatings

The RHEED images showed that there was a mix of small and large grains in the same phase. XRD and RHEED data for the annealed samples similarly confirmed that HA and TiO₂ were the dominant phases (Figure 4-13). The relative intensities similarly match those of the XRD. HA/TiN has less rings and more diffuse, coincide with previous in-house data ¹⁴². It can be concluded that TiO₂ and HA were on the surface of the sample, with Ti₂N and TiN layers below. Therefore perhaps TiN and Ti₂N did not diffuse to the surface.

6.4 XPS investigations

XPS analysis, like RHEED, was performed on only set 1. All as-deposited coatings have Ca/P ratios that are close to stoichiometric HA of 1.67 (Figure 4-15) ^{133; 150}. Natural HA have been investigated using XPS and it was found to have variable Ca/P ratios between 1.6 and 1.7 ⁷³. Each coating has similar Ca at% and P at%, whereas EDX found that Ca at% and P at% for the Si+O₂ sample were significantly lower. Perhaps the phosphate groups for Si+O₂:HA/TiN preferentially resides at the surface of the coating. Perhaps the Si+O₂:HA/TiN surface is thin compared to other coatings because partial

pressure of oxygen lowers the deposition of Ca and P¹²³. Different sputtering conditions affect coating properties^{22; 130; 151}.

Compared to EDX analysis, there was an increase in Ca at% and sharp increase in P at% of as-deposited samples obtained using XPS (Figure 4-14), which gave rise to consistently lower Ca/P values than those of EDX (please refer to as-deposited columns at Table 4-1 and Table 4-2). It could be implied that there was preferential residing of PO₄ and Ca at the surface. Due to the absence of Ti and N peaks, it can be safely assumed that TiN and Ti were not at the surface.

Annealing coatings caused Ca and P loss in the surface as well as in the bulk (Figure 4-14). The only anomaly was annealed Si+O₂:HA/TiN; Ca and P at% increased slightly at 4 h. Both these trends are consistent with EDX. Both Ca and P were lost at different rates and therefore the resulting increase in Ca/P ratio as a function of annealing is consistent with Boyd²⁴. Some of the samples had little or no P, leading to high Ca/P ratio or a ratio of 0, respectively. The mechanism of P evaporation during annealing is not understood²⁴. The increases in fluctuation of at% and ratios as a function of annealing were consistent with that of EDX.

Auger electron spectroscopy (AES) is a complementary technique of XPS. AES study on rabbit bones show that there was a decrease in Ca/P ratio from

healthy to osteoporotic bones⁸⁰. The fluctuation in Ca/P ratio is reminiscent of osteoporotic bone in mammalian bone cells, with high Ca/P regions⁸⁰.

High resolution spectra of samples annealed for 2 h and 4 h had hydrocarbon and adventitious carbon, both of which are common contaminants in the XPS sample chamber (Figure 4-16)^{138; 150; 152; 153}. The as-deposited and annealed samples show that there was a small amount of calcium carbonate (CaCO_3), which may be a contamination formed from the presence of CO_2 and water¹⁵⁴. Carbonate was found in natural HA^{73; 154}, however the amount have been too low to make any significant contribution to the bone-biomaterial interface¹²⁴.

No Si peak was found was as-deposited and annealed samples, neither was there an O1s peak that contains a component peak between 532.1-533.7 eV that was attributable to Si¹²⁷. P 2p was assigned to HA. The binding energies of Ca 2p and O1s for CaTiO_3 overlap and therefore both could be assigned to HA and/or CaTiO_3 ^{115; 126}. The current project may be the first to report that RF magnetron sputtered HA coating formed CaTiO_3 . CaTiO_3 formation was found to increase osteoblast adhesion^{133; 155}.

XRD finding is consistent with that of XPS. All set 1 samples (annealed at 2 h and 4 h) have developed similar species – adventitious C, hydrocarbon contamination, CaCO_3 , HA and CaTiO_3 . The 4 h annealed samples may contain a small amount of tricalcium phosphate $\text{Ca}_3(\text{PO}_4)_2$ ^{8; 40; 72}, however

this needs further clarification. It was expected that Ti peaks will have less intensity than samples without TiN. However Ti peaks fluctuated across samples due to delamination. Perhaps the growth of TiO_2 was non-uniform and had pockets of dense TiO_2 .

Si clumps were found in SEM observations but were not detected using XPS. Perhaps analysis using more sensitive techniques are needed such as Auger electron spectroscopy (AES), Rutherford backscattered spectroscopy (RBS)¹⁰⁸ or even the Kratos XPS instead of the ESCALab XPS. Perhaps the concentration of 2 wt% was too low to be detected by ESCALab XPS. During the previous in-house study by Coe, the Kratos XPS detected Si but not the ESCALab¹⁴². In another study by Xu and Khor, Si peaks in 3-4% Si-substituted HA were detected using the Kratos^{90; 142}. Comparisons between the 2 XPS were performed. Possibly the difference is due to their relative sensitivity factors and the fact that Kratos uses a monochromated Al K x-ray source which permits moieties and species to be distinguished unambiguously¹⁵⁶.

There is awareness that differences in results could arise due to the thinness of the coating and due to delamination of the samples. The relative sensitivity factors are accurate for homogenous materials, smooth samples and samples that do not vary in composition according to depth¹¹⁵. The samples under analysis are the opposite. Also the different Ca/P ratios could be due to the different relative sensitivity factors used by the EDX and XPS methods^{80; 115;}

¹⁴². XPS more accurately represents the surface layer that interacts with the cells as it analyses the top few atomic layers of the coating. Accuracy of 10% is achieved by XPS. The high absorption of low energy X-rays in the HA matrix presents challenges for X-ray analysis. An accurate absorption correction is required, and sensitive roughness effect correction ^{34; 157}.

6.5 Biological cell study – set 1

MG63 osteosarcoma was grown on the annealed samples of set 1 for 1, 3, and 7 days. ALB was performed to gauge the cytotoxicity of the samples. All were compared with a Ti control and 2 way ANOVA was performed to gauge significance at $p < 0.05$.

6.5.1 ALB tests

ALB metabolism test was performed on days 1, 3, 7 with Ti as a control and a 2-way ANOVA was performed Figure 4-17. As expected, each sample showed an increase in cell metabolism as time progresses. When samples for each time point was compared, no significant difference was found ($p > 0.05$), indicating that the cells were no metabolically different regardless of sample type. Further discussion on the suitability on using ALB and its interpretation can be found at the biological tests done on set 2 samples.

6.5.2 SEM imaging of cells

As expected for a cancer cell line, the SEM imaging of the cells grown on both sample sets showed little to no morphological differences between sample types despite differences in surface topography and grew over grooves, cracks and islands ⁴⁵. Morphological changes appeared at each time point (length of incubation). At days 1 and 3, the cells were randomly oriented on the sample and showed polygonal morphologies with lamellipodia and fillopodia ⁴⁵. Starting from day 7, SEM observation of mineralised cell matrices correlated with the initiation of ALP activity. It was difficult to perform EDX analysis during SEM imaging of the cells due to overlapping peaks of gold (Au) signals from the coating used for SEM imaging, and osmium (Os) from the osmium tetroxide fixative. Delaminated HA islands appeared to be poorly adhered to the substrate because HA were found on top of cells Figure 6-1. The morphologies for both sample sets were similar.

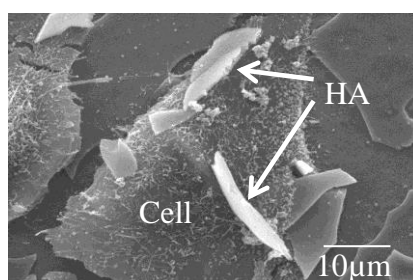


Figure 6-1 Representative SEM image showing HA on top of a growing MG63 cell, implicating that cell growth further delaminated the HA islands.

6.6 Biological cell study –set 2

ALB can be regarded as a *cytotoxicity test* ¹⁵⁸ and may be unsuitable for use on the 3D scaffold-like nature of the coatings ¹⁵⁹, however the degree of

unreliability is uncertain. The result is consistent with those of set 1 therefore both sample sets are considered as non-toxic.

Si:HA annealed for 2 h (set 2) had the 2nd highest DNA activity but it was not significant compared to the control, this lends to the controversy of the true effectiveness of Si:HA on Ti at promoting bone growth⁶². Reported for the first time ever, Si:HA/TiN 2 h significantly enhances cell growth. It is also comparable to Si:HA 4 h. It appears that the cells preferred island/delamination and floccular topographies^{30; 45; 160}.

MTT assay (3-(4, 5-dimethylthiazolyl-2)-2, 5-diphenyltetrazolium bromide) was performed using MG63 cells on TiO₂/HA hybrid coating with Ti6Al4V substrate and found that the coating supported cell growth more effectively compared to HA or TiO₂ only surfaces²⁶. Although the MTT assay was performed for only 3 days, it can be correlated to the current results since both Si:HA/TiN annealed for 2 h contain TiO₂ and HA.

There is a general inverse correlation of relative activities of ALP and DNA assay; a sample with low ALP activity would have a relatively high amount of DNA and vice-versa. However, this correlation cannot be verified as the DNA / growth and ALP correlates differently according to the material of interest^{30; 161}. The ALP activity contradicts with the finding that the ALP activity of MG63 increases when grown on rutile/HA composite prepared using the sol-

gel process ¹⁶¹. However it is consistent with the finding that presence of TiO₂ decreases ALP production in MG 63 cells ⁴⁵.

Due to time constraints, a quick proliferating osteosarcoma cell line (MG63) was used instead of human-derived osteoblasts. The proliferative and early mineralisation activities between MG63 cells do not necessarily reflect those of human osteoblasts (HOB) ^{32; 162; 163}. However, MG63 have been used as quick gauges involving biomaterials including Si:HA ^{45; 62; 164}. Experiments performed *in vitro* may not necessarily be replicated *in vivo* because *in vivo* systems are more complicated and involve exposure to other influences such as the presence of osteoclasts, immune cells, various enzymatic secretions and the overall health of the recipient of a biomaterial ⁶². The coatings are all deemed biocompatible and do not enhance mineralisation. Only Si:HA/TiN annealed at 700°C for 2 h from set 2 has enhanced proliferation and has the added benefit of reduced rutile (TiO₂). Its bulk Ca/P ratio (obtained via EDX) was 1.58±0.19, which is close to that of bulk stoichiometric HA (1.67), which is suitable for cell growth including MG63 cells ²⁸. Natural biological apatite has a ratio of 1.5-1.7 ⁷³. Efforts have to be made to further limit TiO₂ formation in order to limit introduction of large HA particulates into the body ¹⁶⁵. It is recommended that a more full set of data involving dissolution and use of human osteoblasts (HOB) should be performed.

6.7 Dissolution study

The study of dissolution is important to improve our understanding of the processes that lead to enhanced bioactivity ²³. A commonly proposed mechanism is that the calcium and phosphate ions from the HA dissolves into the fluid either through the environment (extracellular fluid) and may be actively mediated by osteoclast cells. The increased Ca and P concentrations in the fluid fill the spaces between the bone and implant. HA precipitation in this space ensures implant incorporation into the existing bone ²³. Immersion time, surface topography, and the presence of cells have been shown to influence the dissolution behaviour of a thin film coating. Further, highly crystalline coatings are stable and less likely to dissolve in biological fluid than amorphous coatings but may impede cellular response. However, relatively more soluble or semi-crystalline calcium phosphate phases release bone-forming Ca and P ions and may increase bone-biomaterial interaction. Therefore, characterisation is necessary to monitor any change that occurs from dissolution as it influences the stability and biological performance of the implant device ²⁴. The current work is most likely the first of its kind as literature on the dissolution behaviour of substituted HA on TiN is yet to be found. It is essential to improve our understanding of processes leading to the enhanced bioactivity of the materials ¹⁶⁶. For set 1, only HA/TiN dissolved for 24 hours was analysed (Figure 4-18 and Figure 4-19). For sample set 2, all 2 h annealed samples were dissolved for 24 hours (Figure 5-10, Figure 5-11 and Figure 5-12).

6.7.1 Set 1

Porter and colleagues have proven that silicate ions increase solubility of HA¹⁶⁶. For the set 1 samples, only HA/TiN was analysed. The XRD patterns were normalised to TiN (111) peak at 36.8° (Figure 4-18 and Figure 4-19). The only peaks remaining were HA (300)/ CaTiO₃ (121) and HA (330), (140), (323). SEM imaging contradicts with TEM imaging on bulk HA that was immersed in ddH₂O for 30 days showed no signs of dissolution¹⁶⁶. The SEM images of the 2 h annealed HA/TiN sample coincides with the above, but not 4 h. Perhaps the delamination of the 4 h sample played a role in affecting the dissolution behaviour of the coating. Evidence of dissolution contradicts previous findings^{55; 62}.

All set 1 samples (annealed 2 h and 4 h) that were dissolved for 24 h had decreased Ca at% and P at% (Figure 4-20). The loss of Ca²⁺¹²⁶ and reduction in PO₄²⁻²² were consistent with previous literature. It is difficult to quantify the rate of dissolution due to the lack of samples, HA delamination and the semi-quantitative nature of EDX, and the penetration depth of the electron beam that is deeper than the HA coating.

6.7.2 Set 2

Annealed set 2 samples were dissolved using the same methodology as set 1. Overall, there was no significant loss of HA, which coincides with the XRD results of Zeng and colleagues¹⁶⁷. All sample types, except for dissolved

HA/TiN annealed 2 h, have an increase in HA (211) peaks. This was consistent with previous work that dissolution of HA is favoured in that direction and dissolution may be preferentially aligned along the c-axis orientation¹²⁴. Also, relatively large amounts of TiO₂ were found in Si:HA and Si:HA/TiN samples (set 2) after dissolution in ddH₂O for 24 h. Si:HA has TiO₂ peaks with the highest intensity and with the largest amount compared to all of the other samples (Figure 5-2), which may infer that TiN does prevent the formation of rutile even in liquid. The more intense and larger amount of TiO₂ peaks in the delaminated (Figure 5-5c) and dissolved Si:HA/TiN 2 h sample (Figure 5-12) compared to the other TiN-containing (Figure 5-10) and non-delaminated sample (Figure 5-5a) may prove that defects in the dissolution behaviour can also be proven *in vitro* and not just *in vivo*¹⁶⁶. The peak broadening at approximately 63° could be due to mixed TiN and TiO₂. No Si was detected, which was expected as it was not detected prior to dissolution. The appearance of the (tentatively assigned) Ti₂O₃ in dissolved Si+O₂:HA/TiN samples is unique compared to other coatings (represented by Figure 10-5). Perhaps a phase transition occurred and it could be due to the unique chemical composition of the sample itself²².

The dissolution of delaminated HA/TiN of set 1 annealed for 2 h (Figure 4-18) appeared to have lost a few of the HA peaks, whereas the dissolved HA/TiN of set 2 did not change in intensity (Figure 5-10). The difference of the HA phases of dissolved HA/TiN 2 h show that the difference in post-deposition treatment determines the dissolution behaviour of the sample. If the XRD results could be extrapolated up to day 14, it is then likely that the same

samples, when immersed with the MG63 cells, would also experience the increase in TiO_2 and respond accordingly. Further work needs to be performed to elucidate the dissolution behaviour, such as analysing via XPS and SEM/EDX for the same amount of days as the cell trials and correlating them to ALP activity.

Chapter 7 Conclusions

There is a need to improve the current bone cell enhancing ability of HA thin films coated Ti due to a rise in demand for dental, plate fixation screws and, in particular, orthopaedic implants. As a result of the rise in demand, there was consequently an increase in the incidence of aseptic loosening and revision surgeries. A possible solution was to substitute the HA with a low amount of silicates, such as 2 wt%, to improve early osseointegration, and adding an inert and biocompatible diffusion barrier layer to reduce ionic diffusion between the HA and Ti which would in turn prevent the formation of unwanted Ti oxide subspecies which disrupt and decompose HA. RF-McoS may offer advantages over the current commercially used plasma spraying method, such as increased control over HA microstructure. ISO, ASTM and FDA standards strongly recommend that HA-related biomaterials intended for surgical implants should be characterised in terms of their *e.g.* Ca/P ratio and crystal structure^{22; 33}.

Although much research has been performed on HA, the novelty of the project is utilising a combination of TiN with HA or Si:HA, fabricated using RF-MS, to enhance bone cell growth. There is a lack of knowledge in terms of the mechanisms at which silicate-substituted HA reacts with biological cells. Also, gaining understanding of the process-structure-property interrelationship would enable increased control and better design of implants. Using commercially pure titanium (CpTi) substrates limits the variability of the results, therefore the fundamental knowledge gained could be applied further

afield on more complicated alloys normally used for orthopaedic implants such as Ti6Al4V.

The work investigated HA and 2 wt% Si-substituted HA with and without an inert and hard-wearing TiN barrier layer that were deposited on commercially pure Ti discs (10mm diameter) using RF magnetron sputtering. The coatings were produced using SiO₂ and HA targets in an Ar atmosphere and reactively sputtering Si target in an atmosphere that contained O₂ and Ar. The coatings were named according to their starting (target) material, namely, HA/TiN, Si:HA, Si:HA/TiN, and Si+O₂:HA/TiN. The as-deposited amorphous HA coatings were re-crystallised by placing the samples into alumina boats and annealing in Ar at 700°C for 2 h (sample sets 1 and 2) and 4 h (sample set 1). The 2nd sample set was prepared due to inadequate biological cell data from set 1. Due to differences in surface and bulk properties, a range of complementary near-surface (RHEED and XPS) and near-bulk characterisation (GA-XRD and SEM/EDX) techniques were used to characterise the biomaterials, followed by *in vitro* characterisation to assess the ability of the coatings to enhance cell growth and differentiation. Due to time constraints, a fast growing bone cancer cell line was used instead of a non-cancerous human-derived osteoblast cell line.

The hypotheses were: Si substitution of nanocrystalline stoichiometric HA is beneficial to bone-like cell growth and apposition, compared to unsubstituted

HA and; TiN acts as an effective barrier layer to prevent unwanted oxidation of Ti substrates and Ti-O scale formation upon high temperature annealing.

The investigation falls into a few themes, namely: 1. the microstructures of the as-deposited and annealed coatings; 2. assessing of the development and variable composition of the various HA layers as a result of annealing, with the challenge of separating real compositional variations from the limitations of each characterisation technique in analysing thin films; 3. analysis on the effectiveness of the TiN to prevent of Ti-O formation and preserving the structural integrity of HA; 4. composition and structure of the TiN diffusion barrier and its association with coating delamination; 5. assessment for silicate substitution into the HA lattice and most importantly; 6. Early cellular growth and maturation on the coatings may determine the long term life of the implant.

RF magnetron sputtering did produce amorphous HA coatings as confirmed by RHEED and XRD. SEM images exhibited smooth morphologies that follow the topography of the Ti. Possibly due to the low amount of substituents, Si was undetectable via all characterisation techniques, with the exception that Si clumps were identified via EDX using the BSE detector. A caveat, however, that that could have been residual polishing substance that was used during the preparation of Ti substrates prior to deposition.

The as-deposited TiN was amorphous (set 1) and led to crystallisation of TiN and Ti₂N upon annealing; as-deposited set 2 samples had crystalline TiN and did not form Ti₂N upon annealing. All Si-substituted TiN-containing samples annealed at 700°C for 2 h had delamination in set 1 whereas only Si:HA/TiN annealed for 2 h (set 2) had delaminated coatings, possibly due to difference in TCE and Si clumps acting as strain centres during annealing. Comparing the GA-XRD data of sets 1 and 2, it can be concluded that crystalline Ti₂N may be responsible for the higher chance for delamination, whereas crystalline TiN reduced the chance of delamination. Therefore efforts must be made to ensure that the deposition parameters produce crystalline TiN.

SEM/EDX found that the delamination was caused at the level of the TiN diffusion barrier; N was detected in the HA islands whereas only Ti and O were detected outside the HA islands. The delamination could have occurred perhaps due to the difference in thermal expansion coefficients between TiN and/or Ti₂N and Ti. Despite having delamination, GA-XRD for both sets showed that the TiN-containing samples had less Ti-O species formation compared to Si:HA. The Si:HA coating did not form islands and therefore the annealed coatings exhibited a floccular state. Possible residual SiO₂ from the substrate polishing stage and the possible presence of trace levels of O₂ during annealing may have aggravated the delamination and Ca/P ratios particularly in sample set 1. RHEED showed that annealed HA regardless of substitution had a mixed phase of small and large grains of HA and TiO₂. XPS high resolution spectra showed that the annealed samples may have HA, CaTiO₃, TiO₂, all of which are complementary to the GA-XRD results.

SEM/EDX showed an overall decrease in Ca/P from as-deposited coatings as a result of annealing – Ca(II) position of the HA lattice is loosely bound and may have evaporated. There are discrepancies between the Ca/P ratios obtained by XPS and EDX, possibly because the composition of Ca and P are different at the surface and at the bulk and/or the use of different relative sensitivity factors to calculate Ca and P atomic percentages. However both techniques registered a higher fluctuation in Ca/P ratios at longer annealing time points, signifying non-uniformity in density during the formation of crystalline coating.

The reactively sputtered Si in a Ar/O₂ atmosphere generated coatings with relatively less Ca and P compared to the other samples and rougher morphology. In particular to Si+O₂:HA/TiN, as a result of annealing, P levels were at times undetectable and therefore not ideal for cell growth.

There was tentative crystallographic and morphological evidence of Si incorporation into the HA lattice. GA-XRD showed that there were differences in relative intensities at the main HA peaks in annealed and dissolved Si-substituted samples compared to unsubstituted samples. Effect on island generation is Si substitution + Ti₂N > Si substitution + TiN > no substitution + TiN. As-deposited crystalline TiN with a preferred orientation at (111) may be effective at preventing rutile (TiO₂) formation. Si:HA/TiN that was annealed at 700°C for 2 h had a bulk Ca/P ratio that was close to

stoichiometric HA and consequently significantly enhanced MG63 cell growth compared to the Ti control but not mineralisation. Although insignificant, the same samples had higher average cell growth activity (DNA concentration) compared to Si:HA that was annealed for 2 h . The increased cell growth may be attributed to a combination of mixed HA/TiO₂ phase and scaffold-like topography, thereby supporting the mechanism that Si-substituted HA has an indirect effect on cell proliferation. In terms of delamination, HA/TiN annealed at 2 h and 4 h (set 1) detected morphological changes (SEM), increase in TiO₂ and disappearance of some HA main peaks with the appearance of other HA peaks after being dissolved in ddH₂O for 24 h . In the same dissolution conditions, HA/TiN 2 h (set 2) had little change in all peaks. The set 2 substituted samples that were dissolved had formation of TiO₂ and increase in existing TiO₂ peaks and increase in HA peaks especially at HA₂₁₁. Perhaps there is evidence of HA re-deposition. The TiN-containing samples had less TiO₂ peaks compared to Si:HA; this is tentative, however, as TiO₂ peaks could overlap with CaTiO₃. The project is proof-of-concept involving the potential of Si:HA/TiN as a biomaterial. Further studies and better process control are needed to inhibit delamination.

Chapter 8 Further Work

There are many directions which could be pursued in the future. A few of the most important ones will be described. Efforts need to be made to prevent the delamination of the HA coating. Processing parameters should be adjusted in order to only produce crystalline TiN, not amorphous TiN. The possible presence of embedded SiO₂ residues from the polishing medium used for substrate polishing, which contains Si, may have acted as strain centres and aggravated the delamination. It is recommended that chemo-mechanical polishing should no longer be used, as any polishing chemicals may be embedded into relatively soft metals, like CpTi¹⁶⁸, and the colloidal SiO₂ polishing suspension proved difficult to wash off. Perhaps alternative non-chemical polishing methods such as electropolishing¹⁶⁸ or laser ablation⁵⁹ should be considered. In the future the furnace should be attached to a mass spectrometer which would enable better monitoring and control of carrier gas levels within the furnace. Also, a vacuum furnace system could be used in the future to remove oxygen effectively from the tube furnace.

A range of annealing times and temperatures should be attempted. Concurrent heating and analysis could be performed to appraise the crystallisation and development of the HA layer by using scanning thermal atomic force microscopy or variable temperature XRD. Rietveld analysis is a feature that is performed on GA-XRD diffraction patterns to quantify the phase composition of the HA, in other words, to gauge any decrease in grain size which could indicate Si substitution¹³⁵. The *in vitro* cell work could use human osteoblast

cells (HOBs) as the metabolic activity resembles normal human cells, therefore more closely mimicking a real world environment.

An extended range of complementary characterisation techniques could be used in order to increase certainty of near-surface properties. Utilising Fourier Transform Infrared (FT-IR) spectrophotometric analysis as an additional tool may be beneficial in confirming the by-products or decomposition products of annealing such as CaTiO_3 and CaCO_3 , respectively³⁵. Perhaps Auger Electron Spectroscopy could be used as it was found to generate similar Ca/P ratios to EDX during the analysis of normal and osteoporotic rabbit bone⁸⁰. As dissolution behaviour is influenced by the medium¹⁶, simulated body fluid instead of ddH₂O could be used in the future. It may be important to know the concentration of dissolved ions in physiological fluid as it was theorised that cellular uptake occur whilst the ions are in solution³². An example test is use of a Ca probe³². Inductively Coupled Plasma could be used to measure Ca and P concentrations¹³¹. The Ca/P ratio of the dissolved products could be obtained via XPS as it may be more suitable for thin films and represents what the cells “see”¹⁵⁴.

Bond strength between HA and Ti is a requirement of implants as it ensures long-term cell adhesion to the implant^{17; 169}. Therefore perhaps after solving the issue of delamination, tests such as tensile testing that conforms to ASTM C-633 standards³³ could be performed in the coatings¹⁶⁹.

Chapter 9 References

- ¹ RATNER B.D. et al. **Biomaterials Science: An introduction to materials in medicine.** Elsevier Academic Press, 2004. 526

- ² FROST; SULLIVAN. World orthopedic devices market - Investment analysis and growth opportunities. 2007.

- ³ GEETHA M. et al. Ti based biomaterials, the ultimate choice for orthopaedic implants - A review. **Progress in Materials Science**, v. 54, n. 3, p. 397-425, 2009.

- ⁴ SHEPHERD J.H.; SHEPHERD D.V.; BEST S. M. Substituted hydroxyapatites for bone repair. **Journal of Materials Science: Materials in Medicine**, v. 23, p. 2335-2347, 2012.

- ⁵ FROST AND SULLIVAN. World orthopedic devices market - Investment analysis and growth opportunities. 2007.

- ⁶ MANTRIPRAGADA V.P. et al. An overview of recent advances in designing orthopedic and craniofacial implants. **Journal of Biomedical Materials Research Part A**, v. 101A, p. 3349-3364, 2013.

- ⁷ HUEBSCH N.; MOONEY D. J. Inspiration and application in the evolution of biomaterials. **Nature**, v. 462, n. 7272, p. 426-432, 2009.

- ⁸ NAG S.; BANERJEE R. Fundamentals of Medical Implant Materials. **ASM Handbook, Materials for Medical Devices**, v. 23, p. 6-17, 2012.

- ⁹ KINSELLA K. AND WAN H. An aging world: U.S. census bureau. **international population reports P95/09-1**, 2009.

- ¹⁰ TOMISA A. P. et al. Nanotechnology approaches to improve dental implants. **The International journal of oral & maxillofacial implants**, v. 26 Suppl, p. 25-44; discussion 45-9, 2011.

- ¹¹ BILLI F. et al. Metal wear particles: What we know, what we do not know, and why. **SAS J.**, v. 3, p. 133-142, 2009.

- ¹² LYNN, A. K.; DUQUESNAY, D. L. Hydroxyapatite-coated Ti-6Al-4V: Part 2: the effects of post-deposition heat treatment at low temperatures. **Biomaterials**, v. 23, n. 9, p. 1947-1953, 2002.

- ¹³ SCHMIDT C. et al. Scanning Electron Microscopy Study of Human Osteoblast Morphology on Five Orthopedic Metals,. **J Biomed Mater Res.**, v. 63, n. 3, p. 252-256, 2001.
- ¹⁴ CADOSCH D. et al. Metal is not inert: Role of metal ions released by biocorrosion in aseptic loosening – current concepts. **J. Biomed. Mater. Res. A.**, v. 91, n. 4, p. 1252-62, 2009.
- ¹⁵ WANG M.L.; SHARKEY P.F.; TUAN R.S. Particle bioreactivity and wear-mediated osteolysis. **J. Arthroplasty**, v. 19, n. 8, p. 1028-1038, 2004.
- ¹⁶ DUCHEYNE P.; QIU Q. Bioactive ceramics: the effect of surface reactivity on bone formation and bone cell function. **Biomaterials**, v. 20, n. 23–24, p. 2287-2303, 1999.
- ¹⁷ SURMENEV R.A.; SURMENEVA M.A.; A.A., I. Significance of calcium phosphate coatings for the enhancement of new bone osteogenesis – A review **Acta Biomaterialia**, v. 10, n. 2, p. 557–579, 2014.
- ¹⁸ THIAN E. S. et al. Silicon-substituted hydroxyapatite (SiHA): A novel calcium phosphate coating for biomedical applications. **Journal of Materials Science**, v. 41, n. 3, p. 709-717, 2006.
- ¹⁹ THIAN E.S et al. Silicon-substituted hydroxyapatite: The next generation of bioactive coatings. **Materials Science and Engineering: C**, v. 27, n. 2, p. 251–256, 2007.
- ²⁰ MAYRHOFER P. H. et al. A comparative study on reactive and non-reactive unbalanced magnetron sputter deposition of TiN coatings. **Thin Solid Films**, v. 415, n. 1–2, p. 151-159, 2002.
- ²¹ JEYACHANDRAN Y.L. et al. Properties of titanium nitride films prepared by direct current magnetron sputtering. **Materials Science and Engineering A**, v. 445-446, p. 233-236, 2006.
- ²² YANG Y.; KIM K. H.; ONG J. L. A review on calcium phosphate coatings produced using a sputtering process--an alternative to plasma spraying. **Biomaterials**, v. 26, n. 3, p. 327-37, Jan 2005.
- ²³ COMBES C.; REY C. Amorphous calcium phosphates: Synthesis, properties and uses in biomaterials. **Acta Biomaterialia**, v. 6, p. 3362–3378, 2010.

- ²⁴ BOYD A.R.; MEENAN B.J.; LEYLAND N.S. Surface characterisation of the evolving nature of radio frequency (RF) magnetron sputter deposited calcium phosphate thin films after exposure to physiological solution. **Surface and Coatings Technology**, v. 200, p. 6008-6013, 2006.
- ²⁵ VAN DIJK K. et al. Influence of annealing temperature on RF magnetron sputtered calcium phosphate coatings. **Biomaterials**, v. 17, p. 405-410, 1996.
- ²⁶ BOYD A.R., B. G. A., DUFFY H., CAIRNS M.L., O'HARE P., MEENAN B.J.,. Characterisation of calcium phosphate/titanium dioxide hybrid coatings. **Journal of Materials Science: Materials in Medicine**, v. 19, p. 485-498, 2008.
- ²⁷ ROŞU R. A. et al. Deposition of titanium nitride and hydroxyapatite-based biocompatible composite by reactive plasma spraying. **Applied Surface Science**, v. 258, n. 8, p. 3871-3876, 2012.
- ²⁸ BOYD A.R. et al. Characterisation of calcium phosphate/titanium dioxide hybrid coatings. **Journal of Materials Science: Materials in Medicine**, v. 19, n. 2, p. 485-498, 2013.
- ²⁹ GERSTEN J.I.; SMITH F.W. The Physics and Chemistry of Materials: John Wiley & Sons 2001.
- ³⁰ BÄCHLE M.; KOHAL R.J. A systematic review of the influence of different titanium surfaces on proliferation, differentiation and protein synthesis of osteoblast-like MG63 cells. **Clinical Oral Implants Research**, v. 15, p. 683-692, 2004.
- ³¹ SCHWARTZ Z.; BOYAN B.D. Underlying mechanisms at the bone-biomaterial interface. **Journal of Cellular Biochemistry**, v. 56, p. 340-347, 1994.
- ³² HOPPE A.; GÜLDAL N.S.; BOCCACCINI A.R. A review of the biological response to ionic dissolution products from bioactive glasses and glass-ceramics. **Biomaterials**, v. 32, n. 11, p. 2757-2774, 2011.
- ³³ MOHSENI E.; ZALNEZHAD E.; BUSHROA A.R. Comparative investigation on the adhesion of hydroxyapatite coating on Ti-6Al-4V implant: A review paper. **International Journal of Adhesion & Adhesives**, v. 48, p. 238-257, 2014.

- 34 BAILEY M.J. et al. Accurate determination of the Ca:P Ratio in rough hydroxyapatite samples by SEM/EDX, PIXE and RBS – A comparative study. **X-ray Spectrometry**, v. 38, p. 343-347, 2009.
- 35 OKAUCHI-YABUUCHI M. et al. Chemical Analysis of a Novel Coating Material, CaTiO₃-aC. **J. Hard Tissue Biol.**, v. 17, n. 3, p. 115-120, 2008 2008.
- 36 EDWARDS H.K. et al. An Appraisal of ultramicrotomy, FIBSEM and cryogenic FIBSEM techniques for the sectioning of biological cells on titanium substrates for TEM investigation. **J. Microsc.**, v. 234, p. 16-25, 2009.
- 37 BAUER S. et al. Engineering biocompatible implant surfaces: Part I: Materials and surfaces. **Progress in Materials Science**, v. 58, n. 3, p. 261–326, 2013.
- 38 XI Y.; FAN H.; LIU W. The effect of annealing treatment on microstructure and properties of TiN films prepared by unbalanced magnetron sputtering. **Journal of Alloys and Compounds**, v. 496, n. 1-2, p. 695-698, 2010. ISSN 0925-8388.
- 39 SCHMIDT C. et al. A Scanning Electron Microscopy Study of Human Osteoblast Morphology on Five Orthopedic Metals. **J Biomed Mater Res.**, v. 63, n. 3, p. 252-256, 2001.
- 40 BOHNER M. Calcium orthophosphates in medicine: from ceramics to calcium phosphate cements. **Injury**, v. 31, Supplement 4, n. 0, p. D37-D47, 12// 2000.
- 41 ALBERTS B. et al. Cellular Communities: Tissues, Stem Cells, and Cancer. In: (Ed.). **Essential Cell Biology**. 3: Garland Science, 2010. p.694-696.
- 42 CARLISLE E. M. Silicon: A Possible Factor in Bone Calcification. **Science**, v. 167, n. 3916, p. 279-280, 1970.
- 43 THIAN E.S., H. J., BEST S.M., BARBER Z.H., BONFIELD W.,. Silicon-substituted hydroxyapatite: The next generation of bioactive coatings. **Materials Science and Engineering: C**, v. 27, n. 2, p. 251–256, 2007.
- 44 ERGUN C. et al. Increased osteoblast adhesion on nanograined hydroxyapatite and tricalcium phosphate containing calcium titanate. **J Biomed Mater Res A**, v. 80, n. 4, p. 990-7, Mar 15 2007.

- 45 VANDROVCOVA M. et al. Effect of different surface nanoroughness of titanium dioxide films on the growth of human osteoblast-like MG63 cells. **J Biomed Mater Res A**, v. 100, n. 4, p. 1016-32, Apr 2012. ISSN 1549-3296.
- 46 KURTZ SM.; DEVINE JN. PEEK biomaterials in trauma, orthopedic, and spinal implants. **Biomaterials**, v. 28, p. 4845-4869, 2007.
- 47 CIOBANU G. et al. SEM and EDX studies of bioactive hydroxyapatite coatings on titanium implants. **Micron.**, v. 40, p. 143–146, 2009.
- 48 RHO J.-Y. Mechanical Properties of Hard Tissues. In: (Ed.). **Encyclopedia of Materials: Science and Technology**: Elsevier Science Ltd, 2001. p.3722-3728.
- 49 AUGAT P.; SCHORLEMMER S. The role of cortical bone and its microstructure in bone strength. **Age and Ageing**, v. 35, n. suppl 2, p. ii27-ii31, 2006.
- 50 CURREY J. Incompatible mechanical properties in bone. **J. Exp. Biol.** , v. 231, p. 569-580, 2004.
- 51 NUSS K.M.R.; B., V. R. Biocompatibility issues with modern implants in bone - A review for clinical orthopedics. **The Open Orthopaedics Journal**, v. 2, p. 66-78, 2008.
- 52 TOWNSEND, P. R. et al. Structure and function of the human patella: The role of cancellous bone. **Journal of Biomedical Materials Research**, v. 10, n. 4, p. 605-611, 1976.
- 53 RHO J.Y.; KUHN-SPEARING L.; ZIUPOS P. Mechanical properties and the hierarchical structure of bone. **Medical Engineering and Physics** v. 20, p. 92-102, 1998.
- 54 RHO J.Y.; KUHN-SPEARING L.; P., Z. Mechanical properties and the hierarchical structure of bone. **Medical Engineering and Physics** v. 20, p. 92-102, 1998.
- 55 NUSS K.M.R.; VON RECHENBERG B. Biocompatibility issues with modern implants in bone - A review for clinical orthopedics. **The Open Orthopaedics Journal**, v. 2, p. 66-78, 2008.
- 56 ANIL S. et al. Dental Implant Surface Enhancement and Osseointegration. In: TURKYILMAZ, P. I. (Ed.). **Implant Dentistry - A Rapidly Evolving Practice**, 2011. ISBN 978-953-307-658-4.

- 57 OKAUCHI-YABUUCHI M. et al. Chemical Analysis of a Novel Coating Material, CaTiO₃-aC. **Journal of Hard Tissue Biology**, v. 17, n. 3, 2008.
- 58 ZHAO G. et al. High surface energy enhances cell response to titanium substrate microstructure. **Journal of Biomedical Materials Research Part A**, v. 74A, n. 1, p. 49-58, 2005.
- 59 GYÖRGYEY Á. et al. Attachment and proliferation of human osteoblast-like cells (MG-63) on laser-ablated titanium implant material. **Materials Science and Engineering: C**, v. 33, n. 7, p. 4251-4259, 2013.
- 60 KIESWETTER K. et al. Surface roughness modulates the local production of growth factors and cytokines by osteoblast-like MG-63 cells. **J Biomed. Mater. Res.**, v. 32, n. 1, p. 55-63, 1996.
- 61 GOEL M. et al. **Biological aspects of dental implant; Current knowledge and perspectives in oral implantology.** 2013..
- 62 BOHNER M. Silicon-substituted Calcium Phosphates - A Critical Review. **Biomaterials**, v. 30, p. 6403-6406, 2009.
- 63 A.D.A.M. MEDICAL ENCYCLOPEDIA. Osteomalacia.
<<http://www.nlm.nih.gov/medlineplus/ency/article/000376.htm>>.
- 64 _____. Alzheimer's Disease. 30 August 2013
<<http://vsearch.nlm.nih.gov/vivisimo/cgi-bin/query-meta?v%3Aproject=medlineplus&query=alzheimer&x=0&y=0>>
- 65 BROWN P.D.; EDWARDS H.K.; M.W., F. Microscopy at the life sciences / physical sciences interface. 2010.
- 66 EVIS Z.; WEBSTER T. J. Nanosize hydroxyapatite: doping with various ions. **Advances in Applied Ceramics**, v. 110, n. 5, p. 311-321, 2011.
- 67 NIRMALA R. et al. Characterisation of bioresourced hydroxyapatite containing silver nanoparticles. **Materials Research Innovations**, v. 16, n. 4, p. 249-256, 2012.
- 68 BANSIDDHI A. et al. Porous NiTi for bone implants: A review. **Acta Biomaterialia**, v. 4, n. 4, p. 773-782, 2008..

- 69 TAMPIERI A. et al. Characteristics of synthetic hydroxyapatites and attempts to improve their thermal stability. **Materials Chemistry and Physics**, v. 64, n. 1, p. 54-61, 2000.
- 70 XU J.L.; KHOR K.A. Chemical analysis of silica doped hydroxyapatite biomaterials consolidated by a spark plasma sintering method. **J. Inorg. Biochem.**, v. 101, p. 187-195, 2006.
- 71 YONGGANG Y. et al. The influence of discharge power and heat treatment on calcium phosphate coatings prepared by RF magnetron sputtering deposition **Journal of Materials Science. Materials in Medicine**, v. 18, n. 6, p. 1061-1069, 2007.
- 72 LIU H. et al. An in vitro evaluation of the Ca/P ratio for the cytocompatibility of nano-to-micron particulate calcium phosphates for bone regeneration. **Acta Biomaterialia**, v. 4, n. 5, p. 1472-1479, 2008.
- 73 NORTON J. et al. Recent developments in processing and surface modification of hydroxyapatite. **Advances in Applied Ceramics**, v. 105, n. 3, p. 113-139, 2006.
- 74 DUFEK M. **Quanta 3D FEG user operation manual**. FEI company, 2008.
- 75 BROWN P.W.; CONSTANTZ B. Hydroxyapatite and Related Materials. In: R.Z., L. (Ed.). **Biological and synthetic apatites**: London, 1994.
- 76 THIAN E. S. et al. Silicon-substituted hydroxyapatite: The next generation of bioactive coatings. **Materials Science and Engineering: C**, v. 27, n. 2, p. 251-256, 2007.
- 77 LEGEROS R. Z. Biological and synthetic apatites. In: BROWN P. W. e B., C. (Ed.). **Hydroxyapatite and Related Materials**. USA: CRC Press, 1994.
- 78 HUGHES J.M.; CAMERON M.; CROWLEY K.D. Structural variations in natural F, OH and Cl apatites. **American Mineralogist**, v. 74, p. 870-876, 1989.
- 79 KAABAR W. et al. Metal deposition at the bone–cartilage interface in articular cartilage. **Applied Radiation and Isotopes**, v. 67, n. 3, p. 475-479, 2009.
- 80 KOURKOUMELIS N.; BALATSOUKAS I.; TZAPHLIDOU M. Ca/P concentration ratio at different sites of normal and osteoporotic rabbit bones evaluated by

Auger and energy dispersive X-ray spectroscopy. **J Biol Phys**, v. 38, n. 2, p. 279-91, Mar 2012.

- 81 CUSHNIE E. K.; KHAN Y. M.; LAURENCIN C. T. Amorphous hydroxyapatite-sintered polymeric scaffolds for bone tissue regeneration: Physical characterization studies. **Journal of Biomedical Materials Research Part A**, v. 84A, n. 1, p. 54-62, 2008.
- 82 DURDU S. et al. Characterization and formation of hydroxyapatite on Ti6Al4V coated by plasma electrolytic oxidation. **Journal of Alloys and Compounds**, v. 551, n. 0, p. 422-429, 2013.
- 83 FURUZONO T.; SONODA K.; TANAK J. A hydroxyapatite coating covalently linked onto a silicone implant material. **J Biomed Mater Res**, v. 56, n. 1, p. 9-16, Jul 2001.
- 84 KOCH C.F. et al. Pulsed laser deposition of hydroxyapatite thin films. **Materials Science and Engineering C**, v. 27, p. 484-494, 2007.
- 85 REFFITT D. M. et al. Orthosilicic acid stimulates collagen type 1 synthesis and osteoblastic differentiation in human osteoblast-like cells in vitro. **Bone**, v. 32, n. 2, p. 127-135, 2003.
- 86 CARLISLE E. M. Silicon: A requirement in bone formation independent of vitamin D1. **Calcified Tissue International**, v. 33, n. 1, p. 27-34, 1981.
- 87 GOUGH J. E.; JONES J. R.; HENCH L. L. Nodule formation and mineralisation of human primary osteoblasts cultured on a porous bioactive glass scaffold. **Biomaterials**, v. 25, n. 11, p. 2039-46, 2004.
- 88 PORTER A. E. et al. Comparison of in vivo dissolution processes in hydroxyapatite and silicon-substituted hydroxyapatite bioceramics. **Biomaterials**, v. 24, n. 25, p. 4609-4620, 11// 2003. ISSN 0142-9612. < <http://www.sciencedirect.com/science/article/pii/S0142961203003557> >.
- 89 LI P. et al. The role of hydrated silica, titania, and alumina in inducing apatite on implants. **Journal of Biomedical Materials Research**, v. 28, n. 1, p. 7-15, 1994. ISSN 1097-4636. < <http://dx.doi.org/10.1002/jbm.820280103> >.
- 90 XU J.L.; KHOR K.A. Chemical analysis of silica doped hydroxyapatite biomaterials consolidated by a spark plasma sintering method. **Journal of Inorganic Biochemistry**, v. 101, p. 187-195, 2007.

- 91 RIBEIRO C.C.; GIBSON I.; BARBOSA M.A. The uptake of titanium ions by hydroxyapatite particles - structural changes and possible mechanisms. **Biomaterials**, v. 27, p. 1749-1761, 2006.
- 92 THIAN E.S., H. J., BEST S.M., BARBER Z.H., BONFIELD W.,. Magnetron co-sputtered silicon-containing hydroxyapatite thin films—an in vitro study. v. 26, n. 16, p. 2947–2956, June 2005 2005. < <http://dx.doi.org/10.1016/j.biomaterials.2004.07.058> >.
- 93 KIVITZ E. et al. Influence of processing parameters on microstructure and biocompatibility of surface laser sintered hydroxyapatite–SiO₂ composites. **Journal of Biomedical Materials Research Part B: Applied Biomaterials**, v. 101B, n. 4, p. 568-575, 2013.
- 94 BOTELHO C. M. et al. Effect of protein adsorption onto the dissolution of silicon-substituted hydroxyapatite **Journal of Encapsulation and Adsorption Sciences**, v. 1, n. 4, p. 72-79, 2011.
- 95 ALBAYRAK O.; EL-ATWANI O.; ALTINTAS S. Hydroxyapatite coating on titanium substrate by electrophoretic deposition method: Effects of titanium dioxide inner layer on adhesion strength and hydroxyapatite decomposition. **Surface and Coatings Technology**, v. 202, n. 11, p. 2482–2487, 2008.
- 96 HÄMMERLE H. et al. Biostability of micro-photodiode arrays for subretinal implantation. **Biomaterials**, v. 23, n. 3, p. 797-804, 2002.
- 97 MARTÍNEZ-MARTÍNEZ D. et al. Exploring the benefits of depositing hard TiN thin films by non-reactive magnetron sputtering. **Applied Surface Science**, v. 275, p. 121-126, 2013.
- 98 KELLY P. J.; ARNELL R. D. Magnetron sputtering: a review of recent developments and applications. **Vacuum**, v. 56, n. 3, p. 159-172, 2000.
- 99 ALAMI J.; S., B.; SAKINOS K. High power pulsed magnetron sputtering: Fundamentals and applications. **Journal of Alloys and Compounds**, v. 483, n. 1–2, p. 530–534, 2009.
- 100 WOLKE J.G.C. et al. Study of the surface characteristics of magnetron-sputter calcium phosphate coatings. **Journal of Biomedical Materials Research**, v. 28, 1994.
- 101 TEER COATINGS LTD. Coating Deposition With The Closed Field Unbalanced Magnetron Sputter Ion Plating System From Teer Coatings For The Production Of Dense, Hard Coatings. 2013.

- 102 TAYLOR B.; WEIDMANN E. Metallographic preparation of titanium. **Struers Application Notes** 2008.
- 103 BALL M. et al. The effect of different surface morphology and roughness on osteoblast-like cells. **Journal of Biomedical Materials Research A**, v. 86, n. 3, p. 637-647, 2008.
- 104 ROHDE S.L. **Sputter Deposition**. Materials Park, Ohio: 1994.
- 105 COMBES C.; REY C. Amorphous calcium phosphates: Synthesis, properties and uses in biomaterials. **Acta Biomaterialia**, v. 6, p. 3362-3378, 2010.
- 106 KRUMEICH F. Bragg's law of diffraction. **Electron microscopy**, 2011.
- 107 CULLITY B.D.; STOCK S. R. **Elements of X-ray diffraction**. 3rd. New Jersey, USA: Prentice Hall, 2001.
- 108 BROWN P.D. Structural Characterization. In: KASSAP S., C. P. (Ed.). **Springer handbook of Electronic and Photonic Materials** Springer 2006. p.345-373.
- 109 NORAN INSTRUMENTS. **Energy-dispersive X-ray microanalysis: An introduction**. Middleton, Wisconsin, USA: NORAN Instruments, 1999.
- 110 GOLDSTEIN J. et al. **Scanning electron microscopy and X-ray microanalysis**. Kluwer Academic / Plenum Publishers, 2003.
- 111 OXFORD INSTRUMENTS NANOANALYSIS. An introduction to energy-dispersive and wavelength-dispersive X-ray microanalysis. **Microscopy and Analysis**, v. 20, n. 4, p. S5-S8, 2006.
- 112 INSTRUMENTS, O. **INCA Energy: Operator Manual** High Wycombe, U.K.: Oxford Instruments Analytical, 2006.
- 113 ASTM. Standard guide for quantitative analysis by energy-dispersive spectroscopy. **ASTM International**, 1998 (2008).
- 114 SMITH G.C. **Surface analysis by electron spectroscopy: Measurement and interpretation**. 1994.
- 115 CASA, S. L. Casa XPS manual 2.3.15. 2009. URL: <
http://www.casaxps.com/help_manual/ >.

- 116 WILLIAMS D. B.; CARTER C. B. **Transmission Electron Microscopy: A textbook for material science**. USA: Springer, 1996.
- 117 MARLAFEKA S. et al. A structural study of phase transitions within GaN layers grown by low-temperature molecular beam epitaxy. **Journal of Crystal Growth**, v. 230, n. 3–4, p. 415–420, 2001.
- 118 BROWN P.D. Structural Characterization. In: KASSAP S., C. P. (Ed.). **Springer handbook of Electronic and Photonic Materials**: Springer, 2006. p.345-373.
- 119 BYTH H.-A. et al. Assessment of a Simple, Non-toxic Alamar Blue Cell Survival Assay to Monitor Tomato Cell Viability. **Phytochemical Analysis**, v. 12, p. 340-346, 2001.
- 120 LABARCA C.; K., P. A simple, rapid, and sensitive DNA assay procedure. **Analytical Biochemistry**, v. 102, p. 344-352, 1980.
- 121 BRAET, F.; DE ZANGER, R.; WISSE, E. Drying cells for SEM, AFM and TEM by hexamethyldisilazane: a study on hepatic endothelial cells. **Journal of Microscopy**, v. 186, n. 1, p. 84-87, 1997.
- 122 PAL S.; ROY S.; BAG S. Hydroxyapatite coating over Alumina – Ultra High Molecular Weight Polyethylene Composite Biomaterials. **Trends Biomater. Artif. Organs**, v. 18, n. 2, 2005.
- 123 VAN DIJK K. et al. Study of the influence of oxygen on the composition of thin films obtained by R.F. sputtering from a $\text{Ca}_5(\text{PO}_4)_3\text{OH}$ target. **Thin Solid Films**, v. 304, n. 1-2, p. 191-195, 1997.
- 124 THIAN E.S. et al. Novel silicon-doped hydroxyapatite (Si-HA) for biomedical coatings: An in vitro study using acellular simulated body fluid. **Journal of Biomedical Materials Research Part B: Applied Biomaterials**, v. 76, n. 2, p. 326-333, 2006.
- 125 PETROV I. et al. Mass and energy resolved detection of ions and neutral sputtered species incident at the substrate during reactive magnetron sputtering of Ti in mixed Ar+N₂ mixtures. **Journal of Vacuum Science and Technology A**, 1994.
- 126 OHTSU N. et al. Calcium phosphates formation on CaTiO₃ coated titanium. **Journal of Materials Science**, v. 18, n. 6, p. 1009-1016, 2007.

- 127 NAUMKIN A. V. et al. **NIST X-ray Photoelectron Spectroscopy Database, Version 4.1 (National Institute of Standards and Technology, Gaithersburg) 2012.**
- 128 KIESWETTER K., S. Z., HUMMERT T.W., COCHRAN D.L., SIMPSON J., DEAN D.D., BOYAN B.D. Surface roughness modulates the local production of growth factors and cytokines by osteoblast-like MG-63 cells. **J Biomed. Mater. Res.**, v. 32, n. 1, p. 55-63, 1996.
- 129 HONG Z. et al. Crystalline hydroxyapatite thin films produced at room temperature — An opposing radio frequency magnetron sputtering approach. **Thin Solid Films**, v. 515, n. 17, p. 6773–6780, 2007.
- 130 YANG S. et al. **Investigation of substoichiometric titanium nitride grown by unbalanced magnetron sputtering.** 2nd Asian-European International Conference on Plasma surface Engineering. Beijing (China): Surface and Coatings Technology, 2000. 228-233 p.
- 131 YONGGANG Y. et al. In vitro evaluation of different heat-treated radio frequency magnetron sputtered calcium phosphate coatings. **Clinical Oral Implants Research**, v. 18, p. 345-353, 2007.
- 132 ERGUN C.; DOREMUS R.H.; LANFORD W.A. Interface reaction/diffusion in hydroxylapatite-coated SS316L and CoCrMo alloys. **Acta Mater.**, v. 52, p. 4767-4772, 2004.
- 133 LONG J. et al. Reactive Plasma-Aided RF Sputtering Deposition of Hydroxyapatite Bio-implant Coatings. **Chemical Vapor Deposition**, v. 13, n. 6-7, p. 299-306, 2007.
- 134 BANG L.T.; ISHIKAWA K.; OTHMAN R. Effect of silicon and heat-treatment temperature on the morphology and mechanical properties of silicon - substituted hydroxyapatite. **Ceramics International**, v. 37, n. 8, p. 3637–3642, 2011.
- 135 ARCOS D. et al. Crystallochemistry, textural properties, and in vitro biocompatibility of different silicon-doped calcium phosphates. **Journal of Biomedical Materials Research Part A**, v. 78A, n. 4, p. 762-771, 2006.
- 136 TARNIOWY A.; MANIA R.; REKAS M. The effect of thermal treatment on the structure, optical and electrical properties of amorphous titanium nitride thin films. v. 311, n. Issues 1–2, p. 93–100, 1997.

- 137 VADIRAJ A.; KAMARAJ M. Fretting fatigue studies of titanium nitride-coated biomedical titanium alloys. **Journal of Materials Engineering and Performance**, v. 15, n. 5, p. 553-557, 2006.
- 138 INAGAKI M.; YOKOGAWA Y.; KAMEYAMA T. Bond strength improvement of hydroxyapatite/titanium composite coating by partial nitriding during RF-thermal plasma spraying. **Surface and Coatings Technology**, v. 173, n. 1, p. 1-8, 2003.
- 139 KUMARI N. et al. Correlations of plasma parameters and properties of magnetron sputtered TiN films. **The European Physical Journal Applied Physics**, v. 59, p. 20302p1-20302p7, 2012.
- 140 KURU Y. et al. Coefficients of thermal expansion of thin metal films investigated by non-ambient X-ray diffraction stress analysis. **Surface and Coatings Technology**, v. 202, n. 11, p. 2306–2309, 2008.
- 141 EL-RAGHY T. et al. Processing and Mechanical Properties of Ti₃SiC₂: II, Effect of Grain Size and Deformation Temperature. **Journal of the American Ceramic Society**, v. 82, n. 10, p. 2855-2860, 1999.
- 142 COE S.C. **The deposition, characterisation and biocompatibility of hydroxyapatite and silicon doped hydroxyapatite thin film coatings for orthopaedic applications**. PhD thesis, University of Nottingham. 2008.
- 143 THIAN E.S. et al. Magnetron co-sputtered silicon-containing hydroxyapatite thin films—an in vitro study. **Biomaterials**, v. 26, p. 2947-2956, 2005.
- 144 SURMENEVA M.A. et al. The structure of an RF-magnetron sputter-deposited silicate-containing hydroxyapatite-based coating investigated by high-resolution techniques. **Surface and Coatings Technology**, v. 218, n. 0, p. 39-46, 2013.
- 145 GERSTEN J.I., S. F. W. **The Physics and Chemistry of Materials**. Wiley, 2001. 856 ISBN 978-0-471-05794-9.
- 146 TADA H. et al. Thermal expansion coefficient of polycrystalline silicon and silicon dioxide thin films at high temperatures. **Journal of Applied Physics**, v. 87, n. 9, p. 4189-4193, 2000.

- 147 SPREADBOROUGH J.; CHRISTIAN J. W. The Measurement of the Lattice Expansions and Debye Temperatures of Titanium and Silver by X-ray Methods. 1959.
- 148 SHACKELFORD J.F.; ALEXANDER W. **CRC Materials Science and Engineering Handbook, Third Edition.** 2013. .
- 149 SHAKHVOROSTOV D.; MÜSER M.H. Effect of dopant size and dopant concentration on the crystallization pressure of phase change materials: The role of local order and non-local interactions. **EPL (Europhysics letters)**, v. 93, n. 3, p. 5, 2011.
- 150 BOYD A.R. et al. Sputter deposition of calcium phosphate/titanium dioxide hybrid thin films. **Materials Science and Engineering C**, v. 28, n. 2, p. 228–236, 2008.
- 151 SRIRAM S. et al. Influence of oxygen partial pressure on the composition and orientation of strontium-doped lead zirconate titanate thin films. **Micron**, v. 40, n. 1, p. 104-108, 2009.
- 152 ZHAO G. et al. High surface energy enhances cell response to titanium substrate microstructure. **Journal of Biomedical Materials Research Part A**, v. 74A, n. 1, p. 49-58, 2005.
- 153 FURUZONO T.; SONODA K.; TANAKA J. A hydroxyapatite coating covalently linked onto a silicone implant material. **Journal of Biomedical Materials Research**, v. 56, n. 1, p. 9-16, 2000.
- 154 LU H.B. et al. Surface Characterization of Hydroxyapatite and Related Calcium Phosphates by XPS and TOF-SIMS. **Analytical Chemistry**, v. 72, n. 13, p. 2886-2894, 2000.
- 155 WEBSTER T.J. et al. Increased osteoblast adhesion on titanium-coated hydroxylapatite that forms CaTiO₃. **Journal of Biomedical Materials Research Part A**, v. 67A, n. 3, p. 975-980, 2003.
- 156 NEVES M.I.B. et al. Surface chemistry of cement pastes: a study by x-ray photoelectron spectroscopy. **Surface and Interface Analysis**, v. 33, n. 10-11, p. 834-841, 2002.
- 157 COE, S. C. **The deposition, characterisation and biocompatibility of hydroxyapatite and silicon doped hydroxyapatite thin film coatings for orthopaedic applications.** PhD thesis, University of Nottingham. 2008.

- 158 RAMPERSAD S.N. Multiple Applications of Alamar Blue as an Indicator of Metabolic Function and Cellular Health in Cell Viability Bioassays. **Sensors**, v. 12, p. 12347-12360, 2012.
- 159 NG K.W.; LEONG D.T.; HUTMACHER D.W. The challenge to measure cell proliferation in two and three dimensions. **Tissue Engineering**, v. 11, n. 1-2, p. 182-191, 2005.
- 160 BALL M. et al. The effect of different surface morphology and roughness on osteoblast-like cells. **Journal of Biomedical Materials Research A**, v. 86, n. 3, p. 637-647, 2008.
- 161 RAMIRES PA. et al. The influence of titania/hydroxyapatite composite coatings on in vitro osteoblasts behaviour. **Biomaterial**, v. 22, n. 12, p. 1467-1474, 2001.
- 162 RAUSCH-FAN X. et al. Differentiation and cytokine synthesis of human alveolar osteoblasts compared to osteoblast-like cells (MG63) in response to titanium surfaces. **Dental Materials**, v. 24, n. 1, p. 102-110, 2008.
- 163 CLOVER J.; GOWEN M. Are MG-63 and HOS TE85 Human Osteosarcoma Cell Lines Representative Models of the Osteoblastic Phenotype? **Bone**, v. 15, n. 6, p. 585-591, 1994.
- 164 BAUER S. et al. Engineering biocompatible implant surfaces Part I: Materials and surfaces. **Progress in Materials Science**, v. 58, p. 261-326, 2013.
- 165 FRISKEN K.W. et al. A study of titanium release into body organs following the insertion of single threaded screw implants into the mandibles of sheep. **Australian Dental Journal**, v. 47, n. 3, p. 214-217, 2002.
- 166 PORTER A.E. et al. Comparison of in vivo dissolution processes in hydroxyapatite and silicon-substituted hydroxyapatite bioceramics. **Biomaterials**, v. 24, p. 4609-4620, 2003.
- 167 ZENG H., L. W. R. The study of surface transformation of pulsed laser deposited hydroxyapatite coatings **Journal of Biomedical Materials Research**, v. 50, n. 2, p. 239-247, 2000.
- 168 BRUNETTE D. M. et al. **Titanium in Medicine: Material Science, Surface Science, Engineering, Biological Responses and Medical Applications (Engineering Materials)**. Germany: Springer, 2001.

- 169 INAGAKI M.; YOKOGAWA Y.; KAMEYAMA T. Bond strength improvement of hydroxyapatite/titanium composite coating by partial nitriding during RF-thermal plasma spraying. **Surface and Coatings Technology**, v. 173, n. 1, p. 1–8, 2003.

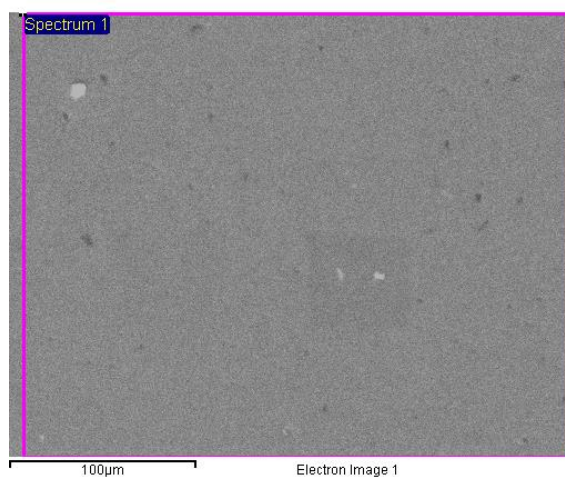
Chapter 10 Appendix

Table 10-1 The modified protocol combined the in-house method and that of Struers in order to successfully remove colloidal silica polishing liquid from the Ti substrates.

In-house protocol used	Modified Protocol
G: 7 grits (P240 – P4000) P: Colloidal Si C: 10 min in acetone (2X), rinse with water, 10 min IMS, 10 min ddH ₂ O, dried in hot air. Ra =37± 10 nm Lots of colloidal silica (CoSi) residues, marks on discs. Cleaning time: 50 mins	G: Unmodified P: Added 10%H ₂ O ₂ Cleaning: 1. 10 min acetone 2. Rinse with ddH ₂ O 3. 1 min ddH ₂ O and concentrated soap solution 4. Rinse with water 5. 1 min with isopropanol 6. Wiped with acetone and cotton wool 7. Rinse in IPA. 8. Dry with hot air. Less marks, no CoSi detected via SEM/EDX Cleaning time = 30 mins

Polishing method

a)



b)

Element	Weight%	Atomic%
Ti K	100.00	100.00
Totals	100.00	

c)

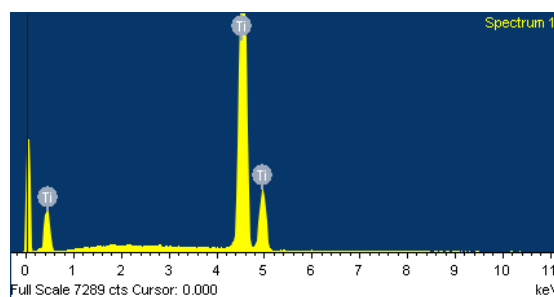


Figure 10-1 EDX of polished Ti substrate showing no evidence of the polishing agent, colloidal silica a) SE image; b) Wt% and At% readings and c) EDX spectrum

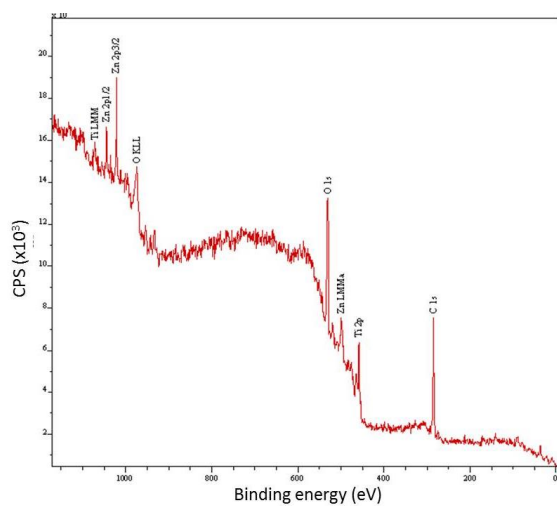


Figure 10-2 XPS of polished Ti. Presence of trace levels of C and Zn.

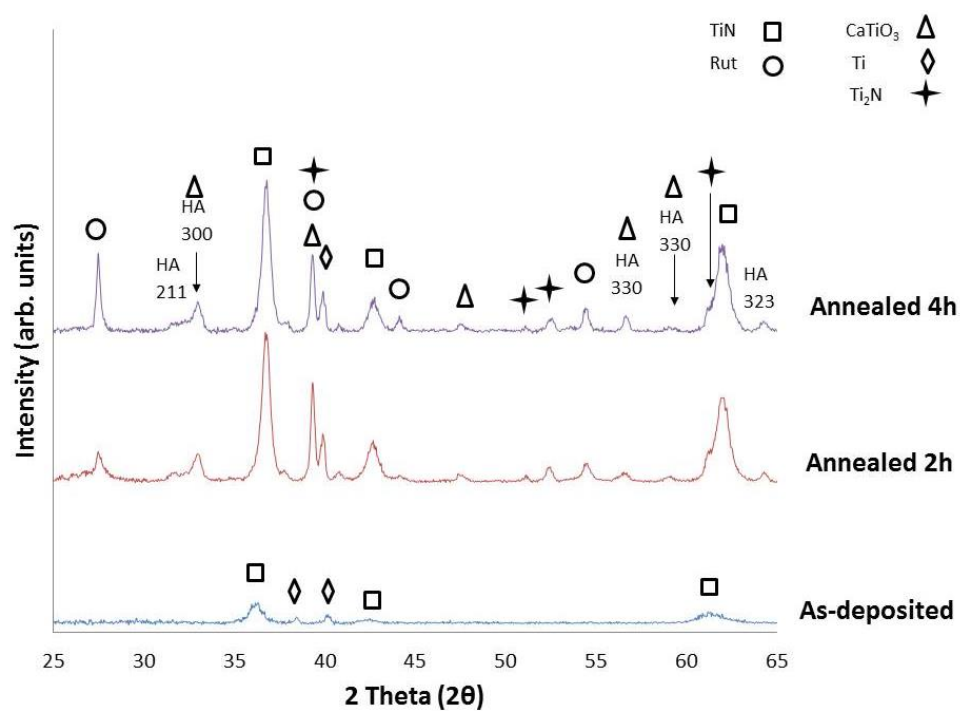
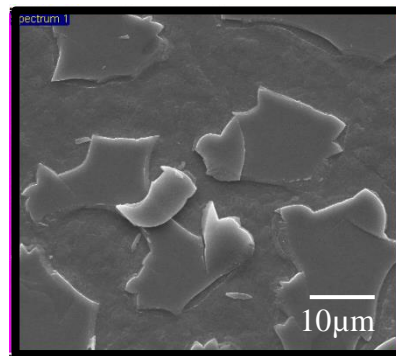
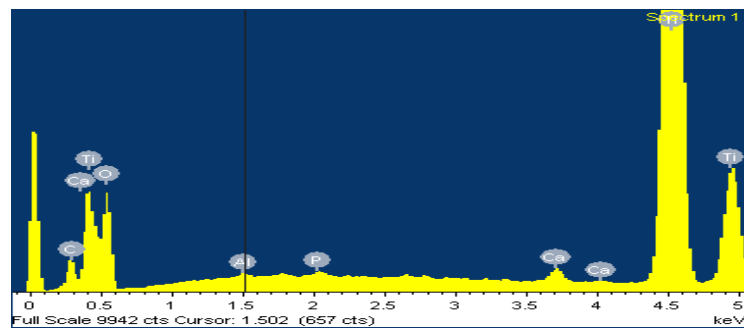


Figure 10-3 XRD of Si:HA/TiN annealed for 2 h and 4 h

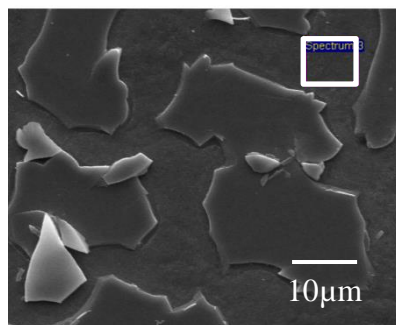
a)



b)



c)



d)

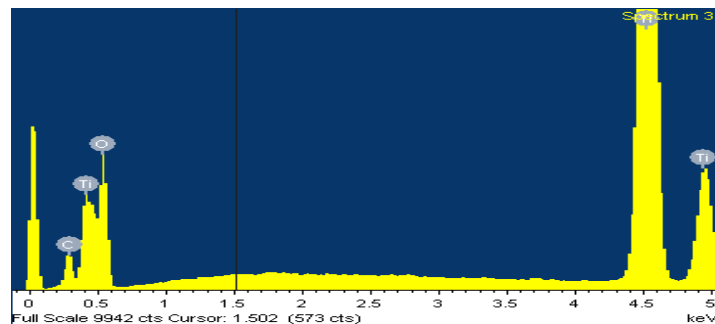


Figure 10-4 Representative EDX analysis of the non-island of delaminated annealed samples. (a) black box on the SEM image depicts the area at which EDX data was obtained and b) the resulting spectrum that presence of HA, Ti and N but no Si. c) White box on the SEM imaged depicts the area at which EDX data was obtained and d) the resulting spectrum that confirms Ti and O. Note the absence of Si.

Table 10-2 XPS - raw data of all samples

XPS			
Coating/Treatment	Ca/P	Ca at%	P at%
ha tin unannealed	1.81	13.6	7.53
ha tin unannealed	1.71	19.5	11.42
ha tin 2h	2.43	14.96	6.16
ha tin 4h	3.82	8.18	2.14
ha tin 4h	15.53	20.04	1.29
ha tin 4h	2.26	8.13	3.59
si ha unannealed	1.75	19.54	11.18
si ha unannealed	1.52	19.05	12.55
si ha 2h	3.23	11.69	3.62
si ha 2h	2.34	13.36	5.71
si ha 4h	4.05	10.48	2.59
si ha 4h	0.00	0.38	0
si ha 4h	1.72	17.57	10.22
si ha tin unannealed	1.91	18.06	9.48
si ha tin unannealed	1.83	17.8	9.72
si ha tin 2h	2.32	13.94	6.02
si ha tin 2h	0.00	0.55	0
si ha tin 4h	3.24	9.07	2.08
si ha tin 4h	2.51	10.62	4.23
si+o2 unannealed	1.85	17.81	9.64
si+o2 unannealed	1.61	19.86	12.36
si+o2 2h	4.19	7.5	1.79
si+o2 4h	1.53	14.47	9.48
si+o2 4h	2.66	10.93	4.11

Table 10-3 Set 1, Day 7: Low (x1000) and high magnification (x4000) SE images of MG63 cells cultured on 4 h annealed coatings. All images have the same scale bar as the top two images.

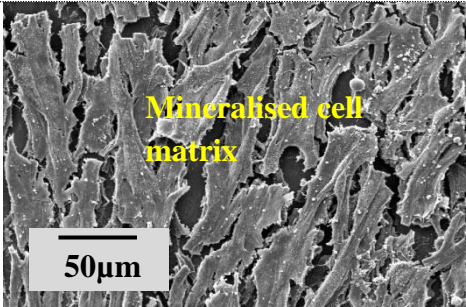
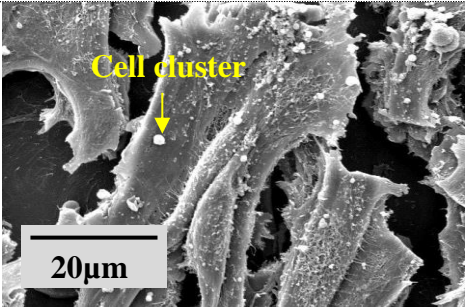
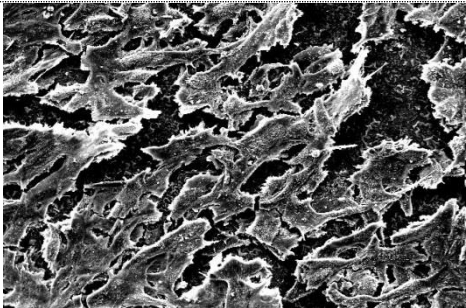
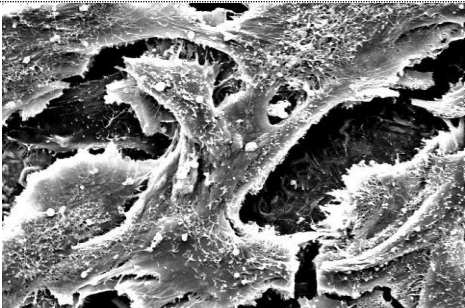
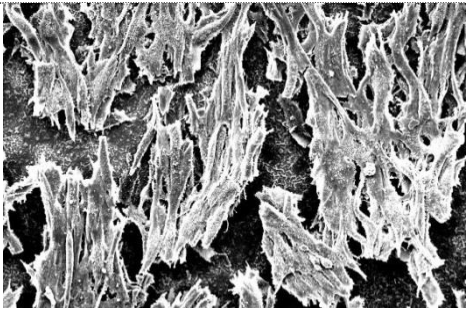
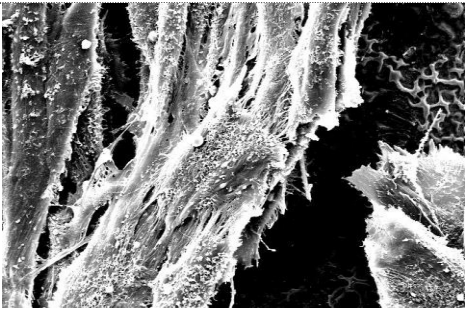
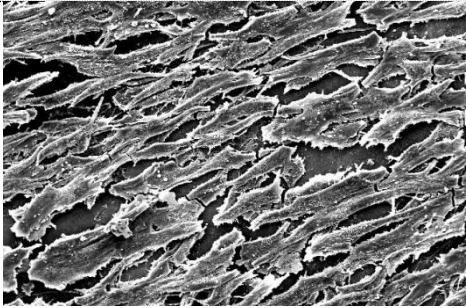
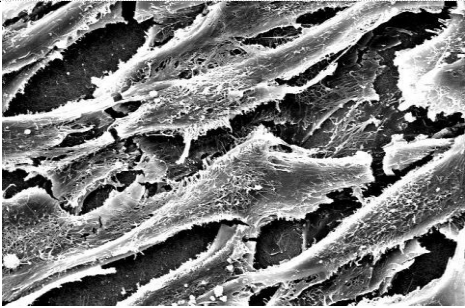
DAY 7	Annealed 700°C 4 h	
	x1000	x4000
HA/TiN		
Si:HA		
Si:HA/TiN		
Si+O ₂ :HA/TiN		

Table 10-4 Set 1, Day 14: Low (x1000) and high magnification (x4000) SE images of MG63 cells cultured on 2 h annealed coatings. All images have the same scale bar as the top two images.

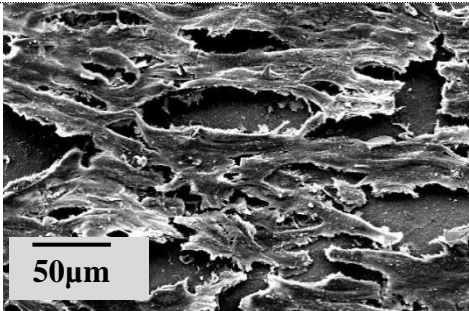
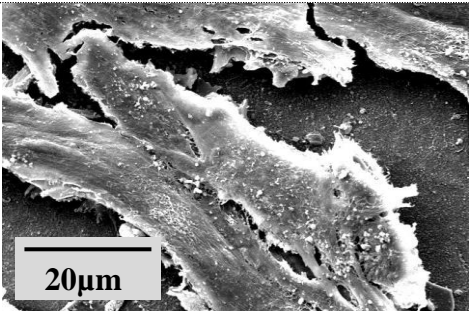
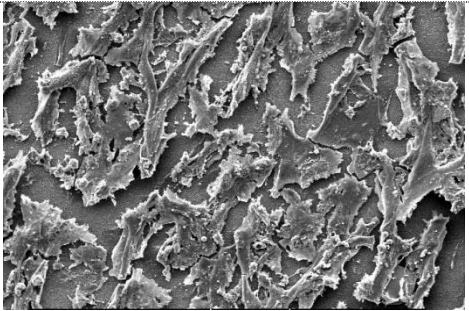
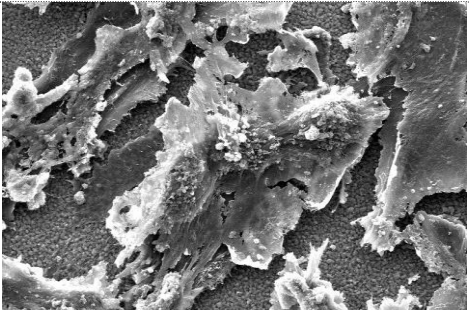
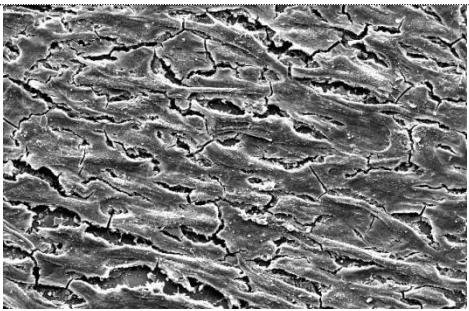
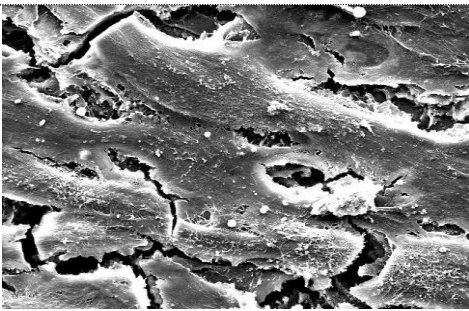
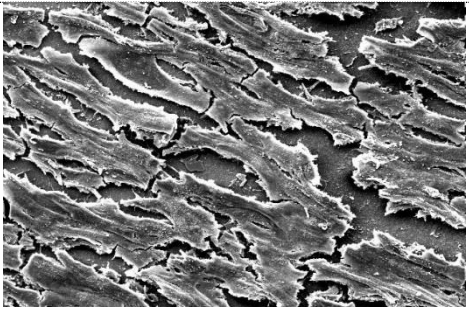
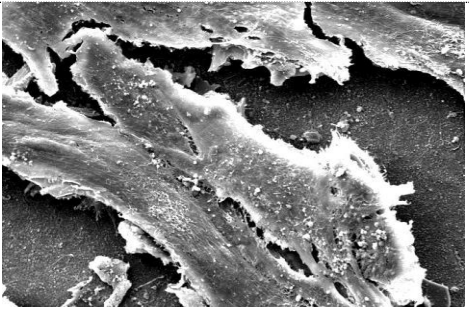
DAY 14	Annealed 700°C 2 h	
	x1000	x4000
HA/TiN		
Si:HA		
Si:HA/TiN		
Si+O ₂ :HA/TiN		

Table 10-5 Set 1, Day 14: Low (x1000) and high magnification (x4000) SE images of MG63 cells cultured on 4 h annealed coatings. All images have the same scale bar as the top two images.

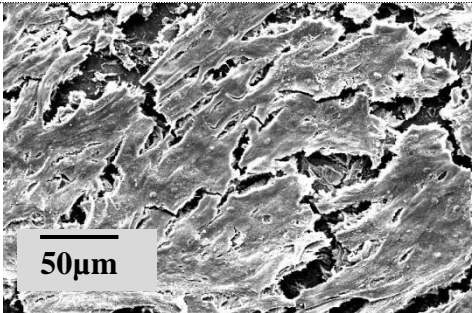
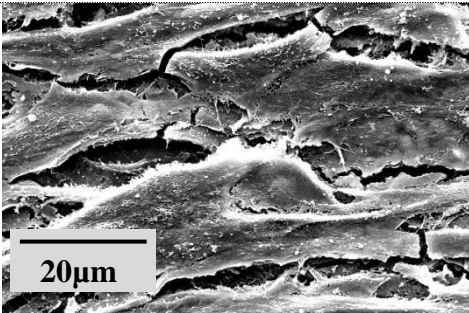
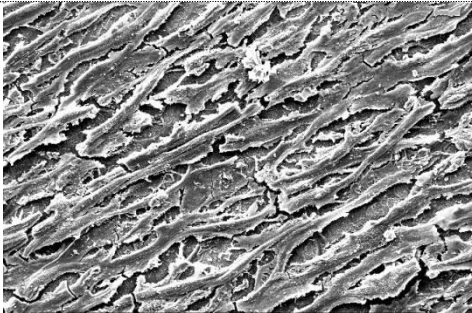
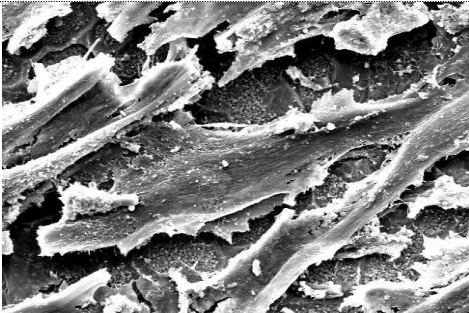
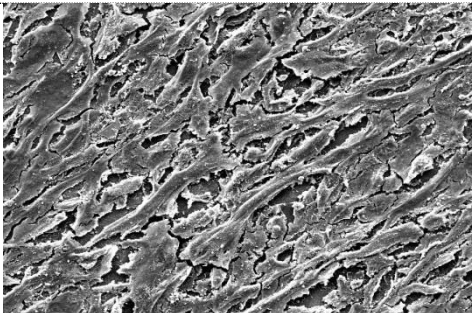
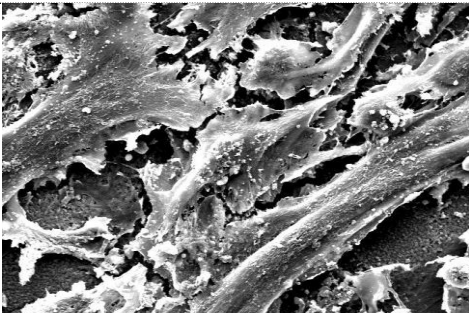
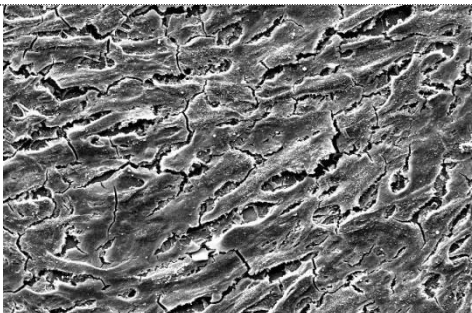
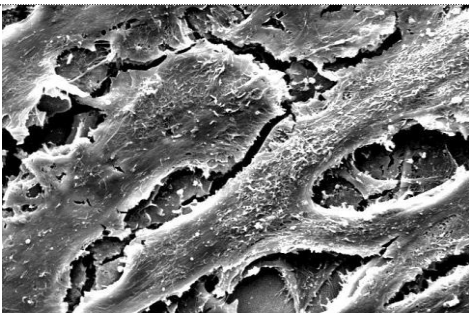
DAY 14	Annealed 700 ^o C 4 h	
	x1000	x4000
HA/TiN		
Si:HA		
Si:HA/TiN		
Si+O ₂ :HA/TiN		

Table 10-6 Set 2 Day 1: Low (x1000) and high magnification (x4000) SE images of MG63 cells cultured on 2 h annealed coatings. All images have the same scale bar as the top two images.

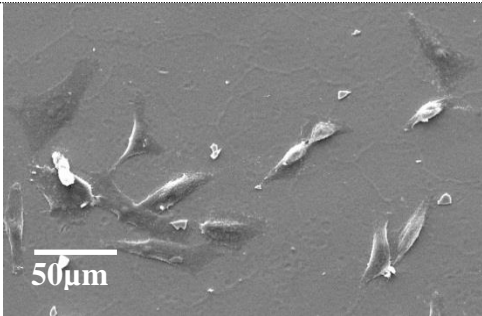
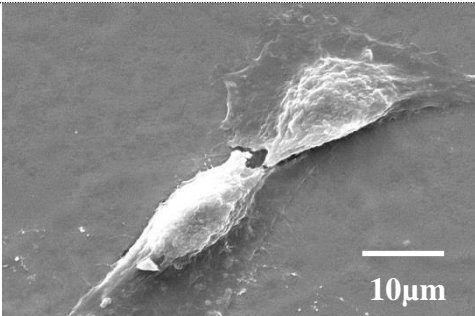
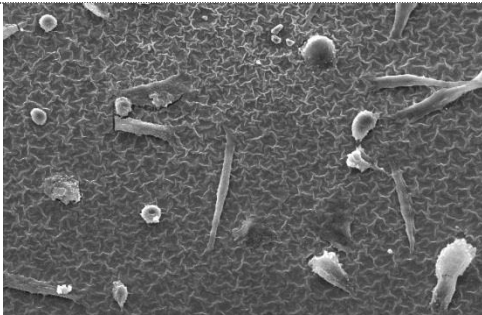
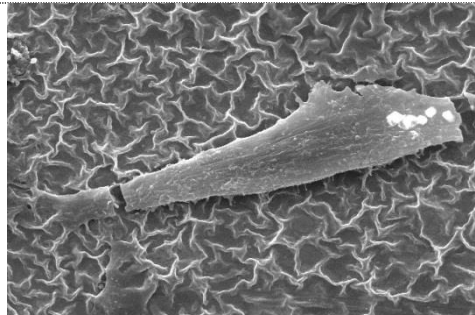
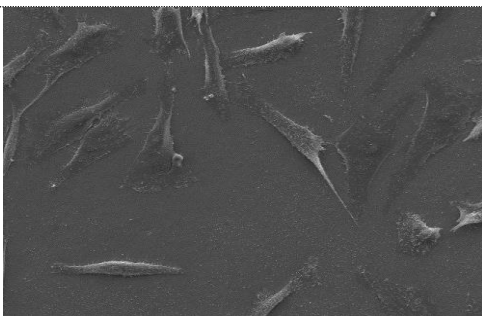
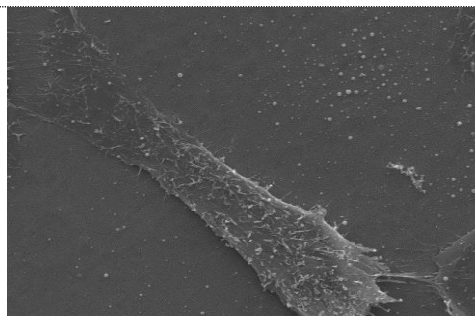
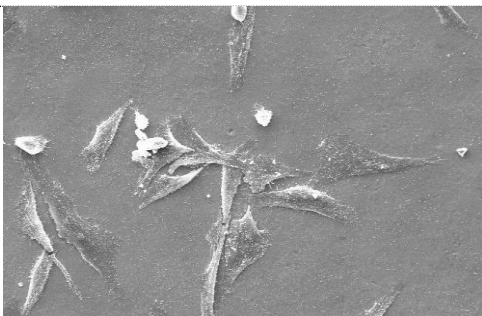
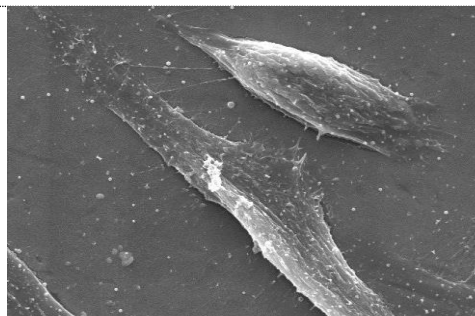
DAY 1	Annealed 700°C 2 h	
	x1000	x4000
HA/TiN		
Si:HA		
Si:HA/TiN		
Si+O ₂ :HA/TiN		

Table 10-7 Set 2, Day 7: Low (x1000) and high magnification (x4000) SE images of MG63 cells cultured on 2 h annealed coatings. All images have the same scale bar as the top two images.

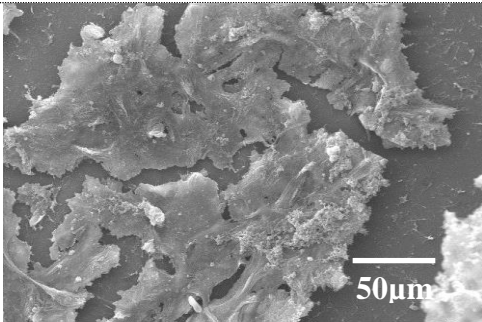
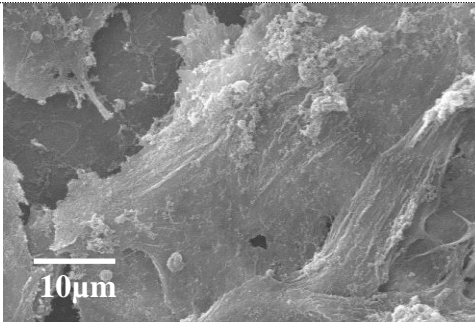
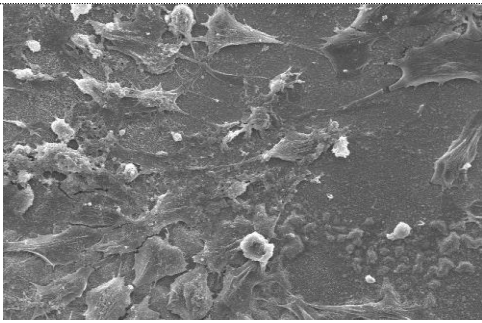
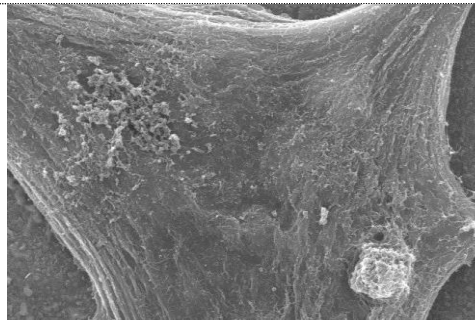
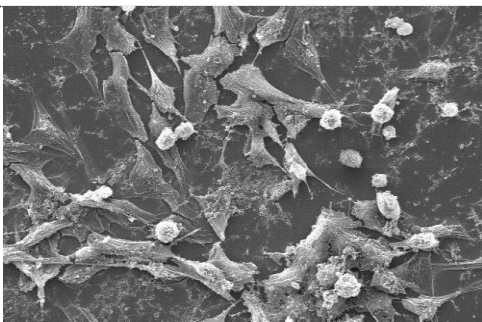
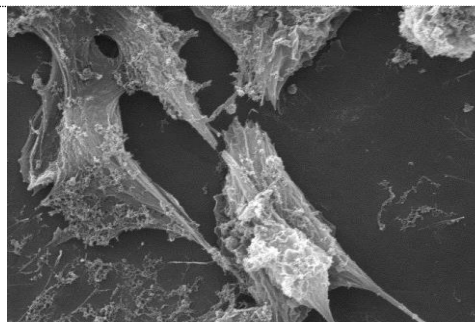
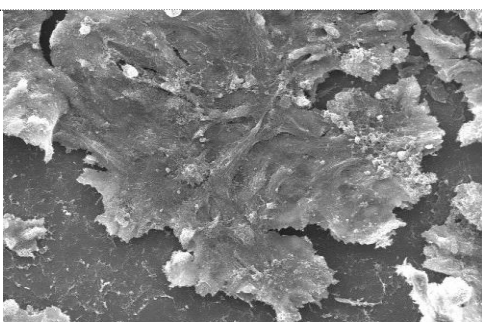
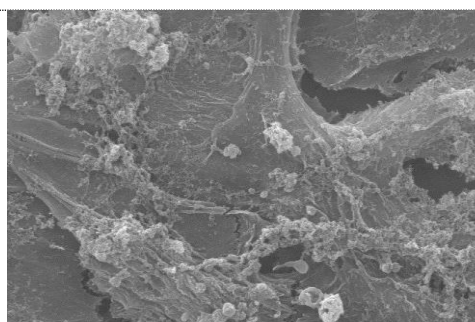
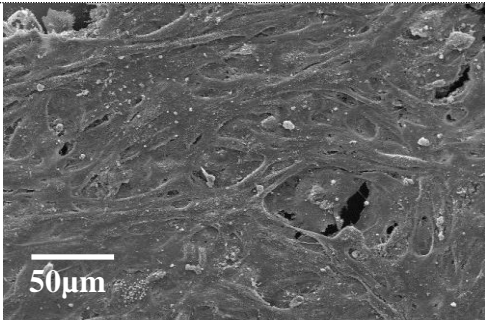
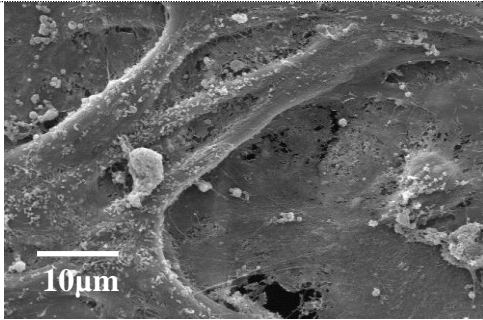
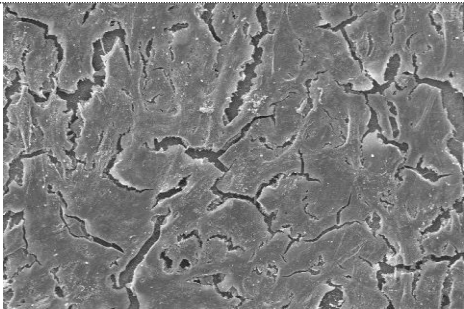
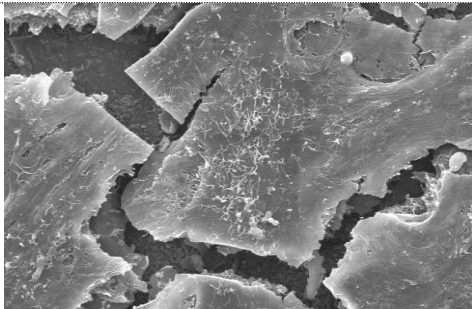
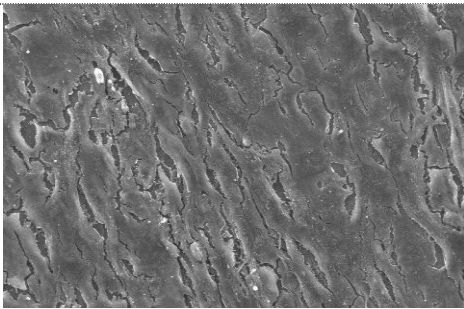
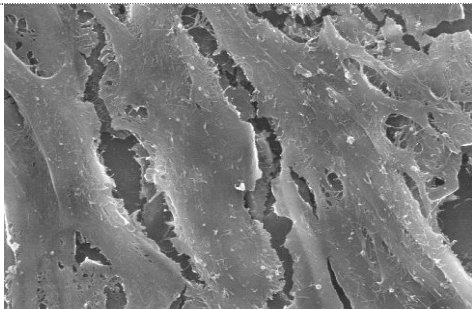
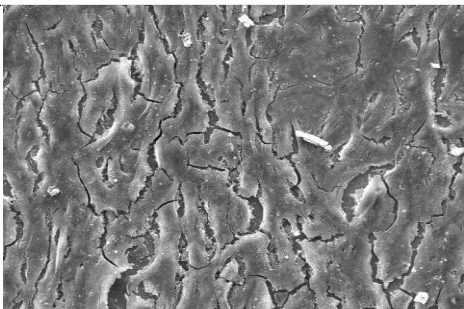
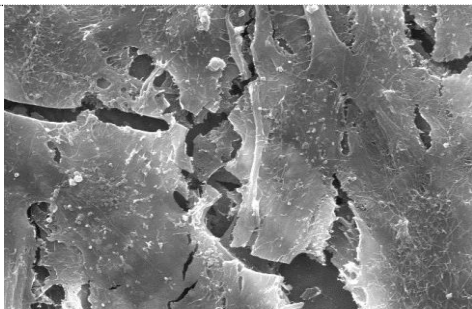
DAY 7	Annealed 700°C 2 h	
	x1000	x4000
HA/TiN		
Si:HA		
Si:HA/TiN		
Si+O ₂ :HA/TiN		

Table 10-8 Set 2, Day 14: Low (x1000) and high magnification (x4000) SE images of MG63 cells cultured on 2 h annealed coatings. All images have the same scale bar as the top two images.

DAY 14	Annealed 700°C 2 h	
	x1000	x4000
HA/TiN		
Si:HA		
Si:HA/TiN		
Si+O ₂ :HA/TiN		

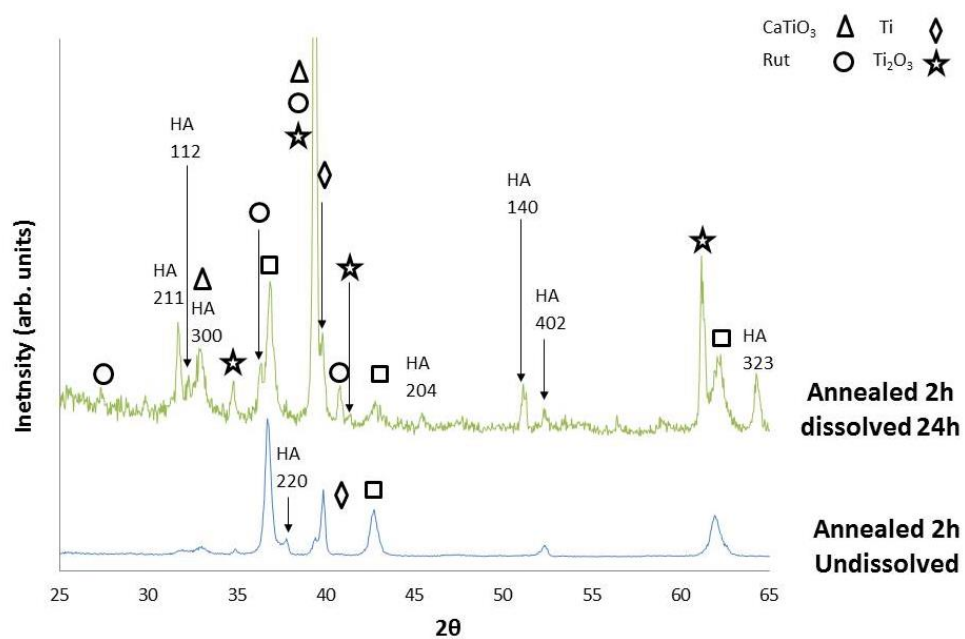


Figure 10-5 Si+O₂:HA/TiN from set 2, annealed for 2 h was dissolved for 24 h in ddH₂O.

Table 10-9 AlamarBlue

Number of comparisons per family	144	
Alpha	0.05	
Bonferroni's multiple comparisons test		
Day 1		
	Significant?	Adjusted P Value
HA TiN 2 h vs. HA TiN 4 h	ns	> 0.9999
HA TiN 2 h vs. Si:HA 2 h	ns	> 0.9999
HA TiN 2 h vs. Si:HA 4 h	ns	> 0.9999
HA TiN 2 h vs. Si:HA / TiN 2 h	ns	> 0.9999
HA TiN 2 h vs. Si:HA/ TiN 4 h	ns	> 0.9999
HA TiN 2 h vs. Si+O2:HA / TiN 2 h	ns	> 0.9999
HA TiN 2 h vs. Si+O2:HA / TiN 4 h	ns	> 0.9999
HA TiN 2 h vs. Ti	ns	> 0.9999
HA TiN 4 h vs. Si:HA 2 h	ns	> 0.9999
HA TiN 4 h vs. Si:HA 4 h	ns	> 0.9999
HA TiN 4 h vs. Si:HA / TiN 2 h	ns	> 0.9999
HA TiN 4 h vs. Si:HA/ TiN 4 h	ns	> 0.9999
HA TiN 4 h vs. Si+O2:HA / TiN 2 h	ns	> 0.9999
HA TiN 4 h vs. Si+O2:HA / TiN 4 h	ns	> 0.9999
HA TiN 4 h vs. Ti	ns	> 0.9999
Si:HA 2 h vs. Si:HA 4 h	ns	> 0.9999
Si:HA 2 h vs. Si:HA / TiN 2 h	ns	> 0.9999
Si:HA 2 h vs. Si:HA/ TiN 4 h	ns	> 0.9999
Si:HA 2 h vs. Si+O2:HA / TiN 2 h	ns	> 0.9999
Si:HA 2 h vs. Si+O2:HA / TiN 4 h	ns	> 0.9999
Si:HA 2 h vs. Ti	ns	> 0.9999
Si:HA 4 h vs. Si:HA / TiN 2 h	ns	> 0.9999
Si:HA 4 h vs. Si:HA/ TiN 4 h	ns	> 0.9999
Si:HA 4 h vs. Si+O2:HA / TiN 2 h	ns	> 0.9999
Si:HA 4 h vs. Si+O2:HA / TiN 4 h	ns	> 0.9999
Si:HA 4 h vs. Ti	ns	> 0.9999
Si:HA / TiN 2 h vs. Si:HA/ TiN 4 h	ns	> 0.9999
Si:HA / TiN 2 h vs. Si+O2:HA / TiN 2 h	ns	> 0.9999
Si:HA / TiN 2 h vs. Si+O2:HA / TiN 4 h	ns	> 0.9999
Si:HA / TiN 2 h vs. Ti	ns	> 0.9999
Si:HA/ TiN 4 h vs. Si+O2:HA / TiN 2 h	ns	> 0.9999
Si:HA/ TiN 4 h vs. Si+O2:HA / TiN 4 h	ns	> 0.9999

Si:HA/ TiN 4 h vs. Ti	ns	> 0.9999
Si+O2:HA / TiN 2 h vs. Si+O2:HA / TiN 4 h	ns	> 0.9999
Si+O2:HA / TiN 2 h vs. Ti	ns	> 0.9999
Si+O2:HA / TiN 4 h vs. Ti	ns	> 0.9999
Day 3		
HA TiN 2 h vs. HA TiN 4 h	ns	> 0.9999
HA TiN 2 h vs. Si:HA 2 h	ns	> 0.9999
HA TiN 2 h vs. Si:HA 4 h	ns	> 0.9999
HA TiN 2 h vs. Si:HA / TiN 2 h	ns	> 0.9999
HA TiN 2 h vs. Si:HA/ TiN 4 h	ns	> 0.9999
HA TiN 2 h vs. Si+O2:HA / TiN 2 h	ns	> 0.9999
HA TiN 2 h vs. Si+O2:HA / TiN 4 h	ns	> 0.9999
HA TiN 2 h vs. Ti	***	0.0005
HA TiN 4 h vs. Si:HA 2 h	ns	> 0.9999
HA TiN 4 h vs. Si:HA 4 h	ns	> 0.9999
HA TiN 4 h vs. Si:HA / TiN 2 h	ns	> 0.9999
HA TiN 4 h vs. Si:HA/ TiN 4 h	ns	> 0.9999
HA TiN 4 h vs. Si+O2:HA / TiN 2 h	ns	> 0.9999
HA TiN 4 h vs. Si+O2:HA / TiN 4 h	ns	> 0.9999
HA TiN 4 h vs. Ti	*	0.0138
Si:HA 2 h vs. Si:HA 4 h	ns	> 0.9999
Si:HA 2 h vs. Si:HA / TiN 2 h	ns	> 0.9999
Si:HA 2 h vs. Si:HA/ TiN 4 h	ns	> 0.9999
Si:HA 2 h vs. Si+O2:HA / TiN 2 h	ns	> 0.9999
Si:HA 2 h vs. Si+O2:HA / TiN 4 h	ns	> 0.9999
Si:HA 2 h vs. Ti	ns	0.8441
Si:HA 4 h vs. Si:HA / TiN 2 h	ns	> 0.9999
Si:HA 4 h vs. Si:HA/ TiN 4 h	ns	> 0.9999
Si:HA 4 h vs. Si+O2:HA / TiN 2 h	ns	> 0.9999
Si:HA 4 h vs. Si+O2:HA / TiN 4 h	ns	> 0.9999
Si:HA 4 h vs. Ti	**	0.0038
Si:HA / TiN 2 h vs. Si:HA/ TiN 4 h	ns	> 0.9999
Si:HA / TiN 2 h vs. Si+O2:HA / TiN 2 h	ns	> 0.9999
Si:HA / TiN 2 h vs. Si+O2:HA / TiN 4 h	ns	> 0.9999
Si:HA / TiN 2 h vs. Ti	**	0.0035
Si:HA/ TiN 4 h vs. Si+O2:HA / TiN 2 h	ns	> 0.9999
Si:HA/ TiN 4 h vs. Si+O2:HA / TiN 4 h	ns	> 0.9999
Si:HA/ TiN 4 h vs. Ti	**	0.0028
Si+O2:HA / TiN 2 h vs. Si+O2:HA / TiN 4 h	ns	> 0.9999
Si+O2:HA / TiN 2 h vs. Ti	ns	0.0787

Si+O2:HA / TiN 4 h vs. Ti	ns	> 0.9999
Day 7		
HA TiN 2 h vs. HA TiN 4 h	ns	> 0.9999
HA TiN 2 h vs. Si:HA 2 h	ns	> 0.9999
HA TiN 2 h vs. Si:HA 4 h	ns	> 0.9999
HA TiN 2 h vs. Si:HA / TiN 2 h	ns	0.4249
HA TiN 2 h vs. Si:HA/ TiN 4 h	ns	> 0.9999
HA TiN 2 h vs. Si+O2:HA / TiN 2 h	ns	> 0.9999
HA TiN 2 h vs. Si+O2:HA / TiN 4 h	ns	> 0.9999
HA TiN 2 h vs. Ti	ns	0.1793
HA TiN 4 h vs. Si:HA 2 h	ns	> 0.9999
HA TiN 4 h vs. Si:HA 4 h	ns	> 0.9999
HA TiN 4 h vs. Si:HA / TiN 2 h	ns	> 0.9999
HA TiN 4 h vs. Si:HA/ TiN 4 h	ns	> 0.9999
HA TiN 4 h vs. Si+O2:HA / TiN 2 h	ns	> 0.9999
HA TiN 4 h vs. Si+O2:HA / TiN 4 h	ns	> 0.9999
HA TiN 4 h vs. Ti	ns	> 0.9999
Si:HA 2 h vs. Si:HA 4 h	ns	> 0.9999
Si:HA 2 h vs. Si:HA / TiN 2 h	ns	> 0.9999
Si:HA 2 h vs. Si:HA/ TiN 4 h	ns	> 0.9999
Si:HA 2 h vs. Si+O2:HA / TiN 2 h	ns	> 0.9999
Si:HA 2 h vs. Si+O2:HA / TiN 4 h	ns	> 0.9999
Si:HA 2 h vs. Ti	ns	> 0.9999
Si:HA 4 h vs. Si:HA / TiN 2 h	ns	> 0.9999
Si:HA 4 h vs. Si:HA/ TiN 4 h	ns	> 0.9999
Si:HA 4 h vs. Si+O2:HA / TiN 2 h	ns	> 0.9999
Si:HA 4 h vs. Si+O2:HA / TiN 4 h	ns	> 0.9999
Si:HA 4 h vs. Ti	ns	> 0.9999
Si:HA / TiN 2 h vs. Si:HA/ TiN 4 h	ns	> 0.9999
Si:HA / TiN 2 h vs. Si+O2:HA / TiN 2 h	ns	> 0.9999
Si:HA / TiN 2 h vs. Si+O2:HA / TiN 4 h	ns	> 0.9999
Si:HA / TiN 2 h vs. Ti	ns	> 0.9999
Si:HA/ TiN 4 h vs. Si+O2:HA / TiN 2 h	ns	> 0.9999
Si:HA/ TiN 4 h vs. Si+O2:HA / TiN 4 h	ns	> 0.9999
Si:HA/ TiN 4 h vs. Ti	ns	> 0.9999
Si+O2:HA / TiN 2 h vs. Si+O2:HA / TiN 4 h	ns	> 0.9999
Si+O2:HA / TiN 2 h vs. Ti	ns	> 0.9999
Si+O2:HA / TiN 4 h vs. Ti	ns	> 0.9999
Day 14		
HA TiN 2 h vs. HA TiN 4 h	ns	> 0.9999
HA TiN 2 h vs. Si:HA 2 h	ns	> 0.9999

HA TiN 2 h vs. Si:HA 4 h	ns	> 0.9999
HA TiN 2 h vs. Si:HA / TiN 2 h	ns	> 0.9999
HA TiN 2 h vs. Si:HA/ TiN 4 h	ns	> 0.9999
HA TiN 2 h vs. Si+O2:HA / TiN 2 h	ns	> 0.9999
HA TiN 2 h vs. Si+O2:HA / TiN 4 h	ns	> 0.9999
HA TiN 2 h vs. Ti	ns	> 0.9999
HA TiN 4 h vs. Si:HA 2 h	ns	> 0.9999
HA TiN 4 h vs. Si:HA 4 h	ns	> 0.9999
HA TiN 4 h vs. Si:HA / TiN 2 h	ns	> 0.9999
HA TiN 4 h vs. Si:HA/ TiN 4 h	ns	> 0.9999
HA TiN 4 h vs. Si+O2:HA / TiN 2 h	ns	> 0.9999
HA TiN 4 h vs. Si+O2:HA / TiN 4 h	ns	> 0.9999
HA TiN 4 h vs. Ti	ns	> 0.9999
Si:HA 2 h vs. Si:HA 4 h	ns	> 0.9999
Si:HA 2 h vs. Si:HA / TiN 2 h	ns	> 0.9999
Si:HA 2 h vs. Si:HA/ TiN 4 h	ns	> 0.9999
Si:HA 2 h vs. Si+O2:HA / TiN 2 h	ns	> 0.9999
Si:HA 2 h vs. Si+O2:HA / TiN 4 h	ns	0.1387
Si:HA 2 h vs. Ti	ns	> 0.9999
Si:HA 4 h vs. Si:HA / TiN 2 h	ns	> 0.9999
Si:HA 4 h vs. Si:HA/ TiN 4 h	ns	> 0.9999
Si:HA 4 h vs. Si+O2:HA / TiN 2 h	ns	> 0.9999
Si:HA 4 h vs. Si+O2:HA / TiN 4 h	ns	0.0890
Si:HA 4 h vs. Ti	ns	> 0.9999
Si:HA / TiN 2 h vs. Si:HA/ TiN 4 h	ns	> 0.9999
Si:HA / TiN 2 h vs. Si+O2:HA / TiN 2 h	ns	> 0.9999
Si:HA / TiN 2 h vs. Si+O2:HA / TiN 4 h	ns	0.0558
Si:HA / TiN 2 h vs. Ti	ns	> 0.9999
Si:HA/ TiN 4 h vs. Si+O2:HA / TiN 2 h	ns	> 0.9999
Si:HA/ TiN 4 h vs. Si+O2:HA / TiN 4 h	ns	> 0.9999
Si:HA/ TiN 4 h vs. Ti	ns	> 0.9999
Si+O2:HA / TiN 2 h vs. Si+O2:HA / TiN 4 h	ns	
Si+O2:HA / TiN 2 h vs. Ti	ns	
Si+O2:HA / TiN 4 h vs. Ti	ns	

Table 10-10 DNA Hoechst Assay

Number of comparisons per family	144	
Alpha	0.05	
Bonferroni's multiple comparisons test		
	Significant?	Adjusted P Value
Day 1		
HA/TiN 2 h vs. HA/TiN 4 h	ns	> 0.9999
HA/TiN 2 h vs. Si:HA 2 h	ns	> 0.9999
HA/TiN 2 h vs. Si:HA 4 h	ns	> 0.9999
HA/TiN 2 h vs. Si:HA/TiN 2 h	ns	> 0.9999
HA/TiN 2 h vs. Si:HA/TiN 4 h	ns	> 0.9999
HA/TiN 2 h vs. Si+O ₂ :HA/TiN 2 h	ns	> 0.9999
HA/TiN 2 h vs. Si+O ₂ :HA/TiN 4 h	ns	> 0.9999
HA/TiN 2 h vs. Ti	ns	> 0.9999
HA/TiN 4 h vs. Si:HA 2 h	ns	> 0.9999
HA/TiN 4 h vs. Si:HA 4 h	ns	> 0.9999
HA/TiN 4 h vs. Si:HA/TiN 2 h	ns	> 0.9999
HA/TiN 4 h vs. Si:HA/TiN 4 h	ns	> 0.9999
HA/TiN 4 h vs. Si+O ₂ :HA/TiN 2 h	ns	> 0.9999
HA/TiN 4 h vs. Si+O ₂ :HA/TiN 4 h	ns	> 0.9999
HA/TiN 4 h vs. Ti	ns	> 0.9999
Si:HA 2 h vs. Si:HA 4 h	ns	> 0.9999
Si:HA 2 h vs. Si:HA/TiN 2 h	ns	> 0.9999
Si:HA 2 h vs. Si:HA/TiN 4 h	ns	> 0.9999
Si:HA 2 h vs. Si+O ₂ :HA/TiN 2 h	ns	> 0.9999
Si:HA 2 h vs. Si+O ₂ :HA/TiN 4 h	ns	> 0.9999
Si:HA 2 h vs. Ti	ns	> 0.9999
Si:HA 4 h vs. Si:HA/TiN 2 h	ns	> 0.9999
Si:HA 4 h vs. Si:HA/TiN 4 h	ns	> 0.9999
Si:HA 4 h vs. Si+O ₂ :HA/TiN 2 h	ns	> 0.9999
Si:HA 4 h vs. Si+O ₂ :HA/TiN 4 h	ns	> 0.9999
Si:HA 4 h vs. Ti	ns	> 0.9999
Si:HA/TiN 2 h vs. Si:HA/TiN 4 h	ns	> 0.9999

Si:HA/TiN 2 h vs. Si+O2:HA/TiN 2 h	ns	> 0.9999
Si:HA/TiN 2 h vs. Si+O2:HA/TiN 4 h	ns	> 0.9999
Si:HA/TiN 2 h vs. Ti	ns	> 0.9999
Si:HA/TiN 4 h vs. Si+O2:HA/TiN 2 h	ns	> 0.9999
Si:HA/TiN 4 h vs. Si+O2:HA/TiN 4 h	ns	> 0.9999
Si:HA/TiN 4 h vs. Ti	ns	> 0.9999
Si+O2:HA/TiN 2 h vs. Si+O2:HA/TiN 4 h	ns	> 0.9999
Si+O2:HA/TiN 2 h vs. Ti	ns	> 0.9999
Si+O2:HA/TiN 4 h vs. Ti	ns	> 0.9999
Day 3		
HA/TiN 2 h vs. HA/TiN 4 h	ns	> 0.9999
HA/TiN 2 h vs. Si:HA 2 h	ns	> 0.9999
HA/TiN 2 h vs. Si:HA 4 h	ns	> 0.9999
HA/TiN 2 h vs. Si:HA/TiN 2 h	ns	> 0.9999
HA/TiN 2 h vs. Si:HA/TiN 4 h	ns	> 0.9999
HA/TiN 2 h vs. Si+O2:HA/TiN 2 h	ns	> 0.9999
HA/TiN 2 h vs. Si+O2:HA/TiN 4 h	ns	> 0.9999
HA/TiN 2 h vs. Ti	ns	> 0.9999
HA/TiN 4 h vs. Si:HA 2 h	ns	> 0.9999
HA/TiN 4 h vs. Si:HA 4 h	ns	> 0.9999
HA/TiN 4 h vs. Si:HA/TiN 2 h	ns	> 0.9999
HA/TiN 4 h vs. Si:HA/TiN 4 h	ns	> 0.9999
HA/TiN 4 h vs. Si+O2:HA/TiN 2 h	ns	> 0.9999
HA/TiN 4 h vs. Si+O2:HA/TiN 4 h	ns	> 0.9999
HA/TiN 4 h vs. Ti	ns	> 0.9999
Si:HA 2 h vs. Si:HA 4 h	ns	> 0.9999
Si:HA 2 h vs. Si:HA/TiN 2 h	ns	> 0.9999
Si:HA 2 h vs. Si:HA/TiN 4 h	ns	> 0.9999
Si:HA 2 h vs. Si+O2:HA/TiN 2 h	ns	> 0.9999
Si:HA 2 h vs. Si+O2:HA/TiN 4 h	ns	> 0.9999
Si:HA 2 h vs. Ti	ns	> 0.9999
Si:HA 4 h vs. Si:HA/TiN 2 h	ns	> 0.9999
Si:HA 4 h vs. Si:HA/TiN 4 h	ns	> 0.9999
Si:HA 4 h vs. Si+O2:HA/TiN 2 h	ns	> 0.9999

Si:HA 4 h vs. Si+O2:HA/TiN 4 h	ns	> 0.9999
Si:HA 4 h vs. Ti	ns	> 0.9999
Si:HA/TiN 2 h vs. Si:HA/TiN 4 h	ns	> 0.9999
Si:HA/TiN 2 h vs. Si+O2:HA/TiN 2 h	ns	> 0.9999
Si:HA/TiN 2 h vs. Si+O2:HA/TiN 4 h	ns	> 0.9999
Si:HA/TiN 2 h vs. Ti	ns	> 0.9999
Si:HA/TiN 4 h vs. Si+O2:HA/TiN 2 h	ns	> 0.9999
Si:HA/TiN 4 h vs. Si+O2:HA/TiN 4 h	ns	> 0.9999
Si:HA/TiN 4 h vs. Ti	ns	> 0.9999
Si+O2:HA/TiN 2 h vs. Si+O2:HA/TiN 4 h	ns	> 0.9999
Si+O2:HA/TiN 2 h vs. Ti	ns	> 0.9999
Si+O2:HA/TiN 4 h vs. Ti	ns	> 0.9999
Day 7		
HA/TiN 2 h vs. HA/TiN 4 h	ns	> 0.9999
HA/TiN 2 h vs. Si:HA 2 h	ns	> 0.9999
HA/TiN 2 h vs. Si:HA 4 h	ns	> 0.9999
HA/TiN 2 h vs. Si:HA/TiN 2 h	ns	> 0.9999
HA/TiN 2 h vs. Si:HA/TiN 4 h	ns	> 0.9999
HA/TiN 2 h vs. Si+O2:HA/TiN 2 h	ns	> 0.9999
HA/TiN 2 h vs. Si+O2:HA/TiN 4 h	ns	> 0.9999
HA/TiN 2 h vs. Ti	ns	> 0.9999
HA/TiN 4 h vs. Si:HA 2 h	ns	> 0.9999
HA/TiN 4 h vs. Si:HA 4 h	ns	> 0.9999
HA/TiN 4 h vs. Si:HA/TiN 2 h	ns	> 0.9999
HA/TiN 4 h vs. Si:HA/TiN 4 h	ns	> 0.9999
HA/TiN 4 h vs. Si+O2:HA/TiN 2 h	ns	> 0.9999
HA/TiN 4 h vs. Si+O2:HA/TiN 4 h	ns	> 0.9999
HA/TiN 4 h vs. Ti	ns	> 0.9999
Si:HA 2 h vs. Si:HA 4 h	ns	> 0.9999
Si:HA 2 h vs. Si:HA/TiN 2 h	ns	> 0.9999
Si:HA 2 h vs. Si:HA/TiN 4 h	ns	> 0.9999
Si:HA 2 h vs. Si+O2:HA/TiN 2 h	ns	> 0.9999
Si:HA 2 h vs. Si+O2:HA/TiN 4 h	ns	> 0.9999

Si:HA 2 h vs. Ti	ns	> 0.9999
Si:HA 4 h vs. Si:HA/TiN 2 h	ns	> 0.9999
Si:HA 4 h vs. Si:HA/TiN 4 h	ns	> 0.9999
Si:HA 4 h vs. Si+O2:HA/TiN 2 h	ns	> 0.9999
Si:HA 4 h vs. Si+O2:HA/TiN 4 h	ns	> 0.9999
Si:HA 4 h vs. Ti	ns	0.3528
Si:HA/TiN 2 h vs. Si:HA/TiN 4 h	ns	> 0.9999
Si:HA/TiN 2 h vs. Si+O2:HA/TiN 2 h	ns	> 0.9999
Si:HA/TiN 2 h vs. Si+O2:HA/TiN 4 h	ns	> 0.9999
Si:HA/TiN 2 h vs. Ti	ns	> 0.9999
Si:HA/TiN 4 h vs. Si+O2:HA/TiN 2 h	ns	> 0.9999
Si:HA/TiN 4 h vs. Si+O2:HA/TiN 4 h	ns	0.4688
Si:HA/TiN 4 h vs. Ti	ns	0.0861
Si+O2:HA/TiN 2 h vs. Si+O2:HA/TiN 4 h	ns	> 0.9999
Si+O2:HA/TiN 2 h vs. Ti	ns	> 0.9999
Si+O2:HA/TiN 4 h vs. Ti	ns	> 0.9999
Day 14		
HA/TiN 2 h vs. HA/TiN 4 h	ns	> 0.9999
HA/TiN 2 h vs. Si:HA 2 h	ns	> 0.9999
HA/TiN 2 h vs. Si:HA 4 h	ns	> 0.9999
HA/TiN 2 h vs. Si:HA/TiN 2 h	ns	> 0.9999
HA/TiN 2 h vs. Si:HA/TiN 4 h	ns	> 0.9999
HA/TiN 2 h vs. Si+O2:HA/TiN 2 h	ns	> 0.9999
HA/TiN 2 h vs. Si+O2:HA/TiN 4 h	ns	> 0.9999
HA/TiN 2 h vs. Ti	ns	> 0.9999
HA/TiN 4 h vs. Si:HA 2 h	ns	> 0.9999
HA/TiN 4 h vs. Si:HA 4 h	ns	> 0.9999
HA/TiN 4 h vs. Si:HA/TiN 2 h	ns	> 0.9999
HA/TiN 4 h vs. Si:HA/TiN 4 h	ns	> 0.9999
HA/TiN 4 h vs. Si+O2:HA/TiN 2 h	ns	> 0.9999
HA/TiN 4 h vs. Si+O2:HA/TiN 4 h	ns	> 0.9999
HA/TiN 4 h vs. Ti	ns	0.7424
Si:HA 2 h vs. Si:HA 4 h	ns	> 0.9999
Si:HA 2 h vs. Si:HA/TiN 2 h	ns	> 0.9999

Si:HA 2 h vs. Si:HA/TiN 4 h	ns	> 0.9999
Si:HA 2 h vs. Si+O2:HA/TiN 2 h	ns	0.7424
Si:HA 2 h vs. Si+O2:HA/TiN 4 h	ns	> 0.9999
Si:HA 2 h vs. Ti	ns	0.0956
Si:HA 4 h vs. Si:HA/TiN 2 h	ns	> 0.9999
Si:HA 4 h vs. Si:HA/TiN 4 h	ns	0.2165
Si:HA 4 h vs. Si+O2:HA/TiN 2 h	ns	0.1062
Si:HA 4 h vs. Si+O2:HA/TiN 4 h	ns	0.6781
Si:HA 4 h vs. Ti	*	0.0102
Si:HA/TiN 2 h vs. Si:HA/TiN 4 h	ns	0.5147
Si:HA/TiN 2 h vs. Si+O2:HA/TiN 2 h	ns	0.2638
Si:HA/TiN 2 h vs. Si+O2:HA/TiN 4 h	ns	> 0.9999
Si:HA/TiN 2 h vs. Ti	*	0.0289
Si:HA/TiN 4 h vs. Si+O2:HA/TiN 2 h	ns	> 0.9999
Si:HA/TiN 4 h vs. Si+O2:HA/TiN 4 h	ns	> 0.9999
Si:HA/TiN 4 h vs. Ti	ns	> 0.9999
Si+O2:HA/TiN 2 h vs. Si+O2:HA/TiN 4 h	ns	> 0.9999
Si+O2:HA/TiN 2 h vs. Ti	ns	> 0.9999
Si+O2:HA/TiN 4 h vs. Ti	ns	> 0.9999

Table 10-11 Alkaline phosphatase

Number of comparisons per family	72	
Alpha	0.05	
Bonferroni's multiple comparisons test		
	Significant?	Adjusted P Value
Day 7		
HA/TiN 2 h vs. HA/TiN 4 h	ns	> 0.9999
HA/TiN 2 h vs. Si:HA 2 h	ns	> 0.9999
HA/TiN 2 h vs. Si:HA 4 h	ns	> 0.9999
HA/TiN 2 h vs. Si:HA/TiN 2 h	ns	> 0.9999

HA/TiN 2 h vs. Si:HA/TiN 4 h	ns	> 0.9999
HA/TiN 2 h vs. Si+O ₂ :HA/TiN 2 h	ns	> 0.9999
HA/TiN 2 h vs. Si+O ₂ :HA/TiN 4 h	ns	> 0.9999
HA/TiN 2 h vs. Ti	ns	> 0.9999
HA/TiN 4 h vs. Si:HA 2 h	ns	> 0.9999
HA/TiN 4 h vs. Si:HA 4 h	ns	> 0.9999
HA/TiN 4 h vs. Si:HA/TiN 2 h	ns	> 0.9999
HA/TiN 4 h vs. Si:HA/TiN 4 h	ns	> 0.9999
HA/TiN 4 h vs. Si+O ₂ :HA/TiN 2 h	ns	> 0.9999
HA/TiN 4 h vs. Si+O ₂ :HA/TiN 4 h	ns	> 0.9999
HA/TiN 4 h vs. Ti	ns	> 0.9999
Si:HA 2 h vs. Si:HA 4 h	ns	> 0.9999
Si:HA 2 h vs. Si:HA/TiN 2 h	ns	> 0.9999
Si:HA 2 h vs. Si:HA/TiN 4 h	ns	> 0.9999
Si:HA 2 h vs. Si+O ₂ :HA/TiN 2 h	ns	> 0.9999
Si:HA 2 h vs. Si+O ₂ :HA/TiN 4 h	ns	> 0.9999
Si:HA 2 h vs. Ti	ns	> 0.9999
Si:HA 4 h vs. Si:HA/TiN 2 h	ns	> 0.9999
Si:HA 4 h vs. Si:HA/TiN 4 h	ns	> 0.9999
Si:HA 4 h vs. Si+O ₂ :HA/TiN 2 h	ns	> 0.9999
Si:HA 4 h vs. Si+O ₂ :HA/TiN 4 h	ns	> 0.9999
Si:HA 4 h vs. Ti	ns	> 0.9999
Si:HA/TiN 2 h vs. Si:HA/TiN 4 h	ns	> 0.9999
Si:HA/TiN 2 h vs. Si+O ₂ :HA/TiN 2 h	ns	> 0.9999
Si:HA/TiN 2 h vs. Si+O ₂ :HA/TiN 4 h	ns	> 0.9999
Si:HA/TiN 2 h vs. Ti	ns	> 0.9999
Si:HA/TiN 4 h vs. Si+O ₂ :HA/TiN 2 h	ns	> 0.9999
Si:HA/TiN 4 h vs. Si+O ₂ :HA/TiN 4 h	ns	> 0.9999
Si:HA/TiN 4 h vs. Ti	ns	> 0.9999
Si+O ₂ :HA/TiN 2 h vs. Si+O ₂ :HA/TiN 4 h	ns	> 0.9999
Si+O ₂ :HA/TiN 2 h vs. Ti	ns	> 0.9999
Si+O ₂ :HA/TiN 4 h vs. Ti	ns	> 0.9999
Day 14		
HA/TiN 2 h vs. HA/TiN 4 h	ns	> 0.9999
HA/TiN 2 h vs. Si:HA 2 h	ns	> 0.9999
HA/TiN 2 h vs. Si:HA 4 h	ns	> 0.9999
HA/TiN 2 h vs. Si:HA/TiN 2 h	ns	> 0.9999
HA/TiN 2 h vs. Si:HA/TiN 4 h	ns	> 0.9999
HA/TiN 2 h vs. Si+O ₂ :HA/TiN 2 h	ns	> 0.9999
HA/TiN 2 h vs. Si+O ₂ :HA/TiN 4 h	ns	> 0.9999
HA/TiN 2 h vs. Ti	ns	> 0.9999
HA/TiN 4 h vs. Si:HA 2 h	ns	> 0.9999
HA/TiN 4 h vs. Si:HA 4 h	ns	> 0.9999
HA/TiN 4 h vs. Si:HA/TiN 2 h	ns	> 0.9999
HA/TiN 4 h vs. Si:HA/TiN 4 h	ns	> 0.9999

HA/TiN 4 h vs. Si+O ₂ :HA/TiN 2 h	ns	> 0.9999
HA/TiN 4 h vs. Si+O ₂ :HA/TiN 4 h	ns	> 0.9999
HA/TiN 4 h vs. Ti	ns	> 0.9999
Si:HA 2 h vs. Si:HA 4 h	ns	> 0.9999
Si:HA 2 h vs. Si:HA/TiN 2 h	ns	> 0.9999
Si:HA 2 h vs. Si:HA/TiN 4 h	ns	> 0.9999
Si:HA 2 h vs. Si+O ₂ :HA/TiN 2 h	ns	> 0.9999
Si:HA 2 h vs. Si+O ₂ :HA/TiN 4 h	ns	> 0.9999
Si:HA 2 h vs. Ti	ns	> 0.9999
Si:HA 4 h vs. Si:HA/TiN 2 h	ns	> 0.9999
Si:HA 4 h vs. Si:HA/TiN 4 h	ns	> 0.9999
Si:HA 4 h vs. Si+O ₂ :HA/TiN 2 h	ns	> 0.9999
Si:HA 4 h vs. Si+O ₂ :HA/TiN 4 h	ns	> 0.9999
Si:HA 4 h vs. Ti	ns	> 0.9999
Si:HA/TiN 2 h vs. Si:HA/TiN 4 h	ns	> 0.9999
Si:HA/TiN 2 h vs. Si+O ₂ :HA/TiN 2 h	ns	> 0.9999
Si:HA/TiN 2 h vs. Si+O ₂ :HA/TiN 4 h	ns	> 0.9999
Si:HA/TiN 2 h vs. Ti	ns	> 0.9999
Si:HA/TiN 4 h vs. Si+O ₂ :HA/TiN 2 h	ns	> 0.9999
Si:HA/TiN 4 h vs. Si+O ₂ :HA/TiN 4 h	ns	> 0.9999
Si:HA/TiN 4 h vs. Ti	ns	> 0.9999
Si+O ₂ :HA/TiN 2 h vs. Si+O ₂ :HA/TiN 4 h	ns	> 0.9999
Si+O ₂ :HA/TiN 2 h vs. Ti	ns	> 0.9999
Si+O ₂ :HA/TiN 4 h vs. Ti	ns	> 0.9999